Multiphoton dynamics and energetics of halogen containing reagents by mass resolved REMPI and velocity map imaging

Arnar Hafliðason

Faculty of Physical Sciences
University of Iceland
2018

Multiphoton dynamics and energetics of halogen containing reagents by mass resolved REMPI and velocity map imaging

Arnar Hafliðason

Dissertation submitted in partial fulfilment of a
Philosophiae Doctor degree in chemistry

Advisor
Ágúst Kvaran

Co-Advisor
Huasheng Wang

PhD Committee
Gísli Jóhannesson
Kristján Matthíasson
Ragnar Björnsson

Opponents
Ragnar Jóhannsson
Timothy Wright

Faculty of Physical Sciences
School of Engineering and Natural Sciences
University of Iceland
Reykjavik, December 2018

Multiphoton dynamics and energetics of halogen containing reagents by mass resolved REMPI and velocity map imaging

Dynamics & energetics of halogen containing reagents

Dissertation submitted in partial fulfilment of a *Philosophiae Doctor* degree in chemistry

Faculty of Natural Sciences
School of Engineering and Natural Sciences
University of Iceland
Dunhagi 3
107, Reykjavik
Iceland

Telephone: 525 4000

Bibliographic information:
Arnar Hafliðason, 2018, *Multiphoton dynamics and energetics of halogen containing reagents by mass resolved REMPI and velocity map imaging*, PhD dissertation, Faculty of Natural Sciences, University of Iceland.

Author ORCID: 0000-0003-4769-8138

ISBN 978-9935-9320-9-9

Printing: Háskólaprent ehf, Fálkagata 2, 107 Reykjavík.
Reykjavik, Iceland, December 2018

Abstract

The research focused on multiphoton dynamics and fragment formation for HBr, DCl, and bromomethanes, using mass resolved multiphoton ionization (MR-MPI) and velocity map imaging (VMI) techniques. Data interpretations were based on analysis of (2+n)REMPI spectra, kinetic energy release spectra (KERs) and angular distributions of ions formed.

Experiments for HBr revealed perturbations due to interactions between triplet ($^3\Sigma$) and singlet ($^1\Sigma$) states, seen as line-shifts (LS) and line-intensity (LI) alterations in MR-REMPI spectra, and intensity anomalies in VMI data.

DCl studies revealed five new Rydberg states, and eight new vibrational states of the ion-pair state, as well as strong perturbation effects between $^1\Sigma$ Rydberg and $^1\Sigma$ ion-pair state, seen as LS and LI effects, and chlorine isotope shifts. Comparison with analogous data for HCl was performed.

Highly perturbed spectral region of four Rydberg states in CH and CD, caused by interaction with a repulsive state, was inspected via multiphoton photodissociation of bromoform in MR-REMPI. In addition to LS and LI effects, linewidth (LW) broadenings, were evident. Four band origins were assigned.

A number of Rydberg states of CH_3Br in two-photon excitation region of 66 000 – 80 000 cm^{-1} were resonantly excited. The multiphoton dynamics was explored with both one- and two-colour excitation schemes. One-, two- and three- photon initial excitations were found to form ground state fragments CH_3 and Br/Br*, whereas CH_3 Rydberg states along with Br/Br* were found to be the major products following three-photon excitations prior to ionization. Interaction between Rydberg and ion-pair states is found to be evident.

Útdráttur

Rannsóknirnar fólust einkum í að kanna áhrif fjölljóseindaörvunar á rofferli HBr, DC l og brómometan sameinda með massagreiningu (MR-MPI aðferð) og myndgreiningu (VMI). Túlkun mæligagna fólst í greiningu á fjölljóseindarófum ((2+n)REMPI róf) sem og á hraða- (KERs) og hornháðum dreifimynstrum jóna sem myndast.

Athuganir á HBr sýndu truflanir vegna víxlverkana á milli þrístigs- og einstigs-orkuástanda sameindarinnar, sem birtust í formi hliðrunar (LS áhrif) og styrkbreytinga (LI áhrif) litrófslína í MR-REMPI litrófum sem og í formi óreglulegra mynstra í VMI myndum.

Samkvæmt DCl mæligögnum fundust fimm ný Rydberg orkuástönd og átta ný titringsástönd jón-para forms sameindarinnar. Sterk víxlverkunaráhrif greindust milli einstigs Rydberg ástanda og jón-para ástandsins sem birtist í formi LS og LI áhrifa og sem samsætuhliðranir. Framkvæmdur var samanburður við sambærileg gögn frá HCl.

Óreglulegt mynstur REMPI litrófa fyrir sameindabrotin CH og CD sem mynduðust við fjölljóseindarof bromoforms báru vitni um hraðvirka rofnun fjögurra Rydberg ástanda. LS og LI áhrif sem og breikkun litrófslína báru þessu vitni. Orka viðkomandi ástanda var auðkennd.

Fjölmörg Rydberg ástönd CH_3Br sameindarinnar voru orkuörvuð á tveggja ljóseinda bylgjutölusviðinu 66 000 – 80 000 cm^{-1}. Rofferli voru könnuð með aðferðum eins- og tvílita fjölljóseindaörvana. Einnar-, tveggja og þriggja ljóseinda örvanir sameindarinnar leiddu allar til myndunar sameindabrotanna CH_3 og Br í grunn-rafeindaástöndum. Meginrofferli sameindarinnar var hins vegar myndun CH_3 Rydberg ástanda ásamt bróm frumeindum í kjölfar þriggja ljóseinda örvunarinnar. Vísbendingar um víxlverkun milli Rydberg ástanda og jón-para ástanda fundust.

For my daughter Elísa Nightingale

Table of Contents

List of Figures

List of Tables

Abbreviations

2D – Two dimensional

3D – Three dimensional

BBO – β-BaB_2O_4 or beta-barium borate

CCD – Charge Coupled Device

CH – Methylidyne

CH_3Br – Bromomethane

CH_2Br_2 – Dibromomethane

$CHBr_3$ – Bromoform

CBr_4 – Tetrabromomethane

$CDBr_3$ – Deuterium bromoform

DCl – Deuterium chloride

FCF – Franck Condon Factor

HBr – Hydrogen bromide

HCl – Hydrogen chloride

KDP – KH_2PO_4 or Potassium dihydrogen phosphate

LCAO – Linear Combination of Atomic Orbitals

LI – Line-Intensity

LS – Line-Shift

LW – Line-Width

MCP – Micro Channel Plate

O_3 – Ozone

REMPI – Resonance Enhanced Multi-Photon Ionization

SHG – Second Harmonic Generator

TOF – Time-Of-Flight

VMI – Velocity Map Imaging

Acknowledgements

First and foremost, I would like to thank my supervisor, Prof. Ágúst Kvaran. He was the reason for me to choose physical chemistry, as his approach on the subject inspired me and made me want to dig deeper. Ágúst is also a great friend and our talks in his office often strayed from experimental subjects and intellectual conversations onto paths of laughter and jokes, which is, in my mind, a very important factor in a good working relationship.

The master of our experimental setup, Viktor Huasheng Wang is a delight to work with and always able to find a way to get the best out of the instruments.

Dr. Helgi Rafn Hróðmarsson, for assistance, companionship and inspiring conversations about the extraordinary world of quantum chemistry.

Our co-authors in Crete, Dr. Pavle Glodic, Greta Koumarianou and Dr. Petros C. Samartzis. Petros also gave me good hints regarding the VMI chapter of my thesis and I thank him for that.

The doctoral committee, Gísli Hólmar Jóhannesson, Kristján Matthíasson, Ragnar Björnsson, for believing in me on this journey.

My family and friends, especially my mother Arndís, my brother Siggi and daughter Elísa. Elísa is the light of my life and she gave me extra strength to carry on when things looked difficult.

The financial support from The Icelandic Science Foundation (RANNÍS) and the Assistantship fund of the University of Iceland, is acknowledged.

Finally, my girlfriend Golda, which was supportive the whole time and gave me good advises along the way. Being a chemist herself, she was able to understand, better, the hard times I was going through as well as the good times.

1 Introduction

Wave-particle duality, i.e. the ability to possess both wave and particle-like characteristics, is a fundamental property of light.[1] A particle of light, i.e. photon, can appear as an electromagnetic wave of various wavelengths. The wavelength of a photon determines its energy. A photon is one of the fundamental elementary particles, and it is the force carrier of electromagnetism in the electromagnetic field. Atoms and molecular species, as well as their electrons, can couple to an electromagnetic radiation. Shining a photon at the electric cloud of a molecule, can cause, the photon to pass, scatter or absorb. Spectroscopic studies focuses on light-matter interaction, the cause and effect of photons interacting with atoms or molecules.[2] Spectroscopic studies of compounds can be conducted for different physical states.[3-8] Thus, gas-phase spectroscopy investigates matter in gas phase, etc. It is useful to apply a coherent beam of light from a laser for such spectroscopic studies. Directing a laser pulse with a well-defined photon energy, at a molecule, can result in photon absorption of the molecule due to energy transfer between quantum energy levels. This can be followed by reactions, molecular dissociation (i.e. photodissociation) or ionization (i.e. photo-ionization) processes. The energy of the absorbed photon can then be associated with the nature of the quantized energy of the molecule, to give insight into the infrastructure of the molecule, such as about vibrational frequencies and binding energies.[9]

Standard absorption spectroscopy, corresponding to one-photon absorption and multi-photon spectroscopy of di- and polyatomic molecules, such as the hydrogen halides[6, 8, 10-34] and the methyl halides[7, 35-55] have been studied quite thoroughly for many years. Most studies have been performed in the low energy region corresponding to the existence of the valence electron in low lying molecular orbitals (the valence state region)[36, 37, 45, 48, 53, 56, 57], whereas less work has been on higher energy states, such as the Rydberg states[42, 43, 46, 58, 59] (the Rydberg state region) of these molecules. The fundamental difference between standard absorption spectroscopy and multiphoton absorption spectroscopy is based on the number of photons used to energy excite the molecules. Thus, a one-photon standard absorption process is limited by selection rules, which only allow transitions between quantum levels which differ by one quantum number or less (e.g. orbital angular momentum difference of $\Delta\Lambda = \pm 1$)[60, 61]. In contrast, more variations are possible for multiphoton excitations (e.g. $\Delta\Lambda = 0$, $\Delta\Lambda = \pm 1$, $\Delta\Lambda = \pm 2$ etc.) depending on the number of photons used.[60, 61] A typical ionization study for multiphoton absorption in gas phase, includes a jet-stream injection of a gas sample into a vacuum chamber where it forms a molecular beam. At a focal point, where a laser pulse beam crosses a molecular beam, molecules (e.g. AB) can for example i) ionize to form AB^+ and an electron (e) or ii) break into fragments (e.g. A + B) prior to further photoionization (e.g. formation of $A^+ + e^- + B$ or $A + B^+ + e^-$). Dynamics of these processes can further be analyzed with various detection methods, e.g. mass spectrometric detection, photoelectron detection and product imaging, to name a few. Further illustration of the processes mentioned above can be see here (see eq. 1 and 2),

Process i)

Step.1	$AB + nh\nu \rightarrow AB^*$	Excitation	(1a)
Step.2	$AB^* + h\nu \rightarrow AB^+ + e^-$	Ionization	(1b)

Process ii)

Step.1	$AB + nh\nu \rightarrow AB^*$	Excitation	(2a)
Step.2	$AB^* \rightarrow A + B$	Dissociation	(2b)
Step.3	$A + nh\nu \rightarrow A^+ + e^-$	Ionization	(2c)

Here, AB is ground state molecule, n is an integer and $h\nu$ photon energy, e^- the detached electron, AB* is excited molecule, A and B are molecular fragments and AB^+ and A^+ the molecular and fragment ions, respectively.

This research focuses on dynamics and interaction mechanisms of excited Rydberg and valence states of hydrogen halides and bromomethanes, and their fundamental properties. It deals with studies of reagents which are of importance in the photochemistry of the atmosphere,[62-64] astrochemistry[65-67] and photosynthesis[68-70], as well as in plasma chemistry /physics[71]. The research will contribute to our understanding of the Rydberg states region effects and involvement in formation processes of reactive species in atmospheres, both terrestrial and extraterrestrial. Furthermore, it will contribute to our understanding concerning its effect in photoionization processes[72], relevant to plasma formation, as well as the energy properties of the corresponding excited states species.

1.1 Diatomic molecules – hydrogen halides

Heteronuclear diatomic molecules like the hydrogen halides are ideal for fundamental studies in spectroscopy. Ever since the early work of Burmeister[73] (1913) and Price[74] (1938), an ever growing interest in the compounds photochemistry such as, photosynthesis and photodecomposition has emerged, as well as playing important roles in chemical reactions like etching of silicon (silicon chips) or reagent in excimer lasers, to name a few. Absorption and multiphoton spectroscopy have helped cast a light on energetics and dynamics behind such processes. Vast spectroscopic data of HBr and HCl in particular have been gathered by using both absorption and emission spectroscopy[10, 16, 18, 21, 24, 75-80] as well as REMPI measurements[6, 11-13, 15, 26, 27, 30-33, 81-89]. Strong absorptions both for single- and multi-photon excitations and rich band-structured spectra make these compounds ideal candidates for molecular spectroscopic and dynamic studies. Number of Rydberg electronic states, repulsive valence states as well as vibrational states of the ion-pair state ($V^1\Sigma^+$) have been identified.[6, 8, 10-13, 15, 25-32, 75, 76, 83, 84] Density of states, which increases with energy, is large in the Rydberg state region. Therefore, the probability of state interaction and mixing of states can be large in that region. Spectral perturbations due to interactions between Rydberg and ion-pair states,[11, 12, 14, 18, 20, 25, 26, 29, 30, 32, 33, 87, 90, 91] as well as due to Rydberg-to-Rydberg state interactions,[83]

have been reported. State interactions / mixing of states have been found to be due to, **a)** -homogenous ($\Delta\Omega$=0) couplings between states of same symmetry (e.g. between the $E^1\Sigma^+$ Rydberg state and the $V^1\Sigma^+$ ion-pair state), and **b)** -heterogeneous ($\Delta\Omega$>0) coupling between states of different symmetry (e.g. between the $D^1\Pi$ Rydberg state and $V^1\Sigma^+$ ion-pair state). Typically spectral perturbations due to homogeneous couplings are large because of strong state interactions, whereas corresponding effects due to hetero-geneous couplings are generally much weaker. The perturbations appear as: **i)** spectral line shifts (LS-effect), **ii)** line intensity alterations (LI-effect) and **iii)** linewidth alterations (LW-effect). Thus, rotational line shifts (**i**; LS) are found to be due to level-to-level interactions between rotational levels of different states with same *J* quantum numbers, line intensity alterations (**ii**; LI), are found to appear as irregularities in relative ion signal intensities and linewidth alterations **(iii**; LW), are due to differences in lifetimes of predissociating states. Near-degenerate and non-degenerate interactions are terms which are used to define level-to-level interactions depending on its strength and appearance in the spectral structure. Thus, near-degenerate interactions are weak interactions (for example due to heterogeneous coupling) which only affects energies of near-resonant rotational energy levels (typically two or three levels only) and the corresponding rotational line positions. Non-degenerate interactions, on the other hand, are stronger interactions (for example due to homogeneous coupling) which affect energies of a large range of rotational energy levels and all the corresponding rotational line positions.

1.1.1 HBr

Since the pioneering work of Price in 1938 much spectroscopic data has been acquired.[74] In 1961, Barrow and Stamper obtained weak emission spectrum, which they later improved by using high-resolution absorption spectroscopy, observing approximately forty unassigned spectra in the wavenumber region of 66 300 – 84 000 cm^{-1}.[22] Effects of a number of predissociation processes to form the ground state atoms were also observed. In 1970-1971, using absorption spectroscopy, Ginter and Tilford reported and assigned many new states observed in the 73 000 – 79 500 cm^{-1} region.[92, 93] Among excitations to the $E^1\Sigma^+$(v'=0) Rydberg state and the $V^1\Sigma^+$ ion-pair state, a strong predissociation, earlier reported by Barrow and Stamper, was also observed. In 1985, by using MPI, Arepalli *et al.*, excited HBr while probing formation of Br atoms.[94] Following this, Callaghan and Gordon employed MPI to generate a spectrum of HBr in the two photon energy region of 74 000 – 85 000 cm^{-1}.[95] By comparing these with the earlier work by Ginter *et al*., an assignment of twelve new electronic states as well as observing numerous vibrationally excited levels in electronic states, were performed. Kvaran *et al*. published a (3+1)REMPI spectrum.[34] In addition to previously identified Σ and Π states, they observed a Φ state ($\Delta\Omega$=3). Ascenzi *et al*. also recorded (3+1)REMPI spectra probing energies in the region of 82 000 – 92 000 cm^{-1} and observed, assigned and characterized thirteen new Rydberg states as either Σ, Π, Δ, or Φ.[15] Furthermore, the corresponding electron configurations were determined. In 2004, Manzhos *et al*. probed HCl and HBr by two-photon excitation, applying the velocity map imaging (VMI) technique.[96] They recorded H photofragment angular distributions for photo-dissociation via selected states by using a polarized light source. In the same year, Rakitzis *et al*. measured Br fragment alignments for HBr photodissociation via the repulsive $A^1\Pi$ state.[97] They also detected formation of highly spin-polarized H atoms, mainly formed along with $Br(^2P_{1/2})$ (spin-orbit excited bromine atom; henceforth denoted as Br*) and to a lesser extent with $Br(^2P_{3/2})$ (ground state bromine atom; henceforth denoted as Br). Romanescu and Loock, in 2006, studied HBr by using (2+1)REMPI as well as VMI of photoelectrons.[98] They

investigated the photo-fragmentation dynamics of low-*n* Rydberg states and the ion-pair state $V^1\Sigma^+(0^+)$. Two-photon resonant transition via the $^{1,3}\Delta_2$ states, followed by a third photon excitation was found to ionize directly into the ground vibrational state (v^+=0) of the molecular ion HBr^+, whereas two-photon resonant transitions to the $V^1\Sigma^+(0^+)$, $E^1\Sigma^+(0^+)$, $g^3\Sigma^-(0^+)$ and $H^1\Sigma^+(0^+)$ states, followed by third photon absorption, showed structure of long vibrational progression. Its appearance was interpreted as being due to interactions (state mixing) at long-range (long internuclear distance) followed by a third photon excitation from the $V^1\Sigma^+(0^+)$ state, to form HBr^+ ($X^2\Pi$) via autoionization of a superexcited state ($HBr^{\#}$). Thus, the use of VMI allowed observations of HBr^+ ion formations in different vibrational states Furthermore, long-range excitations led to formation of electronically excited atomic photofragments. Later, Romanescu and Loock focused on the resonant transitions to $V^1\Sigma^+(v'$=m+3; v'=m+5 –m+8), $E^1\Sigma^+(v'$=0) and $H^1\Sigma^+(v'$=0) (henceforth denoted as $E(v'$=0), $H(v'$=0) and $V(v'$=m+n) where v' is the vibrational level and m is an unknown integer number) via Q(0) or Q(1) lines (repulsive states in the valence region, A-band).[99] Following the third photon excitation to form $HBr^{\#}$, three formation channels for H^+ were identified. i) Dissociation of $HBr^{\#}$ formed H*(n=2) + Br/Br* via a repulsive $B^2\Sigma^+$ state of the ion core, where H^+ formed via one-photon ionization of H*(n=2), ii) vibrational progression, due to transitions to vibrational states in the $HBr^+(v^+)$, formed H^++Br/Br* via one-photon dissociation, iii) one-photon excitation of $HBr^{\#}$ leading to H^+ + Br/Br*. Long *et al*. obtained (2+n)REMPI spectra of HBr following excitations to Rydberg states and vibrational levels of the ion-pair state in the two-photon energy region of 74 000 – 86 000 cm^{-1}.[30] Two Rydberg states, not previously detected in REMPI, but observed in absorption as well as two Rydberg states, $W^1\Sigma^+(v'$=0) and $u^3\Delta_2(v'$=0), never seen before, were identified. Five new vibrational states of the *V* states were assigned. Three of these, $V(v'$=m+17 to m+19), are in the vicinity of the two new Rydberg states. Whereas no interaction was identified between the $u^3\Delta_2$ state and its energy neighbour $V(v'$= m+19) state, the spectrum displayed effects of non-degenerate interactions between $W^1\Sigma^+$ state and both $V(v'$=m+17 and m+18) states, as LS and LI effects. Some evidences were found of interactions between the $6p\pi^3\Sigma^-(v'$=0) Rydberg state and the $V(v'$=m+17) state appearing as LS and LI effects, for $J \approx 8$.

Relevant work on HBr presented here, is to be found in paper 2 (see chapter 4.2). REMPI spectra and VMI of H^+ for HBr were measured for the two-photon resonant excitation region of 84 740 – 85 120 cm^{-1}. The focus of the work was on revealing the connection between excited state interactions on further photofragmentation processes for interacting states with different spin quantum numbers. Data for $6p\pi^3\Sigma^-(\Omega=0^+; v'$=0) Rydberg and the $V^1\Sigma^+(\Omega=0^+; v'$=m+17) ion-pair states were used.

1.1.2 DCl

Near 1932, Linus Pauling constructed a theory about diatomic molecules, their electronic structure and excited states energies and predicted ion-pair states.[100] Furthermore he constructed potential curves and bond energies. Few years later, Mulliken predicted some properties of excited states for HCl, including the ion-pair $V^1\Sigma^+$ state.[101] In 1959, Jacques and Barrow, recorded an emission spectrum, in the UV region, for HCl and DCl gas.[102] They proposed spectroscopic constants for the $V^1\Sigma^+$ ion-pair state and observed its lowest four vibrational levels. Later Stamper published a paper showing an absorption spectrum for DCl and assigned rotational lines to two Rydberg states in the UV region, for which he determined spectroscopic constants with band origin 75 133 and 77 497 cm^{-1}, respectively.[103] Tilford of

Ginter published work in 1970-1971, showing high resolution absorption spectra of HCl and DCl.[16, 75] They identified many new Rydberg states and vibrational levels. Furthermore, they observed transitions to the $V^1\Sigma^+$ ion-pair state as well as isotope splittings. In 1979, Douglas and Greening, identified many new spectral bands for HCl and DCl, as well as eighteen vibrational levels (for v' lower than 26) for the $V^1\Sigma^+$ ion-pair state.[10] They observed strong interactions between the $V^1\Sigma^+$ state and Rydberg states of same symmetry, close in energy. Natalis *et al*., by using photoelectron spectro-scopy, observed vibrational excitations in the ground ionic state, $X^2\Pi$, of HCl and DCl, by exciting the neutral molecules above its ionization limit.[104] The molecular ions were formed in different vibrational states by autoionization. They also observed vibrational structure due to formation of the excited ionic state $A^2\Sigma^+$, slightly higher in energy than the ground state. Callaghan *et al*. reported extensive work on DCl (as well as HCl) by using REMPI in the two photon excitation region of 77 000 – 87 000 cm^{-1}.[85] They observed mainly Σ^+ and Δ states for two-photon resonant transitions in contrast with observations in one-photon absorption spectra where excitations to Π states, dominate. The spectra of the Δ states displayed strong transition for the Q, O, and S line series. They reported finding two vibrational states for the $E^1\Sigma^+$ Rydberg state (v'= 0 and 2), as well as ten vibrational levels for the $V^1\Sigma^+$ ion-pair state (v'=n-1, n+1 to n+9 (later v'=12, 14-22)) for DCl. Furthermore, they observed isotope splitting due to the chlorine atoms, ^{35}Cl and ^{37}Cl. Strong perturbation effects due to interactions between the *E* and *V* states (homogenous coupling) were noticeable. Perturbation effects were observed on the spectra near $V(v'=n+5)$ in the proposed spectral region of the $E(v'=1)$ state, for DCl, while the $E(v'=1)$ spectral band still remains to be assigned. Coxon *et al*., by use of emission spectroscopy, detected the lowest vibrational levels of the *V* ion-pair state (v'=0-7) for DCl, leaving a gap of v' =8-11 still undiscovered and ending a long awaited assignment of the v'=0 level.[77] A thorough work by Green *et al*. addressed various topics regarding HCl, concerning observations and identifications of states, state interactions and chlorine isotope effects.[11-13] Non-degenerate homogenous couplings between the ion-pair and Rydberg states of $^1\Sigma^+(\Omega=0^+)$ symmetry, showed perturbation effects. Contrastingly, near-degenerate hetero-geneous couplings displayed weaker perturbations. More recently, Kvaran *et al*. published papers on (3+1)REMPI of DCl and HCl, which allowed identification of Φ states (e.g. the $L^1\Phi_3$ state).[105, 106]

Relevant work on DCl presented here, is to be found in paper 3 (see chapter 4.3). (2+n)REMPI data and analysis for the two-photon resonance excitation region of 80 500–89500 cm^{-1} for a mixture of DCl and HCl are presented. Number of new spectral observations, for DCl, were assigned. A special attention was paid to perturbation effects which appear as deviation of spacings between vibrational energy levels, rotational constants and chlorine isotope shifts from regular patterns of unperturbed states. The analysis lead to quantitative characterization of states and revealed a characteristic pattern of strong interactions between singlet sigma states, indicating a diversity in dynamical processes in this high energy region. Furthermore, comparison of data for DCl and HCl was performed.

1.2 Polyatomic molecules – bromomethanes

The spectroscopy and photochemistry of the bromomethanes,[36-38, 42, 45, 46, 52, 57-59, 107-114] CH_xBr_{4-x} (x = 0-3), gained prominence in the late 20th century, as the destructive impact of halogenated species in the atmosphere emerged. Halogenated molecules such as the CFCs

(chlorofluorocarbons) play a significant role in the breakdown of the ozone in the stratosphere. Bromine radicals have been identified to have a severe impact an ozone depletion.[115] Therefore, it is important to understand reactions and processes that lead to formation of bromine radicals and breakdown of bromine (Br) containing molecules. It has been shown that bromomethanes and other bromo-carbons are important participants in atmospheric photochemical processes.[45, 46, 48, 52, 53, 59, 116] Radiation from the sun and solar storms in particular,[117] consists of energetic particles which are capable of exciting the molecules in the Earth´s atmosphere to highly energetic states, which can be further dissociated and/or ionized. Such photochemical processes can involve participation of high energy molecular Rydberg states. Most photochemical studies of the bromomethanes have involved the effect of low energy valence states (in the valence state energy region), whereas less emphasis has been on the involvement of higher energy Rydberg states (in the Rydberg state region). In addition to formation of Br atoms photodissociation of the bromomethanes can form small organic fragment species such as the CH_n (n = 1-3) radicals. These are of great interest in astrochemistry, since such hydrocarbon radicals are believed to be the fundamental building blocks of organic molecules in interstellar space.[68-70]

1.2.1 CH_3Br

The spectroscopy and photofragmentation of methyl bromide (CH_3Br) has been studied both experimentally and theoretically for decades. Although CH_3Br is the most studied molecule of the bromomethanes, many aspects of its photochemistry remains unknown. Since the pioneering work of Price in 1936,[107] a number of absorption studies have been accomplish with the main focus on dissociation of CH_3Br in the low energy absorption region (the A band region), where transitions to repulsive valence states dominate.[36, 37, 45, 48, 53, 56, 57] Causley and Russel, in 1975, reported work on all the bromomethanes, where they investigated, assigned and compared absorption spectra in the repulsive valence states region as well as in the Rydberg states region.[108] CH_3Br, with only one bromine atom, shows an absorption in the A band region peaking near 50 000 cm^{-1}. As the number of bromine atoms increase, the absorption bands shift to lower energy to about 40 000 cm^{-1} for CBr_4. As the number of Br atoms increase a larger number of possible transitions of non-bound electrons to Rydberg states also increase. This subsequently leads to an increase in Rydberg band series and enhanced spectral structure complexity in the Rydberg states region. Causley and Russel identified two *s*- and *p*-Rydberg series (and two 4*d* states) for CH_3Br but three *s*-series for CH_2Br_2. Spectral series for $CHBr_3$ and CBr_4 could not be assigned because of the severe overlap of spectral features. Later, Gougousi *et al*. published a paper where the focus was on photodissociation in the first continuum (the A band region), using multiphoton ionization (MPI) and velocity map imaging (VMI).[36] Three main repulsive states (originally reported by Mulliken[118-120]), $^3Q_0$, $^3Q_1$ and $^1Q_1$, are believed to be involved in the dissociation. These repulsive states correlate either to CH_3 + Br or CH_3 + Br*. In 1999, a similar study was conducted by Underwood and Powis, probing the Br/Br* formation.[37] Formation of CH_3^+ was also detected, seemingly due to formation of the CH_3 $3p^2A_2$ Rydberg state prior to ionization. Xu *et al*.,[58] and later Shaw *et al*.,[42] researched ion-pair formations (CH_3^+ , Br^-) and corresponding dissociations. Transitions to the ion-pair molecular state above the dissociation limit, followed by direct dissociation, were believed to be the main cause for the ion-pair formation. This process was assumed to be more probable than transitions to Rydberg states followed by intersystem crossings to the ion-pair state. Few years later, Ridley *et al*. published a paper, providing evidences for the existence of Rydberg-doorway-states in the photoion-pair formation for CH_3Br.[43] Their main focus was to identify $\Omega = 0$ Rydberg states,

using both (2+1) and (3+1)REMPI. In the cases when the $\Omega = 0$ Rydberg states are of the same symmetry as the ion-pair state(s), strong homogeneous couplings ($\Delta\Omega = 0$) between those states exists (analogues to the hydrogen halides). Ridley *et al.* believed that this interaction could be the key to the doorway mechanism. Photoion-pair formation was observed both above and below the ion-pair dissociation threshold and linked to excitations to $\Omega = 0$ Rydberg states of the lower members of the *p*- and *f*-Rydberg series.

Using (2+1)REMPI along with slice imaging and VMI, Wang *et al*. resonantly excited CH_3Br via 5s Rydberg states above the ionization limit to form CH_3Br^+ in the ground and spin-orbit excited ionic states, $^2E_{3/2}$ and $^2E_{1/2}$, respectively.[59] Detection of CH_3^+ formation showed, according to kinetic energy release spectra (KERs), broad peaks with vibrational structures in the low energy region, as well as a sharp peaks located at higher energies. They concluded that the ionization channel for the CH_3^+ formation was via photodissociation of CH_3Br^+, where the vibrational structure and sharp peak corresponded to transitions via the $^2E_{1/2}$ and $^2E_{3/2}$ states respectively. Kvaran *et al*. investigated ion formations for CH_3Br by MR-(2+n)REMPI for the two-photon excitation region of 66 000 – 80 000 cm^{-1}.[46] Main ion signal intensities changed as, $CH_3^+ > CH_2^+ > CH^+ > C^+$. Other signals detected, such as for Br^+, CBr^+, H^+ and CH_xBr^+(x=1,2,3), were very weak. Furthermore, characteristic ion intensity (*I*) variations close to the ion-pair threshold was observed. Thus, the relative ion intensities, $I(M^+)/I(CH_3^+)$, for $M^+ = CH_2^+$, CH^+ and Br^+ were found to reach maxima as the wavenumber values got closer to the ion-pair threshold.

Relevant work presented here on CH_3Br is to be found in papers 4 and 5 (see chapter 4.4 and 4.5)). The two-photon excitation region of 66 000 – 80 000 cm^{-1} was inspected by mass resolved MPI and VMI by use of one-colour (paper 4) and two-colour (paper 5) excitation schemes. Resonant excitations to selected molecular Rydberg states were explored specifically. Photodissociation and photoionization channels were identified and characterized, based on analysis of KER spectra and ion angular distributions.

1.2.2 CH_2Br_2 / $CHBr_3$ / CBr_4

With the exception of methyl bromide (CH_3Br), little work has been done on other bromomethanes. Causley and Russel, using absorption spectroscopy, did extensive work on all the bromomethanes (CH_xBr_{4-x}, x= 0-3), as mentioned before (see section 1.2.1).[108] Due to severe spectra overlap and the complexity no assignments of the spectra for $CHBr_3$ and CBr_4 molecules could be made. Three Rydberg spectral series were assigned for CH_2Br_2, all of which belong to *s*-series. In 1998, Paddison *et al*., conducted an extensive *ab initio* study on the bromomethanes including the parent molecules and radical species, $CH_3\cdot$, $CH_2Br\cdot$, $CHBr_2\cdot$ and $CBr_3\cdot$, calculating physical properties of the optimized structures.[121] Later, a theoretical study of transition probabilities to low-lying singlet and triplet electronic states of $CHBr_3$, was performed by Peterson and Francisco.[52] The calculations showed the existence of a low lying triplet state a^3A_2, with a predicted band origin at about 33 670 cm^{-1}, and maximum absorption near 37 037 cm^{-1}. Excitation in this region formed $CHBr_2$ + Br by photodissociation. Higher in energy, two singlet states, A^1A_2 and B^1E were found. Transition to the *A* states, corresponding to excitation energies lower than 42 735 cm^{-1}, was predicted to be weak. For higher energies overlapping absorption due to a stronger transition to the *B* state was predicted. Sharma *et al*., published an experimental and theoretical study of CH_2Br_2, carried out at 28 170 cm^{-1}, with the focus on photodissociation and photo-ionization.[111] Transition barriers, bond strengths, ion formations and ionization of various CH_2Br_2

fragments were characterized. In 2004, Zou *et al*., performed photo-dissociation experiments for $CHBr_3$ at 40 323 cm^{-1} by using photofragment translational spectroscopy for studying the dynamics of photodissociation processes.[116] The primary ions corresponded to signals of the $CHBr_2^+$ and Br^+ ion fragments and was attributed to dissociation in the first continuum. Other ions formed, e.g. CBr^+, HBr^+, CH^+, were attributed to secondary photo-dissociations processes of $CHBr_2$ and CHBr. Greene *et al*., using MR-REMPI and VMI, studied the photodissociation dynamics of CBr_4, probing for Br and Br* atoms formed.[122] Direct dissociation in the A band region, probed at wavenumber 37 453 cm^{-1}, showed mainly formation of CBr_3 + Br, whereas smaller contribution was detected for formation of CBr_3 + Br*. The main dissociation channel happened via singlet repulsive states, whereas some contribution came from dissociation via triplet states. Greene *et al*. argued, using speed and angular distribution, that an excitation to the lowest triplet repulsive state correlates with the CBr_3 + Br dissociation channel, which is the opposite of what has been proposed for lighter molecules such as CH_3Br. MPI spectra showed formation of the smaller ions CBr^+, C^+ and Br_2^+, whereas no evidence was found for formation of ions of larger molecular fragments such as CBr_2^+, CBr_3^+ nor the parent molecular ion CBr_4^+. In 2007, Ji *et al*., researched the photodissociation dynamics of CH_2Br_2 near 42 735 cm^{-1} and 37 453 cm^{-1}.[123] Using VMI coupled with (2+1)REMPI to obtain angular and translational energy distributions of Br and Br* atoms. Both Br and Br* exhibited anisotropy corresponding to parallel transitions in the A band region for approximately three times more formation of Br than Br*. This was attributed to curve crossing between repulsive states of different symmetries, A_1 and $2B_1$. KER spectra showed the Br^{*+} peak as relatively sharp, whereas the KER spectra for Br^+ appeared much broader. The broader translational energy distribution observed for Br, was attributed to vibrational excitations in the CH_2Br_2 molecule, prior to dissociation. Mass resolved (2+n)REMPI studies by Long *et al*. in the two photon excitation region of 71 200 – 82 300 cm^{-1}, revealed several resonant excitations to n*p* and n*d* Rydberg states of CH_2Br_2.[114] Ions detected were H^+, C^+, CH^+, CH_2^+ and Br^+. Evidence of resonant excitations to the Rydberg states of CH_2Br_2 was found from the ion spectra of CH_2^+, CH^+ and C^+ fragments. The CH^+ ion spectrum exhibited band structures, which were assigned to (1+1)REMPI of $CH^*(A^2\Delta)$ for vibrational level $v'= 0$ (i.e. $A^2\Delta(v'= 0)$) via the main resonant excitation to the $D^2\Pi(v'=2)$ Rydberg state, but also to the $E^2\Pi(v'=0)$ and $F^2\Sigma^+(v'=0)$ Rydberg states, prior to ionization. The formation of $CH^*(A^2\Delta)$ (along with HBr and Br) was attributed to photodissociation of CH_2Br_2 via two-photon resonant excitation to Rydberg states (CH_2Br_2**). The energy difference between CH_2Br_2** and the formation of $CH^*(A^2\Delta)$ is relatively small. Therefore, $CH^*(A^2\Delta)$ was formed in low energy rotational levels to show few rotational lines. Furthermore, the CH^+ spectra displayed severe perturbation effects, making assignments difficult. The perturbations are believed to be caused by fast pre-dissociations via a repulsive state residing in that energy region. A broad peak in the C^+ spectrum at the two-photon excitation energy of 80 663 cm^{-1} was detected. This was attributed to an increase in ionization probability, by changing from three-photon to two-photon ((2+1)MPI to (1+1)MPI) ionization of $C^*(^1D_2)$.

Relevant work, presented here, is on CH, to be found in paper 1 (see chapter 4.1). Bromoform ($CHBr_3$) was chosen as a suitable candidate for producing $CH(A^2\Delta,v')$ in order to assist with assigning the complicated spectral structure associated with its transitions to the higher lying Rydberg states. This is further discussed in the next section.

1.2.3 CH – CD

Following the spectroscopic studies of the CH/CD radicals by Herzberg and Johns in 1969,[124] there have been a number of uncertainties concerning its spectral assignments in the high energy Rydberg states region. Using flash-photolysis of diazomethane (CH_2N_2 / CD_2N_2) Herzberg and Johns obtained absorption spectra for CH and CD corresponding to excitations from the ground state, $X^2\Pi$, to several states. The spectra included bands for the low lying states, $A^2\Delta$, $B^2\Sigma^-$ and $C^2\Sigma^+$, which they identified and assigned for rotational and vibrational transitions as well as deriving relevant spectroscopic constants. Excitations to high energy Rydberg states showed spectra that were more elusive than for the low lying states, being severely perturbed due to strong state interactions. Nevertheless, three high energy states could be identifies, i.e. the $D^2\Pi$, $E^2\Pi$ and $F^2\Sigma^+$ Rydberg states. A year later, Hesser and Lutz,[125] using electron-beam excitations of CH_4 and CD_4 gases, observed the three lower energy states, *A*, *B* and *C*, previously reported by Herzberg and Johns. More recent experiments have mainly involved transitions to lower energy Rydberg states.[126, 127] In 1986, extensive *ab initio* calculations were performed by van Dishoeck for the CH molecule, deriving adiabatic potential curves for number of electronic states of the neutral molecule as well as for the ionic ground state $CH^+(X^1\Sigma^+)$ and threshold energies.[128] In addition, transition dipole moments and probabilities as well as mixing of electronic configurations for states as a function of the internuclear distance were derived. These calculations showed severe mixing of states in the high energy Rydberg states region. Metropoulos and Mavridis calculated predissociation lifetimes of the high energy Rydberg states $D^2\Pi$ and $E^2\Pi$ (which they labelled $E^2\Pi$, $F^2\Pi$, respectively) based on strong avoided crossings with a $^2\Pi$ repulsive state.[129] Thus, by using an adiabatic representation, lifetimes of about 20 fs, 2 fs and 9 fs were obtained for the vibrational state 0, 1 and 2 of the *D* state, respectively. This indicated that the curve crossing could be in the vicinity above the *v*'=1 level. Chen *et al*., performed REMPI of $CHBr_3$ to form CH in the $A^2\Delta(v'=0)$ state via predissociation of the parent molecule.[130] (1+1)REMPI of CH*($A^2\Delta$; *v*'=0) produced spectra showing resonant excitations via CH** Rydberg state. REMPI spectra obtained, showed broad rotational lines, which were assigned to the P, Q and R line series of the CH**($D^2\Pi(v'=2)$) state. Furthermore, the C^+ spectrum, displayed broad signal for one-photon absorption at 40 331 cm^{-1}. In 2007, further *ab initio* calculations were performed by Vázquez *et al*.[131] They derived potential curves and spectroscopic constants for states in the high energy Rydberg states region. Limited avoided crossings were seen for $^2\Sigma^+$ potential curves, whereas avoided crossings for $^2\Pi$ potentials, due to mixing with $^2\Pi$ repulsive states were found to be common. Thus, the effect of predissociation on the $^2\Pi$ Rydberg states short lifetimes could be verified. The predissociation is predicted to be *v*' sensitive, depending on the curve crossing locations.

Relevant work, presented her, is on CH and CD, to be found in paper 1 (see chapter 4.1). The one-photon excitation region 38 000 – 42 000 cm^{-1}, was inspected by (1+1)REMPI of CH*($A^2\Delta$) and CD*($A^2\Delta$). Resonant excitations to the CH**/CD**($D^2\Pi$; *v*'=2) Rydberg state was the focus of the work. One-photon excitation to near lying Rydberg states was to be expected. The effects of isotopic shift was incorporated by using both CH and CD, in the hope of avoiding strong predissociation effects near the curve crossings of Rydberg potentials and repulsive potential. CH/CD fragments were formed via photo-dissociation of $CHBr_3$/$CDBr_3$.

2 Theoretical considerations

2.1 Excitation within molecules

An atom is the smallest component of ordinary matter. Composed of a nucleus and electron(s), the electrons reside in orbitals around the nucleus with discrete energies. Exciting an atom, with just the right energy, causes the electron to transfer to more energetic, electronic state (orbital). These transitions only take place with the right amount of energy; the right quanta of energy. The electrons are, therefore, said to be excited between quantum energy levels. Equal energy is released if the electron drops back to its original quantum level in the form of a photon. A molecule is formed upon the interaction between electronic orbitals of two (or more) near lying atoms. The molecules have extra attributes as they can both vibrate and rotate within specific quantum energy levels. The total energy (ΔE_{total}) of an electronic excitation of a molecule, therefore, can be divided into terms as,

$$\Delta E_{total} = \Delta E_{el} + \Delta E_{vib} + \Delta E_{rot} \qquad (3)$$

where ΔE_{el}, ΔE_{vib} and ΔE_{rot} are the electronic-, vibrational- and rotational- energy differences, respectively. The approximate orders of magnitude for these individual factors are,

$$\Delta E_{el} \approx \Delta E_{vib} \cdot 10^3 \approx \Delta E_{rot} \cdot 10^6 \qquad (4)$$

2.1.1 The Born-Oppenheimer approximation

The Born-Oppenheimer (BO) approximation uses the disparity in masses between nuclei and an electron, to simplify the Hamiltonian operator ($\hat{H}$) for the Schrödinger wave equation. The assumption is made, that because the electrons move much faster than the nuclei, the nuclei are held fixed in position during the period of the electron motions, to allow the energies of the electrons to be determined for stationary nuclei. The Hamiltonian of a diatomic molecule can then be presented as such,

$$\hat{H} = H^{el} + T^N(R) + H^{rot} + H^{SO} \qquad (5)$$

where H^{el} represents the term for the potential energy curve, $T^N(R)$ describes the vibrational motion as a function of r, where r is the internuclear distance. The angular variable is given by H^{rot}, which defines the rotational motion, and H^{SO} gives the spin-orbit interaction. In the BO approximation, each electronic state of a diatomic molecule is represented by a potential energy curve plotted against internuclear distance. Within these potential curves, vibrational energy levels are indicated by horizontal lines. For larger molecules, these potential curves need to be represented by a multi-dimensional potential surface, where the potential energy is plotted against a number of distances and angles that specify the configuration of the molecule. The equilibrium bond distances (located at the bottom of the potential wells) and the shape of potential energy curves are in general diverse for different electronic states of a molecule, and the spacing of vibrational levels, therefore, different. By applying the BO-approximation, these potential energy curves are frozen in space and electronic transitions can be plotted as vertical transitions within, and between those curves (see fig.1).

2.1.2 Electronic energies

Electronic energies depend on the internuclear distance (potential curves). For diatomic molecules the average internuclear distance, r_e, at the lowest energy point of the potential curve for bound state potentials, gives energy commonly referred to as T_e. For the ground state, T_e can be considered as having zero energy. (Alternatively T_0 is set to zero, where $T_0 = T_e + ZPE$ and ZPE is the zero point energy). Assuming that $T_e = 0$ for the ground state, then T_e for excited (bound) Rydberg states can be expressed as,

$$T_e = IE - \frac{\mathcal{R}}{(n-\delta)^2} \qquad (6)$$

where T_e is the energy of the selected state, IE is the ionization energy, $\mathcal{R}$ is the Rydberg constant, n is the principal quantum number and δ is the quantum defect parameter depending on the Rydberg electron orbital. The quantum defect value arises from shielding effects of the core electrons of the molecule.

The values for δ range typically from almost zero for the f orbitals, upwards for decreasing l Rydberg atom quantum numbers. This equation specifies the energy of electronic states within the region between the ground state and the IE limit (for neutral molecular species).

When two atomic orbitals are combined to form molecular orbitals, a method called Linear Combination of Atomic Orbitals (LCAO) can be applied. Table.1 shows different types of atomic orbitals (l) and a molecular combination thereof (λ).

Table 1 *Shows letters defined for orbital quantum numbers for atomic orbitals. LCAO for bonding molecular orbitals, formed by combination of specific atomic orbital.*

Atomic orbital (l)	Bonding molecular orbitals (λ)
s	$s\,\sigma$
p	$p\,\sigma$, $p\,\pi$
d	$d\,\sigma$, $d\,\pi$, $d\,\delta$
f	$f\,\sigma$, $f\,\pi$, $f\,\delta$, $f\,\phi$

Combination of two s orbitals makes a σ orbital, whereas e.g. p atomic orbitals can combine into σ and π molecular orbitals. Rydberg states are accessed by exciting electrons to high energy atomic-like molecular orbitals (MOs) in the Rydberg states spectral region, whereas valence states are accessed in the valence states region by exciting electrons to molecular orbitals formed by linear combination of valence atomic orbitals. Transitions within the valence states region can, for example, lead to, i) -dissociation of the molecule via repulsive or continuum states (typically corresponding to transitions to anti-bonding orbitals), ii) -increased internuclear bond distance between the atoms, held together by Coulomb attraction forces. The latter is referred to as an ion-pair state, which, in case of a diatomic molecule, such as the hydrogen halides HX, corresponds to an electron transfer from a bonding (σ) to an anti-bonding (σ^*) orbital, e.g. $HBr \rightarrow H^+Br^-$.

2.1.3 Vibrational energy levels

The vibrational energy levels within the energy potential curves, can be described empirically by series, as a function of (v + ½),

$$G(v) = \omega_e(v + 1/2) - \omega_e x_e(v + 1/2)^2 + \omega_e y_e(v + 1/2)^3 + \cdots \quad (7)$$

where $G(v)$ denotes the vibrational energy, v is the vibrational quantum number (v = 0, 1, 2 …), ω_e is, to first approximation, the harmonic vibrational wavenumber,

$$\omega_e = \frac{1}{2\pi c}\sqrt{\frac{k}{\mu}} \quad (8)$$

where c is the speed of light, μ is the reduced mass and k is the force constant (spring constant from Hooke's law[2]) of the molecule. The $\omega_e x_e$ term is the anharmonic constant (later terms are correction terms for asymptotic approach), describing the deviation from the simple harmonic oscillator approximation, depending on the potential curve shape.

Fig.1, shows simplified representation of the impact that anharmonic vibrational constant has on the simple harmonic oscillator potential curve approach.

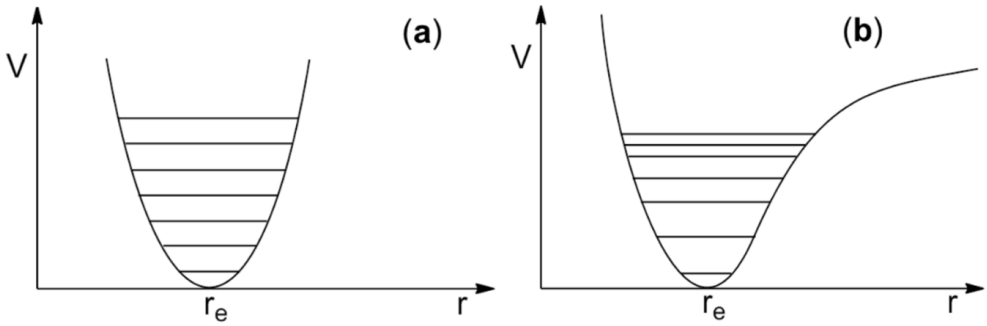

Figure 1 *Potential curves. a) The simple harmonic oscillator potential curve and an acceptable approach for vibrational levels. b) More realistic approach to the potential energy curve, taking into account the anharmonicity of the vibration. The y-axis displays the energy, the x-axis the internuclear distance. r_e is the equilibrium distance. Vibrational energy levels are shown as horizontal lines.*

2.1.4 Rotational energy levels

The rotational energies can be described by the series, as a function of $J(J + 1)$.

$$F_v(J) = B_v J(J + 1) - D_v[J(J + 1)]^2 + H_e[J(J + 1)]^3 + \cdots \quad (9)$$

Here $F_v(J)$ denotes the rotational energy, J is the rotational quantum number, B_v is the rotational constant and D_v is a centrifugal distortion constant (later terms are correction terms for asymptotic approach). Fig.2, shows the deviation rotational energy levels from rigid rotor behaviour to non-rigid rotor,

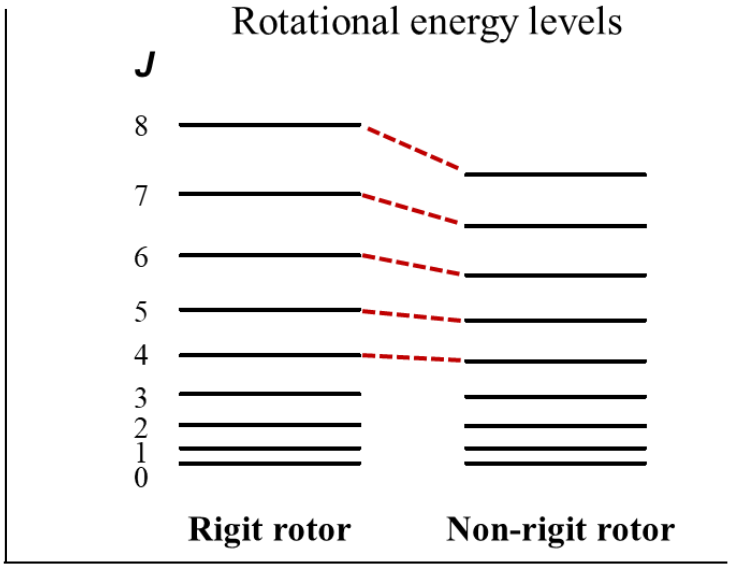

Figure 2 *The change in rotational energy levels when passing from a rigid to a non-rigid diatomic molecule. (For B= 5 and D= 0.005)*

The B_v and D_v, constants are both affected by the change in v, and can be expressed as,

$$B_v = B_e - \alpha_e\left(v + \frac{1}{2}\right) + \gamma\left(v + \frac{1}{2}\right)^2 + \cdots \quad (10)$$

$$D_v = D_e - \beta_e\left(v + \frac{1}{2}\right) + \cdots \quad (11)$$

Here B_e and D_e are the unaffected rotational and centrifugal distortion constants of the individual electronic states, with α_e and β_e as constants describing the impact that increasing vibrational energy (increasing v) has. The B´s (B_v and B_e) depend on internuclear distance, r,

$$B = \frac{\hbar}{4\pi c\mu r^2} \quad (12)$$

where $\hbar$ is the Planck's constant divided by 2π, μ is reduced mass[2] and c is the speed of light.

2.1.5 Summary

With the information described above, one can calculate the total energy ($E^0{}_T$) of a diatomic molecule, consisting of electronic (T_e), vibrational ($G(v)$) and rotational ($F_v(J)$) energies, presented as,

$$E_T^0 = T_e + G(v) + F_v(J) \quad (13)$$

giving the unperturbed energy, E^0, of a molecule.

2.2 Term symbols and Hund's case

2.2.1 Atomic and Diatomic term symbols

Abbreviation for angular momentum quantum numbers in multi electron systems is generally used, called term symbols. Term symbols describe states with respect to quantum numbers,

Atoms $^{2S+1}L_J$ (14a)

Molecules $^{2\Sigma+1}\Lambda_\Omega$ (14b)

where S, L,J and Σ, Λ, Ω are the quantum numbers for, spin angular momentum, orbital angular momentum and total electronic angular momentum, for atoms and diatomic molecules, respectively. The quantum numbers S, Σ and J, Ω are represented with numerical values, whereas for L and Λ, letter designations are used (see table.2).

Table 2 *Designations used to represent orbital angular momenta for atoms and diatomic molecules.*

L / Λ	Atomic designations (L)	Molecular designations (Λ)
0	S	Σ
1	P	Π
2	D	Δ
3	F	Φ

The magnetic quantum number m_l, specifies the orientation of an orbital angular momentum for an electron and refers to the projection of the angular momentum on the z-axis for a given direction.

$$L_Z = m_l \hbar \quad (15)$$

The corresponding total z-projection quantum number for an atom or a molecule can then be defined as

$$M_L = \sum_i m_{l_i} \quad (16)$$

For a molecule, since positive and negative values of M_L are degenerate, then Λ can be defined as

$$\Lambda = |M_L| \quad (17)$$

Λ, therefore, takes the positive numerical values, Λ= 0, 1, 2 … (see table.2), and the vectorial form $\mathbf{\Lambda}$. Similarly Σ refers to the vectorial representation $\mathbf{\Sigma}$, for the molecular spin angular momentum. It can take 2Σ+1 different values, called multiplicity. States with multiplicity 1, 2, 3, 4 and 5 are named singlet, doublet, triplet, quartet and quintet states, respectively. Spin-

orbit coupling lifts the degeneracy of the electronic states. This is because the z-component of spin interacts with the z-component of the orbital angular momentum, generating a total electronic angular momentum along the molecule axis J_z. with different energies. The corresponding quantum number (Ω) is specified as

$$\Omega = \Sigma + \Lambda \qquad (18)$$

for the vector **Ω**.

The implication of z-projection vectors, **Σ**, **Λ** and **Ω**, as well as total vector ***J***, ***L*** and ***S*** are addressed in next section.

2.2.2 Hund's Cases

For a diatomic molecule it is important to include the effect of rotation as well as the electronic motions, when considering the total angular momentum of the system. Hund's cases display in which way these different motions influence one another, depending on the molecules involved. The **Ω**, **Λ** and **Σ** projections are formed from the corresponding total angular moment vectors, ***J***, ***L***, ***S*** as shown in fig.3 for Hund's case (a),[60]

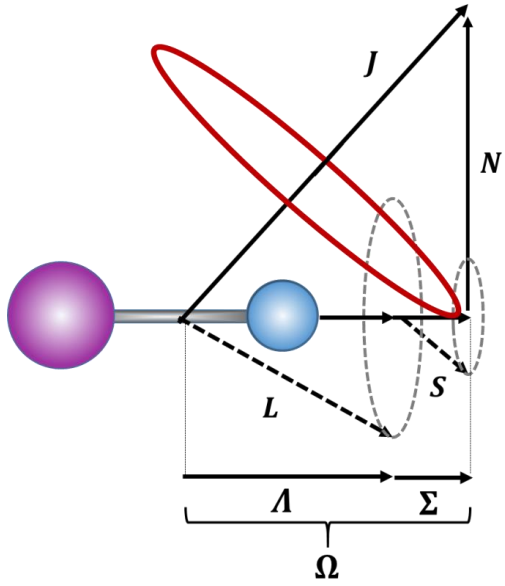

Figure 3 *Schematic representation of angular momenta in a diatomic molecule for Hund's case (a). Vectors* ***J***, ***L*** *and* ***S*** *form projections on the internuclear axis, labeled* **Σ**, **Λ** *and* **Ω**. ***N*** *is the angular momentum vector of nuclear rotation. The nutation of the figure axis is shown as a red solid ellipse. The much faster precessions of* ***L*** *and* ***S*** *about the line joining the nuclei are indicated by broken line ellipses.*

In Hund's case (a) it is assumed that the interaction of the nuclear rotation (angular momentum vector ***N***) with the electronic orbital motion and spin (***L*** and ***S***) is negligible but

that the electronic motion itself is coupled strongly to the internuclear axis. This leads to a well-defined total angular momentum $\boldsymbol{J} = \boldsymbol{\Omega} + \boldsymbol{N}$. (see fig.3).

The rotational energy for a symmetric top approach, with the quantum numbers J and Ω is,

$$F_v(J) = B_v[J(J+1) - \Omega^2] \qquad (19)$$

The Ω^2 term implies a multiplet splitting,[60] for electronic states for different values of Ω, e.g., $^2\Pi_{3/2}$ and $^2\Pi_{1/2,}$ where $\Omega = 3/2$ and $1/2$, which can appear as shifted spectral bands.

There are more configurations of the vector combinations describing the electronic interaction of the molecule. These are known as Hund's cases (a) – (e).[60] Coverage of all the Hund's cases will not be carried out here. Hund's case (a), suitable for light atoms, such as HCl and DCl is displayed in fig.3. Hund's case (c) shown in fig.4, is appropriate for heavier molecules (e.g. HBr.) where the interaction between vectors $\boldsymbol{L}$ and $\boldsymbol{S}$ can be strong.

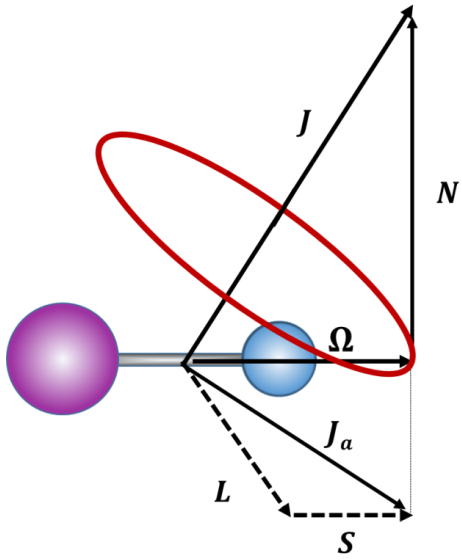

Figure 4 *Schematic representation of angular momenta in diatomic molecule for Hund's case (c).* $\boldsymbol{L}$ *and* $\boldsymbol{S}$ *form the vector* $\boldsymbol{J_a}$*, projected as* $\boldsymbol{\Omega}$ *on the internuclear axis. The nutation of the figure axis is shown as a red solid ellipse.*

For Hund's case (c),[60] the interaction between $\boldsymbol{L}$ and $\boldsymbol{S}$ is stronger than the interaction with the internuclear axis. In that case, the $\boldsymbol{\Lambda}$ and $\boldsymbol{\Sigma}$ are not defined, but rather $\boldsymbol{L}$ and $\boldsymbol{S}$ form a resultant $\boldsymbol{J_a}$ vector which then couples to the internuclear axis, with a z-projection component $\boldsymbol{\Omega}$. In this case, the spin-orbit coupling is very strong. The total angular momentum is defined as $\boldsymbol{J} = \boldsymbol{\Omega} + \boldsymbol{N}$, analogous to Hund's case (a). The rotational energy levels for Hund's case (c), are analogous to those for Hund's case (a).

2.3 Selection rules

2.3.1 Transition dipole moment

A fundamental condition for a transition to take place between two electronic states, is for the dipole moment to change, shown in bra-ket notation as,

$$\langle 1|\boldsymbol{\mu}|0\rangle \neq 0 \qquad (20)$$

Here, $\langle 1|0\rangle$ are the wave functions of the two electronic states involved and μ is the transition dipole moment operator. Zero values of this braket mean that transition is forbidden.

2.3.2 Angular momentum selection rule

During the absorption of a photon, the orbital angular momentum (l) of an atom changes. For the conservation of orbital angular momentum to hold, during the excitation, the dipole needs to change with a transition to an orbital with different angular momentum, or simply,

$$\Delta l = \pm 1 \qquad (21)$$

This rule satisfies the transition moment integral (see eq.20), as a transition between two states of different orbital angular momentum inherently involves a change in the dipole moment.

2.3.3 One- and two-photon selection rules for molecules

When a molecule absorbs a photon, the total angular momentum must be conserved. This gives rise to the following selection rules, for a one-photon excitation

$$J' - J'' = \Delta J = \pm 1 \,;\, for\ \Delta\Omega = 0 \qquad (22a)$$

and

$$J' - J'' = \ \Delta J = 0, \pm 1 \,;\, for\ \Delta\Omega \neq 0 \qquad (22b)$$

For multiphoton excitations, each photon transition fulfils the one-photon selection rules, so it is applied to each of the photon used in the excitation process,

For $\Delta\Omega = 0$

$$J' - J'' = \Delta J = 0, \pm 2 \,;\, for\ n = 2 \qquad (22c)$$

$$J' - J'' = \Delta J = \pm 1, \pm 3 \,;\, for\ n = 3 \qquad (22d)$$

etc…

For $\Delta\Omega \neq 0$

$$J' - J'' = \Delta J = 0, \pm 1, \pm 2, \pm \cdots \pm n \qquad (22e)$$

where *n* is the number of photons used in the excitation process, *J'* is the rotational level in the excited state and *J''* is the rotational level in the ground state. This allows for additional spectral rotational line series (sometimes referred to as branches) for each vibrational transition. These branches are labelled as seen in table 3.

Table 3 *Example for line series that are formed with transitions ΔJ=0, ±1, ±2.*

Rotational selection rules give rise to rotational branches					
Branch:	*O*	*P*	*Q*	*R*	*S*
ΔJ =	*-2*	*-1*	*0*	*1*	*2*

2.3.4 Perturbation selection rules

These following rules are not all rigorous:

1) Both states must have the same total angular momentum *J*, $\Delta J = 0$
2) Both states must have same multiplicity, $\Delta S = 0$
3) The Λ value of the two states must differ only by 0 or 1, $\Delta \Lambda = 0, \pm 1$
4) Both states need to have same parity, either both positive or both negative, + ←→+, –←→–, + ←//→–
5) For homonuclear molecules, both states must have same symmetry in the nuclei

2.4 Intensity of electronic excitation spectral lines

2.4.1 Franck-Condon principle

The Franck-Condon principle addresses the transition probability for transitions between two electronic molecular states. It involves evaluation of Franck-Condon factors (FCFs). For the evaluation the BO approximation is applied. For a transition to take place, a change in dipole moment needs to occur, shown in bra-ket notation as,

$$\langle \psi^1 | \boldsymbol{\mu} | \psi^0 \rangle \neq 0 \qquad (23)$$

where μ is the transition dipole operator, and $|\psi^0>$ and $|\psi^1>$ represent the total wave functions for the two states involved in the transition. If the outcome of this bra-ket is zero due to no change in the dipole moment, the transition is forbidden. For non-zero values the probability amplitude (a^2) is calculated as,

$$a^2 = \langle \psi^1 | \boldsymbol{\mu} | \psi^0 \rangle^2 \qquad (24)$$

This holds for transitions between states which manifest as either excitation or emission. The FCFs are approximation expressions for a^2, evaluated from the overlap integrals for the vibrational wave functions of the two states involved in the transition. The transition probabilities increase with increasing overlap of the vibrational wave functions ($|\psi^0_{v''}>$

, $|\psi_v^1, >$). Calculated potential curves and vibrational wave functions for the first five vibrational states can be seen on fig.5, for the CH molecule.

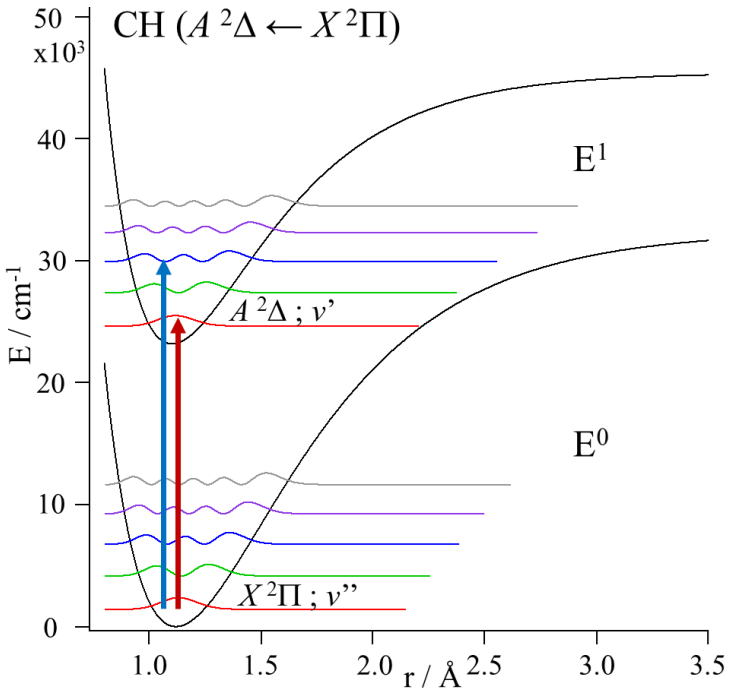

Figure 5 *Two potential curves from the CH molecule, ground state $X^2\Pi$ (E^0) and excited state $A^2\Delta$ (E^1), calculated by using known spectroscopic constants.*[132] *The Overlap of vibrational wave functions of the two states ($E^0$and E^1) gives an estimate (FCFs) of the transition probability between the states. Red arrow is an example of a high probability transition (large vibrational overlap), whereas blue represents a low probability transition (small vibrational overlap).*

2.4.2 Boltzmann distribution

The intensity of rotational lines depends on the population in J'' levels. This influences the number of molecules that are available for specific excitations. The population can be determined by using the Boltzmann distribution,

$$\frac{N_J}{N_0} = exp\left(\frac{-E_J}{k_b T}\right) \qquad (25)$$

where N_J is number of particles with energy E_J, N_0 is the total number of particles in the system, k_b is the Boltzmann constant and T is the temperature. Population shifts to higher levels as T increases. Pictorial representation can be seen in fig.6.

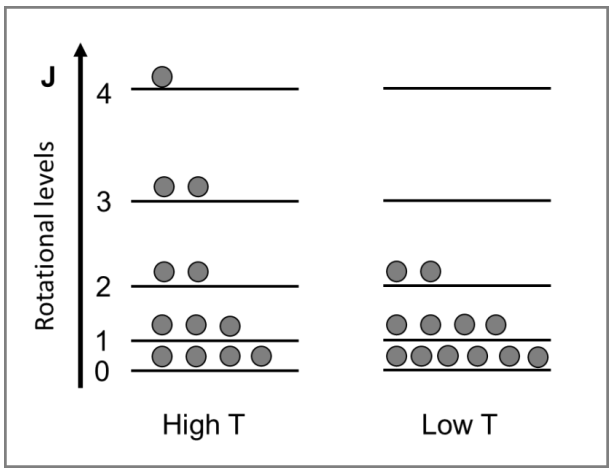

Figure 6 *Pictorial representation of molecular distributions in rotational states depending on temperature (see main text).*

Therefore, for rotational excitation processes, most transitions for a cold gas (low T) will be for low *J* levels, whereas excitations for a hot gas (high T) will include higher energy *J* levels. Therefore, line intensities, as well as number of observed lines, is greatly influenced by the population and temperature. Our REMPI experiments were carried out for jet expansions of molecular samples to give cold gas beams (hence low *J* populations).

2.4.3 Transition strengths

Transition strengths are important factors to determine rotational line intensities for rotational line series. These factors differ for different number of photons in excitations process. Below is an example for one-photon excitations for diatomic molecules, where the orbital angular momentum quantum numbers for the states involved are Λ'', Λ' and $\Delta\Lambda=\Lambda'-\Lambda''$. These factors (denoted as $S_{\Delta\Omega}$ in general form)[34, 81] can be calculated using following formulas seen in table 4.

Table 4 *Example for one-photon excitations for diatomic molecules (often referred to as Hönl-London factors)*

For $\Delta\Lambda=0$	For $\Delta\Lambda=+1$	For $\Delta\Lambda=-1$
$S_J^P = \frac{(J''+\Lambda'')(J''-\Lambda'')}{J''}$	$S_J^P = \frac{(J''-1-\Lambda'')(J''-\Lambda'')}{4J''}$	$S_J^P = \frac{(J''-1-\Lambda'')(J''+\Lambda'')}{4J''}$
$S_J^Q = \frac{(2J''+1)\Lambda''}{J''(J''+1)}$	$S_J^Q = \frac{(J''+1+\Lambda'')(J''-\Lambda'')(2J''+1)}{4J''(J''+1)}$	$S_J^Q = \frac{(J''+1-\Lambda'')(J''+\Lambda'')(2J''+1)}{4J''(J''+1)}$
$S_J^R = \frac{(J''+1+\Lambda'')(J''+1-\Lambda'')}{(J''+1)}$	$S_J^R = \frac{(J''+2+\Lambda'')(J''+1+\Lambda'')}{4(J''+1)}$	$S_J^R = \frac{(J''+2-\Lambda'')(J''+1-\Lambda'')}{4(J''-1)}$

2.4.4 Relative rotational line strength

The relative rotational line intensities (I_{rel}), can be expressed in the following way in the case of a Boltzmann distribution (see eq.26).

$$I_{rel} = C(v', v'')g(J'')S_{\Delta\Omega}\, exp\left(\frac{-E_{J''}}{k_b T}\right) \qquad (26)$$

Where $g(J'')$ is the degeneracy ($2J''+1$) of the ground state rotational energy levels ($E(J'')$) and $S_{\Delta\Omega}$ is the transition strength factor. $C(v', v'')$ is a factor, independent of J' and J'' which can be further expressed as

$$C(v', v'') = K\, F(v', v'')P^n\sigma_1(v') \qquad (27)$$

Here, $F(v', v'')$ is the FCF and K is a parameter dependent on the electronic structure of the molecule, geometric factors and sample concentration. P^n is the laser power (P), where n depends on the number of photons involved in the overall ionization process, e.g. $n \leq 3$, for (2+1)REMPI and the $\sigma_1(v')$ is the resonant excitation cross section.

2.5 One- vs. two-colour with REMPI

REMPI involves resonant photoexcitation to an electronic excited state followed by photoionization. In the case of a multiphoton resonant excitation the resonant step can include dissociation processes forming molecular fragments that can subsequently undergo REMPI. Further excitation following the resonant step can create a superexcited state above the ionization limit and form the molecular ion via autoionization.[6, 7] The autoionization process will not be addressed here further. In "one-colour REMPI", excitations of neutral species and ionizations occur simultaneously by the same laser wavelengths.[7] Adding a second laser wavelength can allow specific REMPI detections of fragment species (see paper 5, chapter 4.5). This is often referred to as pump and probe detections, where the pump laser excites the molecule (AB) (e.g. to a Rydberg state (AB**)), followed by further excitations, dissociations and ionizations. The probe laser can be used to probe a ground state fragment (A or B). Thus, for example, by adjusting its wavelength to resonantly excite it to a Rydberg state its ion signal can be enhanced significantly, whereas by using only one wavelength, such signals may only be observed in cases of "accidental resonant" excitations of the fragments. Fig.7, shows schematic representation of these two excitation schemes, i.e. one- and two-colour REMPI. The figure shows specific example where predissociation of AB** forms A and B followed by non-resonant excitation of A in the former case but resonant excitation of A for the probe excitation / in the latter case.

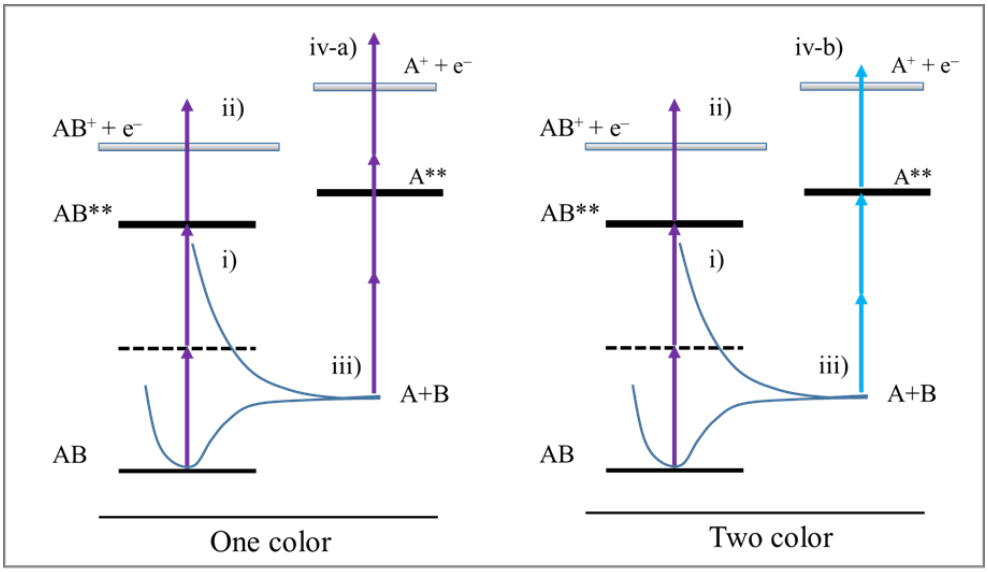

Figure 7 *Schematic representations of the energetics and excitation processes for a molecule AB for one- and two-colour REMPI. i) Two-photon resonant transition to a Rydberg state AB**, ii) one-photon photoionization of AB** Rydberg state, iii) predissociation forming ground state A+B fragments, iv-a) non-resonant MPI for fragment A, iv-b) REMPI for fragment A. Purple vertical arrows are for pump laser excitations, and blue vertical arrows are for probe excitations.*

2.6 State interactions

Perturbations are often observed in rotational structures of molecular spectra. Interactions between different states can cause observed spectral bands to derail away from predicted behaviour (see section 2.2). The interaction strength (W) and effects depend on the nature of these interactions.[6, 30, 83] The interaction strengths are related to the molecular states symmetries and observed effects depend on how close in energy "interacting energy levels" are. When the total electronic angular momentum quantum numbers of interacting states are the same ($\Delta\Omega = 0$), the interactions (couplings) are referred to as homogenous, whereas, otherwise ($\Delta\Omega \neq 0$) these are heterogeneous. In terms of an operator representation, couplings are presented as, $\hat{H} = \hat{H}_0 + W$, where $\hat{H}_0$ is the zero order Hamiltonian without coupling and W is the coupling contribution to $\hat{H}$.

2.6.1 Line alterations

Line shift

Rotational line shifts observed in spectra, indicate interactions between two (or more) rotational energy levels. In the simplest form this corresponds to an effect of two rotational energy levels moving apart. An example can be seen in fig.8.

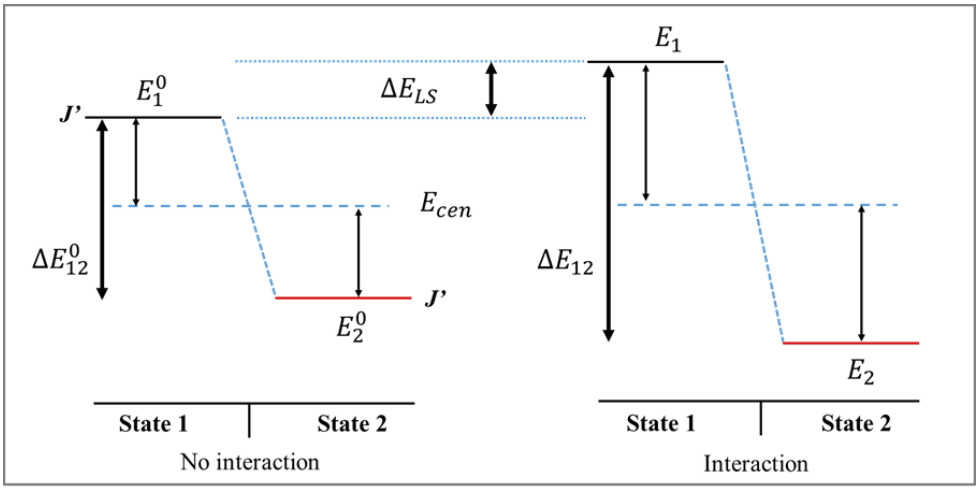

Figure 8 *Line shifts due to state interaction. Left: Unperturbed energy levels E^0_1 and E^0_2, with energy difference ΔE^0_{12}. Right: Interaction between the states causes shifts of the energy levels to E_1 and E_2. ΔE_{LS} (see eq. (20)). E_{cen} is the energy value mid between E_1 and E_2.*

The relationship between the energy expressions shown in fig. 8 and the interaction strength for two interacting state (1) and (2) (W_{12}) forms the basis for further simulations of line shift perturbations (LS-effects):[83],

$$\Delta E_{LS} = \frac{1}{2}\left(\Delta E_{12} - \sqrt{(\Delta E_{12})^2 - 4|W_{12}|^2}\right) \qquad (28)$$

Linewidth broadening

Linewidth is a fundamental attribute of spectral lines, as it is linked to the excited states lifetime. It is more appropriate to say, that a spectral line covers a range of wavelengths, rather than to be of a single wavelength. Furthermore, spectral linewidths can be affected by experimental conditions such as pressure and heat. Lifetime is influenced by bound-to-continuum state coupling, which caused dissociation. Predissociation, is a case of energy potential curve crossing for states of comparable symmetries and can severely shorten the lifetime of the excited state. When spectral peaks are obtained, two commonly used shape functions, Lorentzian and Gaussian can be applied,[133] where the previous is used to estimate homogenous broadening while the latter is used for heterogeneous broadening. The two functions are as follows.

Lorentzian shape function

$$\chi(\nu, \nu_0) = \frac{\Gamma/2\pi}{(\nu-\nu_0)^2+(\Gamma/2)^2} \qquad (29)$$

Gaussian shape function

$$\chi(\nu, \nu_0) = \frac{2}{\Gamma}\left(\frac{ln2}{\pi}\right)^{1/2} e^{-\left[\frac{4ln2(\nu-\nu_0)^2}{\Gamma^2}\right]} \qquad (30)$$

where ν_0 is the central wavenumber and Γ is linewidth full-width-half-maximum (FWHM). A band consisting of number of rotational lines, can display a broadening of the linewidths within the spectral band. If two peaks have overlapping FWHM, they are hard to resolve and will look like one peak. These changes could be caused by interactions of various kind between near lying states.

3 Experimental and analysis methods

3.1 MR-REMPI; Experimental setup

The experimental setup for recording Mass-Resolved Resonance-Enhanced-MultiPhohon-Ionization (MR-REMPI) data, consisted of a set of tunable dye laser, Coherent ScanMatePro, pumped by a Lambda Physic COMPex 205 excimer laser (XeCl, 308 nm)[134]. The linewidth of the tunable dye laser radiation was about 0.1 cm^{-1}. All experiments performed required a second harmonic generator (SHG) to frequency double the dye laser output, using a Sirah frequency doubler instrument equipped with interchangeable BBO-2 (barium borate) or KDP (potassium dihydrogen phosphate) crystals and its energy output was kept stable by an autotracking device. The frequency doubled laser beam was separated from the fundamental beam by a Pellin-Broca prism and directed into a vacuum chamber. It was focused on a jet cooled molecular beam inside an ionization chamber by a 20 cm focal lens. Synchronized molecular beam pulses at 90° with respect to the laser pulses were created by a pulsed nozzle. Typical repetition rate was about 50 pulses for each frequency point. Either neat (undiluted) or argon diluted gas samples were used. A positively charged repeller and extractors (and an electrical lens) on either side (above and below) of the molecular beam, near the focal point, were used to accelerate and direct ions, formed, into a field-free region of a 75 cm long Time-Of-Flight (TOF) tube. At the end of the TOF tube ions were detected by a micro-channel-plate detector (MCP) as a function of the total time of flight (t_{TOF}). Ion masses (Mw) were determined from the approximation expression

$$t_{TOF} = a\sqrt{Mw} + b \qquad (31)$$

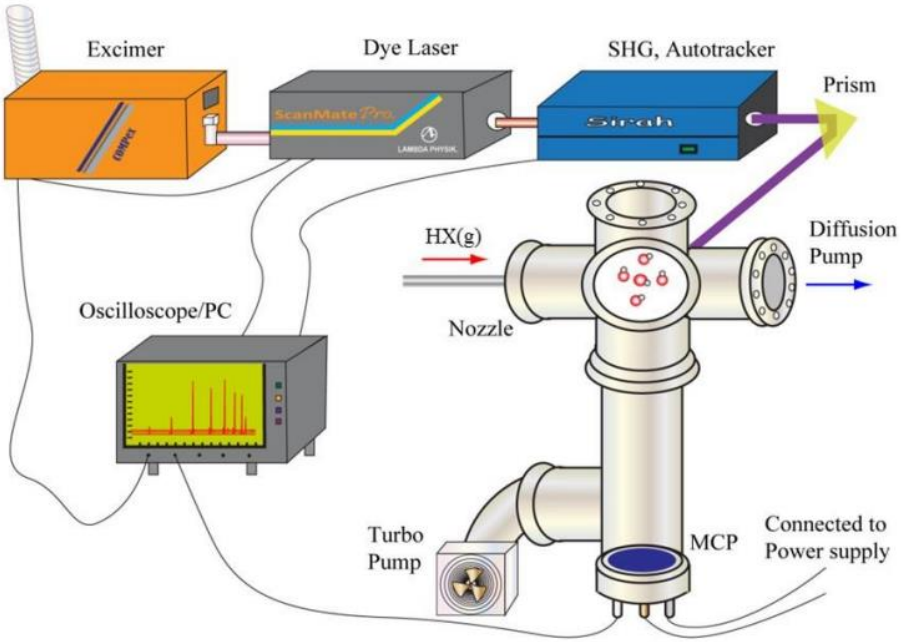

Figure 9 *Schematic representation of REMPI-TOF setup. Excimer laser powers dye laser, SHG doubles the frequency of laser. Samples injected via nozzle into vacuum chamber and get ionized. Ions hit MCP detector that sends signals to oscilloscope and is converted to experimental data.*

where *a* and *b* are constants depending on experimental conditions and Mw is molecular weight of the ions. The pressure inside the ionization chamber, during an experiment, was typically about $1.0 \times 10^{-7} - 1.0 \times 10^{-8}$ mbar, using a liquid nitrogen cooled diffusion pump aided by an Edwards mechanical pump. A Pfeiffer TURBO pump was used to pump the TOF tube. A simplified schematic figure of the equipment can be seen in fig.9 and an example (DCl/ HCl sample; see paper 3 in chapter 4.3) of experimental parameters is to be found in table.5.

Table 5 *Typical equipment and condition parameters for REMPI experiments*

a)	HCl/DCl/Ar sample	~ (DCl 60%: HCl 40%)50% : argon 50%
b)	Laser dyes	C-440, C-460 & C-480
c)	Freq. doubling crystal	Sirah BBO-2
d)	Laser repetition rate	10 Hz
e)	Dye laser linewidth	0.095 cm^{-1}
f)	Laser intensity used	10-16 mJ/pulse Dye laser, 0.5-1.0 mJ after SHG
g)	Nozzle size	0.5 mm
h)	Sample backing pressure	2-3 bar
i)	Pressure inside ion chamber	$5 \cdot 10^{-7}$ mbar

j)	Nozzle opening time	180-250 μs
k)	Delay time for laser excitation	450-500 μs
l)	Excitation step size	0.1 cm^{-1}
m)	Time-Of-Flight step size	10 ns
n)	Time-Of-Flight tube length	70 cm
o)	Focal lens distance	200 mm

Ion signals detected are treated as a function of mass and excitation wavenumber, which gives the mass spectra of the ions, for particular mass and laser excitation wavenumbers.

3.2 Data analysis

Ion signals, detected by the MCP´s, were fed through a coaxial cable and stored by a LeCroy 44MXs-A 400 MHz digital oscilloscope prior to further analysis.

A LabView v8.0 software program written by Dr. Jingming Long[135] was used to integrate mass spectral peaks as a function of ion mass and/or laser excitation wavenumber to create mass and/or MR-REMPI spectra, respectively. Text files, created, were processes by use of the Igor Pro v.6,[136] data analysis software and/or the spectral simulation program (PGOPHER v9.0)[137]. Further inspection of MR-REMPI spectra along with corresponding VMI data analysis (see below, chapter 3.3) allowed determination of multiphoton dynamics involved.

3.2.1 Mass resolved analysis – to – REMPI spectrum

Ions times-of-flight in the TOF mass spectrometer increase with mass. Following mass calibrations, mass spectra were determined from the measurements by the relationship given in eq. (31). The quantity of the ions is proportional to the intensity of the mass spectral peaks. A mass spectrum for a fixed laser excitation wavenumber (68 882 cm^{-1}), obtained by probing the CH_3Br molecule, can be seen in fig.10. A collection of mass spectra as a function of excitation wavenumber, for typical scanning step size of about 0.1 – 0.2 cm^{-1}, over a chosen scanning region, forms a set of REMPI data. Integrated ion peak signals, for a specific ion, as a function of excitation wavenumber, give REMPI spectra for the ion. A relevant REMPI spectrum of CH_3Br for the CH_3^+ ion can be seen in fig.11 for the two-photon excitation energy region of 66 000 – 69 000 cm^{-1}. The peaks seen in fig.11 correspond to two-photon resonant transitions to Rydberg states of the CH_3Br molecule. The assignments shown in the figure specify the Rydberg electron (5p), the spin-orbit states of the CH_3Br^+ ion ([3/2] or [1/2]) and the molecular vibrational modes (ν_i) and the corresponding quantum numbers.

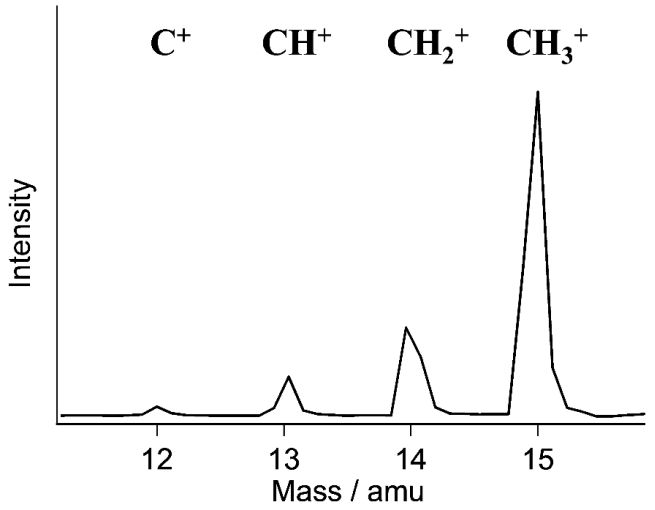

Figure 10 *Mass spectrum for the two-photon 68 882 cm^{-1} laser excitation of CH_3Br, showing ion signals for C^+, CH^+, CH_2^+ and CH_3^+. Intensity (y-axis) shows relative quantity of the ions formed.*

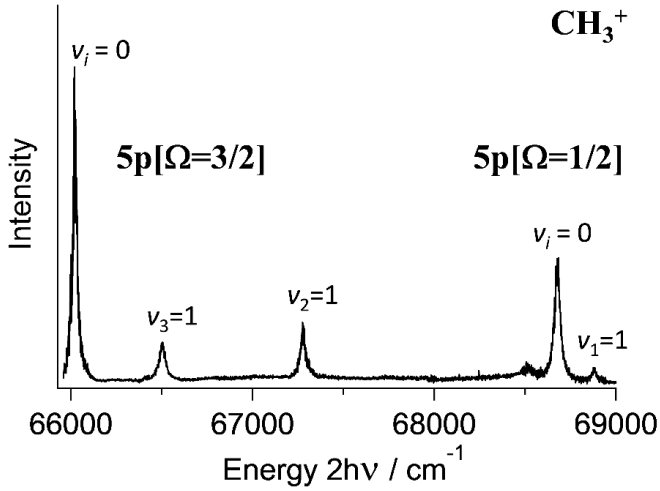

Figure 11 *REMPI spectrum for the CH_3^+ ion / CH_3Br molecule. REMPI spectra are created from ion signals as a function of excitation wavenumber. Peaks represent resonant transition to Rydberg states of the molecule. The v_1 =1 peak belongs to the 5p[Ω=3/2] series.*

3.2.2 Spectral simulations

Simulations of REMPI spectra were performed by using PGOPHER v9.0,[137] a software that can simulate rotationally structured spectra based on spectroscopic properties of the states involved. This, typically allowed determination of first and second order rotational constants (*B* and *D* respectively) as well as spin-orbit and lambda doubling constants for the excited states involved. Spectra simulations by PGOPHER were performed manually. This was done by adjusting spectroscopic constants for the excited states (assuming known parameters for the ground states) and the population in ground state levels (using a modified version of the Boltzmann distribution) until best fits of experimental and calculated spectra were obtained. A simulation for the $D^{35}Cl^{+}$ REMPI spectrum, involving the two-photon resonant transition, $I^{1}\Delta_{2}(v'=0) \leftarrow\leftarrow X^{1}\Sigma^{+}(v''=0)$ for $D^{35}Cl$, (see paper 3, chapter 4.3) is shown in fig.12.

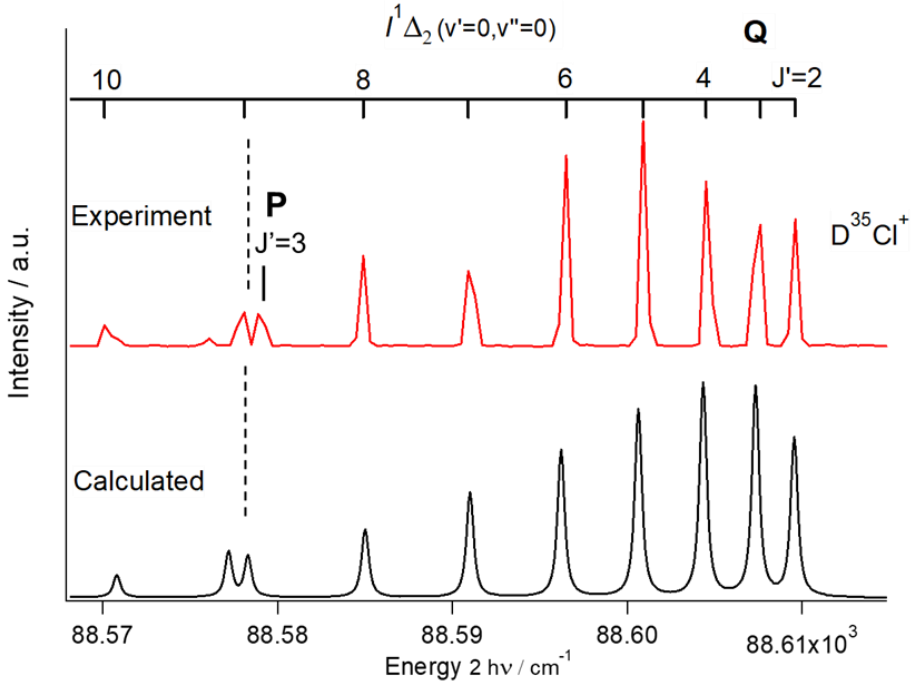

Figure 12 *Spectral simulation: REMPI spectrum (above, red) for the $D^{35}Cl$ molecule, showing the Q band for two-photon resonant transitions to the $I^{1}\Delta_{2}$ Rydberg state. Calculated spectrum (below; black), using the PGOPHER simulation software. The simulation allowed determination of relevant spectroscopic constants for the Rydberg state.*

The spectrum shows number of Q-branch lines along with one line of the P-branch. Judging from observed deviations (perturbations) in rotational line intensities (e.g. *J'*= 7), and positions (e.g. *J'*= 9) from regular patterns, seen in the calculated spectrum, state interactions could be identified and determined.

3.3 Velocity Map Imaging (VMI)

The introduction of the ion imaging method led to many advances when it came to understanding dynamics of molecules. It was first demonstrated by Chandler and Houston back in 1987,[138] looking at the ion distribution of the CH_3^+ fragment, following CH_3I photolysis and CH_3 ionization. The energy resolution of the technique was significantly improved with the introduction of Velocity Map Imaging or VMI by Eppink and Parker in 1997,[139] however the idea is the same. A jet-cooled molecular beam of the target molecule is formed in a reaction vacuum chamber. Linearly polarized laser pulses intersect the molecular beam at right angles, leading to dissociation of the parent molecule and ionization of the photofragments. The ions form inside a homogenous extraction field (defined by repeller and extraction plates) and form so called Newton spheres, which are ions distributed on the surface of a sphere because of their kinetic energy. The sphere of ions is projected towards a position-sensitive/imaging (microchannel plates coupled to a phosphor screen) detector and becomes a ring-like 2D projection on phosphorus screen that is recorded by a CCD camera.

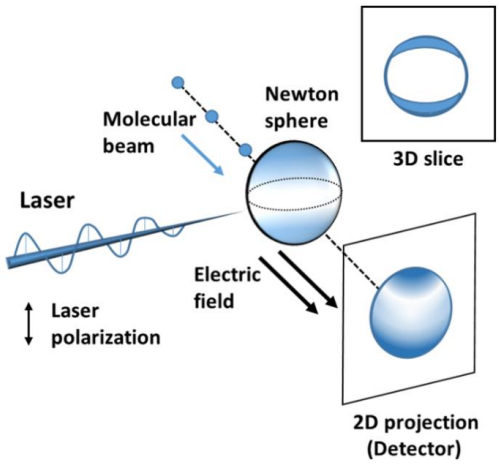

Figure 13 *Simplified schematic representation of VMI spectrometer. Laser ionizes the molecules, and charged particles are accelerated towards a MCP detector. Image is the treated with Abel inversion, to claim initial velocity distribution. After inversion, the 2D projection look more like a 3D slice image.*

To extract information from these 2D projections, a method called inverse Abel transform, is applied to give three-dimensional speed distribution.[140] The distribution of the ions after Abel inversion, is a 2D slice of the original 3D distribution. From the final image, information can be extracted on: 1) kinetic energy release (KER) of the detected photo-fragments, which describes the speed distribution of the ions relative to the centre of the 2D ring, which is also the centre of mass of the photolysis event 2) angular distribution, which describes the spatial distribution of the ions relative to the polarization direction of the laser. Fig.13 shows schematic representation of VMI spectrometer. For vertically polarized light source (similar to Fig.13), parallel to the detector, the transition dipole moment μ will also be parallel to the

laser polarization. For a diatomic molecule, there are two limiting cases for the bond orientation with respect to μ: (1) bond parallel to μ, in which case photofragments are ejected parallel to the laser polarization, the Newton sphere has more intensity at the poles and the transition is called "parallel" or (2) bond perpendicular to μ, in which case photofragments are ejected perpendicularly to the laser polarization, the Newton sphere has more intensity at the equator and the transition is called "perpendicular". State symmetries determine such distributions: a $\pi \leftarrow \pi$ transition is parallel, while a $\pi \leftarrow \sigma$ transition is perpendicular. This, therefore, can provide the experimentalist with information on the state symmetry. An example of a velocity map image can be seen on Fig.14. Bright/coloured regions indicate the intensity of the ions detected and dark regions are where no ions are detected. Centre of image is where ions are formed with little to none translational energy, whereas the outer region has greater translational energy. The double headed arrow, indicates the direction of the linear polarization of the laser. The image is then processed to extract the Kinetic Energy Release (KER) distribution of the ions.

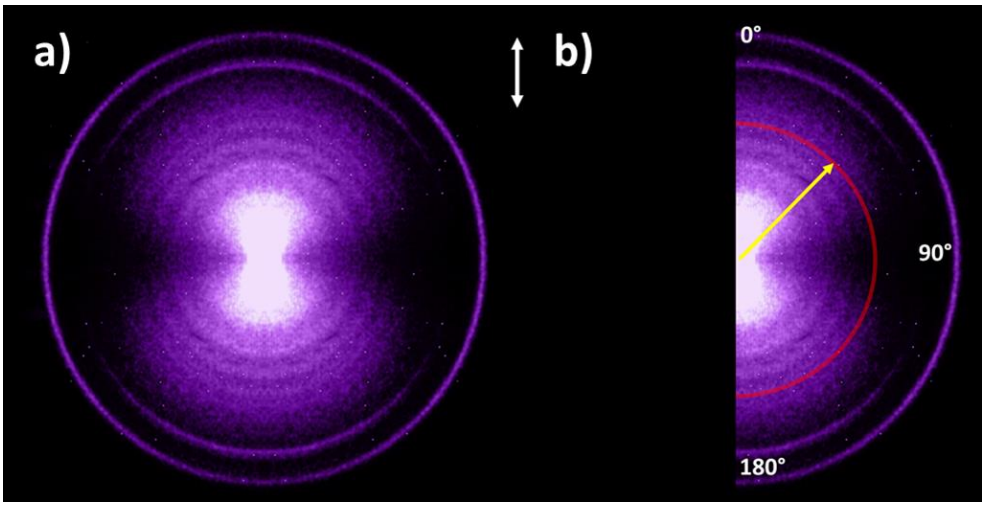

Figure 14 *a) Velocity map image for CH_3^+ ion following CH_3Br excitation at 251.28 nm. Ion intensity is false-coloured from purple to white. b) Shows half of a VMI from CH_3^+. Red line indicates ions formed with same recoil velocities, i.e. radial sector at same distance from centre of image. Double headed arrow indicates the linear polarization of the laser.*

Transforming the image into a KER spectrum is done couple of steps. Image is divided to a half (see Fig.14b). Integration of 0°-180° is carried out, using the fact that the image is cylindrically symmetric to the polarization of the laser. Each ion located in the same distance from the centre (see red half circle in Fig.14b) has the same KER, and therefore is counted on the same column/pixel distance on the KER spectrum. KER spectrum is extracted from the image with the radius in pixels, counted from the centre of the image (ring). The pixels are then converted into electron volts (eV) (or other energy unit of choice) using a simple equation,

$$KER(eV) = KER(pix)^2 * f \qquad (32)$$

where KER(*pix)* is the pixels in the image, *f* is a calibration factor related to the TOF distance, the magnification of the VMI lens and the extraction voltage and KER(eV) is the outcome in

eV. The outer most ring in fig.14, appears here as a sharp peak at about 1.6 eV, seen on KER spectrum, whereas the vibrational structure is formed from the rippled inner signal on fig.14 at about 0.1-0.7 eV (see fig.15b).

KER value assigned to the vibrational structure is found by, using equation (also see Fig.17 for schematic illustration),

$$KER(CH_3^{**} + Br) = 3h\nu + E_{J'',\nu''} - D_0(CH_3Br) - E(CH_3^{**}) \qquad (33)$$

where $h\nu$ is the photon energy, $E_{J'',\nu''}$ is the J'' and ν'' dependent rotational and vibrational energy of the ground state of CH_3Br, D_0 the bond energy for CH_3-Br and $E(CH_3{**})$ is the internal energy of the CH_3 fragment. The vibrational bands come across as relative sharp KER peaks, on top of bigger broader KER peaks. An example of detection of the vibrational bands can be seen in the low KER region (0.1-0.7 eV) seen in fig.15b.

Angular distribution is extracted by integrating ion signals over radius. The result is a distribution of ion intensity vs angle (from θ = 0° to 180°). As the image is cylindrically symmetric, either the left or the right half of the image is used (see fig.16). Signal intensities

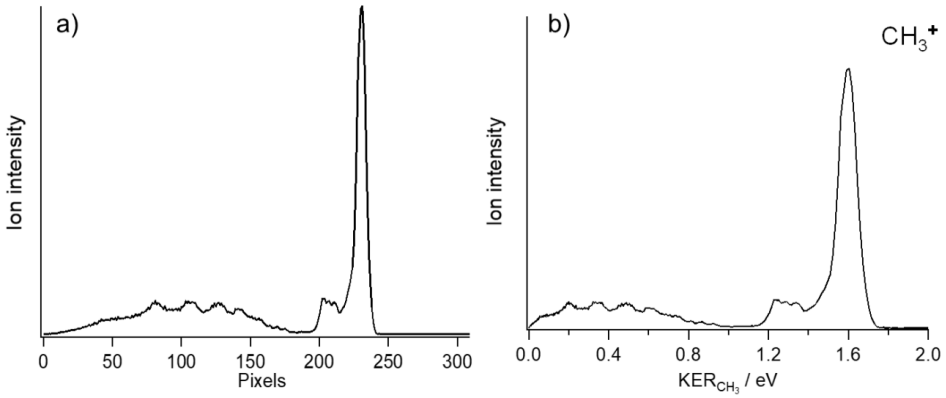

Figure 15 *KER spectra extracted from a velocity map image for detection of the CH_3^+ ion, a) KER with ion intensity vs. radius from the ring(s) centre in pixels, b) KER spectra showing conversion from pixels to electron volts.*

are fitted with the following expression that corresponds to one-step photodissociation,[141]

$$P(\theta) = A[1 + \beta_2 P_2(\cos(\theta)) + \beta_4 P_4(\cos(\theta))] \qquad (34)$$

where A is a scaling factor, P_2 and P_4 are Legendre polynomials, β_2 and β_4 are anisotropy parameters. The β_2 parameter acquires values between +2 (solely parallel transition, where signal appears on poles) and -1 (solely perpendicular transition, where signal appears on the equator). Value of β_2=0 gives isotropic distribution that is detected as an isotropic intensity ring, and is therefore a mixture of parallel and perpendicular transitions. Fig.16 shows an example of a VMI image from photoelectron spectra, showing angular distribution for a parallel transition.

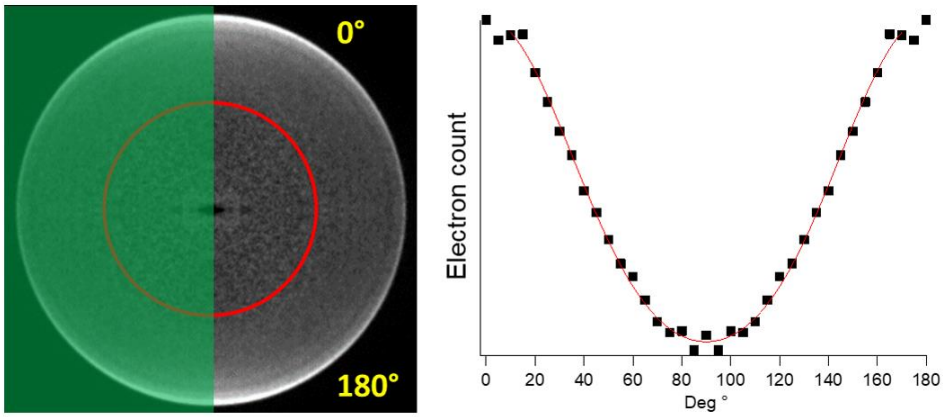

Figure 16 *Image (on the left), where graph (on the right) has been attained. Intensity is high, near 0° and 180°, as can be seen as bright signal on image, whereas dim signal on image at 90°, comes across as valley on the graph. Anisotropic parameter β_2 was found to be around 1.6 for this image, indicating a parallel transition.*

3.3.1 Photoelectron spectroscopy (PES)

Photoelectron spectroscopy studies the electrons formed in an ionization process. When an electron is detached from, e.g. molecule, the excess energy from the photon that ionizes the molecule goes into translational energy of the electron. If the photon energy is chosen carefully and excites the electron to the ionization limit exactly, the translational energy of the electron is approximately zero, whereas electrons that acquire translational energy correlate to the excess energy off the photon above the ionization limit. Those electrons move away from the centre of the VMI image (see fig.16). Here, the representation on fig.17 is taken as example, for calculating the excess energy, is shown in following equation,

$$KER(el) = h\nu + E(CH_3^{**}) - IE(CH_3) - E(CH_3^+(int + KER)) \qquad (35)$$

where $h\nu$ is the photon energy, $E(CH_3{**})$ the internal energy, $IE(CH_3)$ the ionization energy and $E(CH_3^+(\text{int+KER}))$ stands for the internal (J',v') and kinetic energy for the CH_3^+ ion. Fig.17 shows the process from ground state CH_3Br until the ionization of the CH_3 fragment. CH_3Br is excited with three photons to a superexcited, metastable state $CH_3Br^{\#}$. The bond between CH_3 and Br breaks and the CH_3 fragment is formed in a Rydberg state $CH_3{**}$ along with Br. The excess energy seen in the KERs for CH_3^+, would be equivalent to the drop from $CH_3Br^{\#}$ to $CH_3{**}$(see bracket no.1 in fig.17). The methyl fragment gets ionized from the $CH_3{**}$ Rydberg state with one photon, and the excess energy above the ionization limit of CH_3 goes into the electron (see bracket no.2 in fig.17).

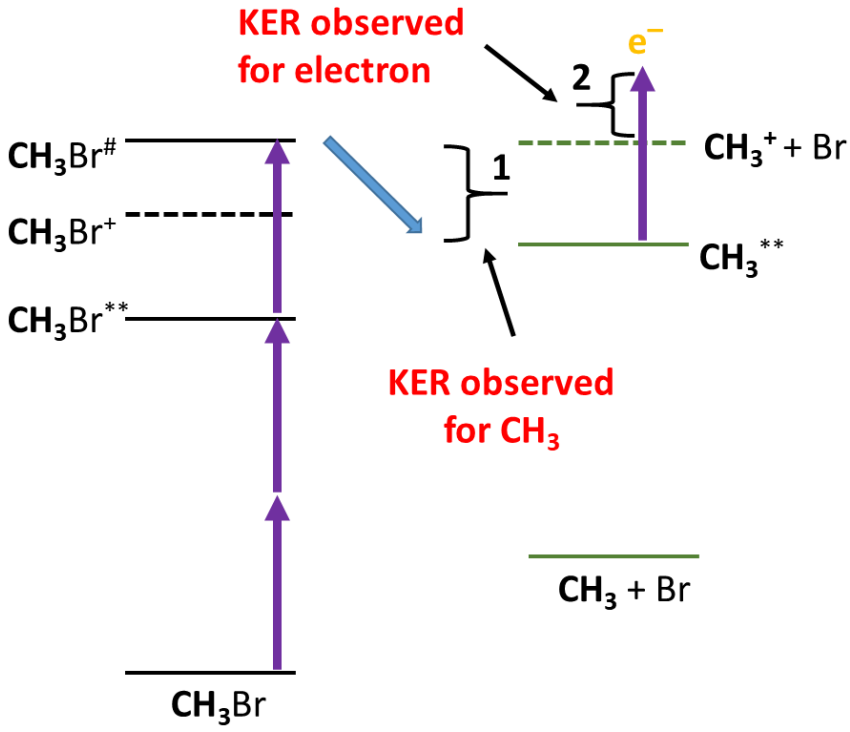

Figure 17 *Schematic representation of excitation of the CH3Br molecule to a superexcited state. Step 1, shows the dissociation process that gives speed distribution on the KER spectra of the CH_3^+ ion. Step 2, shows excess energy for electron (e^-), after ionization of CH_3**, forming $CH_3^+ + e^-$.*

3.3.2 Slice imaging

The Slice Imaging,[142, 143] is an improvement to ion imaging and VMI. VMI requires the inverse Abel transformation, whereas slice imaging cancels the need for that process, while remaining comparable to VMI when it comes to energy resolution. Thus the need to use laser polarizations parallel to the detector is cancelled. In addition using the slice imaging method, the noise introduced by the inverse Abel transformation is eliminated. The name of the method describes the technique: Combining a delayed extraction field with a short detection time (<40 ns), only the centre slice of the 3D Newton sphere is detected. This gives a much clearer image.

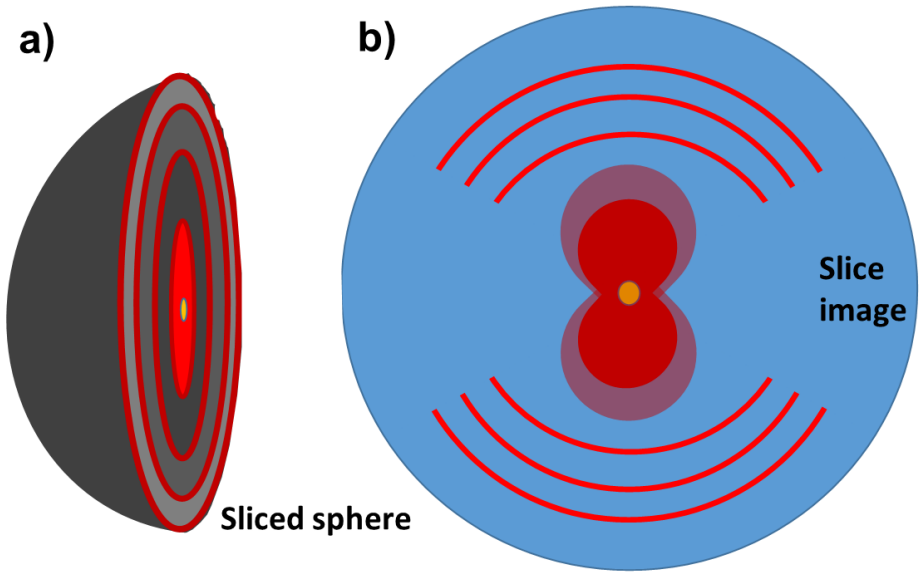

Figure 18 *Artist representation of slice imaging a) Newton sphere sliced in half. Red areas (centre and rings) are ion distribution with different speed distribution. Good timing for slice image to be taken. b) Example of how an image might look like, for a parallel transition for selected ion (for vertical (up-down) polarization of the laser).*

It can be seen on fig.18, where a) shows a sphere cut in half, and red colour indicates where the distribution of formed ions with different kinetic energies are located. The ions hit the imaging detector, creating an image on phosphorus plate that is recorded using a CCD camera. The slice image, looks like the centre slice of the sphere, showing angular distribution and speed distribution (KER), whereas the older VMI process would detect the whole sphere projection.

4 Included papers

1. Arnar Hafliðason, Victor Huasheng Wang, Ágúst Kvaran. *Long term puzzles of the CH and CD energetics and related phenomena revisited; solutions sought through REMPI-photofragmentations of bromomethans*. Physical Chemistry Chemical Physics, 2016, 18, 1797-1806.
1.1. Supporting information

2. Arnar Hafliðason, Pavle Glodic, Dimitris Zaouris, Peter C. Samartzis, Ágúst Kvaran. *Effect of triplet to singlet state interaction on photofragmentation dynamics: highly excited state of HBr probed by VMI and REMPI as a case study*. Physical Chemistry Chemical Physics, 2016, 18, 26291-26299.
2.1. Supporting information

3. Arnar Hafliðason, Victor Huasheng Wang, Ágúst Kvaran. *High energy Rydberg and valence states and state interaction of DCl: New observations by mass resolved REMPI*. Journal of Molecular Spectroscopy, 2017, 341, 1-9.
3.1. Supporting information

4. Arnar Hafliðason, Pavle Glodic, Greta Koumarianou, Peter C. Samartzis, Ágúst Kvaran. *Multiphoton Rydberg and valence dynamics of CH_3Br probed by mass spectroscopy and slice imaging*. Physical Chemistry Chemical Physics, 2018, 20, 17423-17433.
4.1. Supporting information

5. Arnar Hafliðason, Pavle Glodic, Greta Koumarianou, Peter C. Samartzis, Ágúst Kvaran. *Two-color REMPI study of CH_3Br, probing CH_3 and Br formation with MPI and Slice Imaging*. Physical Chemistry Chemical Physics, 2018, (*submitted*).
5.1. Supporting information

4.1 Paper 1

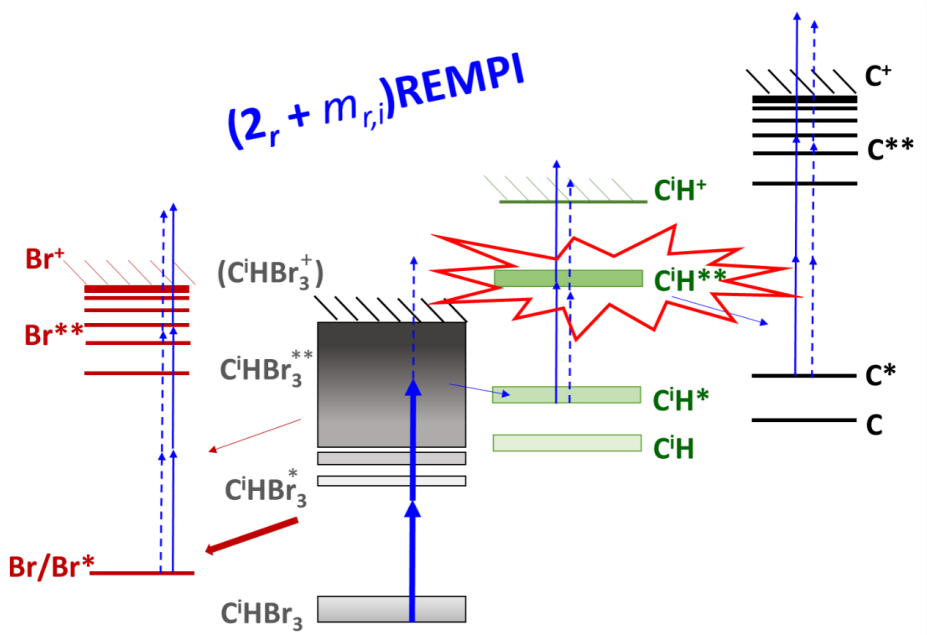

Arnar Hafliðason, Victor Huasheng Wang, Ágúst Kvaran. *Long term puzzles of the CH and CD energetics and related phenomena revisited; solutions sought through REMPI-photofragmentations of bromomethans*. Physical Chemistry Chemical Physics, 2016, **18**, 1797-1806.

DOI: 10.1039/c5cp06097d

PCCP

PAPER

Cite this: *Phys. Chem. Chem. Phys.*, 2016, **18**, 1797

Long term puzzles of the CH and CD energetics and related phenomena revisited; solutions sought through REMPI-photofragmentations of bromomethanes†

Arnar Hafliðason, Huasheng Wang and Ágúst Kvaran*

Received 9th October 2015,
Accepted 7th December 2015

DOI: 10.1039/c5cp06097d

www.rsc.org/pccp

Ever since the pioneering work by Herzberg and Johns in 1969 (*The Astrophysical Journal*, 1969, **158**, 399) the spectral assignment and the energetics of the fundamental molecular fragment CH, in the region of 63 000–65 000 cm^{-1} (7.81–8.06 eV), have remained a puzzle to a large extent. The dissociation of bromoform and deuterated bromoform following two-photon resonance excitations to molecular Rydberg states forms the fragment species CH* and CD* in the excited state $A^2\Delta(v' = 0)$ as well as carbon and bromine atoms in the ground and first excited states, C/C* and Br/Br*. Further $(1_r + 1_i)$REMPI of CH* and CD* resonance excites the fragments to the energy region of concern, whereas the atom fragments were identified by further $(2_r + 1_i)$REMPI. Analysis based on spectral simulations, isotope shifts and comparison with other data allowed spectral identifications, assignments and partial characterization of four highly excited bound states for each of the molecular fragments (CH**/CD**); including the $(3)^2\Pi$ valence state and the $(4)^2\Pi$ Rydberg state, for the first time. Perturbations, shown as line-shifts, line-intensity and/or line-width alterations, due to the level-to-level state interactions between the bound states and predissociations by a repulsive state are recognized. Recording of C^+ signals in REMPI of several bromomethanes for a one-photon energy of about 40 333 cm^{-1} allows the clarification of a mystery concerning a broad C^+ band frequently observed. This work, presented, demonstrates the usefulness of molecular REMPI for fragment analysis.

Introduction

The spectroscopy and photofragmentation of bromomethanes, CH_xBr_{4-x} (x = 0–3), have been studied both experimentally and theoretically for decades.[1–14] Whereas, most of the studies concern the lower energy valence states, limited information is available relevant to higher energy Rydberg states. In addition to being of interest for fundamental studies, the compounds and their photofragmentation species are of importance both in atmospheric chemistry and astrochemistry.[15–21] Thus, photofragmentation processes have been of interest due to bromine atom formation and its ozone depletion effects[3,4,11–13,22,23] in the atmosphere and because CH_n (n = 1–3) radicals and the corresponding ions are believed to be fundamental building units for the formation of bigger organic molecules in the interstellar space.[19,24]

Standard UV absorption spectra of the bromomethanes reveal transitions to repulsive valence states corresponding to $\sigma^* \leftarrow$ nb transitions in the near-UV region of about 180–290 nm[1,23,25,26] and transitions to Rydberg states in the far-UV region of about 110–180 nm.[10,13,14,27,28] REMPI spectra of CH_3Br[10,13] and CH_2Br_2[14] show structures due to transitions to Rydberg states. Generally, less clear Rydberg state progressions are seen as the number of bromine atoms increases. Photodissociation processes, *via* Rydberg states, are believed to form atoms and molecular fragments such as Br, CH and C in ground and excited (Br*, CH* and C*) states. Fig. 1 shows some $(2_r + m_{r,i})$REMPI processes for CH_xBr_{4-x}, (x = 2, 3), where 2_r refers to the two-photon resonance excitation of the parent molecule and $m_{r,i}$ refers to further m photons required for resonance and/or ionization excitations. The fragment ions can be formed by further resonance or non-resonance excitations of the neutral fragments. Thus, for example, the atom ions (Br^+, C^+) and CH^+ can be formed by further $(2_r + 1_i)$ and $(1_r + 1_i)$REMPI, respectively, in which case m_{ri} is $(2_r + 1_i)$ and $(1_r + 1_i)$, respectively. Therefore, the REMPI ion signals can both reflect the parent molecular spectral structure as well as that of the fragments.

Science Institute, University of Iceland, Dunhagi 3, 107 Reykjavík, Iceland. E-mail: agust@hi.is; Web: https://www.hi.is/~agust/; Tel: +354-525-4672, +354-525-4800

† Electronic supplementary information (ESI) available: REMPI spectral lines for C/C* and Br/Br* atoms. See DOI: 10.1039/c5cp06097d

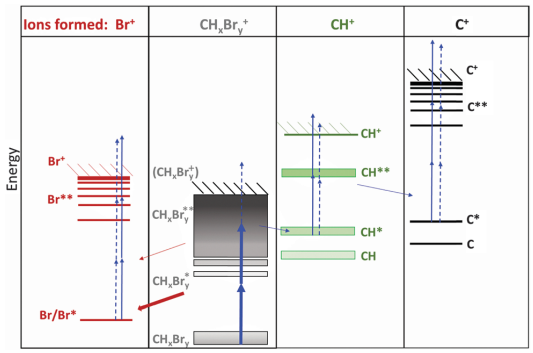

Fig. 1 Schematic figure showing some important excitation and photofragmentation channels in $(2_r + m_{r,i})$REMPI of CH_xBr_{4-x}; x = 2,3 (see the main text, Introduction). Unbroken vertical arrows are for resonance transitions, whereas broken vertical arrows represent non-resonance transitions. Non-vertical arrows represent dissociation paths for the formation of neutral fragments (M, M*). M: ground state species, M*: valence molecular states or low energy excited states, M**: Rydberg states or high energy excited states, and M^+: ionic states.

The CH radical is a fundamental unit for possible photo-assisted formation of organic molecules in interstellar space. Therefore, its high energy electronic states are of great astrochemical interest. Since the UV and VUV spectroscopic studies of the CH radical by Herzberg and Johns in 1969[29] there have been a number of conflicts and unsolved puzzles concerning its spectral assignments in the high energy Rydberg state region. Herzberg and Johns assigned spectra with the band origins 58 981, 64 212 and 64 531 cm^{-1} to transitions from the ground state ($X^2\Pi(v'' = 0)$) to the $D^2\Pi(v' = 0)$, $E^2\Pi(v' = 0)$ and $F^2\Sigma^+(v' = 0)$ states, respectively. Later P. Chen *et al.* assigned a spectrum recorded by the multiphoton ionization technique at 64 150 cm^{-1} to the upper state $D^2\Pi(v' = 2)$, whereas a spectrum near 63 000 cm^{-1} was assigned to a $^2\Sigma^+$ upper state (labeled as $E'^2\Sigma^+$).[30,31] Three bound $^2\Pi$ states and one $^2\Sigma$ state, close in energy, were predicted to be found in this region according to *ab initio* calculations.[32,33] Tjossem and Smyth noticed unusual rotational line intensities in the two-photon REMPI spectrum of CH due to the $D^2\Pi(v' = 2) \leftarrow\leftarrow X^2\Pi(v'' = 0)$ resonance transition because of near-resonance with the intermediate $C^2\Sigma^+(v' = 0)$ state,[34] resulting in enhanced line intensities in the Q branch for rotational quantum numbers close to $N = 8$. This was further verified by Wang *et al.*, who also noticed a sudden onset of predissociation for $N \geq 12$, which they attributed to complex interactions among $^2\Pi$ states, close in energy, in that region.[35] In 2000 Y. Chen *et al.* published a CH REMPI spectrum with a number of rotational lines detected for multiphoton ionization of $CHBr_3$ in argon which they assigned to the single-photon resonance transition $CH^{**}(D^2\Pi(v' = 2)) \leftarrow CH^*(A^2\Delta(v' = 0))$ with the band origin of 40 991.5 cm^{-1}.[36] Recently J. Long *et al.* detected CH bands in the same energy region (40 550–41 250 cm^{-1}) in the REMPI spectra of CH_2Br_2.[14] A less extensive rotational structure, compared to that observed for $CHBr_3$, associated with different exothermicities in photodissociation channels, allowed the identification of three different electronic transitions from the $A^2\Delta(v' = 0)$ state with band origins of 40 762, 40 991.5 and 41 155 cm^{-1}. These were assigned to transitions to the CH** (Fig. 1) states $E^2\Pi(v' = 0)$, $D^2\Pi(v' = 2)$ and $F^2\Sigma^+(v' = 0)$, respectively. Observation of the forbidden $F^2\Sigma^+(v' = 0) \leftarrow A^2\Delta(v' = 0)$ transition was explained as being due to an enhanced transition probability gained by mixing with nearby states.

Different interpretations of broad C^+ ion peaks, observed in REMPI of $CHBr_3$,[36] CH_2Br_2[14] and CH_3Br,[13] for a one-photon wavenumber of about 40 333 cm^{-1}, remain in the literature, without clear confirmations. Y. Chen *et al.* attributed the peak to a one-photon resonance excitation of $CH^*(A^2\Delta(v' = 0))$ to a short lived, predissociating, bound state, $CH^{**}((3)^2\Pi(v' = 0))$ followed by photodissociation to form C^+ and H *via* two-photon excitation to a repulsive CH^+ state.[36] The lifetime of the intermediate state, $((3)^2\Pi(v' = 0))$, was believed to be very short due to predissociation by a repulsive $^2\Pi$ state to form $C^*(^1D_2)$ and H.[32] Long *et al.*,[14] on the other hand, suggested that the peaks are due to intensity enhancements in the REMPI of the molecules in the case of C^+ formation because of an increased transition probability by switching from the three-photon to two-photon non-resonance ionization of $C^*(^1D_2)$.

A large number of bromine atomic lines, due to $(2_r + 1_i)$REMPI of the ground (Br) and spin–orbit excited (Br*) species, are observed in REMPI of CH_3Br[13] and CH_2Br_2.[14] The Br and Br* species are believed to be partly formed by one-photon photodissociation *via* excitations to repulsive molecular valence states and partly due to the predissociation of the parent molecular Rydberg states following two-photon excitation (see Fig. 1).

In this paper we present and analyse mass resolved REMPI data of bromoform, for two-photon excitation to a high energy Rydberg state region. The data show (a) broad spectral features due to excitations to molecular Rydberg states, (b) carbon and bromine atomic spectra as well as (c) spectra due to resonance transitions from $CH^*A^2\Delta$. The mystery concerning the nature of the broad C^+ peaks, seen in REMPI of a number of bromomethanes, mentioned above, for the one-photon excitation of about 40 333 cm^{-1}, is clarified. A special focus is on the energetics and nature of electronic states of CH** in the energy region of 63 000–65 000 cm^{-1} (7.81–8.06 eV), which has been a puzzle for decades (see above). Simulation based analysis of the $CH^*(A^2\Delta(v' = 0))$ spectra as well as the corresponding spectra for CD* derived from REMPI of $CDBr_3$ allow the clarification of the highly mixed electronic states in that region as well as relevant spectroscopy.

Experimental

The equipment used in the experiments is similar to what has been described before.[37–39] Mass spectra were recorded as a function of laser excitations for various bromomethanes corresponding to the two-photon excitation of 76 000–84 000 cm^{-1}/one-photon excitation of 38 000–42 000 cm^{-1}. A Coherent ScanMatePro dye laser was pumped by a XeCl (308 nm) excimer

laser from Lamda Physics (COMPex 205) at a repetition rate of 10 Hz. Outputs for the dyes C-503 and C-480, frequency doubled by a BBO crystal (SHG-215 from Sirah), were used to cover the wavelength range of concern (238–263 nm). The linewidth of the dye laser beam was about 0.095 cm^{-1}. Typical laser intensities used were about 0.1–0.3 mJ per pulse. Argon gas was swept over samples of liquids ($CHBr_3$ (Acros Organics; purity 96%), $CDBr_3$ (Sigma Aldrich; purity 99.5%) and CH_2Br_2 (Merck Schuchardt; purity 98%)) and solids (CBr_4 (Acros Organics; purity 98%)), kept in a trap at room temperature for a total pressure of about 1.0 bar, whereas a sample of pure CH_3Br gas (Merck Schuchardt; purity 99.5%) at about 1.0 to 1.5 bar was used. Samples were let through a pulsed nozzle (500 μm) into an ionization chamber. The pressure in the ionization chamber was kept lower than 10^{-6} mbar during experiments. The nozzle was kept open for about 200–400 μs, and the laser beam was fired for about 450–500 μs after the nozzle was opened. Ions formed were extracted into a 0.75 meter long time-of-flight tube and detected by MCP plates. Signals were fed into a LeCroy WaveSurfer 44MXs-A 400 MHz storage oscilloscope. Signal levels were

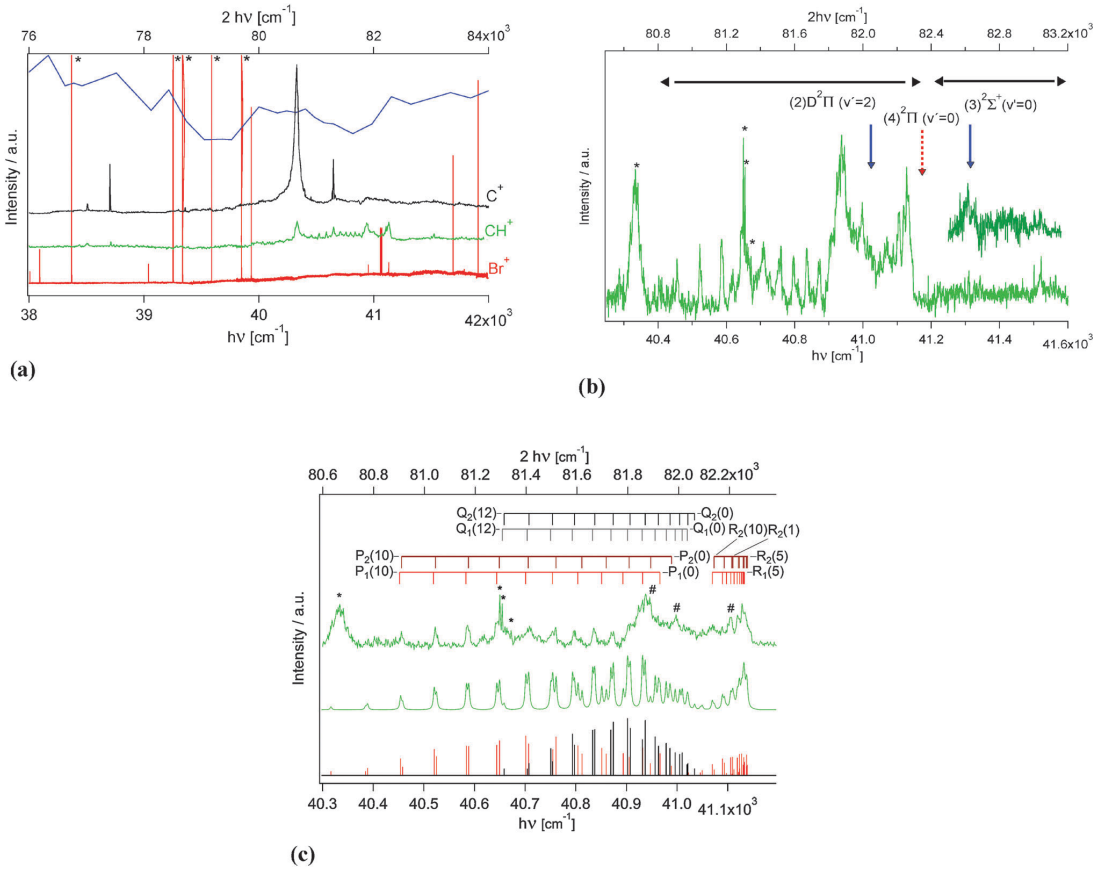

Fig. 2 $CHBr_3$: (a) REMPI spectra of the ions C^+ (black), CH^+ (green) and Br^+ (red) for the two-photon excitation region 76 000–84 000 cm^{-1} (one-photon excitation region of 38 000–42 000 cm^{-1}) along with the absorption spectrum derived by Sander *et al.* (blue; top).[41] The REMPI spectra are proportional in terms of intensity. Markings (*) of atomic lines, seen in the Br^+ spectrum, indicate lines out of range. (b) REMPI spectrum of $CHBr_3$ for the ion CH^+ for the two-photon excitation region of 80 600–82 800 cm^{-1} (one-photon region of 40 300–41 400 cm^{-1}). Peaks marked with * are due to Coulomb broadening of C^+ signals. Spectral structures mainly and solely due to one-photon resonance excitations from $CH^*(A^2\Delta(v' = 0))$ to $CH^{**}((2)D^2\Pi(v' = 2))$ and $CH^{**}((3)^2\Sigma^+(v' = 0))$, respectively, are marked by horizontal black arrows for the spectral ranges and by vertical blue arrows for the band origins (ν^0) (see Table 3). The vertical broken red arrow marks the band origin of the $CH^{**}((4)^2\Pi(v' = 0))$ spectrum estimated from the corresponding CD* spectrum (see the text and Table 3). The inserted $(3)^2\Sigma^+(v' = 0)$ spectrum (above) was recorded for an increased laser power. (c) Simulation of the $CH^*(A^2\Delta(v' = 0))$ $(1_r + 1_l)$REMPI spectrum due to resonance transition to the $(2)D^2\Pi(v' = 2)$ state, derived by REMPI of $CHBr_3$ for CH^+ detection: experimental spectrum (linewidths 4–6 cm^{-1}) at top (green), calculated spectrum for linewidths = 4 cm^{-1} in the middle (green) and *P* (red), *Q* (black) and *R* (red) lines at the bottom. Rotational line assignments are shown at top for the *N*′ numbers given in parentheses. Peaks marked by * are due to Coulomb broadening of C^+ signals. Peaks and spectral features marked with # were not simulated. Simulation was carried out by using the software package PGOPHER.[55] The top and bottom scales, for all figures, are the two- ($2h\nu$) and one- ($h\nu$) photon wavenumbers, respectively.

recorded for a fixed number of 50 laser pulses, for laser wavenumber steps of 0.1 or 0.2 cm^{-1} to give mass resolved REMPI data. REMPI spectra were obtained by integrating signals for a particular mass as a function of laser excitation wavenumber. Saturation and power broadening were avoided by minimizing laser power. Laser calibration was based on observed $(2_r + 1_i)$REMPI halogen atomic lines. The accuracy of the calibration was found to be about ± 2.0 cm^{-1} on the two-photon scale. Overall spectra were constructed using smaller scans which were normalized to each other by using intensities of bands that are common to neighbouring sections.

Results and discussion

Main features and interpretations of REMPI spectra

Mass resolved $(2_r + m_{r,i})$REMPI data were collected for $CHBr_3$ for the two-photon excitation region of 76 000–84 000 cm^{-1} (one-photon excitation region of 38 000–42 000 cm^{-1}). Only the C^+, CH^+ and $^iBr^+$ (i = 79, 81) fragment ions were detected. Fig. 2(a) shows the relevant REMPI spectra along with the one-photon absorption spectrum.[1] Narrow and sharp peaks detected in the atom fragment spectra (C^+ and Br^+) are assigned to $(2_r + 1_i)$REMPI of C/C* and Br/Br*.[40] The majority of peak structures detected in the region of 80 760–82 300 cm^{-1} for CH^+ is assigned to REMPI of $CH^*(A^2\Delta(v' = 0))$. The broad peak at 80 666 cm^{-1}, detected in the C^+ spectrum (also seen in the CH^+ spectrum), is attributed to an enhanced photoionization probability associated with switching from the three-photon to two-photon ionization of $C^*(^1D_2)$ (see below). Judging from the one-photon absorption spectrum of $CHBr_3$, which has been interpreted as being due to transitions to Rydberg states (Fig. 2(a)),[1] the remaining, underlying broad features of the REMPI spectra, largely similar in shape for the three spectra, are likely to be indicative of resonance transitions to parent molecular Rydberg states, with its broad structure being due to short lifetimes of the states. Detected fragments, most likely, are formed by the dissociation of the parent molecular excited Rydberg and valence states. Individual REMPI spectra will now be discussed in more detail.

C/C* REMPI

Energetically, the ground state $C(^2P_{0,1,2})$ and the excited states, $C^*(^1D_2)$ and $C^*(^1S_0)$, can be formed along with some of the fragments Br/Br*, $CH^*(A^2\Delta)$, HBr and Br_2 for the two-photon excitation region of concern (76 000–84 000 cm^{-1}) as listed in Table 1. Ionization of these carbon atom fragments would require further two to three photons (see Fig. 3). A number of $(2_r + 1_i)$REMPI lines are observed for $C(^2P_{0,1,2})$ and $C^*(^1D_2)$ as well as one $(1_r + 1_i)$REMPI line for $C^*(^1S_0)$.[40] Most probably a majority of detected C/C* fragments are formed by the two-photon photodissociation of the parent molecule along with the other fragment species, listed in Table 1, for the lowest energy thresholds.

The broad peak at 80 666 cm^{-1} in the C^+ spectrum has also been seen in our REMPI studies of CH_3Br[13] and CH_2Br_2[14] (see Fig. 4) and by Y. Chen *et al.* for $CHBr_3$.[36] Whereas, Y. Chen *et al.* attributed the peak to $(1_r + 2_i)$REMPI of $CH^*(A^2\Delta)$ *via* the short lived $CH^{**}((3)^2\Pi(v' = 0))$ resonance state[36] an alternative

Table 1 Energy thresholds (in wavenumbers/cm^{-1}) for fragmentations of $CHBr_3$. (a) Within the observation region (76 000–84 000 cm^{-1}) and (b) below the observation region

C/C*	CH/CH*	Br/Br*	Other fragments	Wavenumbers[a]/ cm^{-1}
(a)				
—	$CH(X^2\Pi)$	3Br*(1/2)	—	83806.9
—	$CH^*(A^2\Delta)$	Br*(1/2)	Br_2	83408.3
$C^*(^1D_2)$	—	2Br(3/2)	HBr	80636.7
—	$CH(X^2\Pi)$	Br(3/2), 2Br*(1/2)	—	80121.7
—	$CH^*(A^2\Delta)$	Br(3/2)	Br_2	79723.1
$C(^3P_2)$	—	2Br*(1/2)	HBr	77857.9
$C(^3P_1)$	—	2Br*(1/2)	HBr	77830.9
$C(^3P_0)$	—	2Br*(1/2)	HBr	77814.5
—	$CH(X^2\Pi)$	2Br(3/2), Br*(1/2)	—	76436.4
(b)				
$C^*(^1S_0)$	—	—	HBr, Br_2	75874.9
$C(^3P_2)$	—	Br(3/2), Br*(1/2)	HBr	74172.7
$C(^3P_1)$	—	Br(3/2), Br*(1/2)	HBr	74145.7
$C(^3P_0)$	—	Br(3/2), Br*(1/2)	HBr	74129.3
—	$CH(X^2\Pi)$	3Br(3/2)	—	72751.2
$C(^3P_2)$	—	2Br(3/2)	HBr	70487.4
$C(^3P_1)$	—	2Br(3/2)	HBr	70460.4
$C(^3P_0)$	—	2Br(3/2)	HBr	70444.0
$C^*(^1D_2)$	—	—	HBr, Br_2	64419.5
—	$CH(X^2\Pi)$	Br*(1/2)	Br_2	60219.3
—	$CH(X^2\Pi)$	Br(3/2)	Br_2	56534.1
$C(^3P_2)$	—	—	HBr, Br_2	54270.3
$C(^3P_1)$	—	—	HBr, Br_2	54243.3
$C(^3P_0)$	—	—	HBr, Br_2	54226.9
—	—	Br*(1/2)	$CHBr_2$	24147.5
—	—	Br(3/2)	$CHBr_2$	20462.3

[a] Values derived from bond energies.[56,57]

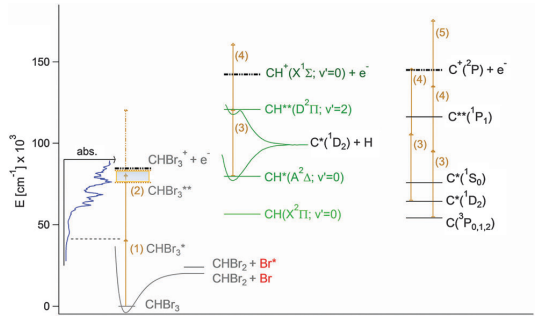

Fig. 3 $CHBr_3$, REMPI: energetics, excitation and photofragmentation processes in REMPI of $CHBr_3$. The shaded area is the scanning region dealt with in this paper. The relative one-photon absorption intensity of $CHBr_3$[1,41] is tilted to the left (blue). For M = molecular or fragment species, M represents the ground state species, M* is a valence molecular state or a low energy excited state, M** is a Rydberg state or high energy excited state and M^+ is an ionic state. Threshold energies (see Table 1) for CH/CH*/CH**/CH^+ and C/C*/C**/C^+ fragment formations and simultaneous Br and Br_2 formations, as well as relevant excitations and ionizations are indicated. Some 40 333 cm^{-1} (one-photon)/80 666 cm^{-1} (two-photon) excitations are shown.

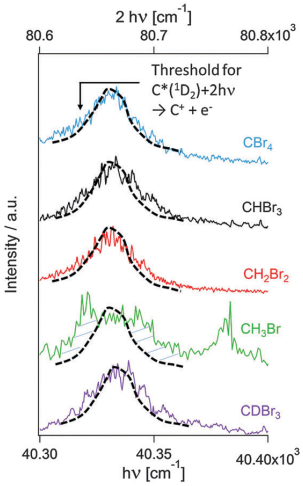

Fig. 4 C^+ REMPI as a function of one- (bottom) and two- (top) photon excitation wavenumber for CH_xBr_{4-x}, x = 0–3, and $CDBr_3$ showing broad peaks centered at about 80 666 cm^{-1}, on the two-photon wavenumber scale. The broad peaks have been normalized to the same height and are highlighted by broken curves to guide the eye. The peaks are attributed to an enhanced non-resonance photoionization probability associated with switching from three-photon to two-photon ionization of $C^*(^1D_2)$ formed by the two-photon dissociation of the parent molecules. The threshold for the two-photon ionization of $C^*(^1D_2)$ is indicated. Spectral bands surrounding the broad peak for CH_3Br are due to transitions to the parent molecular Rydberg states.[13]

explanation was given by J. Long *et al.*, who suggested that it might be attributed to an enhanced photoionization probability.[14] REMPI scans of $CDBr_3$ and CBr_4 both reveal broad peaks for C^+ in the same position and analogous in shape to those recorded for CH_xBr_{4-x} (x = 1–3), just above the threshold for two-photon ionization of $C^*(^1D_2)$ (80625.27 cm^{-1}) (see Fig. 4). This clearly indicates that the peak does not have to be associated with CH/CH* excitation. Instead we conclude that the peak is due to an enhanced non-resonance photoionization probability associated with switching from three-photon to two-photon ionization of $C^*(^1D_2)$ formed by two-photon dissociation of the parent molecule(s). The corresponding, lower intensity, CH^+ peak (Fig. 2) is due to a Coulomb broadening of the C^+ mass signal.

Br/Br* REMPI

The bromine atomic lines, observed (Fig. 2(a), ESI of ref. 40) could partly be due to a (2_r + 1_i)REMPI of bromine atoms formed by one-photon photodissociation *via* excitation to repulsive molecular valence states, since a one-photon excitation corresponds to the low energy tail of the weak absorption band in the near-UV spectral region[1,41] (see Fig. 3). Considering, however, a number of observations for photofragmentation *via* Rydberg states, these must also be, partly, due to REMPI of bromine atoms formed by the predissociation of Rydberg states following two-photon excitation.[13,14,42,43] Energetically, a number of bromine atom formation channels following two-photon excitation to Rydberg states could be involved (see Table 1), of which the simplest channel, involving only single-bond breaking, is likely to be dominant. Generally, lines due to transitions from ground state $Br(^2P_{3/2})$ are found to be more intense than those due to transitions from the spin–orbit excited $Br^*(^2P_{1/2})$[40] (Fig. 2(a)), suggesting that dissociative channels forming ground state Br are more favourable.

CH*/CD* REMPI

A weak CH^+ REMPI spectral structure (Fig. 2(a) and (b)) observed in the two-photon excitation region of 80 760–82 300 cm^{-1} (one-photon excitation region of 40 380–41 150 cm^{-1}) resembles that observed by Y. Chen *et al.*[36] who attributed it to a (1_r + 1_i)REMPI of $CH^*(A^2\Delta(v'=0))$, due to a one-photon resonance transition to the $CH^{**}((2)D^2\Pi(v'=2))$ state. Peaks were assigned to *P*, *Q* and *R* rotational lines. Based on simulation calculations (Fig. 2(c)) we have reassigned the rotational line series (Table 2(a)) as well as re-evaluated relevant spectroscopic constants for the $CH^{**}((2)D^2\Pi(v'=2))$ state (Tables 3 and 4). Splitting of rotational peaks, corresponding to the F_1 ($CH^{**}((2)D^2\Pi$; Ω = 3/2) ← $CH^*(A^2\Delta$; Ω = 5/2)) and F_2 ($CH^{**}((2)D^2\Pi$; Ω = 1/2) ← $CH^*(A^2\Delta$; Ω = 3/2)) transitions, is not clearly seen due to large spectral linewidths (4–6 cm^{-1}), hence short lifetimes. Resolved rotational peaks, observed for high rotational quantum numbers of the

Table 2 (a) $CHBr_3$: $CH^*(A^2\Delta(v'=0))$ (1_r + 1_i)REMPI rotational lines due to transitions to the $(2)D^2\Pi(v'=2)$ state derived from simulation calculations (cm^{-1}).[a] (b) $CDBr_3$: $CD^*(A^2\Delta(v'=0))$ (1_r + 1_i)REMPI rotational lines due to transitions to the $(4)^2\Pi(v'=0)$ state derived from simulation calculations (cm^{-1})[a]

N'	P_2	P_1	Q_2	Q_1	R_2	R_1
(a)						
0	*40 989*	*40 966*	*41 034*	*41 020*		
1	*40 948*	*40 932*	*41 021*	*41 010*	*41 108*	*41 097*
2	*40 905*	*40 893*	*41 005*	*40 996*	*41 121*	*41 112*
3	*40 860*	*40 851*	*40 986*	*40 978*	*41 130*	*41 123*
4	*40 812*	*40 804*	*40 963*	*40 956*	*41 136*	*41 130*
5	40 761	40 754	*40 937*	*40 931*	*41 139*	*41 133*
6	40 706	40 701	*40 907*	*40 902*	*41 137*	*41 132*
7	40 649	40 644	40 874	40 869	*41 132*	*41 127*
8	40 588	40 583	40 837	40 833	*41 123*	*41 118*
9	40 523	40 519	40 797	40 793	*41 110*	*41 106*
10	40 456	40 452	40 754	40 750	*41 093*	*41 089*
11			*40 707*	*40 704*	*41 073*	*41 069*
12			*40 658*	*40 655*		
(b)						
0	*41 147*	*41 132*	41 172	41 162		
1	*41 126*	*41 115*	41 166	41 159		
2	*41 105*	*41 097*	*41 160*	*41 154*		
3	*41 083*	41 076	*41 153*	*41 148*		
4	41 060	41 055	*41 144*	*41 140*		
5	*41 036*	*41 031*	*41 134*	*41 131*		
6	*41 010*	*41 007*	41 126	41 119		
7			41 112	41 109		
8			41 098	41 095		
9			41 084	41 081		
10			41 068	41 065		
11			*41 051*	*41 048*		

[a] Roman type numbers are observable non-overlapped lines. Italic type numbers are overlapped lines.

Table 3 Energetics and spectroscopic parameters for the CH** and CD** states (2)D$^2\Pi$(v' = 2), (3)$^2\Pi$(v' = 0), (4)$^2\Pi$(v' = 0) and (3)$^2\Sigma^+$(v' = 0) (cm^{-1})

	(2)D$^2\Pi$(v' = 2)[a]		(3)$^2\Pi$(v' = 0)[b]		(4)$^2\Pi$(v' = 0)[c]		(3)$^2\Sigma^+$(v' = 0)[d]	
	CH	CD	CH	CD	CH	CD	CH	CD
$\nu^{0\,e}$	41 023	39 726	(40 410–41 090)	(40 500–41 100)	41 175	41 161	41 314	41 339
$T_{v',0}{}^{e}$	64 196	62 951	(63 584–64 264)	(63 725–64 325)	64 348	64 386	64 531	64 564
$B_{v'}$	12.74	6.87			13.41	7.23		
$D_{v'}$	0.00155	0.000451			0.00129	0.000375		
$H_{v'}$	7.5×10^{-7}							
A	−28.75					−19.4		
p^f						−0.4		
q^f						0.008		

[a] CH values derived by a simulation[55] of the CH*(A$^2\Delta$(v' = 0)) (1 + 1)REMPI spectrum of $CHBr_3$ for known parameters for the A state;[58] CD values derived from the corresponding CH values by eqn (1)–(5) and vibrational parameters from ref. 33 (see also Table 4). [b] Ranges for CD estimated from the CD*(A$^2\Delta$(v' = 0)) (1 + 1)REMPI spectrum (Fig. 5). Ranges for CH roughly estimated from the values of CD and eqn (1)–(5). [c] CD values derived by a simulation[55] of the CD*(A$^2\Delta$(v' = 0)) (1 + 1)REMPI spectrum of $CDBr_3$ for known parameters for the A state;[29,59] CH values derived from the corresponding CD values using eqn (1)–(5) and vibrational parameters from ref. 33 (see also Table 4). [d] CH and CD values from the work of Herzberg and Johns.[29] [e] $T_{v',0} = T_{v',0}$(A$^2\Delta$(v' = 0)) + ν^0; CH: $T_{v',0}$(A$^2\Delta$(v' = 0)) = 23 173 cm^{-1} for footnotes (a)–(c)[58] and $T_{v',0}$(A$^2\Delta$(v' = 0)) = 23 217 cm^{-1} for footnote (d).[29] CD: $T_{v',0}$(A$^2\Delta$(v' = 0)) = 23 225 cm^{-1} for footnotes (a)–(d).[59] [f] Λ-Doubling parameters.

Table 4 Summary of spectroscopic parameters (cm^{-1}) for the CH** states (2)D$^2\Pi$(v' = 2), (3)$^2\Pi$(v' = 0), (4)$^2\Pi$(v' = 0) and (3)$^2\Sigma^+$(v' = 0). ν^0 is the band origin for transitions from the A$^2\Delta$(v' = 0) state. $T_{v',0}$ is the energy of the v' levels with respect to the ground state (X$^2\Pi$; v'' = 0). Electron configuration for short internuclear distances is specified[33]

Terms and configuration		Dishoeck[a] *et al.*[32]	Kalemos[a] *et al.*[60]	Vázquez[a] *et al.*[33]	Herzberg[b] *et al.*[29]	Chen[c] *et al.*[36]	Long[c] *et al.*[14]	This work[c]
(3)$^2\Sigma^+$(v' = 0)	$\nu^{0\,d,e}$	*40 004.6*	41 903.5	40 576.2	41 314.0		41 155.0	41 314.0
$2s\sigma^2 2p\sigma^2 3p\sigma^1$	$T_{v',0}{}^{d,e}$	*64 200.9*	65 321.1	64 006.9	64 531.5		64 328.0	64 531.5
	ω_e		2475.1	2373.3				
	$\omega_e x_e$		147.27	50.77				
	$B_{v'}$				12.17			
(4)$^2\Pi$(v' = 0)	$\nu^{0\,d,e}$	*40 730.5*		41 750.8				41 101.0
$2s\sigma^2 2p\sigma^2 3p\pi^1$	$T_{v',0}{}^{d,e}$	*64926.8*		65 181.5				64 318.5
	ω_e			2996.2				
	$\omega_e x_e$			37.0–57.0				
(3)$^2\Pi$(v' = 0)	$\nu^{0\,d,e}$	*39 842.3*	*40 088.0*	*39 881.8*		40 427.0	40 762.0	
$2s\sigma^2 2p\sigma^1 2p\pi^1 2p\sigma^{1*}$	$T_{v',0}{}^{d,e}$	*64 039.6*	*63 505.6*	*63 312.5*		63 600.0	63 935.0	
(2)D$^2\Pi$(v' = 2)	$\nu^{0\,d,e}$		41 016.7	41 021.9	41 038.2	40 991.5	40 991.5	41 022.5
$2s\sigma^2 2p\pi^3$	$T_{v',0}{}^{d,e}$		64 434.3	64 452.6	64 211.7	64 165.0	64 165.0	64 196.0
	ω_e		2743.0	2781.1				
	$\omega_e x_e$		57.63	52.16				
	$B_{v'}$				12.6	12.6	12.7	12.74
	$D_{v'}$					0.00158	0.00158	0.00155
	A				−28.5	−26.6		−28.75

[a] Calculated parameters. [b] Experimental observations. $T_{v',0} = T_{v',0}$(A$^2\Delta$(v' = 0)) + ν^0; $T_{v',0}$(A$^2\Delta$(v' = 0)) from the work of Herzberg *et al.*[29] [c] Experimental values. $T_{v',0} = T_{v',0}$(A$^2\Delta$(v' = 0)) + ν^0; $T_{v',0}$(A$^2\Delta$(v' = 0)) from the work of Bernath *et al.*[58] [d] Roman type numbers are based on vibrational level energies. [e] Italic type numbers are estimated from potential energy curves.

P line series, in particular, and positions of bandheads for individual line series formed the basis of the simulation. To approach the observed relative line intensities, a non-Boltzmann distribution needed to be assumed. Nevertheless, some broad spectral features seen in the high excitation region of the *P*, *Q* and *R* line series (two-photon excitation region of above 81 800–82 150 cm^{-1}) could not be reproduced by the simulation.

Energetically CH*(A$^2\Delta$(v' = 0)) can be formed by two-photon-dissociation of $CHBr_3$ along with a ground state bromine molecule (Br_2) and Br or Br*, within the two-photon excitation region of concern (76 000–84 000 cm^{-1}) (see Table 1 and Fig. 3). Furthermore, as shown in Fig. 3, CH*(A$^2\Delta$(v' = 0)) should be detectable by (1_r + 1_i)REMPI, *via* resonance excitation to CH**((2)D$^2\Pi$(v' = 2)), within the same excitation region. Thus, the overall process could be (2_r + (1_r + 1_i))REMPI (see Introduction). Slope values of between 1.4 and 2.0 were derived from log–log plots of CH^+ peak signals *vs.* laser power, which is what might be expected in the case when the first resonance step (2_r) is saturated.[13,44–46] The analogous laser power dependence observed for peaks which belong to the CH**((2)D$^2\Pi$(v' = 2)) ← CH*(A$^2\Delta$(v' = 0)) resonance transitions (two-photon excitation region below 81 800 cm^{-1}) and those which could only partly be assigned to that transition (see above) makes us believe that the total peak structure corresponds to (1_r + 1_i)REMPI of CH*(A$^2\Delta$(v' = 0)), but involving different resonance excited states, CH**.

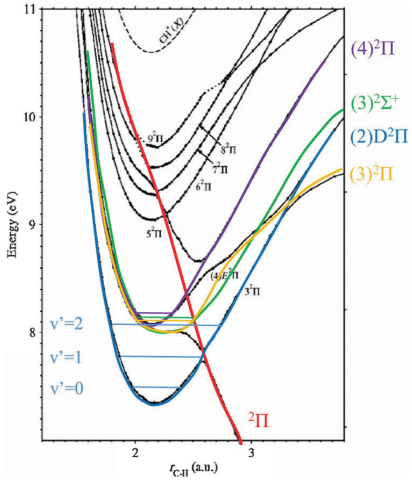

Fig. 5 $^2\Pi$ state potentials (black) and the $(3)^2\Sigma^+$ state potential (green) of CH** reproduced with permission from Vázquez *et al.*, *J. Chem. Phys.*, 2007, **126**, 164302.[33] Copyright 2007, AIP Publishing LLC. The coloured curves (blue, yellow, purple and red) represent our extrapolations and guesses for the diabatic curves of the states indicated ($(2)D^2\Pi$, $(3)^2\Pi$, $(4)^2\Pi$ and the repulsive $^2\Pi$ state).

Table 4 lists the bound CH** states which have been reported experimentally and theoretically in the energy region of concern, which corresponds to a one-photon excitation from $CH^*(A^2\Delta(v' = 0))$ within the range of 38 000–42 000 cm^{-1} or excitation from $CH(X^2\Pi(v' = 0))$ within 61 174–65 174 cm^{-1}.[14,29–31,34–36,47] Theoretically, three diabatic bound $^2\Pi$ potentials (labelled as $(2)D^2\Pi$, $(3)^2\Pi$ and $(4)^2\Pi$)[33] and one diabatic bound $(3)^2\Sigma^+$ potential are predicted to be found in this region (see Fig. 5). Furthermore, a repulsive $^2\Pi$ potential, cutting through the bound states to cause a complicated structure of avoided crossings is also to be expected (Fig. 5). The $CH^{**}((2)D^2\Pi)$ state, with the electron configuration of $2s\sigma^2 2p\pi^3$ at a short internuclear distance is the lowest in energy, whereas the rest of the bound states ($(3)^2\Pi$ ($2s\sigma^2 2p\sigma^1 2p\pi^1 2p\sigma^{*1}$), $(4)^2\Pi$ ($2s\sigma^2 2p\sigma^2 3p\pi^1$) and $(3)^2\Sigma$ ($2s\sigma^2 2p\sigma^2 3p\sigma^1$)) are all predicted to be very close in energy to make the $v' = 2$ level of the $(2)D^2\Pi$ state close in energy to the $v' = 0$ levels of the others. Experimentally, the energy of the $(2)D^2\Pi(v' = 2)$ state has been found to be 40 991.5 cm^{-1}, with respect to excitation from the $A^2\Pi$ state (marked as ν^0 in Tables 3 and 4), corresponding to 64 165 cm^{-1} with respect to excitation from the $X^2\Pi$ state (*i.e.*, $T_{v',0}$ in Tables 3 and 4).[14,36] Herzberg and Johns[29] argued that $T_{v',0}$ = 64 531.5 cm^{-1} for the $(3)^2\Sigma^+$ state (hence ν^0 = 41 314 cm^{-1}) and recently Long *et al.*[14] reported two states at ν^0 = 40 762 cm^{-1} ($T_{v',0}$ = 63 935 cm^{-1}) and ν^0 = 41 155 cm^{-1} ($T_{v',0}$ = 64 328 cm^{-1}) as possible candidates for the $^2\Pi$ and $^2\Sigma$ states, respectively. All in all, therefore, we might expect to see spectral line structures due to transitions from $CH^*(A^2\Delta(v' = 0))$ to four electronic states, *i.e.*, the $(2)D^2\Pi(v' = 2)$, $(3)^2\Pi(v' = 0)$, $(4)^2\Pi(v' = 0)$ and $(3)^2\Sigma^+(v' = 0)$ states. Whereas the short range electron configurations suggest that only the states $(2)D^2\Pi(v' = 2)$ ($2s\sigma^2 2p\pi^3$) and $(3)^2\Pi(v' = 0)$ ($2s\sigma^2 2p\sigma^1 2p\pi^1 2p\sigma^{*1}$) can be accessed by one-photon absorption and one-electron transfers, from the $A^2\Delta(v' = 0)$ ($2s\sigma^2 2p\sigma^1 2p\pi^2$) state, mixing of states in longer ranges will allow transitions to the other states to occur.[32,33] Transition probabilities, hence relative spectral intensities, however, are likely to differ largely. Thus, one might expect, the spectrum due to the two-electron transfer, $\Delta\Lambda = 2$, transition, $(3)^2\Sigma^+$ ($2s\sigma^2 2p\sigma^2 3p\sigma^1$) ← $A^2\Delta$ ($2s\sigma^2 2p\sigma^1 2p\pi^2$), in particular, to be very weak. Furthermore, the, apparently, large state interactions and possible predissociation processes by the repulsive $^2\Pi$ state are likely to appear as perturbation effects in the spectra, as spectral line shifts as well as line intensity and/or as linewidth alterations.[42,48–54]

A close look at the one-photon spectral region of about 41 290–41 350 cm^{-1} revealed some very weak, but reproducible, irregular structure with a prominent peak at about 41 314 cm^{-1} (Fig. 2(b)). Comparison with the data given by Herzberg and Johns for the $(3)^2\Sigma^+(v' = 0)$ ← $X^2\Pi(v' = 0)$ transition[29] (see Table 4) makes us assign it to the transition $(3)^2\Sigma^+(v' = 0)$ ← $A^2\Delta(v' = 0)$. The apparently overlapping spectral structure, to be seen in the CH^+ spectrum in the one-photon spectral region of about 40 900–41 100 cm^{-1} (see # markings in Fig. 2(c)), on the other hand, is too broad and unstructured in order to be able to make any sensible assignments. As an attempt to clarify the energetics of CH further, as well as to explore the corresponding energetics for CD, the CD^+ REMPI signal for $CDBr_3$ in the same energy region was recorded. The additional clarification of the CH energetics was sought through isotope shift effects as well as spectral structure differences.

The difference in the band origin ($\Delta\nu^0$) of the two isotopologues C^iH (i = 1, 2), *i.e.*, the isotope shift, can be estimated from known vibrational constants of the electronic states of concern of either of the isotopologues (i = 1 or 2) (*i.e.*, $\omega_e'(i)$, $\omega_e x_e'(i)$, $\omega_e''(i)$ and $\omega_e x_e''(i)$) and the reduced masses of the species ($\mu(i)$). Thus

$$\Delta\nu^0 = \nu^0(2) - \nu^0(1) = \Delta G(2) - \Delta G(1) \quad (1)$$

where

$$\Delta G(i) = (\omega_e'(i)(v' + 1/2) - \omega_e''(i)(v'' + 1/2)) - (\omega_e x_e'(i)(v' + 1/2)^2 - \omega_e x_e''(i)(v'' + 1/2)^2) \quad (2)$$

$$\omega_e(2) = \rho\omega_e(1) \quad (3a)$$

$$\omega_e x_e(2) = \rho^2\omega_e x_e(1) \quad (3b)$$

$$\rho = \sqrt{\frac{\mu(1)}{\mu(2)}} \quad (4)$$

Furthermore, the relationship between rotational constants of the two isotopologues can be sought through the equations

$$B(2) = \rho^2 B(1) \quad (5a)$$

$$D(2) = \rho^4 D(1) \quad (5b)$$

Based on eqn (1)–(4), band origins due to transitions from the $A^2\Delta(v' = 0)$ state to high energy states, with comparable potential curves (hence similar vibrational constants), will be similar and within the observation region for the same v' in the

upper states (*i.e.* $v' = 0$), whereas band origins for higher v' values of the upper states ($v' = 1, 2$) will be significantly lower for CD than those for CH. Furthermore, based on eqn (4) and (5) the rotational structure will appear to be more compact for CD than for CH.

Fig. 6(a) shows the REMPI spectrum of $CDBr_3$ for CD^+ ion detection in the one-photon region of 40 300–41 500 cm^{-1}. The spectrum shows weak but reproducible band structures, largely irregular in shape. The band origin (ν^0) of the $(2)D^2\Pi(v' = 2)$ spectrum for CD based on the value of 41 023 cm^{-1} for CH was estimated, according to eqn (1), to be about 39 726 cm^{-1} (Table 3), which is outside the observable and the energetically reachable region. It can, therefore, not account for the observed structure in the CD spectrum.

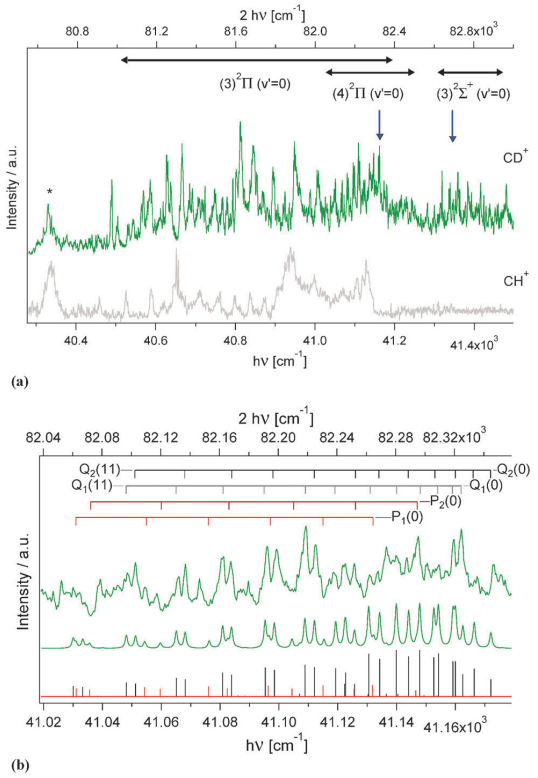

Fig. 6 (a) REMPI spectrum of $CDBr_3$ for the ion CD^+ (green; top) for the two-photon excitation region of 80 600–83 000 cm^{-1} (one-photon region of 40 300–41 500 cm^{-1}) along with the CH^+ spectrum of $CHBr_3$ from Fig. 3(b) (faint grey; bottom). The peak marked by * is due to Coulomb broadening of a C^+ signal. The main spectral features due to transitions from $CD^*(A^2\Delta(v' = 0))$ to $CD^{**}((3)^2\Pi(v' = 0))$, $CD^{**}((4)^2\Pi(v' = 0))$ and $CD^{**}((3)^2\Sigma^+(v' = 0))$ are indicated by black horizontal arrows. Vertical blue arrows mark the band origins (ν^0) for the $(4)^2\Pi(v' = 0)$ and $(3)^2\Sigma^+(v' = 0)$ spectra (see Table 3). (b) Simulation of the $CH^*(A^2\Delta; v' = 0)$ $(1_r + 1_i)$REMPI spectrum due to the resonance transition to the $(4)^2\Pi(v' = 0)$ state derived by REMPI of $CDBr_3$ for CD^+ detection. Experimental spectrum (linewidth 1.5–3.5 cm^{-1}) at top (green), calculated spectrum (linewidths = 1.5 cm^{-1}) in the middle (green) and *P* (red) and *Q* (black) lines at the bottom. Rotational line assignments are shown at top for the N' numbers given in parentheses. Perturbation effects, observed for $N' = 3–6$, appear as line shifts or intensity alterations. A homogenous perturbation from a nearby $^2\Pi$ state for $N' \sim 6$ is needed to be assumed in order to account for the spectral structure in that region. The top and bottom scales, for both figures, are the two- ($2h\nu$) and one- ($h\nu$) photon wavenumbers, respectively.

A spectral structure in the one-photon region of 41 030–41 175 cm^{-1} could be simulated (Fig. 6(b) and Table 2(b)) by *Q* lines of a transition from the $CD^*(A^2\Delta(v' = 0))$ state to a $CD^{**}(^2\Pi)$ state centered at $\nu^0 = 41\,161.5$ cm^{-1}. The simulation revealed some perturbations in the spectrum, shown as line-shifts as well as intensity alterations, which were accounted for by implementing an interaction with a $^2\Pi$ state, close in energy (see Fig. 6(b)). Spectroscopic constants derived from the simulation are listed in Tables 3 and 4. Based on eqn (1) the band origin for the corresponding CH spectrum in the case of a $v' = 0$ state was estimated to be about 41 175 cm^{-1}. This value is (i) higher than that for the $(2)D^2\Pi(v' = 2)$ spectrum, (ii) close to the upper part of the region of the uncertain spectral structure observed for CH (Fig. 2(c)) and (iii) close to the origin of the spectrum assigned by J. Long *et al.*[14] to the $^2\Sigma^+$ state. We assign this spectrum to a transition to the $(4)^2\Pi(v' = 0)$ state.

The band origin (ν^0) of the $(3)^2\Sigma^+(v' = 0)$ spectrum for CD, judged from the work by Herzberg and Johns (see Table 4 and ref. 29), is about 41 346 cm^{-1}. Although the irregular and complicated band structure observed in the region of 41 280–41 480 cm^{-1} in the CD spectrum (Fig. 6(a)) yet remains unassigned, we assign it to the $(3)^2\Sigma^+(v' = 0)$ state. The perturbations of the spectral structure most probably are due to interactions with the $^2\Pi$ state(s), close in energy.

Finally, the remaining, irregular and seemingly perturbed structure, mainly observed on the low wavenumber side of the $(4)^2\Pi(v' = 0)$ spectrum for CD (Fig. 6(a)), in the one-photon region of about 40 500–41 100 cm^{-1}, could correspond to a spectrum in the range of about 40 410–41 090 cm^{-1} for CH^{**}, $v' = 0$ state (see Table 3). The lower part of the region of the uncertain spectral structure observed for CH happens to be within that range. We assign these structures to the $(3)^2\Pi(v' = 0)$ state (see Table 3). The perturbations of the spectral structures most probably are due to interactions with the $^2\Pi$ states as well as the $^2\Sigma$ state, close in energy.

Summary and conclusions

Mass resolved REMPI spectra for two-photon resonance excitations to Rydberg states of $CHBr_3$ were recorded and analysed for the excitation energy region of 76 000–84 000 cm^{-1}. Ion fragments, detected, were C^+, CH^+ and $^iBr^+$ ($i = 79, 81$) (Fig. 2(a)).

The Br^+ spectra revealed number of Br(3/2) and Br*(1/2) $(2_r + 1_i)$REMPI atomic lines.[40]

The spectrum of C^+ showed, along with atomic lines,[40] a broad feature located at 80 666 cm^{-1}. This band, frequently observed in the spectra of related compounds and which has been misinterpreted to be due to a molecular transition, is conclusively found to be associated with the enhanced probability of ionization of $C^*(^1D_2)$ fragments, when switching from

three-photon to two-photon ionization. This conclusion shows that such an effect needs to be considered, carefully, when interpreting REMPI data in spectral analysis.

The CH^+ spectrum shows spectral features due to $(1_r + 1_i)$REMPI of $CH^*(A^2\Delta(v' = 0))$ fragments in the one-photon resonance excitation region of about 40 370–41 380 cm^{-1}, (Fig. 2(b)). An analogous spectrum of CD^+ was also recorded for $CDBr_3$. Detailed analysis of both datasets revealed the identification and assignment of spectra relevant to transitions to four high energy bound states for each fragment as well as characterization of some of the states as follows.

(a) $(2)D^2\Pi(v' = 2)$: CH: a majority of band structures in the region of 40 450–41 150 cm^{-1} was assigned to *P*, *Q* and *R* line series of a transition to the $(2)D^2\Pi(v' = 2)$ state (Fig. 2(c)) and spectroscopic parameters were determined (Table 3) by simulations.[55] CD: as to be expected from isotope shift effects and the energetics relevant to the formation of the state, the spectrum does not appear.

(b) $(3)^2\Sigma^+(v' = 0)$: CH: a weak signal detected near 41 314 cm^{-1} was assigned to the $(3)^2\Sigma^+(v' = 0)$ state (Fig. 2(b)). CD: band spectrum, showing large perturbation effects, in the regions of 41 280–41 480 cm^{-1} was assigned to the $(3)^2\Sigma(v' = 0)$ state (Fig. 6(a)).

(c) $(4)^2\Pi(v' = 0)$: CH: based on comparison with analysis of the CD spectrum some broad spectral features seen in the region of about 41 000–41 150 cm^{-1} are due to transitions to the $(4)^2\Pi(v' = 0)$ state. CD: band spectrum, showing some slight perturbation effects, in the one-photon excitation region of 41 030–41 175 cm^{-1} was assigned to *Q* lines of a transition to the $(4)^2\Pi(v' = 0)$ state (Fig. 6(b)). Spectroscopic parameters were determined (Table 3) by simulation.[55]

(d) $(3)^2\Pi(v' = 0)$: CH: based on comparison with analysis of the CD spectrum some broad spectral features seen in the region of about 40 940–41 000 cm^{-1} are due to transitions to the $(3)^2\Pi(v' = 0)$ state. CD: band spectrum, showing large perturbation effects, in the regions of 40 500–41 100 cm^{-1} was assigned to the $(3)^2\Pi(v' = 0)$ state (Fig. 6(a)).

Broad spectral lines observed, hence short lifetimes, are associated with predissociations by the repulsive $^2\Pi$ state. Whereas, the linewidths of the broad spectra assigned to the $(3)^2\Pi(v' = 0)$ and $(4)^2\Pi(v' = 0)$ states for CH are particularly large, those of the $(2)D^2\Pi(v' = 2)$ spectrum for CH (4–6 cm^{-1}) and the $(4)^2\Pi(v' = 0)$ state for CD (1.5–3.5 cm^{-1}) also are relatively large, suggesting that the predissociation of all the bound $^2\Pi$ states is of importance. Since such predissociation processes will form $C^*(^1D_2) + H$,[32] (see Fig. 2) it can, at least partly, explain the enhanced C^+ signal due to the ionization of $C^*(^1D_2)$, mentioned before. Perturbations observed are associated with interactions between $^2\Pi$ and/or $^2\Sigma$ states in the energy region of concern.

The work on the data for the CH and CD fragments involved analysis of overlapping spectra of the perturbed structure due to state interactions. The use of isotope shift effects as well as spectral simulations along with calculated potential surfaces[32,33] was found to be necessary to clarify and characterise the states involved. Furthermore, this work demonstrates the usefulness of $(2_r + m_{r,i})$REMPI of parent molecules for molecular fragment analysis, where $m_{r,i} = 2$ (*i.e.* $m_{r,i} = 1_r + 1_i$) for CH* and CD* (*i.e.* CH*/CD* $(1_r + 1_i)$REMPI).

Acknowledgements

The financial support of the University Research Fund, University of Iceland and the Icelandic Science Foundation (Grant No. 130259-051) is gratefully acknowledged.

References

1 G. C. Causley and B. R. Russell, *J. Chem. Phys.*, 1975, **62**, 848–857.
2 S. Felps, P. Hochmann, P. Brint and S. P. McGlynn, *J. Mol. Spectrosc.*, 1976, **59**, 355–379.
3 G. N. A. Van Veen, T. Baller and A. E. De Vries, *Chem. Phys.*, 1985, **92**, 59–65.
4 W. P. Hess, D. W. Chandler and J. W. Thoman, *Chem. Phys.*, 1992, **163**, 277–286.
5 T. Gougousi, P. C. Samartzis and T. N. Kitsopoulos, *J. Chem. Phys.*, 1998, **108**, 5742–5746.
6 D. D. Xu, J. H. Huang, R. J. Price and W. M. Jackson, *J. Phys. Chem. A*, 2004, **108**, 9916–9923.
7 R. Locht, B. Leyh, H. W. Jochims and H. Baumgartel, *Chem. Phys.*, 2005, **317**, 73–86.
8 R. Locht, B. Leyh, D. Dehareng, H. W. Jochims and H. Baumgartel, *Chem. Phys.*, 2005, **317**, 87–102.
9 R. Locht, B. Leyh, D. Dehareng, K. Hottmann, H. W. Jochims and H. Baumgartel, *Chem. Phys.*, 2006, **323**, 458–472.
10 T. Ridley, J. T. Hennessy, R. J. Donovan, K. P. Lawley, S. Wang, P. Brint and E. Lane, *J. Phys. Chem. A*, 2008, **112**, 7170–7176.
11 V. Blanchet, P. C. Samartzis and A. M. Wodtke, *J. Chem. Phys.*, 2009, **130**, 034304.
12 F. Y. Wang, M. L. Lipciuc, X. M. Yang and T. N. Kitsopoulos, *Phys. Chem. Chem. Phys.*, 2009, **11**, 2234–2240.
13 K. Matthiasson, Á. Kvaran, H. Wang and A. Bodi, *J. Phys. Chem. A*, 2010, **114**, 9991–9998.
14 J. Long, H. Wang and Á. Kvaran, *J. Phys. Chem. A*, 2014, **118**, 1826–1831.
15 Y. L. Yung, J. P. Pinto, R. T. Watson and S. P. Sander, *J. Atmos. Sci.*, 1980, **37**, 339–353.
16 M. J. Prather and R. T. Watson, *Nature*, 1990, **344**, 729–734.
17 R. von Glasow, R. von Kuhlmann, M. G. Lawrence, U. Platt and P. J. Crutzen, *Atmos. Chem. Phys.*, 2004, **4**, 2481–2497.
18 J. I. Lunine, *Astrobiology*, Pearson - Addison-Wesley, 2005.
19 P. Ehrenfreund and M. A. Sephton, *Faraday Discuss.*, 2006, **133**, 277–288.
20 N. J. Warwick, J. A. Pyle and D. E. Shallcross, *J. Atmos. Chem.*, 2006, **54**, 133–159.
21 J. Aschmann and B.-M. Sinnhuber, *Atmos. Chem. Phys.*, 2013, **13**, 1203–1219.
22 K. A. Peterson and J. S. Francisco, *J. Chem. Phys.*, 2002, **117**, 6103–6107.

23 P. Zou, J. Shu, T. J. Sears, G. E. Hall and S. W. North, *J. Phys. Chem.*, 2004, **108**, 1482–1488.
24 A. M. Shaw, *Astrochemistry; From Astronomy to Astrobiology*, Wiley, 2006.
25 D. Gillotay, P. C. Simon and L. Dierickx, *Aeron. Acta A*, 1988, **335**, 1–25.
26 D. A. Gillotay, B. Jenouvrier, B. Coquert, M. F. Merienne and P. C. Simon, *Planet. Space Sci.*, 1989, **37**, 105–108.
27 T. Munakata and T. Kasuya, *Chem. Phys. Lett.*, 1989, **154**, 604–609.
28 R. Locht, B. Leyh, H. W. Jochims and H. Baumgartel, *Chem. Phys.*, 2005, **317**, 73–86.
29 G. Herzberg and J. W. C. Johns, *Astrophys. J.*, 1969, **158**, 399–418.
30 P. Chen, W. A. Chupka and S. D. Colson, *Chem. Phys. Lett.*, 1985, **121**, 405–407.
31 P. Chen, J. B. Pallix, W. A. Chupka and S. D. Colson, *J. Chem. Phys.*, 1987, **86**, 516–520.
32 E. F. van Dishoeck, *J. Chem. Phys.*, 1986, **86**, 196–214.
33 G. J. Vázquez, J. M. Amero, H. P. Liebermann, R. J. Buenker and H. Lefebvre-Brion, *J. Chem. Phys.*, 2007, **126**, 164302–164313.
34 P. J. H. Tjossem and C. Smyth, *Chem. Phys. Lett.*, 1987, **144**, 51–57.
35 Y. Wang, L. Li and W. A. Chupka, *Chem. Phys. Lett.*, 1992, **192**, 348–352.
36 Y. Chen, J. Jin, L. Pei, X. Ma and C. Chen, *J. Electron Spectrosc. Relat. Phenom.*, 2000, **108**, 221–224.
37 K. Matthiasson, J. Long, H. Wang and Á. Kvaran, *J. Chem. Phys.*, 2011, **134**, 164302.
38 J. Long, H. Wang and Á. Kvaran, *J. Chem. Phys.*, 2013, **138**, 044308.
39 K. Matthiasson, H. Wang and Á. Kvaran, *Chem. Phys. Lett.*, 2008, **458**, 58–63.
40 See ESI†.
41 S. P. Sander, J. Abbatt, J. R. Barker, J. B. Burkholder, R. R. Friedl, D. M. Golden, R. E. Huie, C. E. Kolb, M. J. Kurylo, G. K. Moortgat, V. L. Orkin and P. H. Wine, *JPL Publication*, 2011, 10-6.
42 B. G. Waage, Á. Kvaran and H. Wang, *J. Chem. Phys.*, 2000, **113**, 1755–1761.
43 Á. Logadóttir, Á. Kvaran and H. Wang, *J. Chem. Phys.*, 2000, **112**, 10811–10820.
44 J. Long, Á. Kvaran, K. Sveinbjörnsson and H. Wang, *Chem. Phys. Lett.*, 2011, **516**, 12–16.
45 H. M. Lambert, P. J. Dagdigian and M. H. Alexander, *J. Chem. Phys.*, 1998, **108**, 4460–4466.
46 Y.-L. He and D. Wang, *Struct. Chem.*, 2009, **20**, 461–479.
47 P. Chen, J. B. Pallix, W. A. Chupka and S. D. Colson, *J. Chem. Phys.*, 1986, **84**, 5208–5209.
48 Á. Logadóttir, Á. Kvaran and H. Wang, *J. Chem. Phys.*, 1998, **109**, 5856–5867.
49 Á. Kvaran and H. Wang, *J. Mol. Spectrosc.*, 2004, **228**, 143–151.
50 K. Matthiasson, Á. Kvaran, H. Wang, A. Bodi and E. Jónsson, *J. Chem. Phys.*, 2008, **129**, 164313.
51 K. Matthiasson, Á. Kvaran and H. Wang, *J. Chem. Phys.*, 2009, **131**, 044324.
52 K. Matthiasson, Á. Kvaran and H. Wang, *J. Mol. Spectrosc.*, 2009, **255**, 1–5.
53 H. R. Hróðmarsson, H. Wang and Á. Kvaran, *J. Mol. Spectrosc.*, 2013, **290**, 5–12.
54 H. R. Hróðmarsson, H. Wang and Á. Kvaran, *J. Chem. Phys.*, 2014, **140**, 244304.
55 C. M. Western, *PGOPHER, a Program for Simulating Rotational Structure, C. M. Western, University of Bristol*, http://pgopher.chm.bris.ac.uk, University of Bristol, 2003–2015.
56 V. Chikan, F. Fournier and S. R. Leone, *J. Chem. Phys.*, 2006, **110**, 2850–2857.
57 W. M. Haynes and D. R. Lide, *CRC handbook of chemistry and physics: A ready-reference book of chemical and physical data*, CRC, Boca Raton, FL, 2010.
58 P. F. Bernath, C. R. Brazier, T. Olsen, R. Hailey, W. T. M. L. Fernando, C. Woods and J. L. Hardwick, *J. Mol. Spectrosc.*, 1991, **147**, 16–26.
59 Constants of diatomic molecules, NIST Chemistry WebBook, http://webbook.nist.gov/cgi/cbook.cgi?ID = C13776700&Units = SI&Mask = 1000, accessed October 2015.
60 A. Kalemos, A. Mavridis and A. Metropoulos, *J. Chem. Phys.*, 1999, **111**, 9536–9548.

4.1.1 Supporting information

Long term puzzles of the CH and CD energetics and related phenomena revisited; Solutions sought through REMPI-photofragmentations of bromomethanes

Arnar Hafliðason, Huasheng Wang, and Ágúst Kvaran*
Science Institute, University of Iceland, Dunhagi 3, 107 Reykjavík, Iceland.

Supporting information

Content: **page:**

Table S1. $CHBr_3$: Excitation wavenumbers of REMPI spectral lines for C/C* atoms. The accuracy of atomic lines is about ± 2.0 cm^{-1} on the two-photon scale.

Configurations / Term symbols	$C(2s^22p^2; {}^3P_0)$ [a]		$C(2s^22p^2; {}^3P_1)$ [a]		$C(2s^22p^2; {}^3P_2)$ [a]		$C(2s^22p^2; {}^1D_2)$ [a]		$C(2s^22p^2; {}^1S_0)$ [b]	
	This work [c] (intensity)	NIST[1]	This work [c] (intensity)	NIST[1]	This work [c] (intensity)	NIST[1]	This work [c] (intensity)	NIST[1]	This work [c] (intensity)	NIST[1]
$2s^22p3s$ / ${}^3P°_1$									38706.0 (m)	38704.6
$2s^22p4p$ / ${}^3D_3$					80793.6 (vw)	80791.2				
$2s^22p4p$ / ${}^3P_0$					81268.1 (vw)	81267.6				
$2s^22p4p$ / ${}^3P_1$					81281.8 (vw)	81282.4				
$2s^22p4p$ / ${}^3P_2$					81299.4 (m)	81300.6				
$2s^22p4p$ / ${}^3P_0$	81310.8 (vw)	81311.0								
$2s^22p4p$ / ${}^3P_1$			81308.4 (w)	81309.4						
$2s^22p4p$ / ${}^3P_2$			81326.7 (vw)	81327.6						
$2s^22p4p$ / ${}^3P_2$	81342.1 (vw)	81344.0								
$2s^22p6p$ / ${}^1D_2$							77024.4 (vw)	77025.6		
$2s^22p8p$ / ${}^1D_2$							78719.3 (vw)	78720.9		
$2s^22p9p$ / ${}^1D_2$							79157.1 (vw)	79157.5		

a. $(2_r + 1_i)$REMPI atomic lines
b. $(1_r + 1_i)$REMPI atomic lines

vw: very weak, w: weak, m: medium, s: strong, vs: very strong

Table S2. $CHBr_3$: Excitation wavenumbers of REMPI spectral lines for Br/Br* atoms. The accuracy of atomic lines is about ± 2.0 cm^{-1} on the two-photon scale.

Configurations / Term symbols	$Br(4s^24p^5; {}^2P_{3/2})$ [a]		$Br(4s^24p^5; {}^2P_{1/2})$ [a]	
	This work [b] (intensity)	NIST[1]	This work [b] (intensity)	NIST[1]
$4s^24p4(^3P_2)5p / {}^4D°_{3/2}$	76742.2 (m)	76743.1		
$4s^24p4(^3P_1)5p / {}^2S°_{1/2}$	78079.2 (vw)	78076.0		
$4s^24p4(^3P_1)5p / {}^2D°_{5/2}$	78509.8 (s)	78511.6		
$4s^24p4(^3P_1)5p / {}^2D°_{3/2}$	78674.6 (s)	78676.7		
$4s^24p4(^3P_1)5p / {}^4S°_{3/2}$	79177.2 (m)	79178.3		
$4s^24p4(^3P_0)5p / {}^2P°_{3/2}$	79697.0 (vs)	79695.9		
$4s^24p4(^3P_0)5p / {}^2P°_{1/2}$	79866.6 (m)	79868.0		
$4s^24p4(^3P_0)5p / {}^2P°_{3/2}$			76014.4 (vw)	76010.7
$4s^24p4(^3P_0)5p / {}^2P°_{1/2}$			76186.8 (w)	76182.8
$4s^24p4(^3P_0)6p / {}^4P°_{3/2}$			81903.0 (vw)	81901.1
$4s^24p4(^3P_0)6p / {}^4P°_{1/2}$			82117.0 (w)	82114.0
$4s^24p4(^3P_2)6p / {}^4D°_{5/2}$			82136.6 (w)	82135.3
$4s^24p4(^3P_2)6p / {}^4D°_{3/2}$			82258.8 (vw)	82258.6
$4s^24p4(^1D)5p / {}^2F°_{5/2}$			83375.4 (m)	83376.0
$4s^24p4(^1D)5p / {}^2P°_{1/2}$			83812.8 (m)	83813.8

a. $(2_r + 1_i)$ REMPI
b. vw: very weak, w: weak, m: medium, s: strong, vs: very strong

REFERENCE

1. NIST Chemistry WebBook - NIST Atomic Spectra Database Levels Data, http://webbook.nist.gov/, Accessed August 2015.

4.2 Paper 2

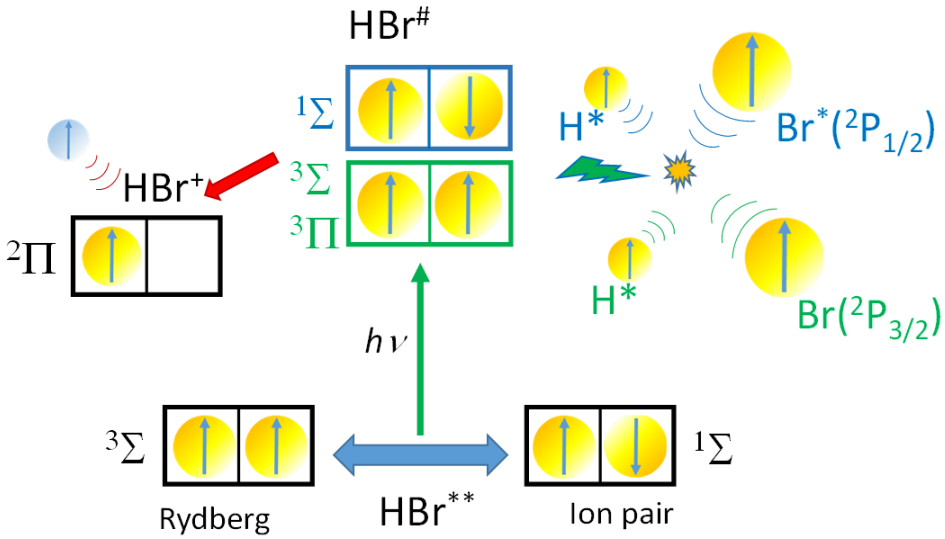

Arnar Hafliðason, Pavle Glodic, Dimitris Zaouris, Peter C. Samartzis, Ágúst Kvaran. *Effect of triplet to singlet state interaction on photofragmentation dynamics: highly excited state of HBr probed by VMI and REMPI as a case study*. Physical Chemistry Chemical Physics, 2016, **18**, 26291-26299.

DOI: 10.1039/c6cp0408f

PCCP

PAPER

Cite this: *Phys. Chem. Chem. Phys.*, 2016, **18**, 26291

Effect of a triplet to singlet state interaction on photofragmentation dynamics: highly excited states of HBr probed by VMI and REMPI as a case study†

Pavle Glodic,[a] Dimitris Zaouris,‡[a] Peter C. Samartzis,[a] Arnar Hafliðason[b] and Ágúst Kvaran*[b]

Received 13th June 2016,
Accepted 22nd August 2016

DOI: 10.1039/c6cp04108f

www.rsc.org/pccp

Analysis of mass resolved spectra as well as velocity map images derived from resonance enhanced multiphoton ionization (REMPI) of HBr *via* resonance excitations to mixed Rydberg ($6p\pi\ ^3\Sigma^-(v'=0)$) and valence (ion-pair) ($V\ ^1\Sigma^+(v'=m+17)$) states allows characterization of the effect of a triplet-to-singlet state interaction on further photoexcitation and photoionization processes. The analysis makes use of rotational spectra line shifts, line intensity alterations, kinetic energy release spectra as well as angular distributions. Energy-level-dependent state mixing of the resonance excited states is quantified and photoexcitation processes, leading to H^+ formation, are characterized in terms of the states and fragmentation processes involved, depending on the state mixing.

I. Introduction

While molecular photodissociation studies have mostly been associated with excitations to relatively low energy states, there is a growing interest in the effects of higher energy Rydberg states in this context. Due to an increasing density of states, state mixing is gradually playing a more important part in photofragmentation processes as excitation energy increases. This can involve interactions between Rydberg and valence states or between different Rydberg states. The effect of such high energy state interactions on further photodissociation, as well as photoionization processes, is largely an unexplored but very interesting research area.

UV/Vis spectra of hydrogen halides are rich in structured, vibrationally and rotationally resolved electronic spectra due to transitions to Rydberg as well as ion-pair valence states.[1–24] The frequently observed perturbation effects, appearing as line-shifts, line intensity and/or linewidth alterations, are indicative of state interactions and photodissociation processes. Thus, the hydrogen halides have turned out to be ideal candidates for studying state interactions and their effects on photodissociation and photoionization processes, involving molecular Rydberg states on a quantum state level basis.[2,3,5,8,9,12,16,19–31] A similar work on superexcited states of O_2 has been reported by Ehresman *et al.*[32,33] and Mo *et al.*[34]

Mass resolved REMPI spectra of hydrogen halides reveal a number of interactions between Rydberg states and ion-pair valence states of varying strength and nature.[2,3,5,8,9,13,14,16–25,35,36] Evidence of Rydberg–Rydberg state interactions has also been reported.[29] Direct predissociation of the Rydberg states through repulsive valence states is found to be common as well as indirect predissociation, *via* state interactions, of ion-pair states and Rydberg states. State interactions have been interpreted in terms of level-to-level interactions between quantum states of the same total angular momentum quantum numbers, J'.[18,22–24,29,30] Weak interactions are normally limited to near-degenerate levels, which, typically, appear as line-shifts or line-intensity alterations for one to three rotational lines only, in line series. The effects of stronger interactions on the other hand, can be seen for non-degenerate levels, hence a range of spectral lines. ''Non-degenerate interactions'', typically, are found for states of equal symmetries ($\Delta\Omega = \Delta\Lambda = \Delta\Sigma = 0$), whereas ''near-degenerate interactions'' can be found for different state symmetries. The interaction between the $6p\pi\ ^3\Sigma^-(0^+; v'=0)$ Rydberg state and the $V^1\Sigma^+(0^+; v'=m+17)$ ion-pair state for HBr is an example of a ''near-degenerate interaction'' appearing as a slight shift of the Q rotational lines of the Rydberg state for $J' = 7$ and 8 and as relative enhancement of the Br^+ ion signals compared to that of the HBr^+ signals for $J' \approx 8$.[21,37,38] The observed perturbation effects were used to identify and characterise the $V^1\Sigma^+(0^+; v'=m+17)$ state.[21]

[a] *Institute of Electronic Structure and Laser, Foundation for Research and Technology-Hellas, Vassilika Vouton, 71110 Heraklion, Greece*
[b] *Science Institute, University of Iceland, Dunhagi 3, 107 Reykjavík, Iceland. E-mail: agust@hi.is; Web: www.hi.is/~agust; Tel: +354-525-4800, +354-484-1259*
† Electronic supplementary information (ESI) available. See DOI: 10.1039/c6cp04108f
‡ Present address: Department of Physics and Astronomy, University College London, Gowen Street London WC1E, 6BT, UK.

Velocity map imaging (VMI) measurements, coupled with REMPI, of hydrogen halides have further revealed the effect of state interaction on photofragmentation of the mixed states. Thus, enhanced H^+ signals were observed in images of HCl recorded for the resonance excitations to two Rydberg states by changing the excitations from non-degenerate to near-degenerate energy levels.[27] Photofragmentation processes originating from the $E^1\Sigma^+(0^+; v' = 0)$ Rydberg and $V^1\Sigma^+(0^+; v')$ ion-pair states of HBr, and leading to $H^*(n = 2)$ and H^+ formation, have been found to depend on the "degree of energy level degeneracy".[30]

Based on the work by Loock *et al.*[39] and Zaouris *et al.*[30] the major paths for H^+ and HBr^+ formation by multiphoton excitation of HBr, following two-photon resonance excitations to Rydberg or ion-pair states (HBr**), involve one-photon excitation to superexcited Rydberg state(s) ($HBr^{\#}$) followed by:

$$HBr^{\#} \rightarrow H^*(n = 2) + Br^*/Br; \text{ dissociation}$$

$$H^*(n = 2) + h\nu \rightarrow H^+ + e^-; \text{ photoionization}$$

$$\text{channels } H^* + Br^*/Br \qquad (1a/1b)$$

$$HBr^{\#} \rightarrow HBr^{+*}(v^+)/HBr^+(v^+); \text{ autoionization}$$

$$HBr^{+*}(v^+)/HBr^+(v^+) + h\nu \rightarrow HBr^{+\#} \rightarrow H^+ + Br^*/Br; \text{ photodissociation}$$

$$\text{channels } HBr^{+*}/HBr^+. \qquad (2a/2b)$$

The kinetic energies released in the dissociation products H^* (1(a) and (b)) and H^+ (2(a) and (b)) typically vary as 1(a) < 1(b) < 2(a) ≈ 2(b) (see Fig. 1a). Br^+ formation is likely to involve the dissociation of a superexcited state to form Rydberg bromine atoms (Br**) followed by a one-photon photoionization, *i.e.*,

$$HBr^{\#} \rightarrow H + Br^{**}; \text{ dissociation}$$

$$Br^{**} + h\nu \rightarrow Br^+ + e^-; \text{ photoionization.} \qquad (3)$$

The relative contributions of various channels will depend on the nature of the resonance excited state HBr**. Typically, channels which give fragment ions *via* the neutral dissociative channels (1 and 3) are favoured in long range – hence ion-pair state – excitations, whereas both short and long range – hence both ion-pair and Rydberg states – excitations are likely to form the molecular ions. In the case of the strongly interacting $E^1\Sigma^+(0^+; v' = 0)$ and $V^1\Sigma^+(0^+; v')$ states[30] the relative contribution of the two dissociative H^+ formation channels (1(a) and 1(b)) is found to differ such that 1(a) is typically favoured for long-range – ion-pair state – excitations, whereas 1(b) is favoured for short-range – Rydberg state – excitations. This has been ascribed to varying contributions of different transitions to superexcited Rydberg states, which correlate with H^* + Br^*/Br (Fig. 1b).[30] Furthermore, HBr^+ and HBr^{+*} are believed to be formed *via* autoionization of those Rydberg states, in which case low v^+ states of HBr^+ and HBr^{+*} are favoured for short-range (Rydberg state) excitations and higher v^+ are favoured for long-range (ion-pair) excitations. The energetics and relevant transitions are shown in Fig. 1b.

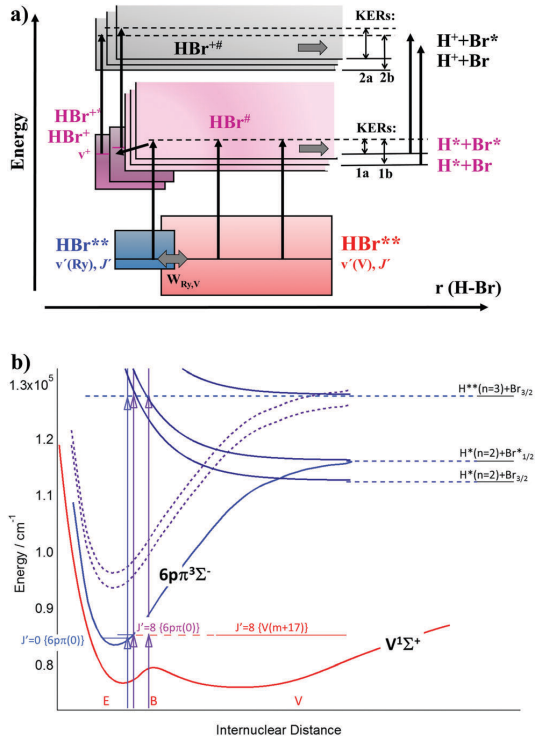

Fig. 1 (a) Schematic representation of the major H^+ formation channels based on VMI studies of (2 + *n*) REMPI of HBr following two-photon resonance excitations to the $E^1\Sigma^+$ Rydberg and $V^1\Sigma^+$ valence/ion-pair states (HBr**)[21–23,26,30] (see the main text for details). (b) Potential curves of the states involved in H^+ formations following two-photon resonance excitation of HBr to the 6pπ(0) and 6pπ(0)/V(*m* + 17) mixed state(s), asymptotic energies of fragments and relevant transitions (see the main text). The potential curve for the B states (red solid curve) was derived from Fig. 1 in ref. 39. The potential curves for the ionic states (broken curves) were derived from ref. 51. The shape of the ground ionic state was assumed to hold for the 6pπ Rydberg state (blue curve), whereas the shape of the repulsive states correlating with H* + Br/Br* and H** + Br are based on preliminary *ab initio* calculations,[54] which suggest that the curves might be of shapes close to that of the $B^2\Sigma$ ionic state.[51]

The focus of this paper is on revealing the connection between excited state interactions and further photodissociation and photoionization processes for interacting states with different spin quantum numbers. We use the 6pπ $^3\Sigma^-(0^+; v' = 0)$ Rydberg and $V^1\Sigma^+(0^+; v' = m + 17)$ ion-pair states for HBr (herein named as the 6pπ(0) and V(*m* + 17) states), mentioned above, as a case study. We make use of mass-resolved REMPI data for two-photon resonance excitation to both states,[21] as well as velocity map images of H^+ for resonance excitation to the Rydberg state, as a function of J'. Energy-level-dependent state mixing of the resonance excited states is quantified and photoexcitation processes, leading to H^+ formation, are characterized in terms of states and fragmentation processes involved, depending on the state mixing.

II. Experimental

VMI

The VMI setup used in this work has been described previously.[40,41] A molecular beam of HBr is formed by a 15–30% HBr mixture in He expanding through a homemade piezo-electrically actuated nozzle valve (1 mm diameter) and is skimmed before entering the detection chamber where the ion optics are positioned. Appropriate conditions (*e.g.* denser mixtures and/or use of the hotter part of the molecular beam) were used to probe high J states. After passing through a 2 mm diameter hole in the repeller electrode, the molecular beam is intersected at right angles by a laser beam focused at the geometric focus position of a single-electrode repeller-grid arrangement. The laser beam is generated by an Nd^{3+}:YAG pumping a master oscillator power oscillator system (Spectra Physics MOPO, 0.2 cm^{-1} linewidth, FWHM). The energy per pulse was ~2 mJ and the pulse duration was typically 10 ns (FWHM). The laser beam (~5 mm in diameter) was focused using a 30 cm lens on the molecular beam. Laser polarization is parallel to the detector plane and perpendicular to the molecular beam propagation direction.

For the VMI experiments reported here, the repeller is always ON, *i.e.*, the apparatus is operated in the "VMI mode". The photofragments traverse a field-free time-of-flight region (45 cm) and a gated, position-sensitive detector (dual, imaging-quality MCP array coupled to a phosphor screen) images the photofragment sphere. The image frame is recorded asynchronously every second (~10 laser shots) using a CCD camera and several thousand frames are averaged to form velocity map images. The 2D slice of the 3D ion distribution from each final image is extracted by inverse Abel transformation and integrated from its center over angle to extract the speed, and over radius to extract the angular distributions of the photofragments.

H^+ photoion images are recorded following HBr two-photon excitation in steps of 0.005 nm for a laser excitation in the wavelength region of 235.816–235.926 nm. Background images are recorded with the laser on and the molecular beam off and subtracted from the signal images.

III. Results

A. Mass resolved REMPI

Rotational peaks due to resonance transitions to the 6pπ $^3\Sigma^-(0^+; v' = 0)$ (O, Q and S lines) and $V^1\Sigma^+(0^+, v' = m + 17)$ states of $H^{79}Br$ and $H^{81}Br$, as well as some bromine atomic lines, appear in the two-photon excitation region of 84 740–85 120 cm^{-1}.[21,42] The observed Q lines of the 6pπ(0) spectrum are found to appear between those for $J' = 7$ and 8 of the V(m + 17) spectrum. While the rotational lines of the $H^{79}Br$ and $H^{81}Br$ molecules, for the same J' quantum numbers, overlap for the 6pπ(0) Rydberg state spectrum, those of the V(m + 17) spectrum are separated, due to isotope shift effects. Spectral perturbations, appearing as line-shifts and line-intensity alterations of the $J' = 7$ and 8 lines in the Q line series of the 6pπ(0) spectrum, in particular, are due to interactions between the corresponding near-degenerate energy levels of the 6pπ(0) and V(m + 17) states.

Line shift effects. Rotational energy levels ($E_{J'}(1)$ and $E_{J'}(2)$), of the two states, 6pπ(0) (labelled 1) and V(m + 17) (labelled 2), have been derived from the spectra.[21,42] A simplified two-state deperturbation analysis of the spectra, based on the diagonalization of the Hamiltonian matrix elements for the state interactions, described in more detail in ref.23, 29 and 31, revealed a moderate interaction strength of about W_{12} = 7.0 cm^{-1} and the zero order energies ($E^0_{J'}(i)$; i = 1, 2) corresponding to the non-perturbed states. Furthermore, the analysis allowed the determination of improved (zeroth order) spectroscopic constants for the 6pπ(0) state, ν^0 = 84 810 cm^{-1}, B' = 7.89 ± 0.03 cm^{-1} and D' = +0.0004 cm^{-1}. Fig. 2a shows the energy difference between the perturbed and the non-perturbed energy levels ($E_{J'}(i) - E^0_{J'}(i)$) as a function of J' for both states, *i.e.*, a "reduced term value plot". The graph of the 6pπ(0) state shows a typical effect of a near-degenerate interaction with an ion-pair state, which appears as a gradually increasing negative difference in $E_{J'}(1) - E^0_{J'}(1)$ from J' = 4 to 7 followed by an upward jump for J' = 8 and a decrease for J' = 9. This is due to an interaction between

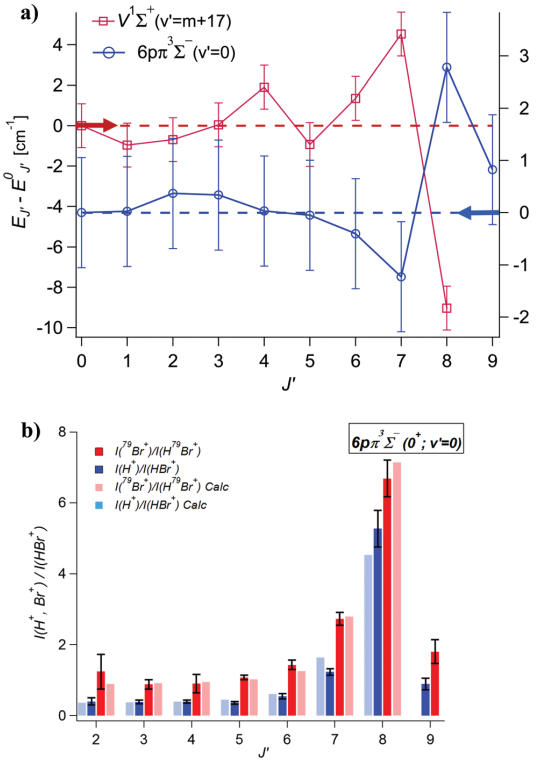

Fig. 2 (a) Line shift (LS) effects: reduced term value plots for the 6pπ(0) and V(m + 17) states derived from perturbed ($E_{J'}$) and deperturbed ($E^0_{J'}$) energy levels for $H^{81}Br$. (b) Line intensity (LI) effects: experimental and calculated relative ion-signal intensities ($I(H^+)/I(HBr^+)$ (blue) and $I(^{79}Br^+)/I(H^{79}Br^+)$ (red)) derived for the Q rotational lines for the 6pπ(0) state. An interaction strength of W_{12} = 7.0 cm^{-1} between the 6pπ(0) and V(m + 17) states was assumed in the calculations.

levels of the same J' quantum numbers which results in level repulsions which increase as the energy difference ($|\Delta E_{J'}| = |E_{J'}(1) - E_{J'}(2)|$) between the levels decreases. Based on the number of observations for the ion-pair states of hydrogen halides[21,23,24,29,30] the V(m + 17) state is likely to interact with a number of Rydberg states which could explain a larger irregularity in the ''reduced term value plot'' for the V(m + 17) state. Nevertheless, a ''near mirror effect'' is seen in the plots for J' = 6–8, such that increases in values for V(m + 17) correspond to decreases in the corresponding values for the 6pπ(0) state and *vice versa*. This is a clear indication that the observed near-degenerate interaction found for the 6pπ(0) state is indeed due to mixing with the V(m + 17) state.

Line intensity effect. Fig. 2b shows the ion intensity ratios $I(Br^+)/I(HBr^+)$ and $I(H^+)/I(HBr^+)$ as a function of J' for the Q lines of the 6pπ(0) spectrum. Since fragment ion formations are favoured in long-range/ion-pair state excitations (see Introduction) the sharp increase in the ratios, observed for $J' \sim 8$, is also an indication of a near-degenerate interaction between the 6pπ(0) and V(m + 17) states. Furthermore, the graphs could be reproduced reasonably well by a corresponding model function, which depends on the interaction strength (W_{12} = 7.0 cm^{-1}) and the energy differences, $\Delta E_{J'}$,[19,20,26,29,31,43] as shown in Fig. 2b.

Finally, the fractional mixing of the states, ${c_1}^2$ and ${c_2}^2$, which depends on W_{12} and $\Delta E_{J'}$,[17,19,20,22,29,43,44] was evaluated. As seen in Table 1 the percentage mixing of the ion-pair state with the Rydberg state reaches a small, but significant, maxima of about 4.7% and 1.7% for the J' = 8 and 7 levels, respectively.

B. Velocity map imaging (VMI)

H^+ images and kinetic energy release (KER) spectra. H^+ images were recorded for two-photon resonance excitation from the ground state, $X^1\Sigma^+(0^+;\ v' = 0)$, to the 6pπ $^3\Sigma^-(0^+;\ v' = 0)$ Rydberg state in steps of 0.005 nm for a laser excitation in the wavelength region of 235.816–235.926 nm, which covers the two-photon excitations ($2h\nu$) for $J' = J''$ = 0–8 (Q lines) ($2h\nu$ = 84772.3–84811.9 cm^{-1}). The H^+ signals for two-photon resonance excitations to the $V^1\Sigma^+(v' = m + 17)$ ion-pair state, on the other hand, were too weak to allow H^+ images to be recorded. All the images show rings which could be identified as being due to the four major channels for H^+ formation, H*(n = 2) + Br* (1a), H*(n = 2) + Br (1b), HBr^+*(v^+) (2a) and $HBr^+(v^+)$ (2b) (see the text in Introduction and Fig. 1), where the ring intensities, hence the kinetic energy release (KER's), change as 1(a) < 1(b) < 2(a) ≈ 2(b). Furthermore, for the longest excitation wavelength region (λ = 235.896–235.926 nm; $2h\nu$ = 84772.3–84783.1 cm^{-1}) a ring of low KER was observed, which is assigned to the path

Table 1 $H^{79}Br$: fractional mixing of the Rydberg state 6pπ $^3\Sigma^-(0^+;v' = 0)$ and the ion-pair state $V^1\Sigma^+(0^+,\ v' = m + 17)$, ${c_1}^2$ and ${c_2}^2$, with respect to the 6pπ $^3\Sigma^-(0^+;v' = 0)$ state as a function of J' for the interaction strength, W_{12} = 7.0 cm^{-1}

J'	2	3	4	5	6	7	8
${c_1}^2$	0.999	0.999	0.999	0.998	0.996	0.983	0.953
${c_2}^2$	0.001	0.001	0.001	0.002	0.004	0.017	0.047

$$HBr^{\#} \rightarrow H^{**}(n = 3) + Br;\ \text{dissociation},$$

$$H^{**}(n = 3) + h\nu \rightarrow H^+ + e^-;\ \text{photoionization channel H}^{**} + Br. \quad (4)$$

Selected images (for λ = 235.841, 235.886 and 235.911 nm), along with the corresponding KER spectra, are shown in Fig. 3. Fig. 4a shows all the KER spectra stacked according to the varying two-photon excitation energy along with the H^+ REMPI spectrum (to the right, tilted vertically). KER spectra derived for excitation energies closest to those for the Q rotational lines are highlighted in red in Fig. 4a. The KERs for the channels H** + Br (4), H* + Br* (1a) and H* + Br (1b) are almost independent of the excitation energies, of about 0.014, 1.43 and 1.87 eV, respectively, in agreement with predicted values according to

$$KER(H^* + Br^*;\ 1a) = 3h\nu + E_{J''} - D_0(HBr) - E(H^*) - E(Br^*) \quad (5a)$$

$$KER(H^* + Br;\ 1b) = 3h\nu + E_{J''} - D_0(HBr) - E(H^*) \quad (5b)$$

$$KER(H^{**} + Br;\ 4) = 3h\nu + E_{J''} - D_0(HBr) - E(H^{**}) \quad (5c)$$

where $h\nu$ is the photon energy, $E_{J''}$ is the J''-dependent rotational energy of the ground state, determined from known rotational constants[45] and D_0(HBr) (30 210 cm^{-1} [46]) is the bond energy for HBr. E(H*), E(H**) and E(Br*) are the energies of the H*(n = 2) (82259.158 cm^{-1} [47]), H**(n = 3) (97492.304 cm^{-1} [47]) and Br*(J = 1/2) (3685.24 cm^{-1} [47]) excited state atoms with respect to their ground states. The ''multi-peak structure'' associated with the HBr^+* (2a) and HBr^+ (2b) channels, in the range between about 2.0 and 3.6 eV, is due to photodissociation of several vibrational levels of $HBr^+(^2\Pi_{3/2})$ and HBr^+*$(^2\Pi_{1/2})$ of increasing quantum numbers v^+ as the KER increases and $v^+(HBr^+) > v^+(HBr^+$*). The KERs are calculated according to

$$KER(HBr^+) = h\nu + IE(HBr) + \Delta G_0(HBr^+,v^+) - D_0(HBr) - IE(H) \quad (5d)$$

$$KER(HBr^+*) = h\nu + IE^*(HBr) + \Delta G_0\ (HBr^+*,v^+) - D_0(HBr) - IE(H) - E(Br^*) \quad (5e)$$

where IE(HBr) (94150.672 cm^{-1} [48]) and IE(H) (109678.77 cm^{-1} [47]) are the ionization energies of HBr and H, respectively, and IE*(HBr) (96796.17 cm^{-1} [48]) is the ionization of HBr with respect to the formation of HBr^+*. $\Delta G_0(HBr^+,v^+)$ and $\Delta G_0(HBr^+*,v^+)$ are the differences in the vibrational terms for v^+ and $v^+ = 0$ for HBr^+ and HBr^+*, respectively.[47] We note that ''double'' or ''split'' rings observed for the Br and Br* channels in some of the images (see, for example, the inner ring corresponding to H* + Br* in Fig. 3), which also result in partial ''splitting'' of the corresponding KER peaks, are due to recoil effects as the hydrogen atoms H* ionize to form $H^+ + e^-$.[49,50]

The relative signal strengths (I_{rel}) of various channels, defined as the integrated signal intensities of the channels (i) ($I(i)$) divided by the total integrated intensities ($\sum I(i)$ (*i.e.* I_{rel}) = $I(i)/\sum I(i)$) differ significantly, depending on the resonance excitation wavenumber (and J') (Fig. 4b). For low J's (($J' < 7$) corresponding to the noninteraction region) the branching

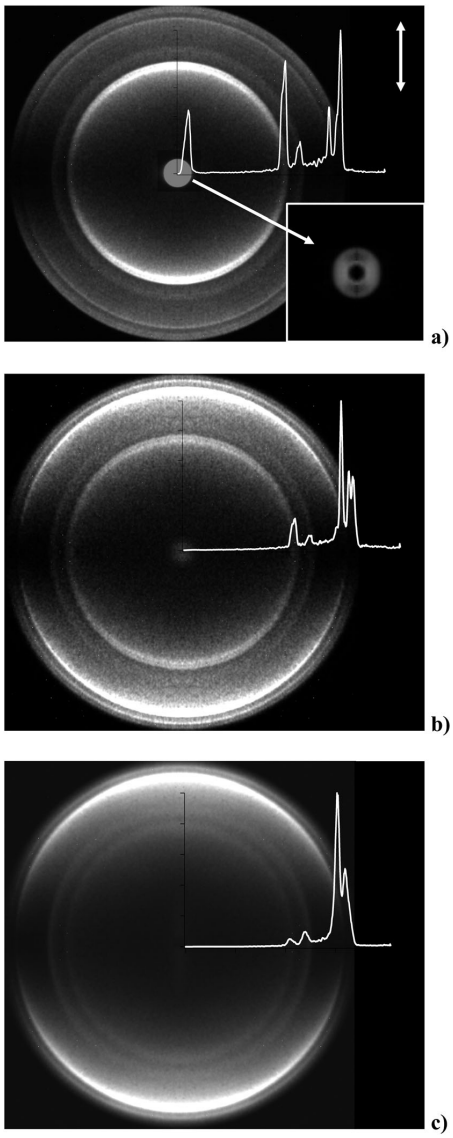

Fig. 3 H^+ velocity map images and kinetic energy release spectra of two-photon resonance excitations *via* the *Q* branch of the 6pπ(0) state spectrum for, (a) 235.911 nm laser excitation/corresponding to excitation to *ca.* the J' = 8 level, (b) 235.886 nm laser excitation/corresponding to *ca.* the J' = 6 level and (c) 235.841 nm laser excitation/corresponding to *ca.* the J' = 2 level. The laser polarization is indicated by the double arrow in (a). The inserted figure in the bottom right corner of (a) shows the 2D (Abel transformed) slice of the innermost ring.

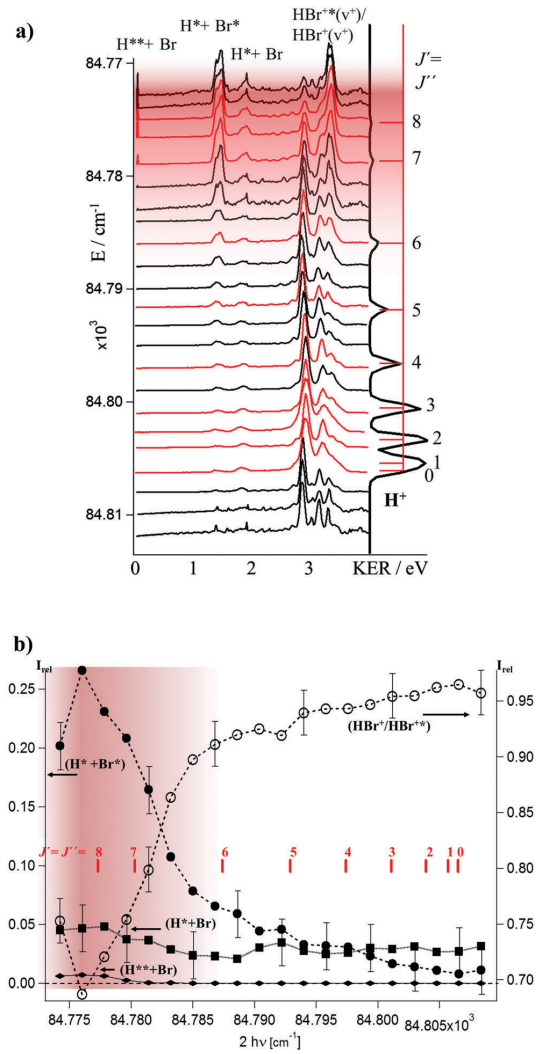

Fig. 4 (a) KERs: stacked kinetic energy release (KER) spectra as a function of two-photon excitation wavenumber along with the H^+ REMPI spectrum of the *Q* lines for the 6pπ(0) state spectrum (tilted to the right). Rotational lines are marked by J'/J'' and KER spectra close to the $J' \leftarrow J''$ resonance transitions are highlighted in red. KER spectra of various H^+ formation channels (H** + Br(4); H* + Br* (1(a)); H* + Br (1(b)); HBr^{+*}/HBr^+ (2(a) and (b)); see the main text) are marked. The area corresponding to the near-degenerate interaction between the 6pπ(0) and V(m + 17) states for $J' \approx 7$–8 is shaded in red. (b) Branching ratios: relative integrated H^+ signal intensities (I_{rel}; see the main text) of various H^+ formation channels as a function of the two-photon excitation wavenumber ($2h\nu$). The filled dots refer to the left axis and unfilled dots refer to the right axis, as indicated by arrows. Error bars for selected values are shown. *Q*-rotational line positions of the 6pπ(0) state spectrum are marked by J'/J''. The area corresponding to the near-degenerate interaction between the 6pπ(0) and V(m + 17) states for $J' \approx 7$–8 is shaded in red.

fractions of the H* + Br/Br* and H** + Br channels are small or negligible (0–0.04) and the HBr^{+*}/HBr^+ channels dominate (>0.95). For high J's ($J' \sim 7$–8) corresponding to the interaction region) the branching fractions of the H*/H** + Br channels are only marginally larger (0.01–0.05), whereas those of the H* + Br* and HBr^{+*}/HBr^+ channels have increased (0.20–0.26) and decreased (0.69–0.75) respectively.

Furthermore, the relative signal intensities (I_{rel}) of various channels are found to vary with J' in the following way (see Fig. 4a and b):

(1) I_{rel} for the H* + Br* channel (1a) gradually increases with J' for J' = 0–6, after which it increases rapidly to a maximum value for $J' \sim 8$, followed by a decrease.

(2) I_{rel} for the H* + Br channel (1b) is virtually unchanged with J' for J' = 0–8.

(3) I_{rel} for the HBr^{+}* and HBr^{+} channels (2(a) and 2(b)) shows a near-mirror effect to that for the H* + Br* channel, *i.e.*, it gradually decreases with J' for J' = 0–6, after which it decreases rapidly to a minimum value for $J' \sim 8$, followed by an increase.

(4) A closer look at the HBr^{+}* and HBr^{+} channels reveals that the I_{rel}'s due to lower v^{+}'s (KER < 3 eV) show a sharp decrease with J' for J' =6–8, whereas, the I_{rel}'s due to higher v^{+}'s (KER > 3 eV) show a sharp-increase with J' for J' = 6–8.

(5) I_{rel} for the H** + Br channel (4) only appears just below J' = 7 and reaches a maximum for J' = 8.

Angular distributions of H^{+}. Significant angular distribution variations are observed for the H^{+} ions depending on the rings/channels as well as a function of the resonance excitation energy/J' (Fig. 3). The rings for the HBr^{*+}/HBr^{+} and H* + Br* channels all display shapes corresponding to parallel transitions, whereas the ring for the H* + Br channels are all close to isotropic in shape and the rings for the H** + Br channels exhibit a perpendicular character. A slight trend towards an increasing "perpendicular shape" with J' is observed for the HBr^{*+}/HBr^{+} rings/channels, whereas the opposite effect is found for both the H* + Br* and H* + Br rings/channels.

In an attempt to quantify the anisotropy of the rings/channels the angular distributions were fitted by a simplified expression corresponding to a one-step photodissociation,

$$P(\theta) = A[1 + \beta_2 P_2(\cos(\theta)) + \beta_4 P_4(\cos(\theta))]$$

where P_2 and P_4 are the second and fourth order Legendre polynomials and β_2 and β_4 are the corresponding anisotropy parameters and A is a scaling factor. The beta parameters, being "effective" parameters for the overall photodissociation processes, can then be related to the overall transition symmetry and the corresponding dynamics. The β_2 parameter for various channels as a function of the resonance excitation wavenumber (and J'), seen in Fig. 5, shows variations consistent with the observed trends in the ring shapes mentioned above. They are found to vary largely in value between the limits of −1 and +2, corresponding to purely perpendicular and parallel transitions, respectively. The observed trends are discussed in the next section. The fourth Legendre polynomial coefficient (β_4) was used more in order to improve fits rather than to evaluate vector correlation effects, since multi-photon processes and state interactions are involved. Their values for the H* + Br*/Br (1) and H** + Br (4) channels fluctuate around zero (ranging between −0.4 and +0.4), whereas the values for the HBr^{+}*/HBr^{+} (2) channels are mostly negative (−0.6 to 0). The recoil effect ("peak splitting"), observed due the ejection of the electron during the H* ionization processes in some images, does not significantly affect the beta parameter measured and is within the error bars shown in Fig. 5.

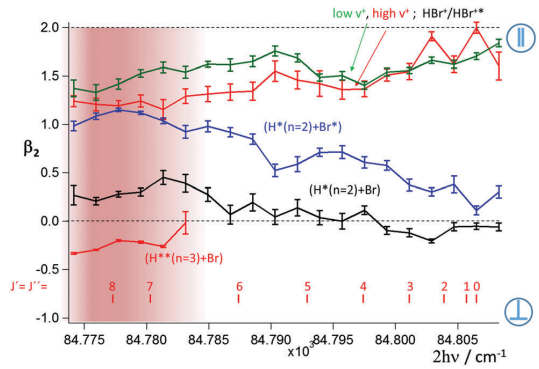

Fig. 5 Angular distributions: anisotropy parameters (β_2) extracted from H^{+} images for various channels (as labelled), by a "single step analysis" of the angular distributions as a function of the two-photon excitation wavenumber. Q-rotational line positions of the 6pπ(0) state spectrum are marked by J'/J''. The limiting values of +2 and −1, for β_2, corresponding to purely parallel (∥) and purely perpendicular (⊥) transitions, respectively, are highlighted. The area corresponding to the near-degenerate interaction between the 6pπ(0) and V(m + 17) states for $J' \approx 7$–8 is shaded in red.

IV. Discussion

The H^{+} formation channels, observed, are all likely to occur *via* one-photon transitions from the 6pπ(0) state ($J' < 7$) or the mixed 6pπ(0)/V(m + 17) state ($J' \sim 7$–8) (HBr^{**}) to repulsive states ($HBr^{\#}$) in the Rydberg series which converges to the ionic states, $B^2\Sigma^+$ and $^2\Pi$[26,30,51] and which correlate with H*(n = 2) + Br*/Br and H**(n = 3) + Br. Considering one-electron transitions and the principal electron configurations ($[\sigma^2\pi^3]6p\pi^1$) and the ($\sigma^1\pi^4\sigma^{*1}$) for the 6pπ(0) and V(m + 17) states, respectively, the Rydberg electron must occupy a 6pπ orbital in which case the possible Rydberg states are $^{1,3}\Pi$ ($[B^2\Sigma^+; \sigma^2(\pi_x^1\pi_y^1)\sigma^{*1}]6p\pi^1$) and $^{1,3}\Sigma$ ($[^2\Pi;\sigma^1\pi^3\sigma^{*1}]6p\pi^1$). The rule of spin conservation will favour the involvement of triplet states in the case of transitions from ($[\sigma^2\pi^3]6p\pi^1$) (corresponding to a pure 6pπ $^3\Sigma^-(0)$ state) and singlet states in the case of transitions from ($\sigma^1\pi^4\sigma^{*1}$) (corresponding to a pure $V^1\Sigma^+$ state). Three major transitions are, therefore, expected to be involved, two from ($[\sigma^2\pi^3]6p\pi^1$) (6pπ $^3\Sigma^-(0)$; dominating short-range excitations) and one from ($\sigma^1\pi^4\sigma^{*1}$) ($V^1\Sigma^+$); longer-range excitations), as (orbital transitions are highlighted, underlined and bold)

(a) $HBr^{**}\{6p\pi^3\Sigma^-([^2\Pi;\sigma^2\underline{\boldsymbol{\pi}}^3]6p\pi^1)\} + h\nu$

$\rightarrow HBr^{\#}\{^3\Pi([B^2\Sigma^+;\sigma^2(\pi_x^1\pi_y^1)\underline{\boldsymbol{\sigma}}^{*1}]6p\pi^1)\}$;

perpendicular core electron transition/$\underline{\boldsymbol{\pi}} \rightarrow \underline{\boldsymbol{\sigma}}^*$

(b) $HBr^{**}\{6p\pi^3\Sigma^-([^2\Pi;\underline{\boldsymbol{\sigma}}^2\pi^3]6p\pi^1)\} + h\nu$

$\rightarrow HBr^{\#}\{^3\Sigma([^2\Pi;\sigma^1\pi^3\underline{\boldsymbol{\sigma}}^{*1}]6p\pi^1)\}$;

parallel core electron transition/$\underline{\boldsymbol{\sigma}} \rightarrow \underline{\boldsymbol{\sigma}}^*$

(c) $HBr^{**}\{V^1\Sigma(\sigma^1\underline{\pi}^4\sigma^{*1})\} + h\nu \rightarrow HBr^{\#}\left\{^1\Sigma\left([^2\Pi;\sigma^1\pi^3\sigma^{*1}]6\underline{p\pi}^1\right)\right\}$;

parallel core to Rydberg electron transition/$\underline{\pi} \rightarrow \underline{p\pi}$

Based on previous as well as unpublished works relevant to two-photon resonance transitions to $\Omega' = 0$ Rydberg and ion-pair states[26,30,52] there is a reason to believe that the resonance transitions are largely perpendicular (*i.e.* $\Sigma \leftarrow \Pi \leftarrow \Sigma$). Furthermore, there isn't a reason to expect a large variation in the character of those transitions over the relatively short excitation region of concern here (see Fig. 1b). We, therefore, believe that the major variations in the overall parallel *vs.* perpendicular transition characters as a function of J', as well as for the different channels (see above), are associated with the final photodissociation steps following the resonance excitations. Therefore, in the cases of the H* + Br*/Br and H** + Br channels, variations in the transition characters will be determined by the relative contributions of the steps (a)–(c) above. In the case of the HBr^+/HBr^{+}* channels both the steps (a)–(c) and the photodissociation of HBr^+/HBr^{+}* need to be considered.

In light of the above discussion and the results derived from the KER's and the angular distributions, mentioned above, we propose the following major photodissociation processes leading to the formation of various channels.

HBr^{+}*/HBr^+

The HBr^{+}*/HBr^+ channels dominate for low J'/the non-interaction region (Fig. 4b), suggesting that autoionization processes of the superexcited triplet states $^3\Pi([B^2\Sigma^+]6p\pi^1)$ and $^3\Sigma([^2\Pi_{3/2}]6p\pi^1)$ accessed by the short range transitions from $([\sigma^2\pi^3]6p\pi^1)$ (pure $6p\pi\ ^3\Sigma^-(0)$ state) are more favourable than the alternative dissociation processes to form H* + Br/Br*. Since the overall transitions for the H^+ formation *via* the HBr^{+}*/HBr^+ channels are parallel in nature (Fig. 5), the parallel ($\sigma \rightarrow \sigma^*$) transitions (i) from the ground ionic state(s) HBr^{+}*/$HBr^+(X^2\Pi(\sigma^2\pi^3))$ to the $HBr^{+\#}(2^2\Pi(\sigma^1\pi^3\sigma^{*1}))$ state prior to dissociation and ii) for the excitations of the $HBr^{**}(6p\pi^3\Sigma^-([^2\Pi;\sigma^2\pi^3]6p\pi^1))$ to the $HBr^{\#}(^3\Sigma([^2\Pi;\sigma^1\pi^3\sigma^{*1}]6p\pi^1))$ superexcited state are likely to be favoured over the perpendicular ($\pi \rightarrow \sigma^*$) transitions to the $HBr^{+\#}(B^2\Sigma^+;\sigma^2(\pi_x^1\pi_y^1)\sigma^{*1})$ and $HBr^{\#}(^3\Pi([B^2\Sigma^+;\sigma^2(\pi_x^1\pi_y^1)\sigma^{*1}]6p\pi^1))$ states respectively. Therefore, the autoionization process would involve a perpendicular transition of the 6pπ Rydberg electron to the σ valence orbital rather than a parallel transition to a π valence orbital followed by an ejection of an Auger electron from a σ* orbital. The branching fraction of the HBr^{+}*/HBr^+ channels as a function of J' closely mirrors that of the H* + Br* channels, by showing a large decrease with increasing J' (*i.e.* by moving from the non-interaction region ($J' < 7$) to the interaction region ($J' \sim 7$–8)). This could be due to joined transitions from the resonance excited state(s) followed by competition between the HBr^{+}*/HBr^+ and H* + Br* formation depending on the degree of state mixing. Thus, for low J', dominating triplet-to-triplet short-range transitions from $([\sigma^2\pi^3]6p\pi^1)$ (pure $6p\pi\ ^3\Sigma^-(0)$ state), HBr^{+}*/HBr^+ are favoured, whereas for high J's where the weight of long-range transitions from $(\sigma^1\pi^4\sigma^{*1})$ (pure $V^1\Sigma^+$ state; transition) to the $^1\Sigma([^2\Pi_{1/2}]6p\pi^1)$ state increases, and H* + Br* formation is enhanced. The observed sharp decreases in the lower v^+ signals and the corresponding increases in the higher v^+ signals with J' (Fig. 4a) suggest that high v^+ is favoured *via* the long-range transitions from $(\sigma^1\pi^4\sigma^{*1})$ (pure $V^1\Sigma^+$ state; transition). Since the autoionization rate depends on the Franck–Condon-factor overlap between the superexcited repulsive states and the v^+ states of the ionic states, one might, indeed, expect a favourable Franck–Condon-factor overlap between the repulsive states and high v^+ states in the long-range and between repulsive states and low v^+ in the short-range (Fig. 1b).

H* + Br*

A large increase in the branching fraction of the H* + Br* channel (Fig. 4b), and a gradual increase in the parallel character of the corresponding transition (Fig. 5) with increasing J' (*i.e.* by moving from the non-interaction region ($J' < 7$) to the interaction region ($J' \sim 7$–8)), suggests that long-range parallel excitations from $(\sigma^1\pi^4\sigma^{*1})$ (pure $V^1\Sigma^+$ state; transition (c)) to the $^1\Sigma([^2\Pi_{1/2}]6p\pi^1)$ state in the mixing region are of major importance. The very low branching fraction observed for the lowest J' ($J' \sim 0$–2) (Fig. 4b), in fact suggests that the transitions (a) and (b) from $([\sigma^2\pi^3]6p\pi^1)$ (pure $6p\pi\ ^3\Sigma^-(0)$ state) are of minor importance.

H* + Br

The observation of negligible or only small enhancements in the branching fractions of the H* + Br channel (Fig. 4b) and the parallel character of the corresponding transition (Fig. 5) with increasing J' (*i.e.* by moving from the non-interaction region ($J' < 7$) to the interaction region ($J' \sim 7$–8)) suggests that long-range parallel excitations *via* $(\sigma^1\pi^4\sigma^{*1})$ (pure $V^1\Sigma^+$ state; transition (c)) are of minor importance. The values for β_2 of about −0.25 to +0.50 (Fig. 5), however, suggest that both the perpendicular (a) and the parallel transitions (b) from $([\sigma^2\pi^3]6p\pi^1)$ (pure $6p\pi\ ^3\Sigma^-(0)$ state) to the $^3\Pi([B^2\Sigma^+]6p\pi^1)$ and $^3\Sigma([^2\Pi_{3/2}]6p\pi^1)$ states, respectively, are involved.

H** + Br

There is reason to believe that the transitions, prior to the H** + Br formation, are comparable to those of the H* + Br channel, mentioned above for the corresponding superexcited states which correlate with H** + Br (instead of H* + Br). Signals due to the H** + Br channels only appear for high J's ($J' \sim 7$–8). Based on the bond energy of HBr (30 210 ± 40 cm^{-1} [46]) and the energy of H**($n = 3$) (97492.3 cm^{-1} [53]) the threshold for the formation of H** + Br from HBr($v'' = 0, J'' = 0$) is about 127 702 ± 40 cm^{-1}, which can only be reached *via* $J' > 7$ excitations in Q transitions ($J' = J''$). The three-photon excitations *via* the $J' = 8$ level correspond to the energy of 127 764 cm^{-1}, whereas excitations for lower J's ($J' < 8$) all correspond to energies lower than 127 702 cm^{-1}. In light of this fact, the comparison with the results obtained for the analogous channel of H* + Br above, as well as the overall perpendicular nature of the transition involved (Fig. 5), there is a reason to believe that both the perpendicular (a) and the parallel transitions (b) from

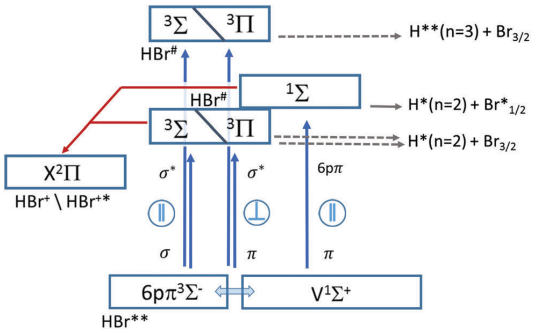

Fig. 6 Schematic figure of the major one-photon transitions (blue arrows) as well as photodissociation (gray arrows) and autoionization (red arrows) processes following two-photon resonance transitions to the 6pπ(0) and 6pπ(0)/V(m + 17) mixed state(s), prior to ionization (see main text). Orbital transitions and the nature (parallel/perpendicular transitions) of the photo-excitations are indicated.

([$\sigma^2\pi^3$]6pπ^1) (pure 6pπ $^3\Sigma^-$(0) state) to the $^3\Pi$([$B^2\Sigma^+$]6pπ^1) and $^3\Sigma$([$^2\Pi_{3/2}$]6pπ^1) states, respectively, are involved.

V. Conclusions

A mass resolved and H^+ velocity map imaging analysis of HBr REMPI, in the two-photon resonance excitation region of 84 740–85 120 cm^{-1}, has revealed a clear picture of the effect of triplet to singlet state interactions on photofragmentation processes. Rotational line-shifts and intensity alterations of mass resolved REMPI spectra due to resonance excitations to the 6pπ $^3\Sigma^-(v' = 0)$ Rydberg and $V^1\Sigma^+(v' = m + 17)$ valence (ion-pair) states are indicative of interactions between these states. Deperturbation analysis of the data revealed the interaction strength as well as zero order spectroscopic parameters for the 6pπ $^3\Sigma^-$(0) state. The fractional mixing is found to vary with J' to reach maxima for the near-resonance levels J' = 7–8. H^+ velocity map images derived as a function of the excitation wavenumber in the region of the Q branch of the 6pπ $^3\Sigma^-$(0) state spectrum revealed signals due to five major formation channels corresponding to the intermediate species H*(n = 2) + Br*/Br (1(a) and (b)), H**(n = 3) + Br (4), and $HBr^{+*}(v^+)/HBr^+(v^+)$ (2(a) and (b)) prior to the H* and H** atom photoionization processes (1(a), (b) and 4) and molecular ion (HBr^{+*}/HBr^+) photodissociation processes. Branching fractions and anisotropy parameters were derived from the kinetic energy release (KER) spectra and angular distributions, respectively, as a function of the excitation wavelengths/J'. Considering these data, the KER spectra structural variations as well as the resonance excited state interactions, the following major photoexcitations of the resonance excited state(s) 6pπ $^3\Sigma^-$(0) mixed with V(m + 17), prior to the H^+ formations, are proposed (see Fig. 6).

For a limited state mixing (pure [$\sigma^2\pi^3$]6pπ $^3\Sigma^-$(0) state/low J') triplet-to-triplet, parallel short-range transitions to a super-excited repulsive $^3\Sigma$ state, followed by autoionization to form $HBr^{+*}(\Omega = 1/2)$ and $HBr^+(\Omega = 3/2)$ dominates over a minor dissociation channel forming H* + Br. A small but significant perpendicular transition to a superexcited repulsive $^3\Pi$ state, followed by dissociation to form H* + Br, is also involved. For an increased state mixing (enhanced ($\sigma^1\pi^4\sigma^{*1}$) $V^1\Sigma^+$ state character/J' = 7–8 in particular) a singlet-to-singlet, parallel long-range transition to a superexcited repulsive $^1\Sigma$ state is brought in followed by autoionization to form $HBr^{+*}(\Omega = 1/2)$ and $HBr^+(\Omega = 3/2)$ as well as dissociation to form H* + Br*. For $J' \sim 8$ triplet-to-triplet, perpendicular and parallel short-range transitions to superexcited repulsive $^3\Pi$ and $^3\Sigma$ states, respectively, followed by dissociation to form H** + Br occur.

Acknowledgements

The financial support from the University Research Fund, University of Iceland and the Icelandic Science Foundation (Grant No. 130259-051) is gratefully acknowledged. The research leading to these results received funding from LASERLAB-EUROPE (grant agreement no. 228334, EC's Seventh Framework Programme). This work was supported by Greek Secretariat for Research and Technology programs ERC03:ITSSUED and THALIS: ISEPUMA, co-financed by EU (European Social Fund) and national funds under NSRF2007–2013. PCS gratefully acknowledges support from an EU Marie Curie Reintegration Grant (GPSDI, Grant No. PIRG07-GA-2010-268305). DZ gratefully acknowledges EU Marie Curie IAPP program SOFORT (GA 251598). We wish to thank Gabriel J. Vázquez, H. P. Liebermann and H. Lefebvre-Brion for useful information concerning HBr potential curves based on unpublished calculations.

References

1 A. E. Douglas and F. R. Greening, *Can. J. Phys.*, 1979, **57**, 1650–1661.
2 D. S. Green, G. A. Bickel and S. C. Wallace, *J. Mol. Spectrosc.*, 1991, **150**, 303–353.
3 D. S. Green, G. A. Bickel and S. C. Wallace, *J. Mol. Spectrosc.*, 1991, **150**, 354–387.
4 D. S. Green, G. A. Bickel and S. C. Wallace, *J. Mol. Spectrosc.*, 1991, **150**, 388–469.
5 D. S. Green and S. C. Wallace, *J. Chem. Phys.*, 1992, **96**, 5857–5877.
6 D. Ascenzi, S. Langford, M. Ashfold and A. Orr-Ewing, *Phys. Chem. Chem. Phys.*, 2001, **3**, 29–43.
7 Á. Kvaran, H. Wang and Á. Logadóttir, *Recent Res. Devel. in Physical Chem.*, Transworld Research Network, 1998, vol. 2, pp. 233–244.
8 Á. Logadóttir, Á. Kvaran and H. Wang, *J. Chem. Phys.*, 1998, **109**, 5856–5867.
9 Á. Logadóttir, Á. Kvaran and H. Wang, *J. Chem. Phys.*, 2000, **112**, 10811–10820.
10 S. G. Tilford and M. L. Ginter, *J. Mol. Spectrosc.*, 1971, **40**, 568–579.
11 M. L. Ginter, S. G. Tilford and A. M. Bass, *J. Mol. Spectrosc.*, 1975, **57**, 271.

12 D. S. Ginter, M. L. Ginter and S. G. Tilford, *J. Mol. Spectrosc.*, 1981, **90**, 152.
13 D. S. Ginter, M. L. Ginter, S. G. Tilford and A. M. Bass, *J. Mol. Spectrosc.*, 1982, **92**, 55.
14 D. S. Ginter, M. L. Ginter and S. G. Tilford, *J. Mol. Spectrosc.*, 1982, **92**, 40.
15 J. B. Nee, M. Suto and L. C. Lee, *J. Chem. Phys.*, 1986, **85**, 4919.
16 Á. Kvaran and H. Wang, *J. Mol. Spectrosc.*, 2004, **228**, 143–151.
17 K. Matthiasson, Á. Kvaran, H. Wang, A. Bodi and E. Jónsson, *J. Chem. Phys.*, 2008, **129**, 164313.
18 K. Matthiasson, H. Wang and Á. Kvaran, *J. Mol. Spectrosc.*, 2009, **255**, 1–5.
19 K. Matthiasson, Á. Kvaran and H. Wang, *J. Chem. Phys.*, 2009, **131**, 044324.
20 K. Matthiasson, J. Long, H. Wang and Á. Kvaran, *J. Chem. Phys.*, 2011, **134**, 164302.
21 J. Long, H. Wang and A. Kvaran, *J. Mol. Spectrosc.*, 2012, **282**, 20–26.
22 J. Long, H. R. Hrodmarsson, H. Wang and A. Kvaran, *J. Chem. Phys.*, 2012, **136**, 214315.
23 J. Long, H. Wang and Á. Kvaran, *J. Chem. Phys.*, 2013, **138**, 044308.
24 H. R. Hróðmarsson, H. Wang and Á. Kvaran, *J. Mol. Spectrosc.*, 2013, **290**, 5–12.
25 Y. Xie, P. T. A. Reilly, S. Chilukuri and R. J. Gordon, *J. Chem. Phys.*, 1991, **95**, 854–864.
26 C. Romanescu and H. P. Loock, *J. Chem. Phys.*, 2007, **127**, 124304.
27 S. Kauczok, C. Maul, A. I. Chichinin and K. H. Gericke, *J. Chem. Phys.*, 2010, **133**, 24301.
28 R. Liyanage, R. J. Gordon and R. W. Field, *J. Chem. Phys.*, 1998, **109**, 8374–8387.
29 H. R. Hróðmarsson, H. Wang and Á. Kvaran, *J. Chem. Phys.*, 2014, **140**, 244304.
30 D. Zaouris, A. Kartakoullis, P. Glodic, P. C. Samartzis, H. R. Hróðmarsson and Á. Kvaran, *Phys. Chem. Chem. Phys.*, 2015, **17**, 10468–10477.
31 H. R. Hróðmarsson, H. Wang and Á. Kvaran, *J. Chem. Phys.*, 2015, **142**, 244312.
32 H. Liebel, S. Lauer, F. Vollweiler, R. Muller-Albrecht, A. Ehresmann, H. Schmoranzer, G. Mentzel, K.-H. Schartner and O. Wilhelmi, *Phys. Lett. A*, 2000, **267**, 357–369.
33 P. V. Demekhin, V. L. Sukhorukov, H. Schmoranzer and A. Ehresmann, *J. Chem. Phys.*, 2010, **132**, 204303.
34 Y. Zhou, Q. Meng and Y. Mo, *J. Chem. Phys.*, 2014, **141**, 014301.
35 D. S. Ginter and M. L. Ginter, *J. Mol. Spectrosc.*, 1981, **90**, 177–196.
36 S. T. Pratt and M. L. Ginter, *J. Chem. Phys.*, 1995, **102**, 1882–1888.
37 M. A. Baig, J. Hormes, J. P. Connerade and W. R. S. Garton, *J. Phys. B: At., Mol. Opt. Phys.*, 1981, **14**, L147–L151.
38 R. Callaghan and R. J. Gordon, *J. Chem. Phys.*, 1990, **93**, 4624–4636.
39 C. Romanescu and H.-P. Loock, *Phys. Chem. Chem. Phys.*, 2006, **8**, 2940–2949.
40 C. R. Gebhardt, T. P. Rakitzis, P. C. Samartzis, V. Ladopoulos and T. N. Kitsopoulos, *Rev. Sci. Instrum.*, 2001, **72**, 3848–3853.
41 V. Papadakis and T. N. Kitsopoulos, *Rev. Sci. Instrum.*, 2006, **77**, 5.
42 See ESI†.
43 J. Long, H. Wang and Á. Kvaran, *Acta Phys.-Chim. Sin.*, 2013, **62**, 163302.
44 H. Lefebvre-Brion and R. W. Field, *Perturbations in the Spectra of Diatomic Molecules*, Academic Press, Inc., London, 1986.
45 "Constants of diatomic molecules", NIST Chemistry WebBook, http://webbook.nist.gov/cgi/cbook.cgi?ID=C10035106&Units=SI&Mask=1000, accessed March 2016.
46 P. M. Regan, S. R. Langford, A. J. Orr-Ewing and M. N. R. Ashfold, *J. Chem. Phys.*, 1999, **110**, 281–288.
47 NIST Atomic Spectra Database (ver. 5.3), [Online], http://physics.nist.gov/asd, accessed March 2016, National Institute of Standards and Technology, Gaithersburg, MD.
48 A. J. Yencha, A. J. Cormack, R. J. Donovan, K. P. Lawley, A. Hopkirk and G. C. King, *Chem. Phys.*, 1998, **238**, 133–151.
49 R. L. Toomes, P. C. Samartzis, T. P. Rakitzis and T. N. Kitsopoulos, *Chem. Phys.*, 2004, **301**, 209–212.
50 F. Aguirre and S. T. Pratt, *J. Chem. Phys.*, 2004, **121**, 9855.
51 A. Banichevich, R. Klotz and S. D. Peyerimhoff, *Mol. Phys.*, 1992, **75**, 173–188.
52 D. Zaouris, P. Glodic, P. C. Samartzis, H. R. Hróðmarsson, H. Wang and Á. Kvaran, unpublished work.
53 NIST Chemistry WebBook - NIST Atomic Spectra Database Levels Data, http://webbook.nist.gov/, accessed April 2016.
54 G. J. Vázquez, H. P. Liebermann and H. Lefebvre-Brion, unpublished work.

4.2.1 Supporting information

Effect of a triplet to singlet state interaction on photofragmentation dynamics: Highly excited states of HBr probed by VMI and REMPI as a case study

Pavle Glodic[1], Dimitris Zaouris[1a], Peter C. Samartzis[1],
Arnar Hafliðason[2] and Ágúst Kvaran[2]*

1. *Institute of Electronic Structure and Laser, Foundation for Research and Technology-Hellas, Vassilika Vouton, 71110 Heraklion, Greece.*
2. *Science Institute, University of Iceland, Dunhagi 3, 107 Reykjavík, Iceland.*
a. *Present address: Department of Physics and Astronomy, University College London, Gowen Street London WC1E, 6BT, UK*

Supporting information

Content: page:

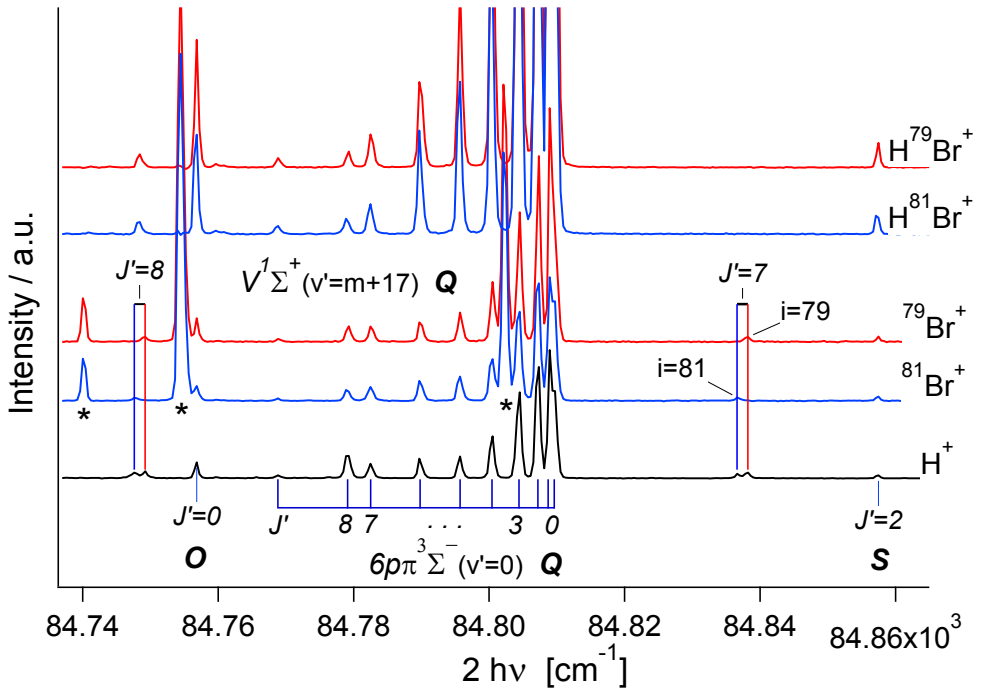
Intensity / a.u.
H79Br+
H81Br+
79Br+
81Br+
H+
J'=8
V1Σ+(v'=m+17) Q
J'=7
i=79
i=81
*
*
*
J'=0
O
J'
8 7 . . . 3 0
6pπ3Σ−(v'=0) Q
J'=2
S
84.74
84.76
84.78
84.80
84.82
84.84
84.86x10^3
2 hν [cm-1]

Fig. S1

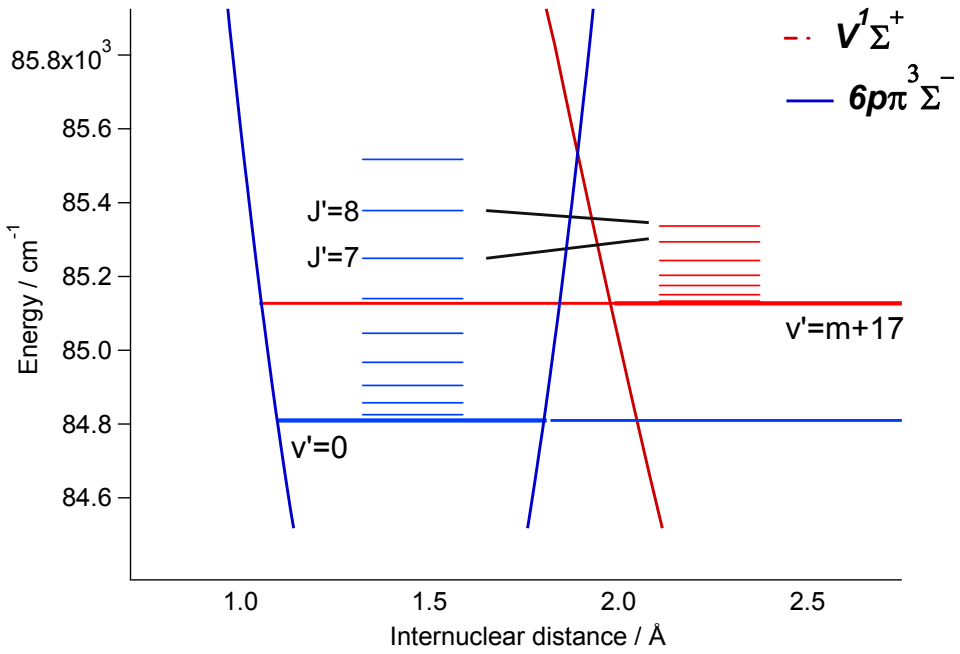
V1Σ+
6pπ3Σ−
85.8x10^3
85.6
85.4
85.2
85.0
84.8
84.6
Energy / cm-1
J'=8
J'=7
v'=m+17
v'=0
1.0
1.5
2.0
2.5
Internuclear distance / Å

Fig. S2

References

1. A. Banichevich, R. Klotz and S. D. Peyerimhoff, *Molecular Physics*, 1992, **75**, 173-188.

2. Á. Logadóttir, Á. Kvaran and H. Wang, *J. Chem. Phys.*, 2000, **112**, 10811-10820.

4.3 Paper 3

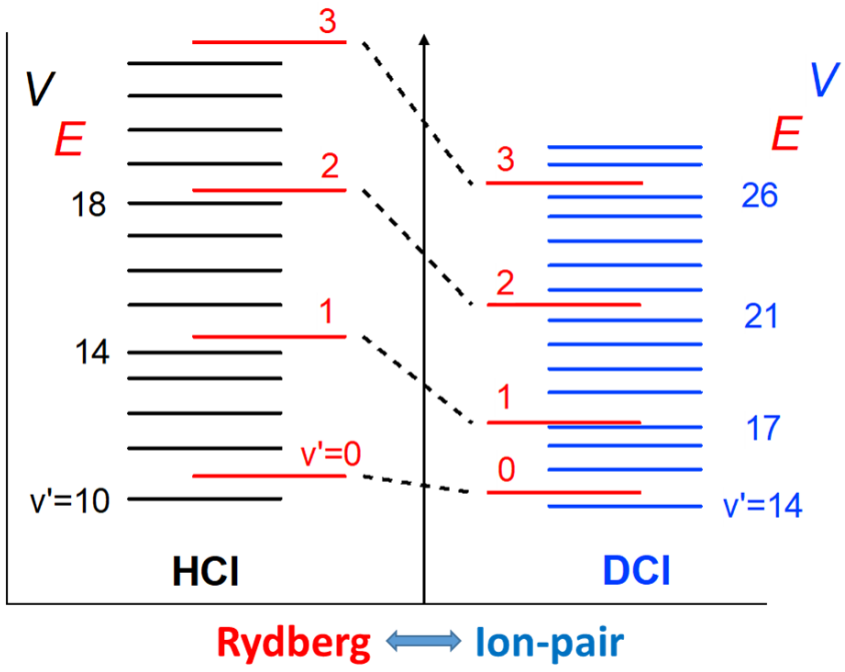

Arnar Hafliðason, Victor Huasheng Wang, Ágúst Kvaran. *High energy Rydberg and valence states and state interaction of DCl: New observations by mass resolved REMPI.* Journal of Molecular Spectroscopy, 2017, **341**, 1-9.

DOI: 10.1016/j.jms.2017.09.002

Journal of Molecular Spectroscopy 341 (2017) 1–9

Contents lists available at ScienceDirect

Journal of Molecular Spectroscopy

journal homepage: www.elsevier.com/locate/jms

High energy Rydberg and valence states and state interactions of DCl: New observations by mass resolved REMPI

Arnar Hafliðason, Huasheng Wang, Ágúst Kvaran *

Science Institute, University of Iceland, Dunhagi 3, 107 Reykjavík, Iceland

ARTICLE INFO

Article history:
Received 12 July 2017
In revised form 21 August 2017
Accepted 4 September 2017
Available online 12 September 2017

ABSTRACT

Mass resolved resonance enhanced multiphoton ionization (REMPI) spectra of a mixture of DCl and HCl were recorded for two-photon resonance excitation in the region of 80 500–89 500 cm^{-1}. Spectra due to resonance transitions to rovibrational states of number of Rydberg and ion-pair states of DCl, were identified and assigned. Five new spectral bands due to transitions to Rydberg states and eight new bands due to transitions to vibrational states of the ion-pair state were identified and analysed to derive energetic parameters. Irregularities observed in vibrational energy level spacing, rotational constants and isotope shifts of chlorine isotopologues from what to expect for unperturbed states, as well as relative signal intensities, are indicative of strong homogeneous interaction between the $E^1\Sigma^+$ Rydberg state and the $V^1\Sigma^+$ ion-pair state. These observations are found to be due to level-to-level interaction between E and V rovibrational states of same J' quantum numbers. Comparison of the data for DCl and HCl is performed.

1. Introduction

UV–Vis molecular spectroscopy and photofragmentation studies, presented in the literature, are largely associated with photoexcitations in a relatively low energy valence state region. Corresponding studies relevant to excitation to higher energy region of Rydberg states or mixed Rydberg and valence states are much fewer. Partly, this is due to a larger density of states and state mixing within molecules, which adds to the complexity of spectroscopic and photofragmentation analysis. Nevertheless, photoexcitation to the higher energy region of molecules are of great relevance to number of intriguing research fields such as atmospheric chemistry, astrochemistry, photosynthesis and plasma physics.

The simplicity of the diatomic hydrogen halides makes them ideal candidates for such fundamental studies. Relatively well resolved rotational spectral structures for excitations to high energy Rydberg and ion-pair (valence) states has allowed detailed quantum energy level based studies of spectroscopy [1–27] and photofragmentation [5,7,9–11,13,15–22,28–34] processes. Spectroscopic information have been sought by means of standard spectroscopy methods [1–3,24,28,35–40] as well as by REMPI [4–6,8–10,12–14,16–23,26,27,29,41–43] to characterize the energetics of large number of Rydberg states and ion-pair vibrational states. The use of varying number of photons for resonance excitations has proved to be useful in the search for, and characterization of, states. Spectral perturbations, showing as spectra line shifts or intensity alterations, are frequently observed. These have been taken account of by deperturbation calculations [18,20,21,31,44] and made use of to predict the energetics of hidden (or dark) states [26] as well as to determine state interaction strengths and properties [15–17,19,20,22,26] and to characterize dissociation processes [12,13,21,22]. Additionally, ion velocity map imaging studies, coupled with REMPI, have been used successfully to characterize photofragmentation (both photodissociation and photoionization) and excitation processes involved [21,22,44–47]. Furthermore, the methodology of *ab initio* calculations, relevant to electronically excited molecular states, has gained from an association with the experimental work and proved to be useful as a guiding tool in data interpretations [48–56].

Largest amount of data has been collected for HCl [1,4–6,10,11,29,31,35,39,41,42,57,58], whereas a lot less data are available for its deuterated counterpart, DCl. The early work on the absorption spectroscopy of DCl by Tilford and Ginter in 1971 [35] and by Douglas and Greening in 1979 [3], resulted in discovery of a number of Rydberg states and medium high energy vibrational states of the $V^1\Sigma$ ion-pair state. Later, Callaghan et al. [23] published work on $(2+n)$ REMPI of HCl and DCl. Coxon et al., [24] observed the lowest vibrational bands of the $V^1\Sigma^+$ state by emission spectroscopy. Vibrational bands of the $V^1\Sigma^+$ ion-pair state for $v' = 8–11$ and from $v' = 22$ upwards, for DCl, are yet to be observed.

* Corresponding author.
E-mail address: agust@hi.is (Á. Kvaran).

http://dx.doi.org/10.1016/j.jms.2017.09.002
0022-2852/

More recently, through (3 + 1) REMPI, Kvaran et al. reported previously unobserved Rydberg states, for HCl and DCl [11,58]. No data, relevant to the dynamics or photofragmentation of DCl involving states in this high energy region, are available in the literature. Whereas theoretical interpretation of high energy state interaction has been performed for HCl [48], no such work is available for DCl.

In this paper we present (2 + n) REMPI data and analysis for the two-photon resonance excitation region of 80 500–89 500 cm^{-1} for a mixture of DCl and HCl. Number of new spectral observations, for DCl, are assigned, including previously unobserved vibrational bands of the $V^1\Sigma^+$ ion-pair state and for Rydberg states. Detailed analysis of the data involve standard spectral structure fit analysis and/or simulation calculations. A special attention is paid to perturbation effects which appear as deviation of spacings between vibrational energy levels, rotational constants and chlorine isotope shifts from regular patterns of unperturbed states/Morse potentials. The analysis lead to quantitative characterization of states and reveal a characteristic pattern of strong interactions between singlet sigma states, indicating a diversity in dynamical processes in this high energy region. Comparison of data for DCl and HCl is performed.

2. Experimental

DCl was produced by a reaction of benzoyl chloride and deuterated water to give a mixture of DCl and HCl in a ratio of about 60:40 ratio [59]. The product was transferred to and stored in a gas cylinder. Mass resolved REMPI spectra were recorded for the mixture of HCl and DCl diluted in argon (HCl/DCl 50%, Argon 50%) after a jet expansion of the mixture through a pulsed nozzle to form a molecular beam. The apparatus used has been described before [58,60,61]. Equipment and condition parameters are listed in Table 1. Excitation radiation was generated with a Lambda Physik COMPex 205 excimer laser (XeCl, 308 nm) pumped Coherent ScanMatePro dye laser followed by a frequency doubling by a BBO crystal. The laser beam was focused on the molecular beam by a 200 mm quartz focal lens between a repeller and extractor plates. Ions produced were directed into a 70 cm time-of-flight tube and detected by MCP detector plates. Signals were fed into a LeCroy WaveSurfer 44 MXs-A, 400 MHz storage oscilloscope and recorded as mass spectra vs. laser excitation wavenumber. To prevent saturation effects and power broadening, laser power was minimized. Calibration was based on known spectral peaks of the major HCl REMPI signals [4]. Accuracy was found to be about ±1.0 cm^{-1} on the two-photon wavenumber scale.

Table 1
Typical equipment and condition parameters for REMPI experiments.

(a)	HCl/DCl/Ar sample	About (DCl 60%: HCl 40%) 50%: argon 50%
(b)	Laser dyes	C-440, C-460 & C-480
(c)	Freq. doubling crystal	Sirah BBO-2
(d)	Laser repetition rate	10 Hz
(e)	Dye laser linewidth	0.095 cm^{-1}
(f)	Laser intensity used	10–16 mJ/pulse from Dye laser, 0.5–1.0 mJ after SHG
(g)	Nozzle size	0.5 mm
(h)	Sample backing pressure	2–3 bar
(i)	Pressure inside ion chamber	5·10^{-7} mbar
(j)	Nozzle opening time	180–250 μs
(k)	Delay time for laser excitation	450–500 μs
(l)	Excitation step size	0.1 cm^{-1}
(m)	Time-Of-Flight step size	10 ns
(n)	Time-Of-Flight tube length	70 cm
(o)	Focal lens distance	200 mm

3. Results and analysis

Ion yields as a function of two-photon wavenumber excitation (mass resolved REMPI spectra) were derived for all observed ions formed by REMPI of H^{i}Cl and D^{i}Cl; i = 35, 37 (see Table 2), for the excitation region of 80 500–89 500 cm^{-1}. Signals due to (2 + n) REMPI of D^{i}Cl, for both i = 35 and 37 were used to assign spectra and to characterize vibrational states of electronically excited D^{35}Cl and to derive isotope shifts for the two isotopologues D^{i}Cl; i = 35, 37, whereas those due to REMPI of known H^{35}Cl states [4–6] were used for wavelength calibration. Fig. 1a–c shows D^{i}Cl REMPI spectra for two-photon resonance transitions to the Rydberg states $E^1\Sigma^+(0^+)$ ($v' = 0$) (a) and $I^1\Delta_2(v' = 0)$ (c) and to the valence/ion-pair state $V^1\Sigma^+(0^+)(v' = 22)$ (b). More spectra, relevant to the analysis of D^{35}Cl, are to be found in Supplementary material [62]. In agreement with observations for H^{i}Cl [10,15,18,30,34] the $\Omega = 0$ Rydberg states (the $E^1\Sigma^+$ state in particular) and the ion-pair state spectra show relatively large signals for both the fragment and parent molecular ions (dominating 1a and 1b), whereas, those of Rydberg states for $\Omega > 0$ and triplet states show dominating parent molecular ion signals (Fig. 1c). The former observation is believed to indicate large mixing of the $\Omega = 0$ Rydberg and ion-pair states due to strong homogeneous interactions [23,24,33–35]. D^{35}Cl spectra due to resonance transitions to Rydberg states were either analysed by use of the PGOPHER simulation program [63], or by fitting analytical expressions for peak positions as a function of quantum numbers of the energy levels involved [9,12,18,62], to give rotational parameters (B', D') and band origins (v^0) for given rotational constants for the ground state [64] (see Table 3). Most D^{35}Cl spectra, previously detected in this excitation region, were identified and assigned. In addition, several new spectral bands and/or new rotational lines were observed and assigned (see Table 3 and Ref. [62]). These will now be dealt with in more detail. Shorter abbreviations for the Rydberg and ion-pair vibrational states involved will be frequently used, e.g., $V(17)$ for $V^1\Sigma^+(v' = 17)$ and $E(0)$ for $E^1\Sigma^+(v' = 0)$.

3.1. Spectra due to two-photon resonance transitions to Rydberg states

Number of Rydberg state spectra, previously assigned [3,23,35] were identified [62] and analysed to give spectroscopic parameters of good agreement with values derived before (Table 3). In addition five new bands (unreported) were observed:

A new band was observed in the two-photon wavenumber region of 88 200–88 280 cm^{-1} showing weak Q, R and S lines (Fig. 2a) [62]. Only signals due to the parent molecular ion, DCl$^+$ were observed, which is typical for an excited state of negligible mixing with the $V^1\Sigma^+$ ion-pair state [15–20,22,30,34,65]. Spectroscopic parameters for D^{35}Cl, evaluated from analysis of the spectra are listed in Table 3. Chlorine isotope shift ($\Delta v^0(35, 37)$ for ^{i}Cl; i = 35, 37 [66,67]) of about 8 cm^{-1} was obtained. The values of the band origin (v^0), rotational constant ($B_{v'}$) and isotope shift ($\Delta v^0(35, 37)$) are logical continuation of the corresponding values

Table 2
Ions formations in REMPI of H^{i}Cl and D^{i}Cl; i = 35, 37.

Mass numbers/amu	Parent molecules/ions formed		
	H^{i}Cl	H^{i}Cl/D^{i}Cl	D^{i}Cl
1	H$^+$		
2			D$^+$
35		^{35}Cl$^+$	
36	H^{35}Cl$^+$		
37		^{37}Cl$^+$	D^{35}Cl$^+$
38	H^{37}Cl$^+$		
39			D^{37}Cl$^+$

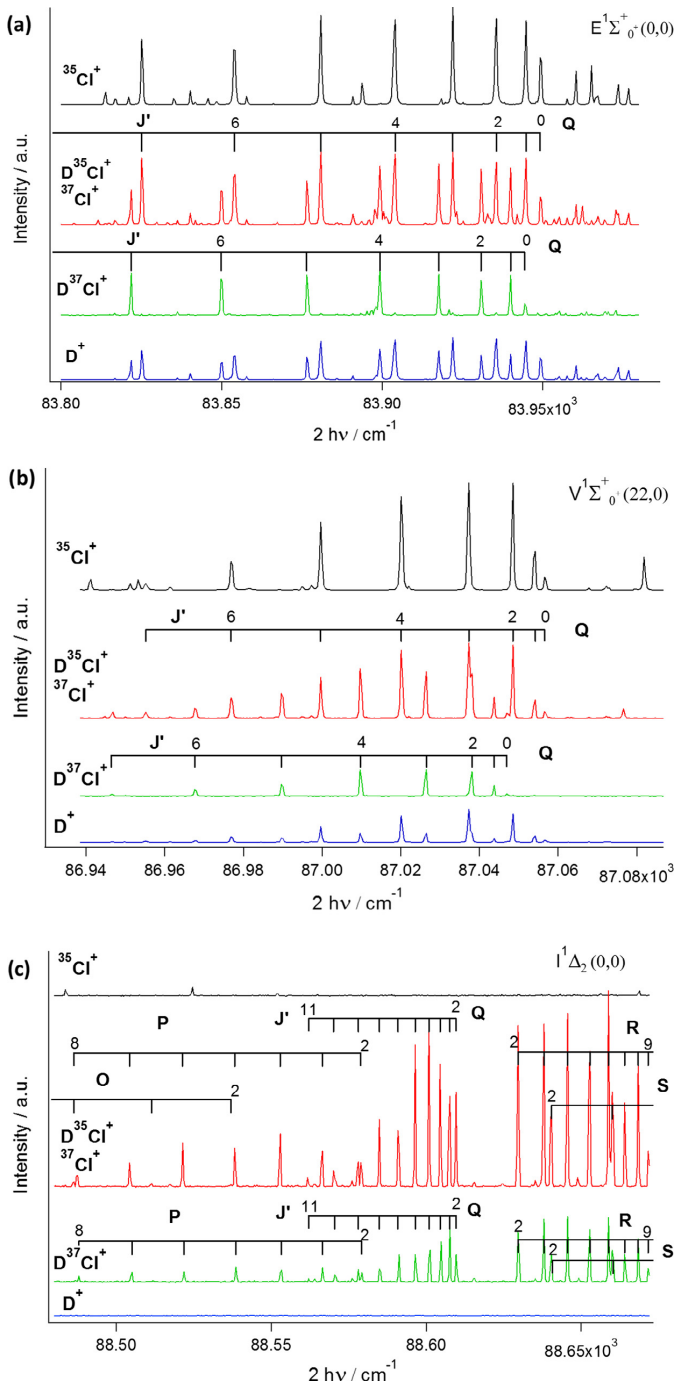

Fig. 1. REMPI spectra of mixtures of D^{i}Cl(g) and H^{i}Cl(g); i = 35, 37 for the ions $^{35}Cl^+$ (mass 35; black), $D^{35}Cl^+$ and $^{37}Cl^+$ (37; red), $D^{37}Cl^+$ (39; green) and D^+ (2; blue) (see Table 2). *J'*-quantum numbers for the excited states of rotational peaks corresponding to two-photon resonance excitation from the ground state to the $E^1\Sigma^+(v' = 0)$ (*Q* lines) (a), $V^1\Sigma^+(v' = 22)$ (*Q* lines) (b) and $I^1\Delta_2(v' = 0)$ (*O, P, Q, R, S* lines) (c) of $D^{35}Cl$ and $D^{37}Cl$ are indicated. (For interpretation of the references to colour in this figure legend, the reader is referred to the web version of this article.)

Table 3
Vibrational (band origins and spacing between v′ levels) and rotational parameters (B' and D') for (a) ion-pair and (b) Rydberg states of $D^{35}Cl$.

State	v′	ν^0/cm^{-1}		B'/cm^{-1}		D'/cm^{-1}	
		Our work	Others' work	Our work	Others' work	Our work	Others' work
(a) Rydberg states							
$E^1\Sigma^+$	0	83949.4	83944[a]	3.181	3.0	0.0004	
	1	85014		3.19		−0.0021	
	2	86823.8	86812[a]	3.40	3.7	0.0007	
	3	88667		3.58		0.01435	
$H^1\Sigma^+$	0	88689.1	88694[c]	4.620	4.658	0.00038	0.00095
$D^1\Pi_1$	0	82528.0	82525.8[b]	5.039	5.077	0.00015	0.00028
$F^1\Delta_2$	0	82908.8	82907[a]	5.136	5.195	0.00003	0.0002
	1	84737.0	84735[a]	5.043	5.447	0.00005	0.0028
	2	86511.3	86504[a]	4.928	4.934	0.00002	0.0004
	3	88227.2		4.820		0.00005	
$I^1\Delta_2$	0	88611.8		5.021		0.00015	
$d^3\Pi_1$	0	81787.5	81784[a]	5.286	5.167	0.0026	
$f^3\Delta_2$	0	82076.6	82074.2[b]	5.301	5.329	0.00031	0.00039
$f^3\Delta_1$	0	82561.0		5.115		−0.00032	
$i^3\Delta_2$	0	87678.1		5.084		0.00011	
$g^3\Sigma^-$	0	83133.6	83131[a]	4.381	4.40	−0.0013	
$j^3\Sigma^-$	0	89286.3	89287.6[c]	5.120	5.080	0.0005	0.0057
(b) $V^1\Sigma_g^+$ion-pair vibrational states							
$V^1\Sigma^+$	11	82494	82582[a]	(2.916)[d]	3		0.0099
	12	82943	82942[c]	1.792	1.822	0.0013	0.0018
	13	83390	83389[c]	1.941	2.198	−0.0047	0.0111
	14	83738	83734[a]	2.965	3.0	0.0056	
	15	84297	84294[a]	2.208	2.1	−0.0005	
	16	84666	84660[a]	2.342	2.3	0.0010	
	17	84950	84948[a]	3.417	3.1	0.0049	
	18	85478	85474[a]	2.590	2.3	0.0006	
	19	85844	85838[a]	2.049	2.1	−0.0014	
	20	86217	86217[a]	2.224	2.4	0.0015	
	21	86588	86580[a]	2.408	2.3	0.0056	
	22	87053		2.637		−0.0074	
	23	87417		2.102		0.0007	
	24	87804		1.736		−0.0017	
	25	88173		2.222		0.0043	
	26	88475		2.233		0.0039	
	27	88978		1.630		−0.0082	
	28	89242		2.653		−0.0105	

[a] Ref. [23].
[b] Ref. [35].
[c] Ref. [3].
[d] The B' value for v′(V) = 11 is "abnormally" high, which could be due to a near-degenerate interaction between the $D^1\Pi_1$(v′ = 0) and V(11) states for low J' levels.

for the v′ = 0–2 states of the $F^1\Delta_2$ Rydberg state for the v′ = 3 state (see Table 3 for ν^0 and B_v; ^{i}Cl isotope shifts of 0.4 cm^{-1}, 2.4 cm^{-1} and 5.2 cm^{-1} were derived for the v′ = 0, 1 and 2 spectra, respectively). We, therefore, assign the spectrum at ν^0 = 88 227.2 cm^{-1} to the $F^1\Delta_2$ (v′ = 3), $(\sigma^2\pi^3)4p\pi$ Rydberg state. Assuming a Morse potential and the relationship $B_v = B_e - \alpha_e(v' + ½)$ to hold [68] values of T_e = 81973.3 cm^{-1}, ω_e = 1885.1 cm^{-1}, $\omega_e x_e$ = 28.075 cm^{-1}, B_e = 5.199 cm^{-1} and α_e = 0.1083 cm^{-1} were derived for the $F^1\Delta_2$ electronic state of $D^{35}Cl$.

A relatively strong band, with a clear structure of *O, P, Q, R* and *S* lines for a Δ Ω = 2 (ΔΛ = 2) two-photon transition (i.e. $\Delta_2 \leftarrow\leftarrow \Sigma$), was observed in the region of 88 350–88 810 cm^{-1} (Fig. 2b). Only signals due to the parent molecular ion, DCl^+ were observed (see also Fig. 1c for comparison). Evaluated spectroscopic parameters are listed in Table 3. The band origin is +29.4 cm^{-1} higher than that of the $I^1\Delta_2$ (v′ = 0) state spectrum for $H^{35}Cl$ [4], typical for a hydrogen isotope shift ($\Delta\nu^0$(1, 2)) for a v′ = 0 Rydberg state. We assign the spectrum at ν^0 = 88 611.8 cm^{-1} to the $I^1\Delta_2$ (v′ = 0), $(\sigma^2\pi^3)3d\pi$ Rydberg state.

A relatively strong band, also with a clear structure of *O, P, Q, R* and *S* lines for a Δ Ω = 2 (ΔΛ = 2) two-photon transition, was observed in the region of 87 500–87 850 cm^{-1} (Fig. 2c). Only signals due to the parent molecular ion, DCl^+ were observed. Evaluated spectroscopic parameters are listed in Table 3. The band origin is +21.1 cm^{-1} higher than that of the $i^3\Delta_2$ (v′ = 0) state spectrum for $H^{35}Cl$ [4]. We, therefore, assign the spectrum at ν^0 = 87 678.1 cm^{-1} to the $i^3\Delta_2$ (v′ = 0), $(\sigma^2\pi^3)3d\pi$ Rydberg state.

A new band was observed in the two-photon wavenumber region of 84 790–85 000 cm^{-1} showing only weak *Q* lines analogous to that found for $E(0)$ (see Fig. 1a) [62]. Signals due to the parent molecular ion, DCl^+ and to a lesser extent, the fragment ions, D^+ and Cl^+ were observed, which is typical for a mixing of the Rydberg state with the $V^1\Sigma^+$ ion-pair state due to a strong homogeneous (Δ Ω = 0) interaction [10,15,16,18–20,30]. Assuming the lowest J' level peak, observed, to be J' = 3, the spectroscopic parameters listed in Table 3 were derived. The proximity of the $V^1\Sigma^+$(v′ = 17) state (ν^0 = 84 950 cm^{-1}; $\Delta\nu^0$ = 64 cm^{-1}) makes it a likely candidate for the strongly interacting state. An enhanced energy gap between the V(v′ = 17) and V(v′ = 18) states in the series of ion-pair vibrational states (see Fig. 3a and the section below) is a further indication of a homogeneous interaction analogous to that observed between the $E^1\Sigma^+$(v′) and $V^1\Sigma^+$(v′) states for HCl [10,15,18,69,70]. We, therefore, assign the spectrum at ν^0 = 85 014 cm^{-1} to the $E^1\Sigma^+$(v′ = 1), $(\sigma^2\pi^3)4p\pi$ Rydberg state.

A new, very weak band is observed in the two-photon wavenumber region of 88 590–88 670 cm^{-1} showing only weak *Q* lines (Fig. 2d) [62]. Both signals due to the parent molecular ion, DCl^+ and the fragment ion, Cl^+ are observed. Assuming the lowest J' level peak, observed, to be J' = 1, the spectroscopic parameters listed in Table 3 were derived. The proximity of the $V^1\Sigma^+$(v′ = 26)

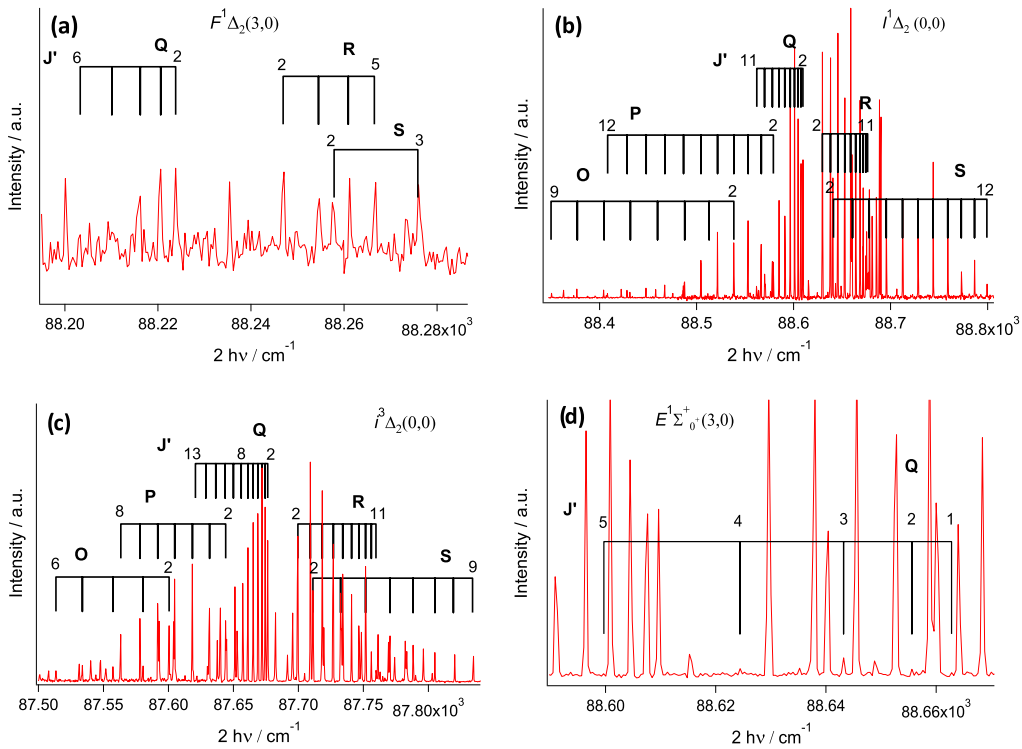

Fig. 2. REMPI spectra of mixtures of D^{i}Cl(g) and H^{i}Cl(g); i = 35, 37 for the ions D^{35}Cl$^+$ and ^{37}Cl$^+$ (mass 37) (see Table 2). J'-quantum numbers for the Rydberg excited states of rotational peaks corresponding to two-photon resonance excitation from the ground state to the $F^1\Delta_2(v' = 3)$ (*Q, R, S* lines) (a), $I^1\Delta_2$ ($v' = 0$) (*O, P, Q, R, S* lines) (b), $i^3\Delta_2(v' = 0)$ (*O, P, Q, R, S* lines) (c) and $E^1\Sigma^+(v' = 3)$ (*Q* lines) (d) of D^{35}Cl are indicated.

state ($\nu^0 = 88\,475\ cm^{-1}$; $\Delta\nu^0 = 192\ cm^{-1}$) makes it a likely candidate for a strongly interacting state. An enhanced energy gap between the $V(v' = 26)$ and $V(v' = 27)$ states in the series of ion-pair vibrational states (see Fig. 3a and the section below) is a further indication of a homogeneous interaction. We, therefore, assign the spectrum at $\nu^0 = 88\,667\ cm^{-1}$ to the $E^1\Sigma^+(v' = 3)$, $(\sigma^2\pi^3)4p\pi$ Rydberg state.

3.2. Spectra due to two-photon resonance transitions to ion-pair states and state interactions

Signals of DCl$^+$ as well as D$^+$ and Cl$^+$ for *Q* lines, only, due to transitions to $V(v')$, previously detected in absorption ($v' = 12$–21) [3] and REMPI ($v' = 14$–21) [23,25] were identified (Fig. 1b) [62] and analysed to give spectroscopic parameters in good agreement with values derived before (Table 3). In addition analogous signals due to transitions to $V(v')$; $v' = 11$, 22–28 were observed, assigned and analysed to give ν^0, $B_{v'}$ and $D_{v'}$ values for D^{35}Cl (Table 3). Fig. 3a–c shows the band origins for D^{35}Cl along with the corresponding energy levels for H^{35}Cl [4], and plots of the vibrational energy level spacings ($\Delta\nu^0(v' + 1, v')$) (a), values of $B_{v'}$ (b) and isotope shifts ($\Delta\nu^0(35, 37)$) (c) as a function of energy/v' tilted to the right (DCl) and left (HCl). All the plots in Fig. 3a–c show irregular structures for high v's of about $v' > 11$ for DCl and $v' > 8$ for HCl, for analogous energy thresholds in both cases. The irregularities in the $\Delta\nu^0(v' + 1, v')$ (a) and $B_{v'}$ (b) values observed for HCl have been explained to be due to an interaction, repulsive in nature, between *E* and *V* rovibrational states of same J' quantum numbers [9]. This is according to a level-to-level interaction between states, which depends on the interaction strength ($W_{E,V}$) and the energy gap between the corresponding levels ($\Delta E_{E,V}(J') = E_E(J') - E_V(J')$), which results in a shift of the energy level for the *V* state ($\Delta E_V(J') = E_V(J') - E^0{}_V(J')$) according to [17,68],

$$\Delta E_V(J') = (1/2)(\Delta E_{E,V}(J') - ((\Delta E_{E,V}(J'))^2 - 4(W_{E,V})^2)^{1/2} \quad (1)$$

where E^0 and E are the unperturbed and perturbed energies, respectively.

Vibrational energy level spacing vs. v' (Fig. 3a): The vibrational energy level spacing ($\Delta\nu^0(v' + 1, v')$) as a function of energy/v' for $V(v'(V))$ in the case of $v'(V) \approx 1$–12 for DCl is found to decrease almost linearly with $v'(V)$ as to be expected for an unperturbed state/Morse potential [68]

$$\Delta\nu^0(v' + 1, v') = \omega_e - 2\omega_e x_e(v' + 1) \quad (2)$$

analogous to that found for HCl in the case of $v'(V) \approx 4$–10. Irregularities, on the other hand, are observed for higher energies/$v'(V)$ (see Fig. 3a). As for HCl the irregularities observed for DCl we believe to be mostly due to a homogeneous interaction between the $E^1\Sigma^+((\sigma^2\pi^3)4p\pi)$ Rydberg state and the $V^1\Sigma^+(\sigma^1\pi^4\sigma^{*1})$ ion-pair state, resulting in a repulsion of rovibrational energy levels with same J' quantum numbers, inversely proportional to the energy differences. This appears as shift of vibrational and rotational energy levels of the interacting states as well as the corresponding spectral lines [9,10]. Thus, enhanced energy gaps appear between $v'(V) = 14$ and 15, 17 and 18, 21 and 22 as well as 26 and 27 due to the interactions with the $E(0)$, $E(1)$, $E(2)$ and $E(3)$ states, respectively, analogous to those observed between $v'(V)$

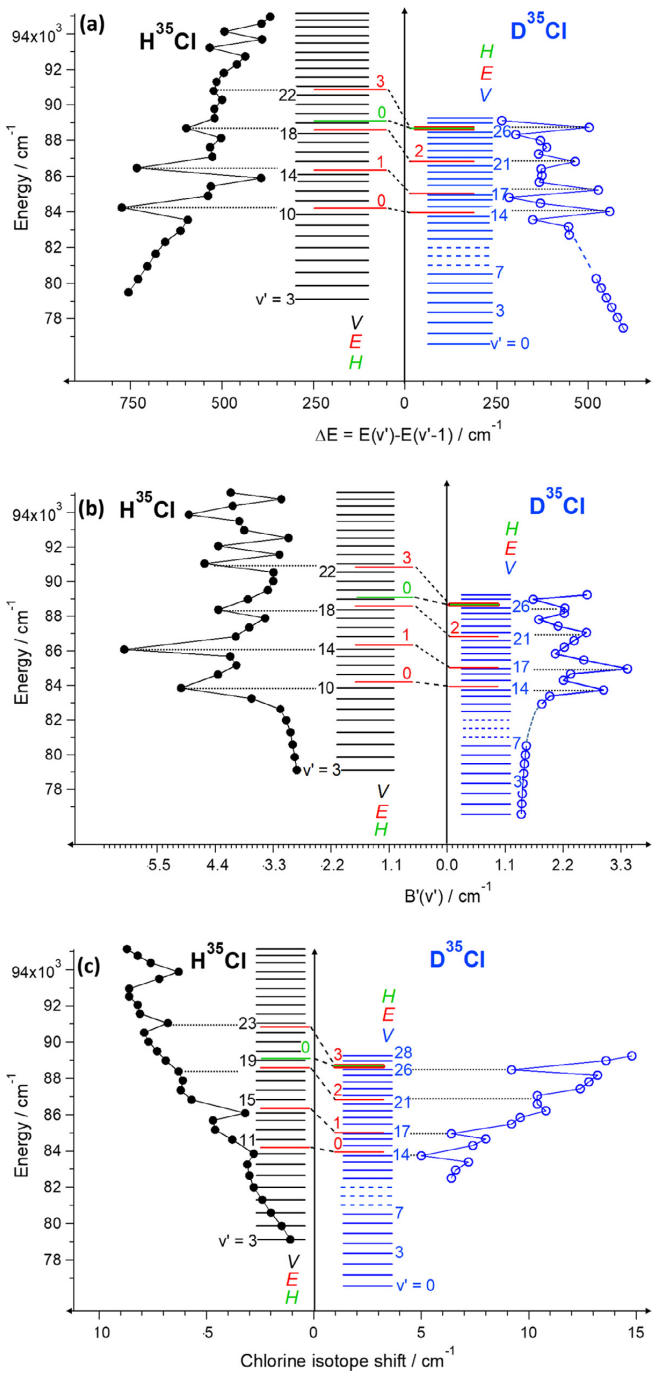

Fig. 3. $D^{35}Cl$ and $H^{35}Cl$: Vibrational energy levels for the $E^1\Sigma^+$ (red), $H^1\Sigma^+$ (green) and $V^1\Sigma^+$ (blue ($D^{35}Cl$); black ($H^{35}Cl$)) states as well as vibrational energy level spacing ($\Delta\nu^0(v'+1, v') = \nu^0(v'+1) - \nu^0(v')$; cm^{-1}) (a), rotational constants ($B_{v'}$) (b) and chlorine isotope shifts ($\Delta\nu^0(35, 37) = \nu^0(35; v', v''=0) - \nu^0(37; v', v''=0)$) (c) as a function of v' for the $V^1\Sigma^+$ states of $D^{35}Cl$ (blue curves tilted to the right) and $H^{35}Cl$ (black curves, tilted to the left). The energies (cm^{-1}; y-axis) are normalized to a zero value for the ground state $v''=0$ level for $D^{35}Cl$. Notice that the scales for $\Delta\nu^0(v'+1, v')$ (a), $B_{v'}$ (b) and $(\Delta\nu^0(35, 37)$ (c) are directed to left for HCl and to right for DCl. Values for HCl are derived from Ref. [4]. Values relevant to $v'(V) = 0$–7 for DCl are from Ref. [24]. Broken lines relevant to $v'(V) = 8$–10(11) (DCl) are guess values. Values relevant to $v'(V) = 11$–28 (DCl) are from this work. Levels for the Rydberg states of DCl are from this work. v'quantum numbers are indicated. (For interpretation of the references to colour in this figure legend, the reader is referred to the web version of this article.)

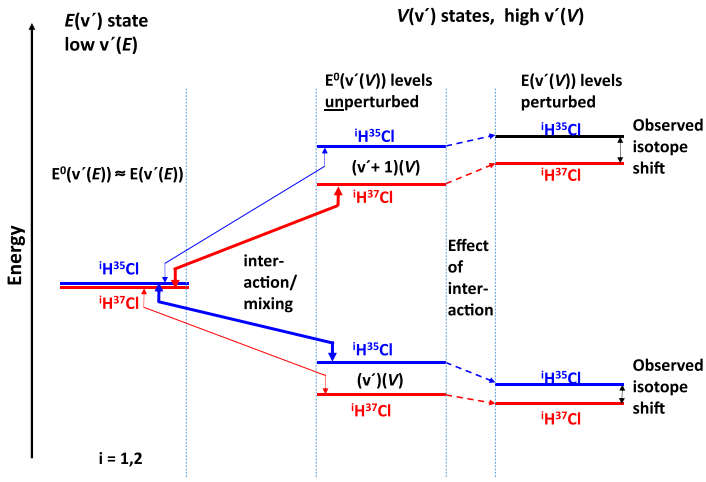

Fig. 4. Effect of interactions between $E(v')$ states and $V(v'+1)$ and $V(v')$ states on chlorine isotope shifts ($\Delta\nu^0(35, 37)$) for zero order energies (E^0) as, $E^0((v'+1)(V)) > E^0(v'(E)) > E^0(v'(V))$. $^iH^{35}Cl$ are in blue and $^iH^{37}Cl$ in red. Horizontal levels are energy levels, boldness of which indicates strength of mixing/repulsion effect. Double arrows represent repulsion interactions and single arrows represent effect of interactions. $v'(E)$ and $v'(V)/(v'+1)(V)$ are vibrational states of the E and V electronic states, respectively.

= 10 and 11, 14 and 15, 18 and 19 as well as 22 and 23 due to the interactions with the $E(v')$; $v' = 0$–3 states for HCl. It is worth noting that, by analogy to observations for HCl, corresponding interaction effects are believed to be negligible due to the $H^1\Sigma^+((\sigma^2\pi^3)3d\pi)$ Rydberg state (see Fig. 3a for $H(0)$).

Rotational constants vs. $v'(V)$ (Fig. 3b): Vibrational state rotational constants ($B_{v'}$) for an unperturbed electronic state/Morse potential are expected to decrease linearly with v' [68]

$$B_{v'} = B_e - \alpha_e(v' + 1) \tag{3}$$

However, the values for the low $v'(V)$ are found to increase gradually for $v'(V) = 0$–7 and to show irregularity as a function of $v'(V)$ for $v'(V) > 11$ (see Fig. 3b). Analogous effects are observed for HCl. The major effects, most likely, also are due to the above mentioned homogeneous interaction between the $E(v')$ and $V(v')$ states. Effectively it results in an expansion of the $V(v')$ states rotational levels and compression of those for the $E(v')$ states, hence an increase and decrease in the corresponding rotational constants, respectively [9,10]. This effect is inversely proportional to the energy differences between the interacting levels. Thus, the maxima in the $B_{v'}$ vs. $v'(V)$ plot for DCl for $v'(V) = 14$, 17, 22 and 26 (25) (see Fig. 3b) are indicative of the largest mixing of those vibrational states with $E(0)$, $E(1)$, $E(2)$ and $E(3)$, respectively. Lowering in the $B_{v'}$ values for the $v'(V)$ states on both sides (higher and lower in energy), as observed, is a consequence of a decreasing mixing with energy difference.

Chlorine isotope shift vs. $v'(V)$ (Fig. 3c): To a first approximation the chlorine isotope shift ($\Delta\nu^0(35, 37)$) for $^iH^{35}Cl$ and $^iH^{37}Cl$; i = 1, 2, is expected to increase linearly with v' for an unperturbed state/Morse potential [66,67]

$$\Delta n^0(35,37) = \nu^0(35; v', v'' = 0) - \nu^0(37; v', v'' = 0); \tag{4a}$$

$$\Delta\nu^0(35,37) \approx [\omega'_e(35)(v' + 1/2) - \omega'_e(35)(1/2)][1 - \rho(35,37)] \tag{4b}$$

$$\rho(35,37) = \sqrt{\mu_{37}/\mu_{35}} \tag{4c}$$

where $\nu^0(35; v', v'' = 0)$ and $\nu^0(37; v', v'' = 0)$ are the band origins for the two isotopologues, $\omega'_e(35)$ and $\omega''_e(35)$ are the vibrational frequencies (in cm^{-1}) of $^iH^{35}Cl$ for the excited and ground states, respectively. μ_{37} and μ_{37} are the reduced masses of the isotopologues. The plots of $\Delta\nu^0(35, 37)$ vs. $v'(V)$, both for DCl and HCl (Fig. 3c), however, show clear deviations from increasing linearities. Dips in the plots show close correlation with the corresponding observations (increases) for the vibrational energy level spacing ($\Delta\nu^0(v' + 1, v')$) (Fig. 3a) and rotational constants ($B_{v'}$) (Fig. 3b), which were interpreted as being due to the interactions with the $E(v')$ states above. Thus, for example, the lowering in the values of $\Delta\nu^0(35, 37)$ for $v'(V) = 14$, 17, 22(21) and 26 for DCl and of $v'(V) = 10$, 14, 18(17) and 23 for HCl match the enhanced values observed for $B_{v'}$. This can be explained to be due to a different degree of repulsion between $E(v')$ and $V(v')$ levels, for equal J' values ($\Delta E_{J'}$) for $D^{35}Cl$ ($H^{35}Cl$) and $D^{37}Cl(H^{37}Cl)$ levels associated with different spacing between the levels as shown in Fig. 4. Thus, a $v'(V)$ level of $^iH^{35}Cl$ (higher in energy than a $v'(V)$ level for $^iH^{37}Cl$), experiences larger downward energy shift than a $v'(V)$ level for $^iH^{37}Cl$ in the case when the $v'(V)$ levels are lower in energy than the interacting $v'(E)$ state, whereas a $(v' + 1)(V)$ level of $^iH^{35}Cl$, experiences less upwards energy shift than a $(v' + 1)(V)$ level for $^iH^{37}Cl$ in the case when the $v'(V)$ levels are higher in energy than the interacting $v'(E)$ state. In both cases this results in a lowering of the chlorine isotope shifts (see Fig. 3c).

4. Conclusion

Mass resolved REMPI spectra were recorded for a supersonic jet expansion of a mixture of $^iH^jCl(g)$; i = 1, 2; j = 35, 37 in argon for two-photon resonance excitation in the region of 80 500–89 500 cm^{-1}. Peaks due to resonance transitions from the ground states of D^jCl; j = 35, 37 to vibrational states of a number of Rydberg states and the ion-pair state, $V^1\Sigma^+$, depending on $J' \leftarrow\leftarrow J''$ transitions (line series) were identified and assigned. Spectral bands of the ion-pair states and the $E^1\Sigma^+$ states showed significant REMPI signals for both fragment ions (D^+, $^jCl^+$) and the parent molecular ions (D^jCl^+), whereas spectra of other Rydberg states showed very small or negligible fragment ion signals. The former is characteristic of an ion-pair character of the excited state, which, in the case of the E state is indicative of a large mixing of the E and V states due to strong homogeneous interaction. In addition to

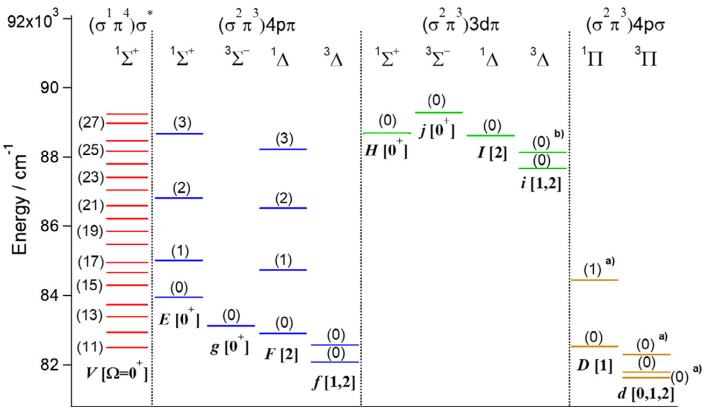

Fig. 5. Energy level diagram of known electronic states of $D^{35}Cl$ within the wavenumber range of 80 500–89 500 cm^{-1}. Vibrational quantum numbers are indicated inside brackets as (v′). Electronic states are labelled as *Y*[Ω′, ...] for characteristic letters *Y*. Electron configurations and term symbols are shown on top. Levels are from this work except those marked by (a) (from Ref. [35]) and (b) (from Ref. [3]).

number of previously observed spectral bands, five new bands due to transitions to Rydberg states and eight new bands due to transitions to vibrational states of *V* were identified and analysed. Detailed analysis resulted in values of band origin (ν^0) and effective rotational constants ($B_{v'}$ and $D_{v'}$) for $D^{35}Cl$ (see Table 3). New Rydberg states, observed, were the $F^1\Delta_2$ (v′ = 3), $I^1\Delta_2$ (v′ = 0), $i^3\Delta_2$ (v′ = 0), $E^1\Sigma^+$(v′ = 1) and $E^1\Sigma^+$(v′ = 3) states. New vibrational states of *V* ($V^1\Sigma^+$(v′)), observed, were for v′ = 11, 22–28 (see Table 3 and summary Fig. 5).

The strong homogeneous interaction between the $E^1\Sigma^+$and $V^1\Sigma^+$(v′) states appears as perturbation effects (i.e. deviation of spectroscopic parameters from regular patterns of unperturbed states) in the DCl spectra analogous to what has been found for HCl to some extent: (A) Characteristic enhancement in energy gaps between neighbouring vibrational levels of the *V* state ($\Delta\nu^0$(v′ + 1, v′)) are observed for (v′ + 1) and v′ states higher and lower in energy than *E*(v′) levels (see Fig. 3a). (B) Enhancement in rotational constants ($B_{v'}$) were observed for *V*(v′) states closest in energy to neighbouring *E*(v′) states (see Fig. 3b). (C) Lowering in chlorine isotope shifts ($\Delta\nu^0$(35, 37)) were observed for *V*(v′) states closest in energy to neighbouring *E*(v′) states (see Fig. 3c). All these observations (A-C) can be explained to be due to level-to-level interaction between *E* and *V* rovibrational states of same *J*′ quantum numbers, which appears as a repulsion between the corresponding energy levels.

The results of this paper adds to information relevant to the energetics, state interactions and fragmentation processes in the region of high energy Rydberg states of DCl. It will hopefully render further theoretical interpretation of the characteristic state interaction within the hydrogen halides [48].

Acknowledgements

The financial support of the University Research Fund, University of Iceland and an assistant teacher grant from University of Iceland for A.H. are gratefully acknowledged.

Appendix A. Supplementary material

Supplementary data associated with this article can be found, in the online version, at http://dx.doi.org/10.1016/j.jms.2017.09.002.

References

[1] S.G. Tilford, M.L. Ginter, J.T. Vanderslice, J. Mol. Spectrosc. 33 (1970) 505–519.
[2] S.G. Tilford, M.L. Ginter, A.M. Bass, J. Mol. Spectrosc. 34 (1970) 327.
[3] A.E. Douglas, F.R. Greening, Can. J. Phys. 57 (10) (1979) 1650–1661.
[4] D.S. Green, G.A. Bickel, S.C. Wallace, J. Mol. Spectrosc. 150 (2) (1991) 303–353.
[5] D.S. Green, G.A. Bickel, S.C. Wallace, J. Mol. Spectrosc. 150 (2) (1991) 354–387.
[6] D.S. Green, G.A. Bickel, S.C. Wallace, J. Mol. Spectrosc. 150 (2) (1991) 388–469.
[7] D.S. Green, S.C. Wallace, J. Chem. Phys. 96 (8) (1992) 5857–5877.
[8] D. Ascenzi, S. Langford, M. Ashfold, A. Orr-Ewing, PCCP 3 (1) (2001) 29–43.
[9] Á. Logadóttir, Á. Kvaran, H. Wang, J. Chem. Phys. 109 (14) (1998) 5856–5867.
[10] Á. Logadóttir, Á. Kvaran, H. Wang, J. Chem. Phys. 112 (24) (2000) 10811–10820.
[11] Á. Kvaran, H. Wang, J. Mol. Spectrosc. 228 (1) (2004) 143–151.
[12] K. Matthiasson, Á. Kvaran, H. Wang, A. Bodi, E. Jónsson, J. Chem. Phys. 129 (17) (2008) 164313.
[13] K. Matthiasson, Á. Kvaran, H. Wang, J. Chem. Phys. 131 (4) (2009) 044324.
[14] K. Matthiasson, H. Wang, Á. Kvaran, J. Mol. Spectrosc. 255 (1) (2009) 1–5.
[15] K. Matthiasson, J. Long, H. Wang, Á. Kvaran, J. Chem. Phys. 134 (16) (2011) 164302.
[16] J. Long, H. Wang, A. Kvaran, J. Mol. Spectrosc. 282 (2012) 20–26.
[17] J. Long, H.R. Hrodmarsson, H. Wang, A. Kvaran, J. Chem. Phys 136 (2012) 214315.
[18] J. Long, H. Wang, Á. Kvaran, J. Chem. Phys. 138 (4) (2013) 044308.
[19] H.R. Hróðmarsson, H. Wang, Á. Kvaran, J. Mol. Spectrosc. 290 (2013) 5–12.
[20] H.R. Hróðmarsson, H. Wang, Á. Kvaran, J. Chem. Phys. 140 (2014) 244304.
[21] D. Zaouris, A. Kartakoullis, P. Glodic, P.C. Samartzis, H.R. Hróðmarsson, Á. Kvaran, PCCP 17 (2015) 10468–10477.
[22] P. Glodic, D. Zaouris, P.C. Samartzis, A. Hafliðason, Á. Kvaran, PCCP 18 (2016) 26291–26299.
[23] R. Callaghan, S. Arepalli, R.J. Gordon, J. Chem. Phys 86 (10) (1987) 5273–5280.
[24] J.A. Coxon, P.G. Hajigeorgiou, K.P. Huber, J. Mol. Spectrosc. 131 (1988) 288–300.
[25] P.J. Dagdigian, D.F. Varley, R. Liyanage, R.J. Gordon, R.W. Field, J. Chem. Phys. 105 (23) (1996) 10251–10262.
[26] H.R. Hróðmarsson, H. Wang, Á. Kvaran, J. Chem. Phys. 142 (2015) 244312.
[27] R. Callaghan, R.J. Gordon, J. Chem. Phys. 93 (1990) 4624–4636.
[28] D.S. Ginter, M.L. Ginter, S.G. Tilford, J. Mol. Spectrosc. 90 (1981) 152.
[29] Y. Xie, P.T.A. Reilly, S. Chilukuri, R.J. Gordon, J. Chem. Phys. 95 (2) (1991) 854–864.
[30] C. Romanescu, H.P. Loock, J. Chem. Phys. 127 (12) (2007) 124304.
[31] R. Liyanage, R.J. Gordon, R.W. Field, J. Chem. Phys. 109 (19) (1998) 8374–8387.
[32] H. Lefebvre-Brion, M. Salzmann, H.-W. Klausing, M. Müller, N. Böwering, U. Heinzmann, J. Phys. B 22 (1989) 3891.
[33] H. Lefebvre-Brion, F. Keller, J. Chem. Phys. 90 (12) (1989) 7176–7183.
[34] A.J. Yencha, D. Kaur, R.J. Donovan, Á. Kvaran, A. Hopkirk, H. Lefebvre-Brion, F. Keller, J. Chem. Phys. 99 (7) (1993) 4986–4992.
[35] S.G. Tilford, M.L. Ginter, J. Mol. Spectrosc. 40 (1971) 568–579.
[36] J.A. Coxon, U.K. Roychowdhury, Can. J. Phys. 63 (1985) 1485–1497.
[37] R.F. Barrow, J.G. Stamper, Proc. Roy. Soc. Ser. A. 263 (1961) 259–276.
[38] J. Nee, M. Suto, L. Lee, J. Phys. B: At. Mol. Phys. 18 (1985) L293–L294.
[39] J.B. Nee, M. Suto, L.C. Lee, J. Chem. Phys. 85 (1986) 719–724.
[40] J.B. Nee, M. Suto, L.C. Lee, J. Chem. Phys. 85 (1986) 4919.
[41] T.A. Spiglanin, D.W. Chandler, D.H. Parker, Chem. Phys. Lett. 137 (5) (1987) 414–420.
[42] E.d. Beer, W.J. Buma, C.A.d. Lange, J. Chem. Phys. 99(5) (1993) 3252–3261.

[43] B.G. Waage, Á. Kvaran, H. Wang, J. Chem. Phys. 113 (5) (2000) 1755–1761.
[44] H.R. Hróðmarsson, A. Kartakoullis, D. Zaouris, P. Glodic, H. Wang, P.C. Samartzis, Á. Kvaran, PCCP 19 (18) (2017) 11354–11365.
[45] S. Kauczok, C. Maul, A.I. Chichinin, K.H. Gericke, J. Chem. Phys. 133 (2) (2010) 24301.
[46] S. Manzhos, C. Romanescu, H.P. Loock, J.G. Underwood, J. Chem. Phys 121 (23) (2004) 11802–11809.
[47] C. Romanescu, H.-P. Loock, PCCP 8 (25) (2006) 2940–2949.
[48] H. Lefebvre-Brion, H.P. Liebermann, G.J. Vázquez, J. Chem. Phys. 134 (2011) 204104.
[49] S. Engin, N. Sisourat, S. Carniato, J. Chem. Phys. 137 (2012) 154304.
[50] D.M. Hirst, M.F. Guest, Mol. Phys. 41 (6) (1980) 1483–1491.
[51] W.J. Stevens, M. Krauss, J. Chem. Phys. 77 (1982) 1368–1372.
[52] M. Bettendorff, R.J. Buenker, S.D. Peyerimhoff, J. Romelt, Z. Phys. a-Hadrons Nuclei 304 (2) (1982) 125–135.
[53] Y. Li, O. Bludsky, G. Hirsch, R.J. Buenker, J. Chem. Phys. 112 (1) (2000) 260–267.
[54] E. Jonsson, Ab initio REMPI Spectra of HCl and HF, Chemistry, University of Iceland, Reykjavik, 2008.
[55] E.F.v. Dishoeck, M.C.v. Hemert, A. Dalgarno, J. Chem. Phys. 77(7) (1982) 3693–3702.
[56] M. Bettendorff, S.D. Peyerimhoff, R.J. Buenker, Chem. Phys. 66 (1982) 261–279.
[57] E.d. Beer, B.G. Koenders, M.P. Koopmans, C.A.d. Lange, J. Chem. Soc. Faraday Trans. 86(11) (1990) 2035–2041.
[58] Á. Kvaran, H. Wang, Mol. Phys. 100 (22) (2002) 3513–3519.
[59] D.P. Shoemaker, C.W. Garland, J.W. Nibler, Experiments in Physical Chemistry, fifth ed., McGraw-Hill Book Company, 1989.
[60] W. Huasheng, J. Ásgeirsson, Á. Kvaran, R.J. Donovan, R.V. Flood, K.P. Lawley, T. Ridley, A.J. Yencha, J. Mol. Struct. 293 (1993) 217–222.
[61] Á. Kvaran, H. Wang, J. Ásgeirsson, J. Mol. Spectrosc. 163 (1994) 541–558.
[62] a.D. See supplementary material, for REMPI spectra and tables of rotational lines for Rydberg states and ion-pair states of DCl.
[63] C.M. Western, PGOPHER, a Program for Simulating Rotational Structure, C. M. Western, University of Bristol, 9.0.116 ed., University of Bristol 2003-2015. <http://pgopher.chm.bris.ac.uk>.
[64] "Constants of diatomic molecules", NIST Chemistry WebBook. <http://webbook.nist.gov/cgi/cbook.cgi?ID=C7698057&Units=SI&Mask=1000> (accessed May 2017).
[65] H.R. Hróðmarsson, 2D-REMPI of HBr: Study of Singlet and Triplet Rydberg States and the Ion-pair State, Chemistry, BS, University of Iceland, Reykjavik, 2011.
[66] G.H. Jóhannesson, H. Wang, Á. Kvaran, J. Mol. Spectrosc. 179 (1996) 334–341.
[67] Á. Kvaran, H. Wang, G.H. Jóhannesson, J. Phys. Chem. 99 (13) (1995) 4451–4457.
[68] G. Herzberg, Molecular Spectra and Molecular Structure; I. Spectra of Diatomic Molecules, second ed., Van Nostrand Reinhold Company, New York, 1950.
[69] C. Romanescu, S. Manzhos, D. Boldovsky, J. Clarke, H. Loock, J. Chem. Phys 120 (2) (2004) 767–777.
[70] A.I. Chichinin, C. Maul, K.H. Gericke, J. Chem. Phys. 124 (22) (2006) 224324.

4.3.1 Supporting information

New REMPI Observations and Analysis for Rydberg and Ion-Pair states of DCl

Arnar Hafliðason, Huasheng Wang and Ágúst Kvaran*

Science Institute, University of Iceland, Dunhagi 3, 107 Reykjavík, Iceland.

Supplementary material

Content: **pages:**

Fig. S1:

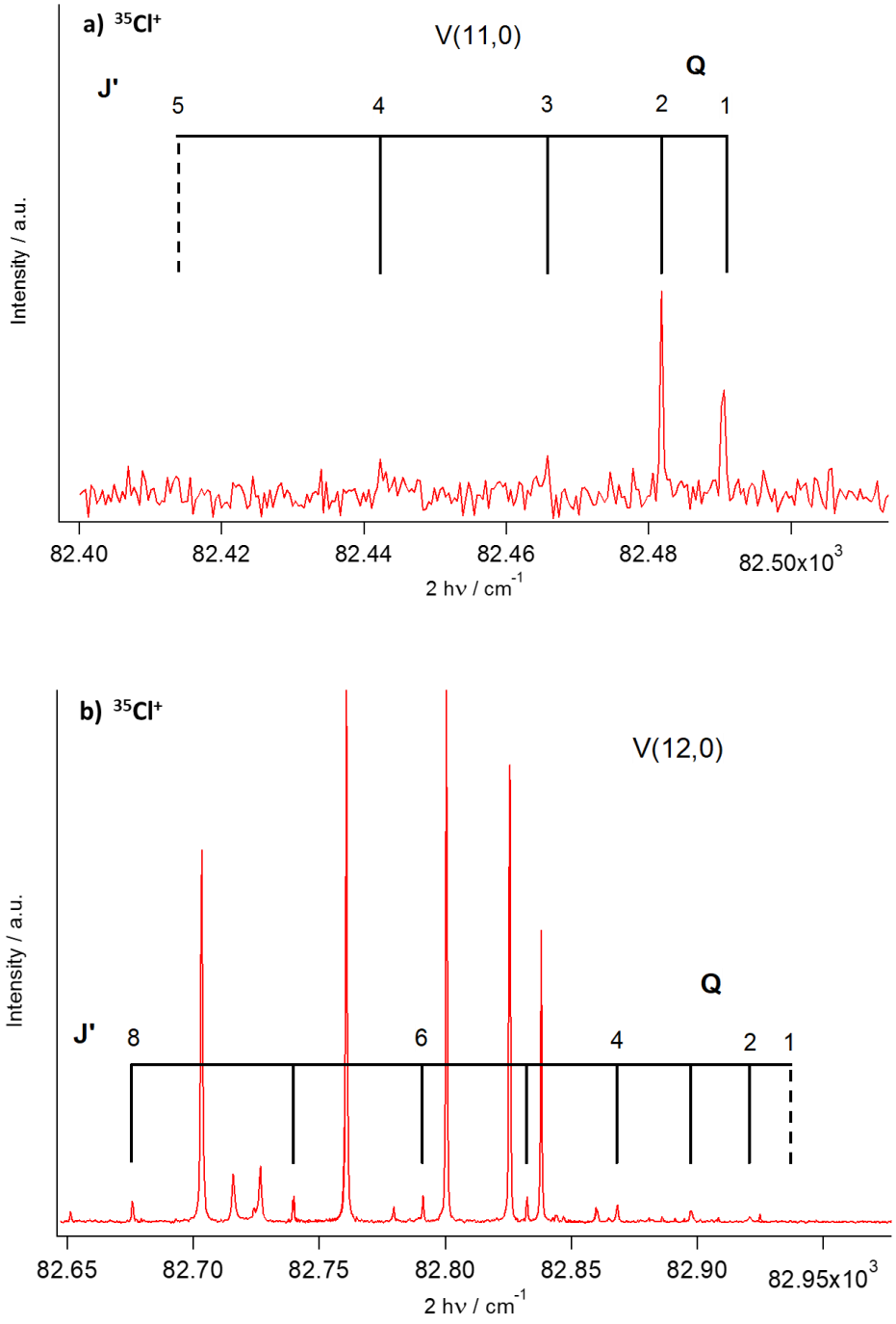
a) 35Cl+
V(11,0)
Q
J'
5
4
3
2
1
Intensity / a.u.
82.40
82.42
82.44
82.46
82.48
82.50x10^3
2 hν / cm^-1
b) 35Cl+
V(12,0)
Q
J'
8
6
4
2
1
Intensity / a.u.
82.65
82.70
82.75
82.80
82.85
82.90
82.95x10^3
2 hν / cm^-1

Fig. S1:

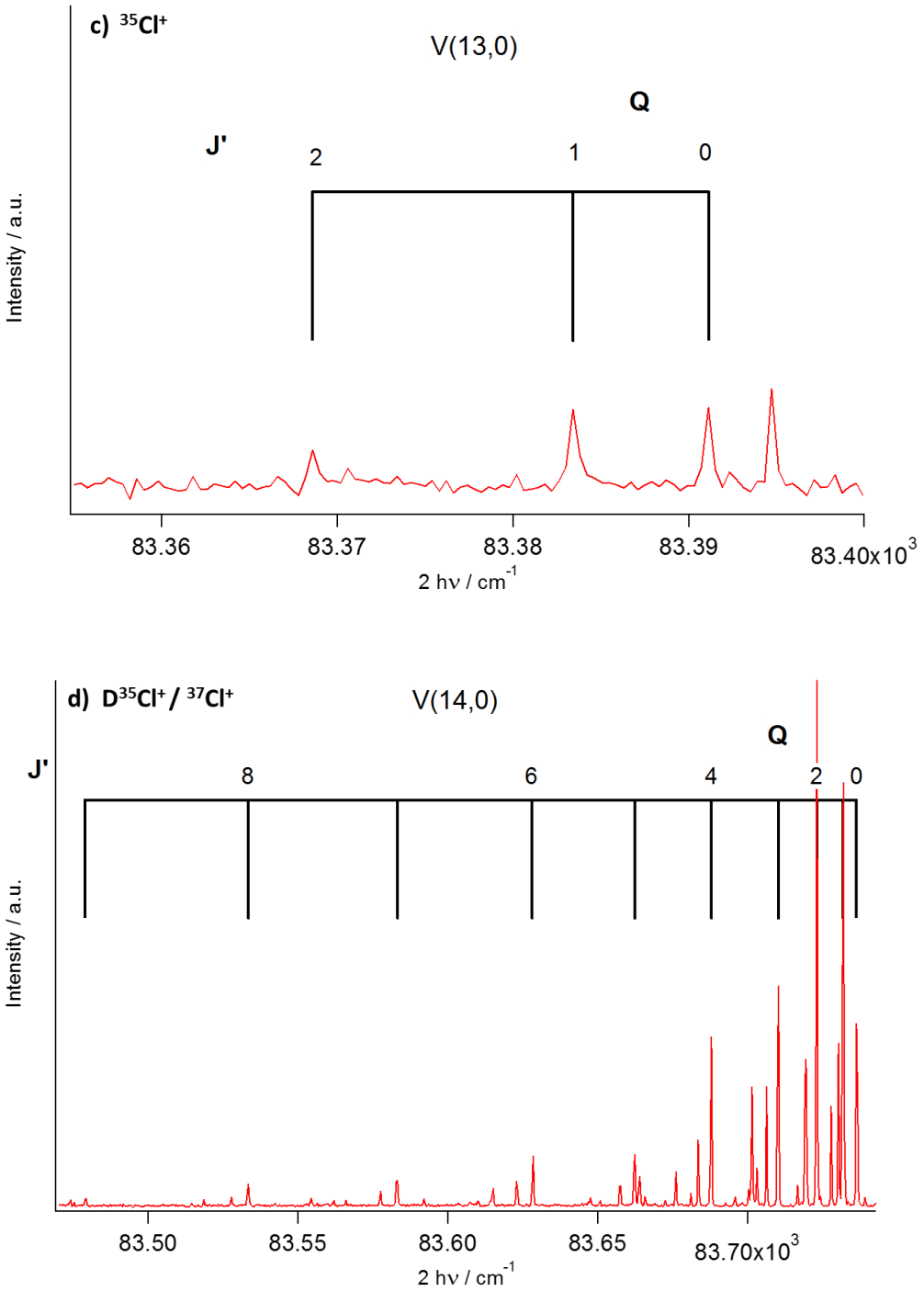
c) $^{35}Cl^+$
V(13,0)
Q
J'
2
1
0
Intensity / a.u.
83.36
83.37
83.38
83.39
83.40x10^3
2 hν / cm^{-1}
d) D$^{35}Cl^+$ / $^{37}Cl^+$
V(14,0)
Q
J'
8
6
4
2
0
Intensity / a.u.
83.50
83.55
83.60
83.65
83.70x10^3
2 hν / cm^{-1}

Fig. S1:

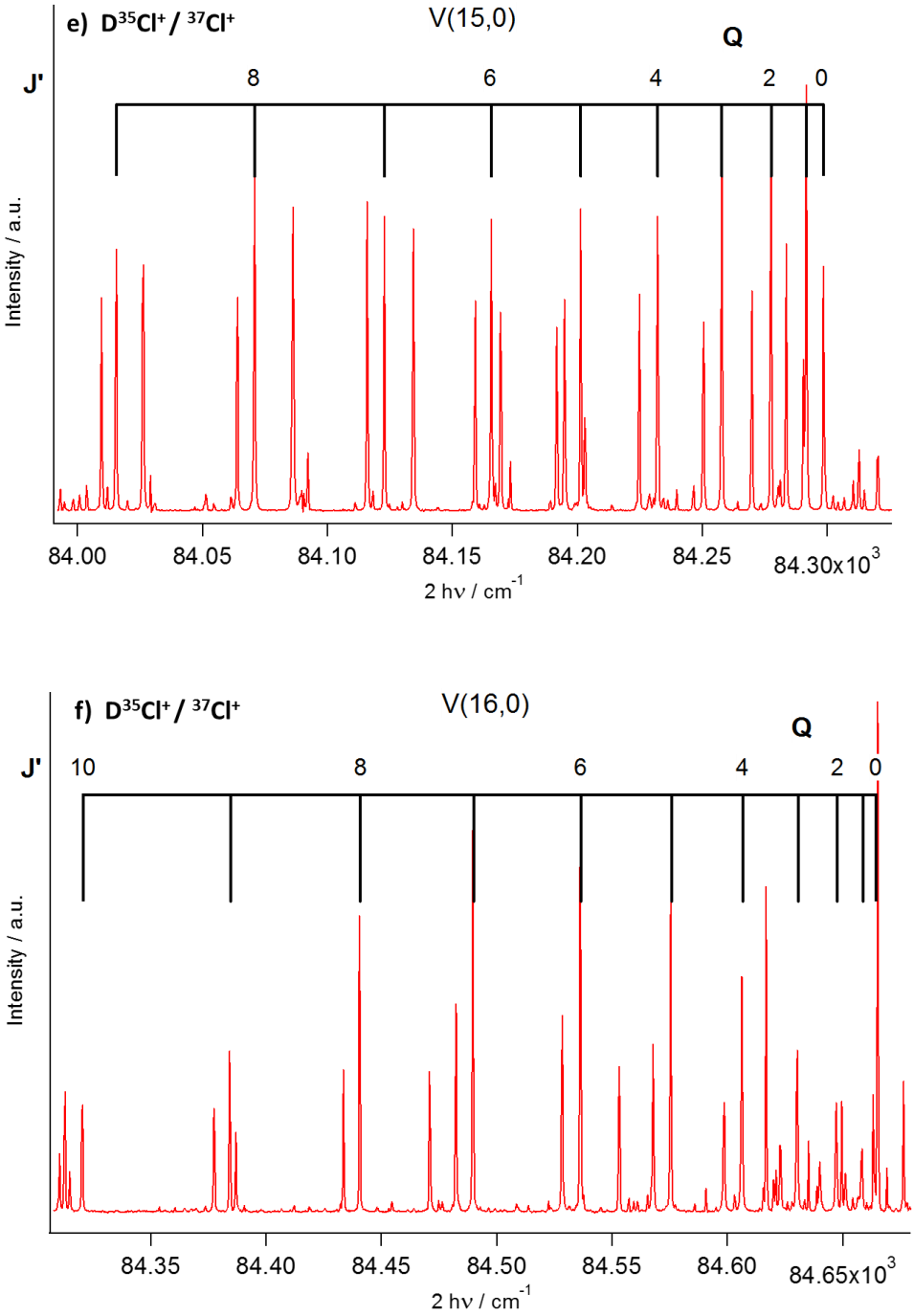
e) D35Cl+ / 37Cl+
V(15,0)
Q
J'
8
6
4
2
0
Intensity / a.u.
84.00
84.05
84.10
84.15
84.20
84.25
84.30x10^3
2 hν / cm^-1
f) D35Cl+ / 37Cl+
V(16,0)
Q
J'
10
8
6
4
2
0
Intensity / a.u.
84.35
84.40
84.45
84.50
84.55
84.60
84.65x10^3
2 hν / cm^-1

Fig. S1:

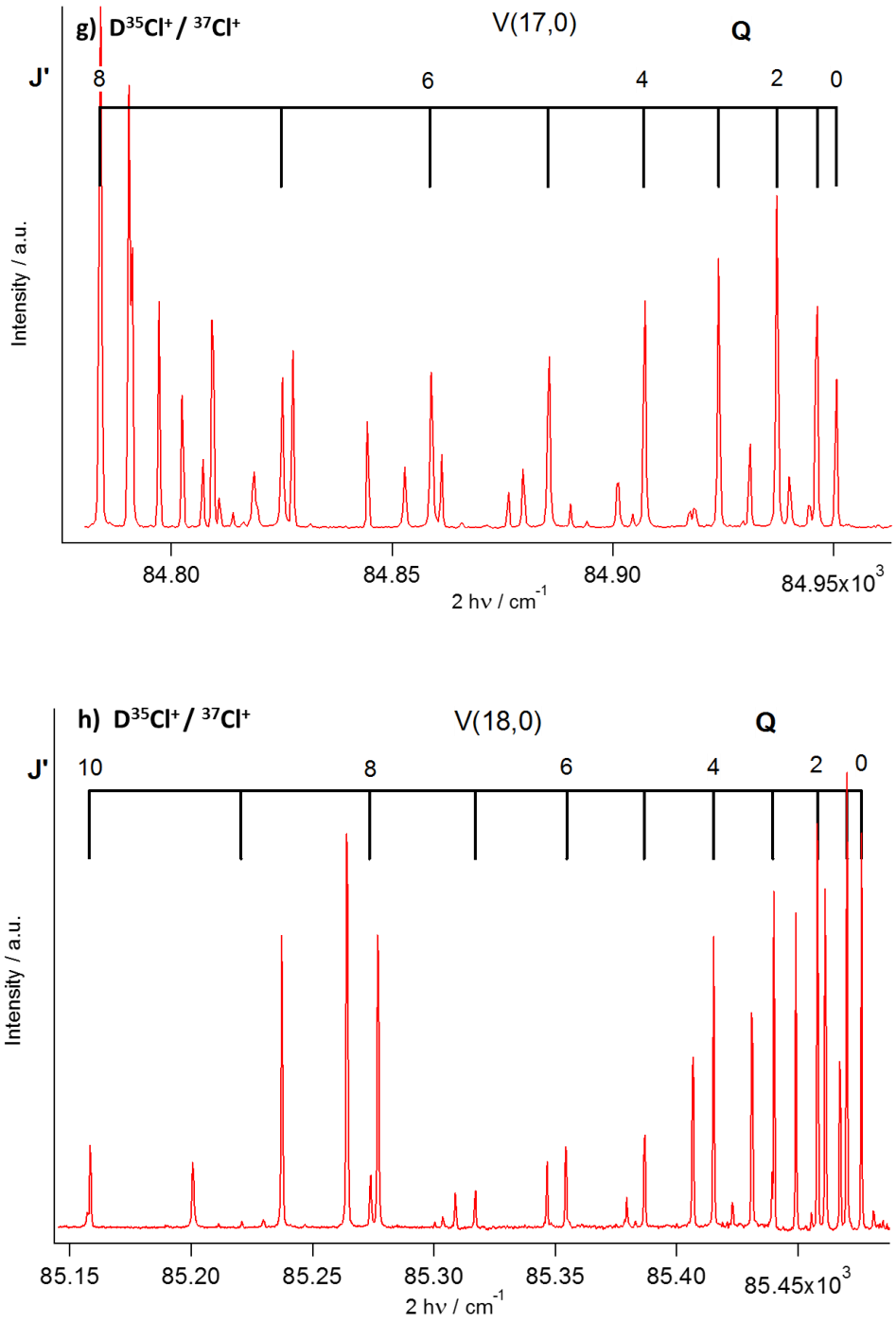
g) D35Cl+ / 37Cl+
V(17,0)
Q
J'
8
6
4
2
0
Intensity / a.u.
84.80
84.85
84.90
84.95x10^3
2 hν / cm^-1
h) D35Cl+ / 37Cl+
V(18,0)
Q
J'
10
8
6
4
2
0
Intensity / a.u.
85.15
85.20
85.25
85.30
85.35
85.40
85.45x10^3
2 hν / cm^-1

Fig. S1:

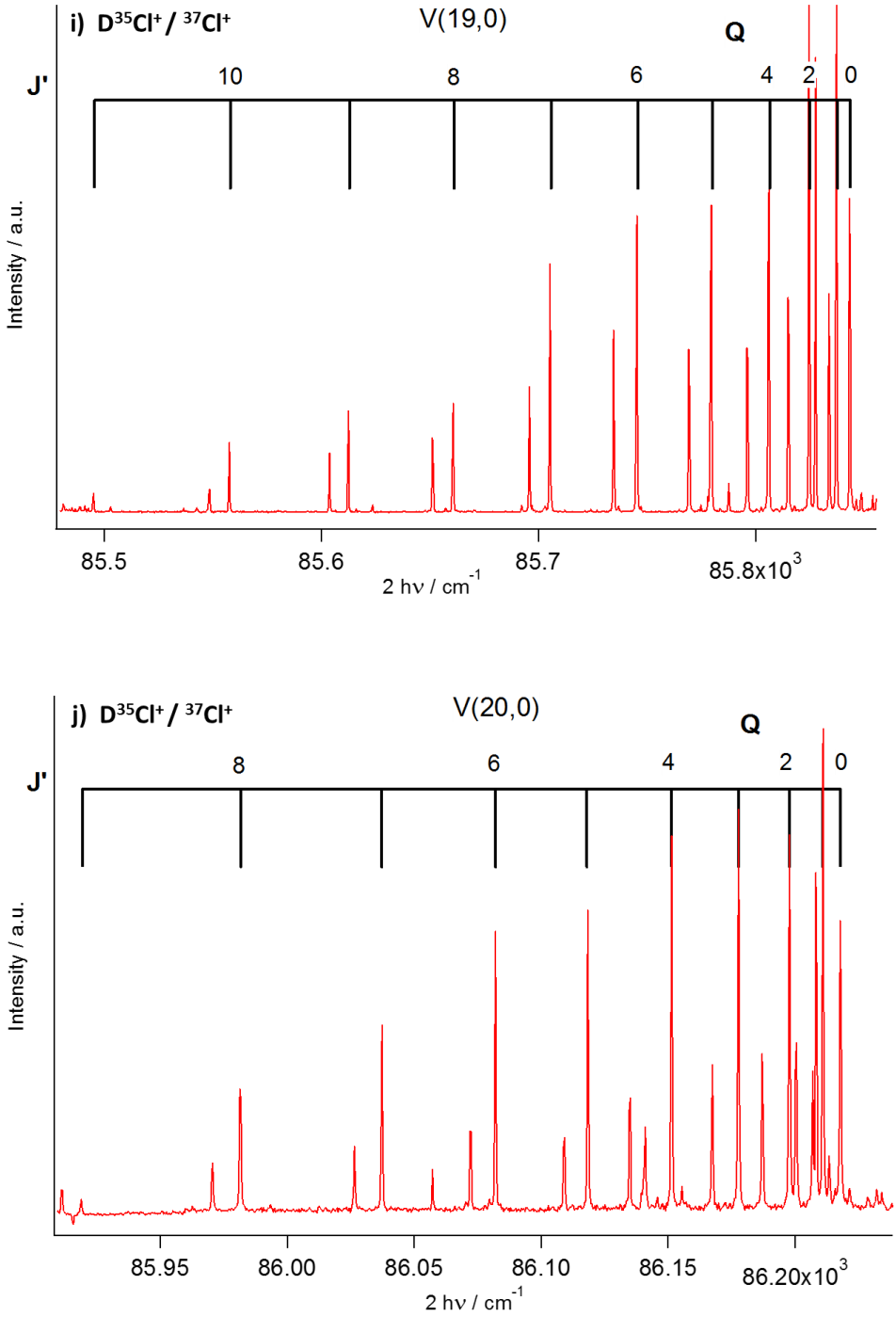
i) D35Cl+ / 37Cl+
V(19,0)
Q
J'
10
8
6
4
2
0
Intensity / a.u.
85.5
85.6
85.7
85.8x10^3
2 hν / cm^-1
j) D35Cl+ / 37Cl+
V(20,0)
Q
J'
8
6
4
2
0
Intensity / a.u.
85.95
86.00
86.05
86.10
86.15
86.20x10^3
2 hν / cm^-1

Fig. S1:

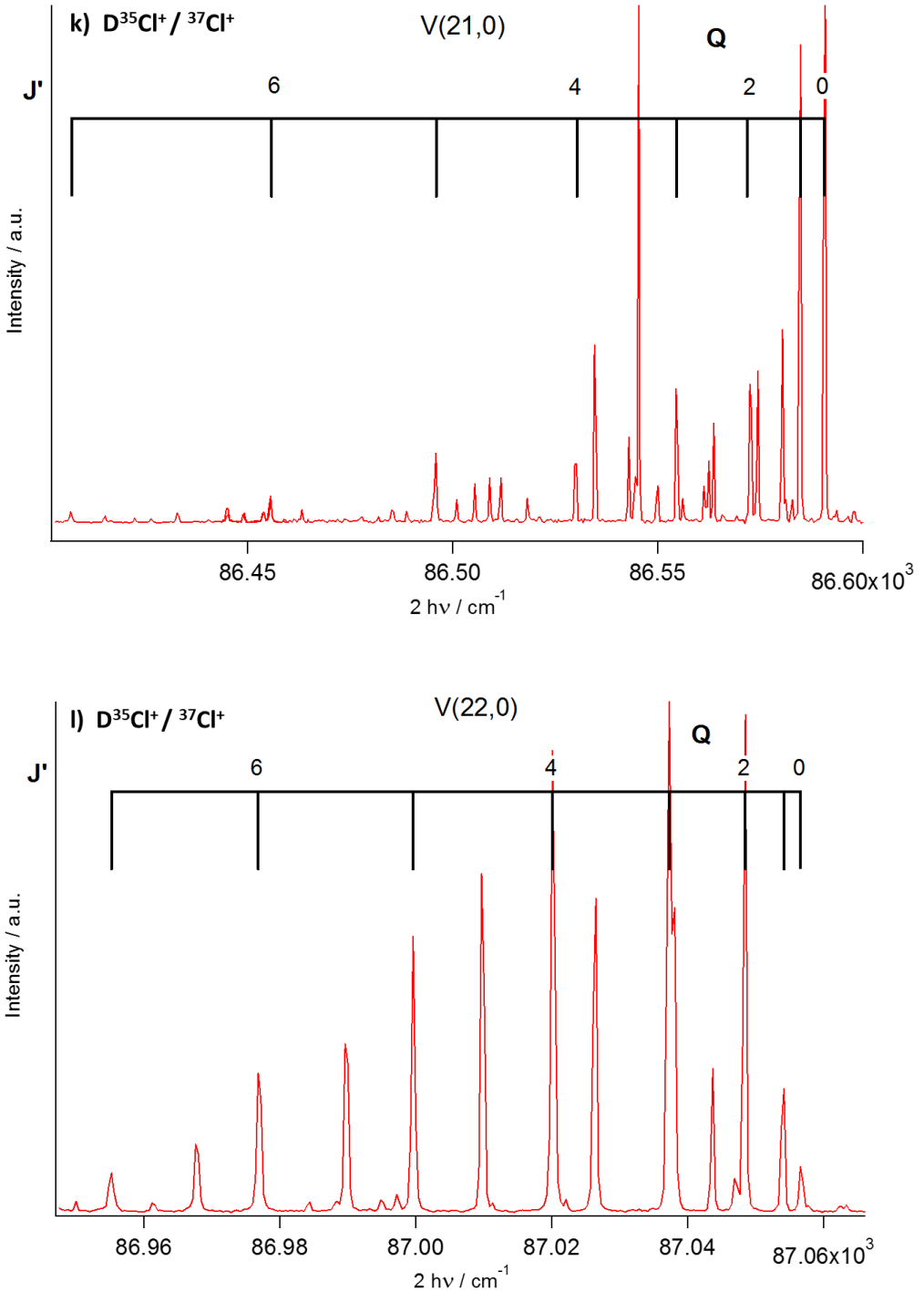
k) D35Cl+ / 37Cl+
V(21,0)
Q
J'
6
4
2
0
Intensity / a.u.
86.45
86.50
86.55
86.60x10^3
2 hν / cm^-1
l) D35Cl+ / 37Cl+
V(22,0)
Q
J'
6
4
2
0
Intensity / a.u.
86.96
86.98
87.00
87.02
87.04
87.06x10^3
2 hν / cm^-1

Fig. S1:

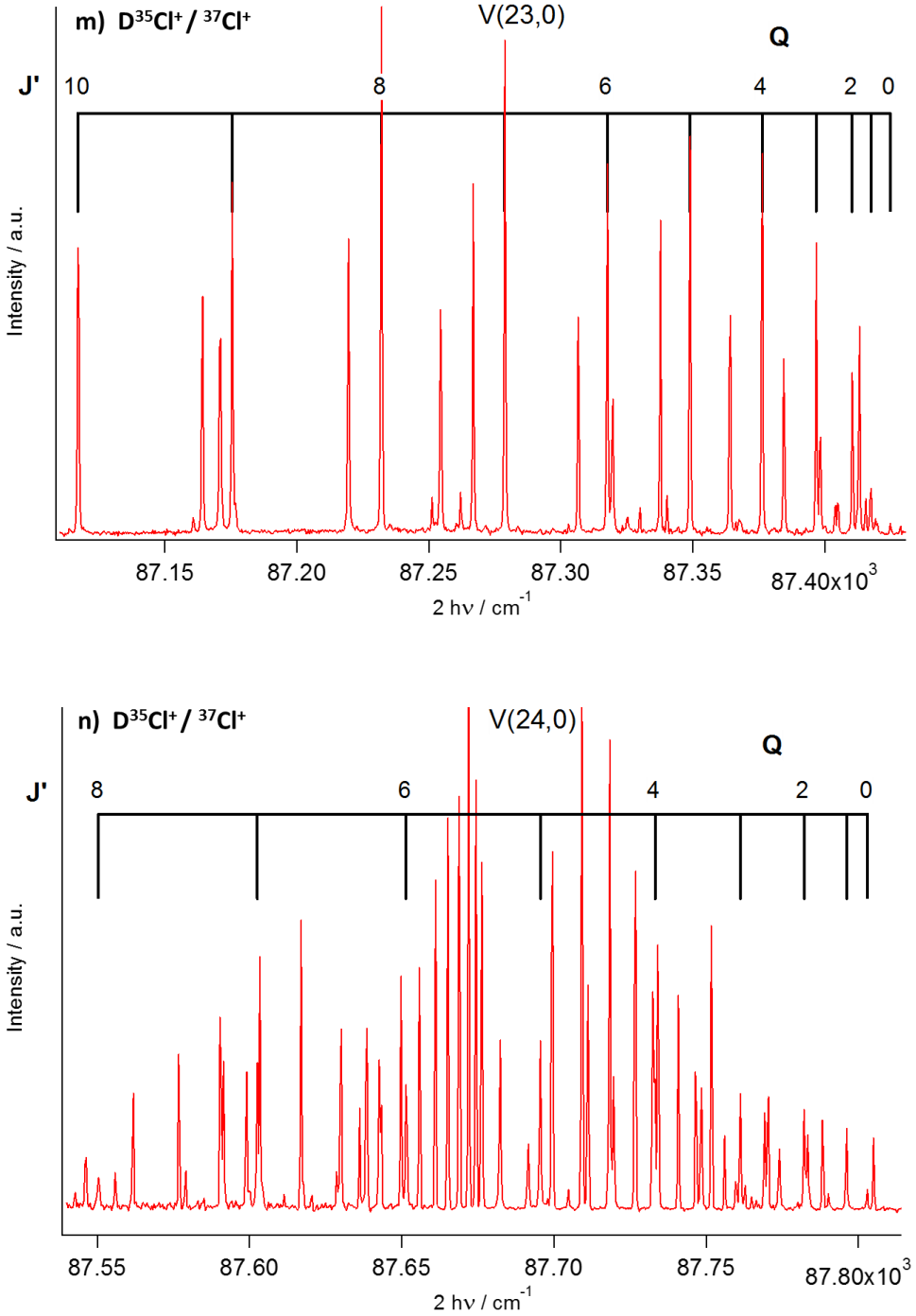
m) D35Cl+ / 37Cl+
V(23,0)
Q
J'
10
8
6
4
2
0
Intensity / a.u.
87.15
87.20
87.25
87.30
87.35
87.40x10^3
2 hν / cm^-1
n) D35Cl+ / 37Cl+
V(24,0)
Q
J'
8
6
4
2
0
Intensity / a.u.
87.55
87.60
87.65
87.70
87.75
87.80x10^3
2 hν / cm^-1

Fig. S1:

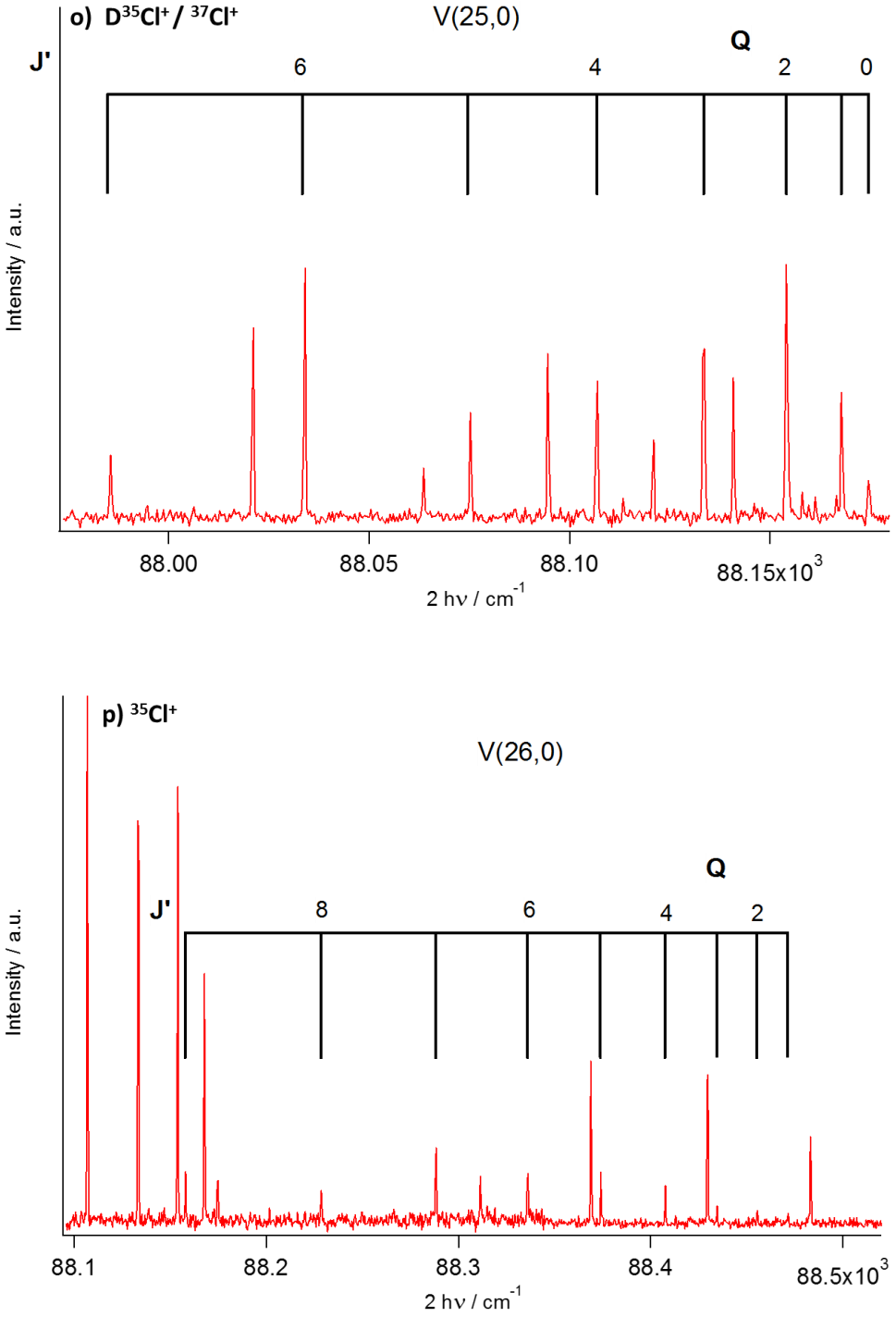
o) D35Cl+ / 37Cl+
V(25,0)
Q
J'
6
4
2
0
Intensity / a.u.
88.00
88.05
88.10
88.15x10^3
2 hν / cm^-1
p) 35Cl+
V(26,0)
Q
J'
8
6
4
2
Intensity / a.u.
88.1
88.2
88.3
88.4
88.5x10^3
2 hν / cm^-1

Fig. S1:

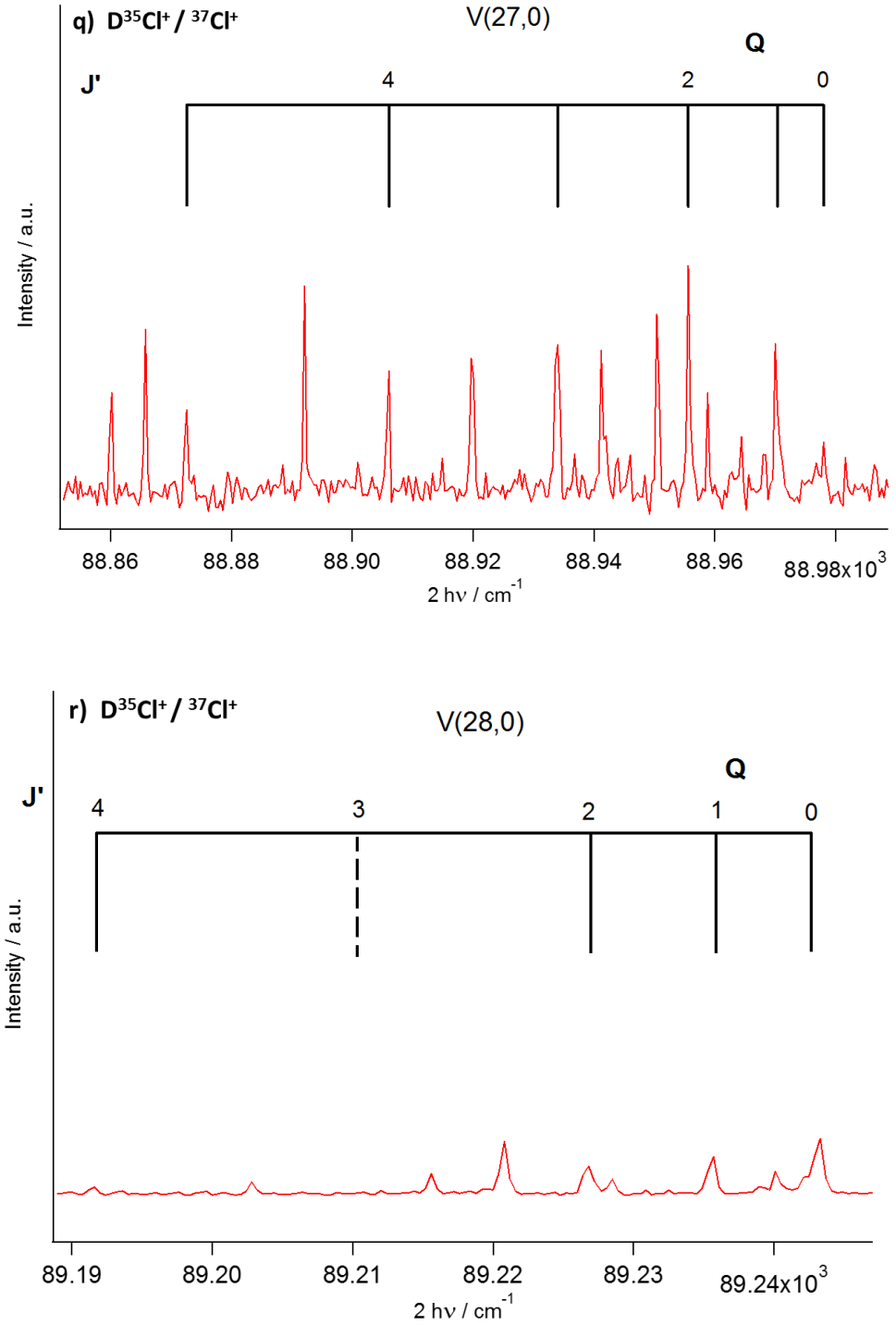
q) D35Cl+ / 37Cl+
V(27,0)
Q
J'
4
2
0
Intensity / a.u.
88.86
88.88
88.90
88.92
88.94
88.96
88.98x10^3
2 hν / cm^-1
r) D35Cl+ / 37Cl+
V(28,0)
Q
J'
4
3
2
1
0
Intensity / a.u.
89.19
89.20
89.21
89.22
89.23
89.24x10^3
2 hν / cm^-1

Fig. S2:

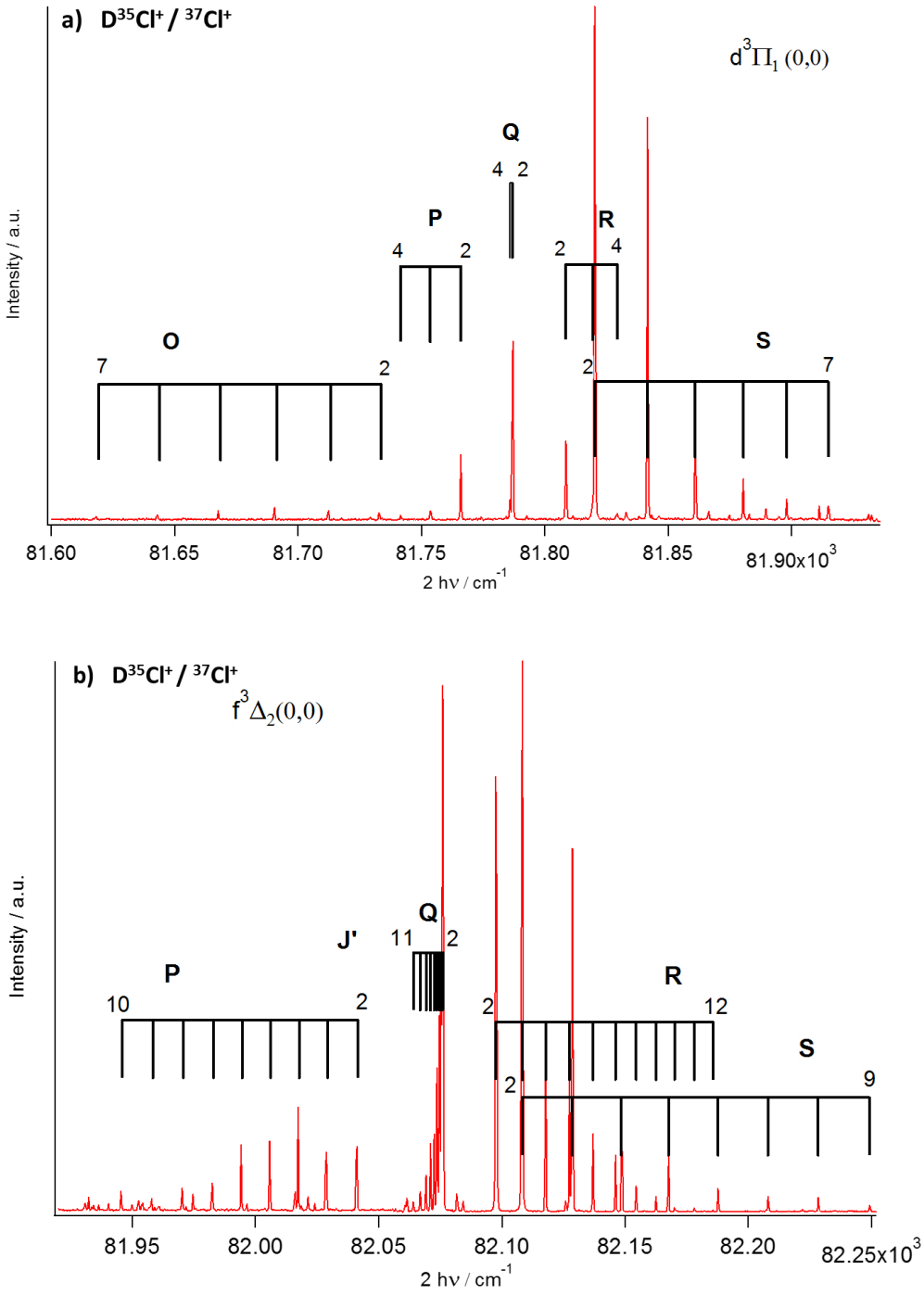
a) D35Cl+ / 37Cl+
d3Π1 (0,0)
Q
4 2
P
4 2
R
2 4
O
7 2
S
2 7
Intensity / a.u.
81.60
81.65
81.70
81.75
81.80
81.85
81.90x10^3
2 hν / cm-1
b) D35Cl+ / 37Cl+
f3Δ2(0,0)
J'
Q
11 2
P
10 2
R
2 12
S
2 9
Intensity / a.u.
81.95
82.00
82.05
82.10
82.15
82.20
82.25x10^3
2 hν / cm-1

Fig. S2:

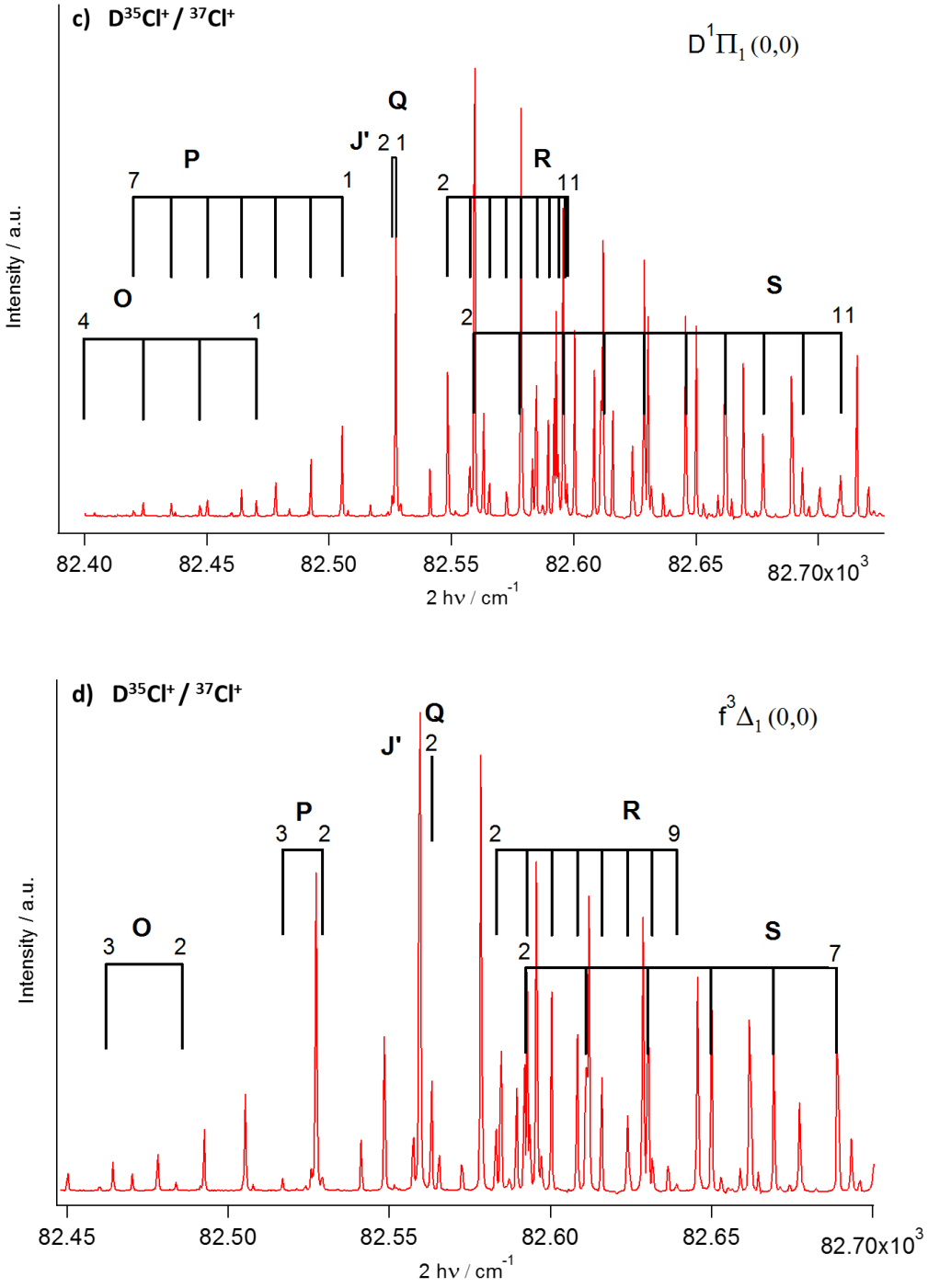
c) D35Cl+ / 37Cl+
D1Π1 (0,0)
Q
J'
2 1
P
7
1
R
2
11
O
4
1
S
2
11
Intensity / a.u.
82.40
82.45
82.50
82.55
82.60
82.65
82.70x10^3
2 hν / cm-1
d) D35Cl+ / 37Cl+
f3Δ1 (0,0)
Q
J'
2
P
3
2
R
2
9
O
3
2
S
2
7
Intensity / a.u.
82.45
82.50
82.55
82.60
82.65
82.70x10^3
2 hν / cm-1

Fig. S2:

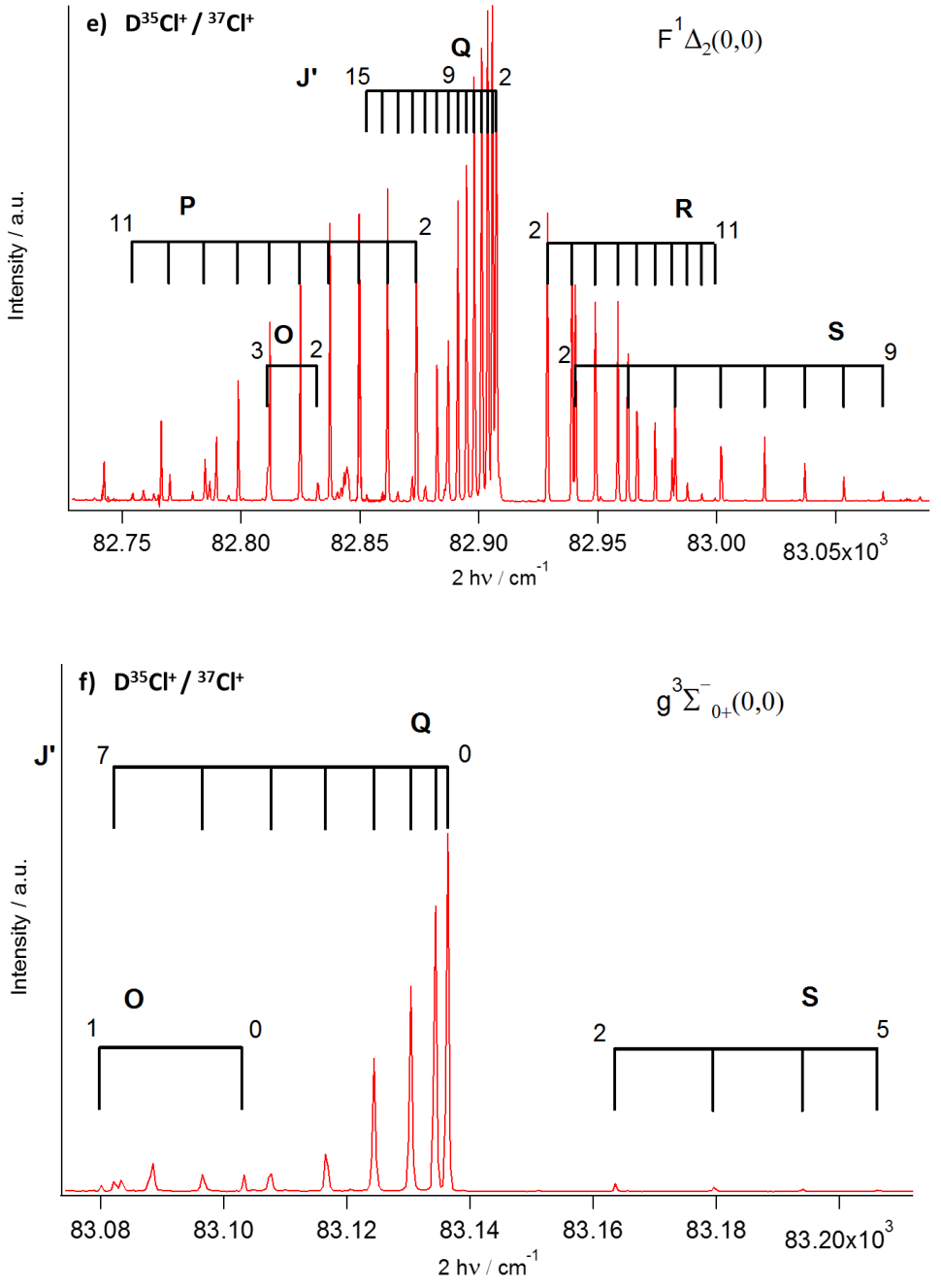
e) D35Cl+ / 37Cl+
F 1Δ2(0,0)
Q
J'
15
9
2
P
11
2
R
2
11
O
3
2
S
2
9
Intensity / a.u.
82.75
82.80
82.85
82.90
82.95
83.00
83.05x10^3
2 hν / cm-1
f) D35Cl+ / 37Cl+
g 3Σ−0+(0,0)
Q
J'
7
0
O
1
0
S
2
5
Intensity / a.u.
83.08
83.10
83.12
83.14
83.16
83.18
83.20x10^3
2 hν / cm-1

Fig. S2:

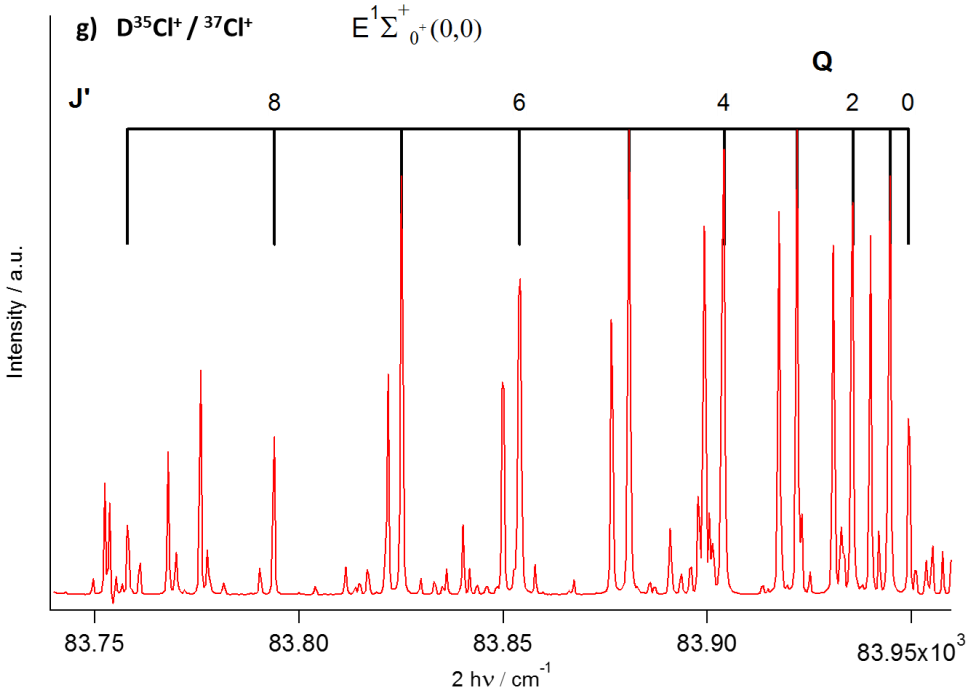
g) D35Cl+ / 37Cl+
E1Σ+0+(0,0)
J'
Q
8
6
4
2
0
Intensity / a.u.
83.75
83.80
83.85
83.90
83.95x10^3
2 hν / cm-1

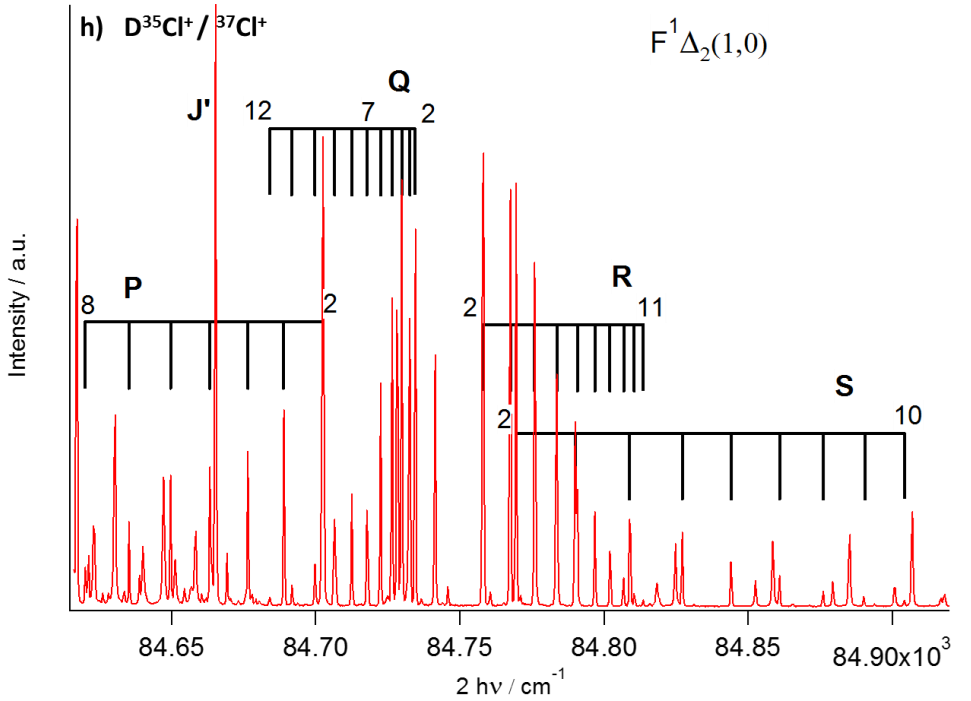
h) D35Cl+ / 37Cl+
F1Δ2(1,0)
J'
Q
12
7
2
P
8
2
R
2
11
S
2
10
Intensity / a.u.
84.65
84.70
84.75
84.80
84.85
84.90x10^3
2 hν / cm-1

Fig. S2:

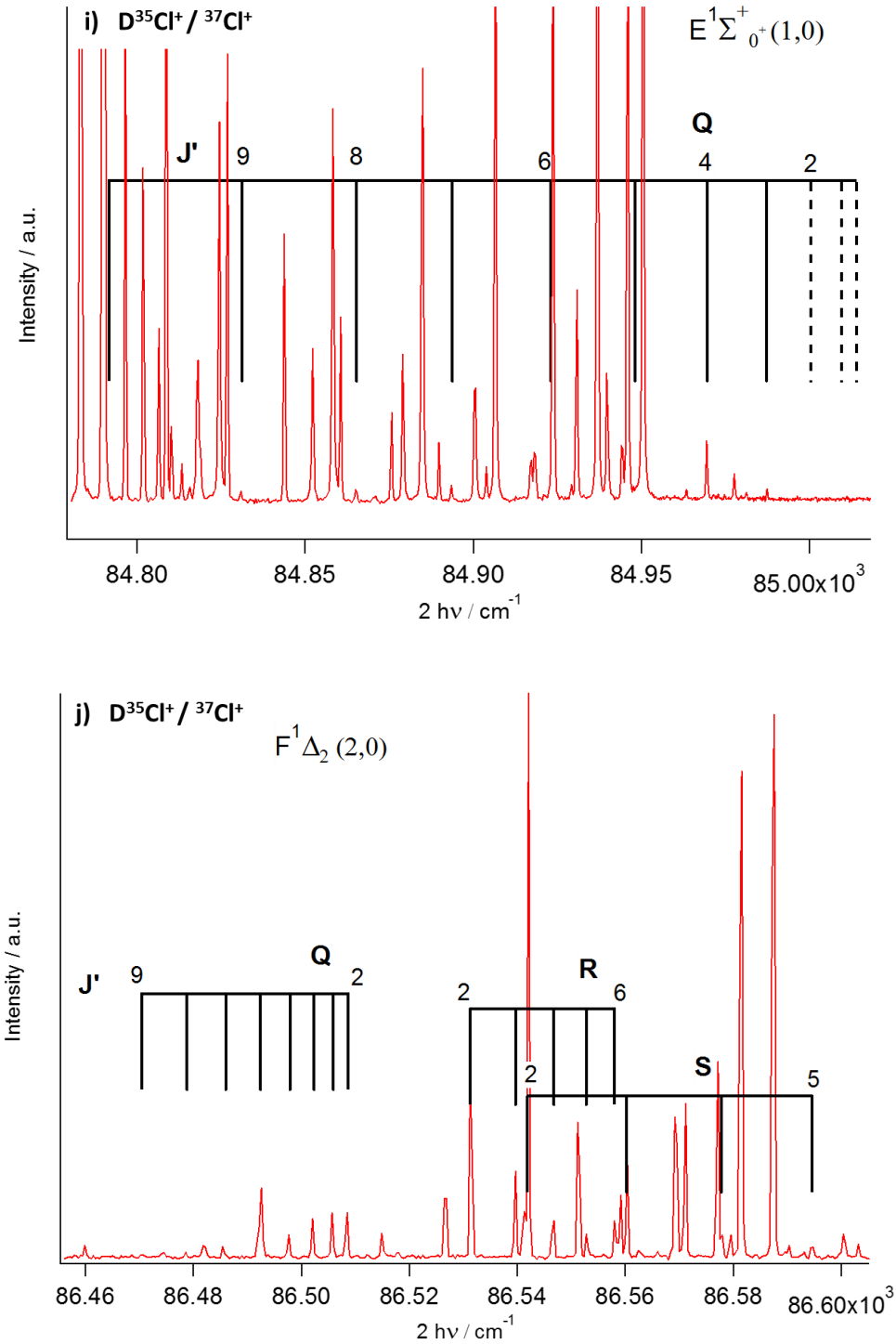
i) D35Cl+ / 37Cl+
E 1Σ+ 0+ (1,0)
Q
J'
9
8
6
4
2
Intensity / a.u.
84.80
84.85
84.90
84.95
85.00x10^3
2 hν / cm^-1
j) D35Cl+ / 37Cl+
F 1Δ2 (2,0)
J'
9
Q
2
R
2
6
2
S
5
Intensity / a.u.
86.46
86.48
86.50
86.52
86.54
86.56
86.58
86.60x10^3
2 hν / cm^-1

Fig. S2:

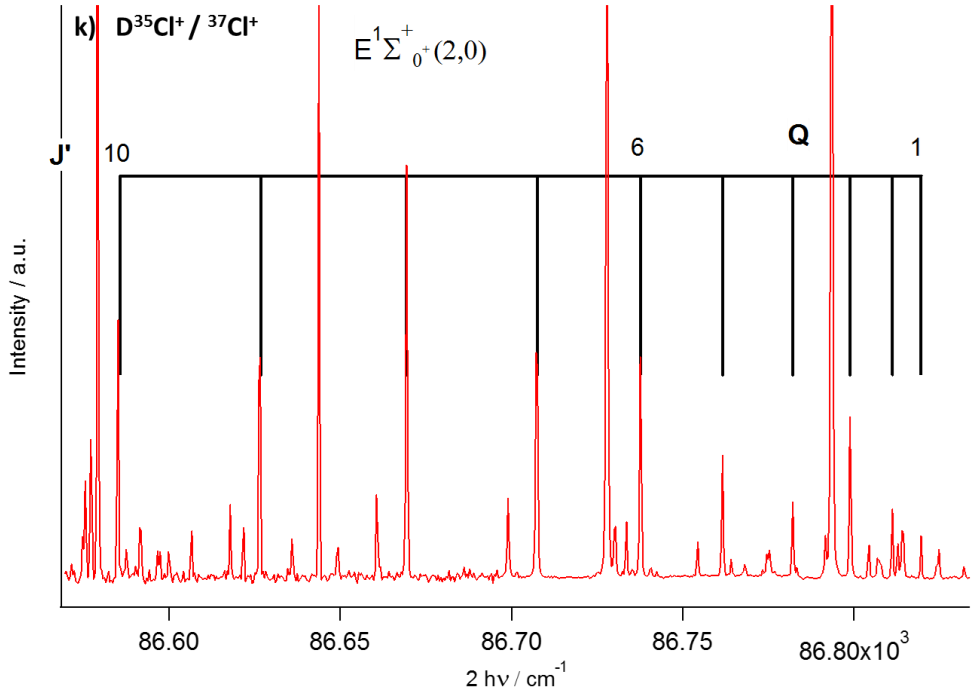
k) D35Cl+ / 37Cl+
E1Σ+0+(2,0)
J'
10
6
Q
1
Intensity / a.u.
86.60
86.65
86.70
86.75
86.80x10^3
2 hν / cm-1

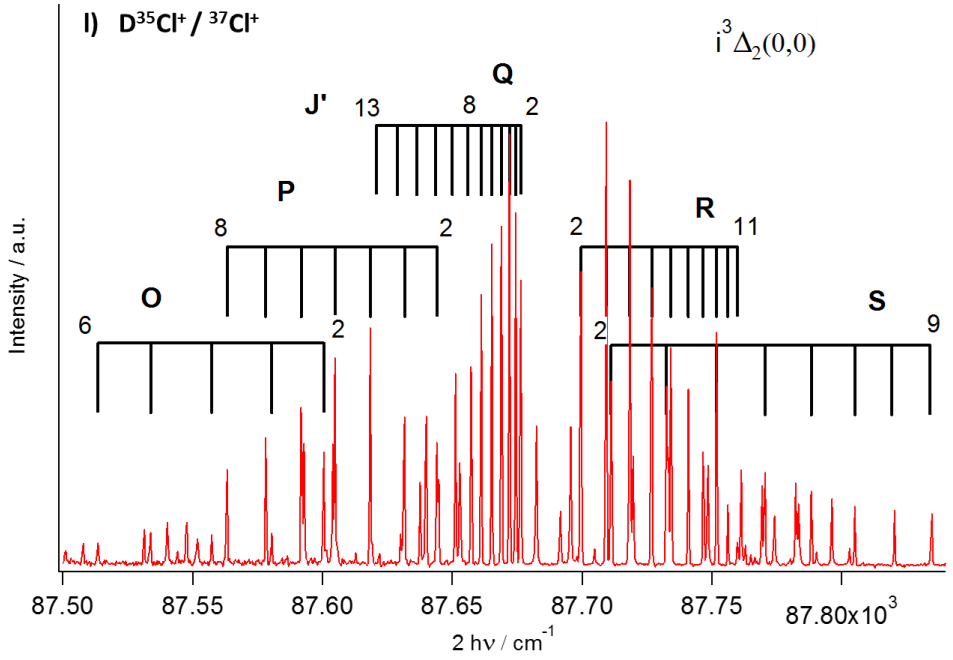
l) D35Cl+ / 37Cl+
i3Δ2(0,0)
Q
J'
13
8
2
P
8
2
R
2
11
O
6
2
S
2
9
Intensity / a.u.
87.50
87.55
87.60
87.65
87.70
87.75
87.80x10^3
2 hν / cm-1

Fig. S2:

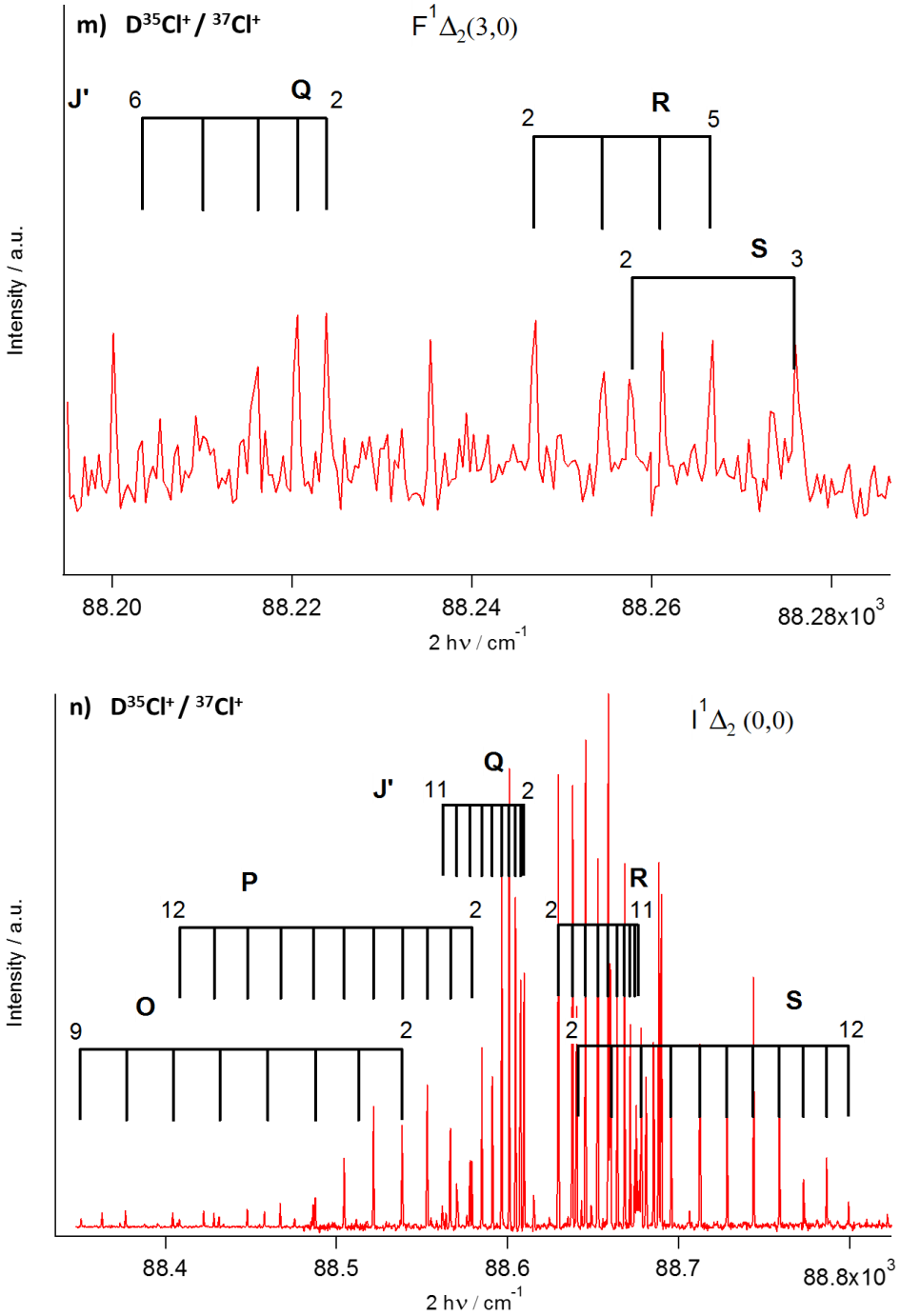
m) D35Cl+ / 37Cl+
F 1Δ2(3,0)
J'
Q
6
2
R
2
5
S
2
3
Intensity / a.u.
88.20
88.22
88.24
88.26
88.28x10^3
2 hν / cm^-1
n) D35Cl+ / 37Cl+
I 1Δ2 (0,0)
J'
Q
11
2
P
12
2
R
2
11
O
9
2
S
2
12
Intensity / a.u.
88.4
88.5
88.6
88.7
88.8x10^3
2 hν / cm^-1

Fig. S2:

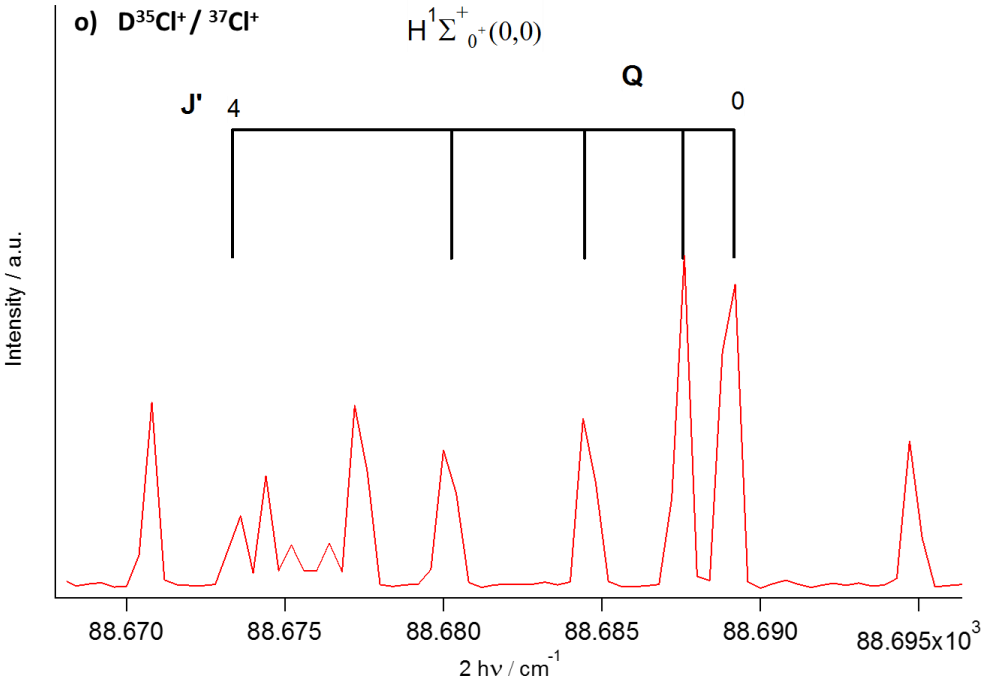
o) D35Cl+ / 37Cl+
H1Σ+0+(0,0)
Q
J'
4
0
Intensity / a.u.
88.670
88.675
88.680
88.685
88.690
88.695x10^3
2 hν / cm-1

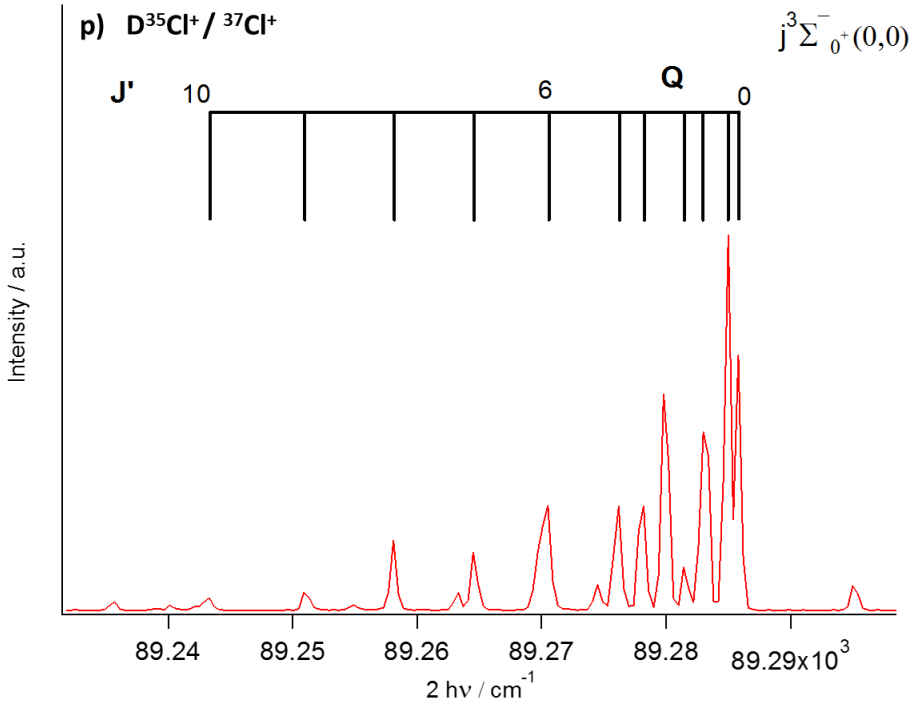
p) D35Cl+ / 37Cl+
j3Σ−0+(0,0)
J'
10
6
Q
0
Intensity / a.u.
89.24
89.25
89.26
89.27
89.28
89.29x10^3
2 hν / cm-1

Fig. S2:

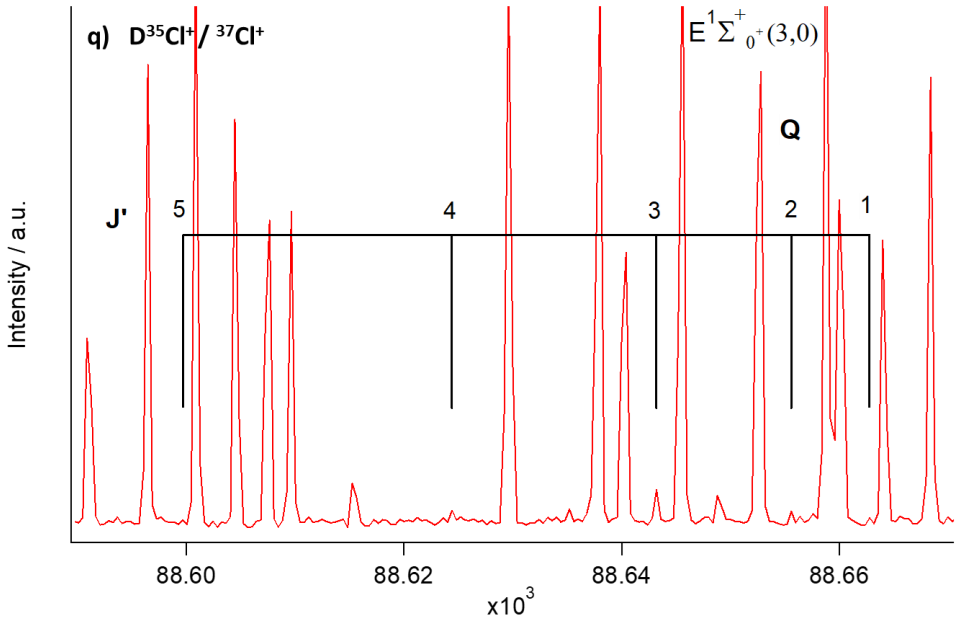
q) D35Cl+ / 37Cl+
E1Σ+0+(3,0)
Q
J'
5
4
3
2
1
Intensity / a.u.
88.60
88.62
88.64
88.66
x10^3

Tables S1 a):

Table 1. Measured transition wavenumbers for the $D^{35}Cl$ $d^3\Pi_1$ - $X^1\Sigma^+$ (0,0)

J''	*O (J)*	*P (J)*	*Q (J)*	*R (J)*	*S (J)*
		(0,0) band			
0					81820.2
1				81808.6	81841.7
2			81787.1	81819.4	81860.9
3		81766.0	81786.7	81829.3	81880.4
4	81732.8	81753.6	81785.9		81898.0
5	81712.4	81741.6			81914.8
6	81690.5				
7	81667.7				
8	81643.0				
9	81618.3				

Table 2. Measured transition wavenumbers for the $D^{35}Cl$ $f^3\Delta_2$ - $X^1\Sigma^+$ (0,0)

J''	*O (J)*	*P (J)*	*Q (J)*	*R (J)*	*S (J)*
		(0,0) band			
0					82108.3
1				82097.5	82128.6
2			82076.2	82108.3	82148.5
3		82042.2	82075.8	82117.8	82167.7
4		82029.8	82075.2	82127.4	82187.7
5		82018.3	82074.6	82136.9	82208.0
6		82006.7	82073.6	82146.1	82228.4
7		81995.1	82072.5	82154.5	82249.2
8		81983.5	82071.0	82162.5	
9		81971.2	82069.2	82170.1	
10		81958.8	82066.8	82178.1	
11		81946.4	82064.1	82185.7	

Table 3. Measured transition wavenumbers for the $D^{35}Cl$ $D^1\Pi_1$ - $X^1\Sigma^+$ (0,0)

J''	*O (J)*	*P (J)*	*Q (J)*	*R (J)*	*S (J)*
		(0,0) band			
0					82559.6
1			82527.3	82548.4	82578.4
2		82505.3	82525.7	82557.6	*82596.4*
3	82470.2	82492.6		82565.6	*82612.8*
4	82447.1	82478.2		82572.4	*82629.2*
5	82424.0	82464.2		82578.4	82646.5
6	82399.7	82450.3		82585.2	82662.5
7		82435.5		82590.0	82678.1
8		82420.0		82594.0	82694.2
9				82596.4	82709.8
10				82597.6	

Table 4. Measured transition wavenumbers for the $D^{35}Cl$ $f^3\Delta_1$ - $X^1\Sigma^+$ (0,0)

J''	*O (J)*	*P (J)*	*Q (J)*	*R (J)*	*S (J)*
		(0,0) band			
0					82592.4
1				82583.2	82610.8
2			82563.2	82592.8	82630.0
3		82529.3		82600.4	82649.7
4	82483.8	82516.9		82608.4	82668.9
5	82460.3			82616.0	82688.5
6				82624.0	
7				82631.6	
8				82639.2	
9					
10					
11					

Table 5. Measured transition wavenumbers for the $D^{35}Cl$ $F^1\Delta_2$ - $X^1\Sigma^+$ (0,0), (1,0), (2,0), (3,0)

J''	*O (J)*	*P (J)*	*Q (J)*	*R (J)*	*S (J)*
		(0,0) band			
0					82939.6
1				82928.0	82962.0
2			82907.2	82938.4	82981.6
3		82873.6	82905.6	82948.0	83000.9
4	82831.7	82861.6	82903.6	82957.6	83019.3
5	82810.9	82849.6	82901.2	82965.6	83036.2
6		82836.9	82898.0	82973.2	83052.6
7		82824.5	82894.8	82980.4	83069.1
8		82811.7	82891.2	82986.8	
9		82798.4	82887.2	82992.9	
10		82784.4	82882.4	82998.5	
11		82769.6	82877.4		
12		82754.0	82872.0		
13			82866.0		
14			82859.4		
15			82852.8		
		(1,0) band			
0					84769.5
1				84758.2	84790.0
2			84734.5	84767.5	84808.8
3		84701.7	84732.6	84775.9	84827.2
4		84688.9	84729.8	84783.6	84844.1
5		84676.4	84726.5	84790.8	84860.9
6		84663.2	84722.5	84796.8	84876.1
7		84649.6	84717.7	84802.0	84890.6
8		84635.2	84712.5	84806.8	84904.2
9		84619.9	84706.5	84810.4	
10			84699.7	84813.6	
11			84691.6		
12			84684.1		
		(2,0) band			
0					86542.1
1				86531.3	86560.4
2			86508.5	86539.7	86578.0
3			86505.7	86546.8	86594.8
4			86502.1	86552.8	
5			86497.7	86558.0	
6			86492.2		
7			86485.8		
8			86478.6		
9			86470.2		

			(3,0) band		
0					88258.0
1				88247.2	88276.0
2			88223.8	88254.8	
3			88220.6	88261.2	
4			88216.2	88266.8	

Table 6. Measured transition wavenumbers for the $D^{35}Cl$ $g^3\Sigma^-_{0+}$ - $X^1\Sigma^+$ (0,0)

J''	***O (J)***	***P (J)***	***Q (J)***	***R (J)***	***S (J)***
			(0,0) band		
0			83134.1		83163.6
1			83131.6		83179.6
2	83103.3		83130.4		83194.1
3	83080.1		83127.2		83206.3
4			83121.2		
5			83113.6		
6			83104.8		
7			83093.6		

Table 7. Measured transition wavenumbers for the $D^{35}Cl$ $E^1\Sigma^+_{0+}$ - $X^1\Sigma^+$ (0,0), (1,0), (2,0), (3,0)

J''	***O (J)***	***P (J)***	***Q (J)***	***R (J)***	***S (J)***
			(0,0) band		
0			83949.2		
1			83944.8		
2			83935.6		
3			83922.1		
4			83904.1		
5			83880.9		
6			83854.0		
7			83825.1		

(1,0) band	
0	*85014.0*
1	*85009.5*
2	*85000.5*
3	84987.3
4	84969.6
5	84948.2
6	84923.1
7	84893.8
8	84865.3
9	84831.2
10	84791.6
(2,0) band	
0	86819.6
1	86811.2
2	86798.8
3	86782.1
4	86761.6
5	86737.6
6	86707.6
7	86669.4
8	86626.9
9	86585.8
(3,0) band	
0	
1	88662.8
2	88655.6
3	88643.2
4	88624.4
5	88599.7

Table 8. Measured transition wavenumbers for the $D^{35}Cl\ i^3\Delta_2$ - $X^1\Sigma^+$ (0,0)

J''	***O (J)***	***P (J)***	***Q (J)***	***R (J)***	***S (J)***
		(0,0) band			
0					87711.2
1				87699.6	87732.5
2			87676.4	87709.2	87751.7
3		87642.8	87674.4	87718.4	87770.5
4	87600.5	87630.4	87672.0	87726.9	87788.2
5	87580.5	87617.2	87668.8	87734.1	87805.1
6	87556.1	87603.6	87665.2	87740.9	87819.2
7	87532.6	87590.5	87661.2	87746.5	87834.0

8	87512.3	87576.9	87656.0	87751.7	
9		87562.1	87650.0	87756.1	
10			87643.6	87759.7	
11			87636.4		
12			87628.8		
13			87620.8		

Table 9. Measured transition wavenumbers for the $D^{35}Cl$ $I^1\Delta_2$ - $X^1\Sigma^+$ (0,0)

J''	***O (J)***	***P (J)***	***Q (J)***	***R (J)***	***S (J)***
		(0,0) band			
0					88640.4
1				88629.6	88660.0
2			88609.6	88638.0	88677.2
3		88578.9	88607.6	88645.6	88694.7
4	88537.0	88566.5	88604.5	88652.8	88711.5
5	88511.5	88552.9	88600.9	88658.8	88727.4
6	88486.4	88538.2	88596.5	88664.0	88742.9
7	88458.4	88521.4	88590.9	88668.4	88758.1
8	88430.4	88504.3	88584.9	88671.6	88772.1
9	88403.3	88486.3	88578.1	88674.4	88785.7
10	88375.7	88467.1	88570.1	88676.4	88798.5
11	88348.6	88447.8	88562.1		
12		88428.2			
13		88408.1			

Table 10. Measured transition wavenumbers for the $D^{35}Cl$ $H^1\Sigma^+_{0+}$ - $X^1\Sigma^+$ (0,0)

J''	***O (J)***	***P (J)***	***Q (J)***	***R (J)***	***S (J)***
		(0,0) band			
0			88689.2		
1			88687.6		
2			88684.4		
3			88680.0		
4			88673.6		

Table 11. Measured transition wavenumbers for the $D^{35}Cl\ j^3\Sigma^-_{0+}$ - $X^1\Sigma^+$ (0,0)

J''	*O (J)*	*P (J)*	*Q (J)*	*R (J)*	*S (J)*
			(0,0) band		
0			*89285.8*		
1			89284.9		
2			89282.9		
3			89281.4		
4			89278.2		
5			89276.2		
6			89270.5		
7			89264.5		
8			89258.1		
9			89250.9		
10			89243.3		

Tables S1 b):

Table 12. Measured transition wavenumbers for the Q-branch lines $D^{35}Cl$ $V^1\Sigma^+$ - $X^1\Sigma^+$ (v',0)

J''	*11*	*12*	*13*	*14*	*15*	*16*	*17*
0			83391.1	83736.4	84298.4	84664.0	84950.7
1	82491.0	82938.0	83383.4	83732.0	84291.6	84658.4	84946.4
2	82481.8	82920.9	83368.6	83723.2	84277.6	84647.2	84937.2
3	82465.8	82897.6		83710.4	84257.8	84630.4	84924.0
4	82442.3	82868.4		83688.0	84232.1	84606.3	84907.0
5	82413.6	82832.5		83662.5	84201.3	84575.4	84885.3
6		82791.2		83628.1	84165.6	84536.1	84858.5
7		82739.9		83583.2	84122.8	84489.6	84824.8
8		82675.7		83533.4	84070.9	84440.4	84783.7
9				83478.9	84015.6	84384.1	
10						84320.2	
11							

J''	*18*	*19*	*20*	*21*	*22*	*23*	*24*
0	85479.8	85843.2	86217.7	86587.2	87056.6	87424.8	87803.0
1	85473.8	85837.3	86210.9	86581.4	87054.2	87417.6	87796.2
2	85461.6	85824.5	86197.7	86568.4	87048.5	87410.4	87782.2
3	85443.2	85806.0	86177.7	86551.2	87037.3	87317.7	87761.3
4	85418.8	85779.6	86151.4	86526.9	87020.1	87396.8	87733.3
5	85390.2	85745.3	86118.0	86492.6	86999.6	87376.4	87695.6
6	85358.3	85705.3	86082.0	86452.3	86976.8	87349.0	87651.4
7	85320.6	85660.7	86037.3	86403.6	86955.2	87317.7	87602.6
8	85277.0	85612.5	85981.8			87278.8	87550.4
9	85224.1	85557.6	85919.5			87232.0	
10	85161.5	85495.0				87175.5	
11						87117.0	

J''	*25*	*26*	*27*	*28*
0	88174.5		88978.0	
1	88167.7	88471.4	88970.4	89242.5
2	88154.0	88455.3	88955.6	89235.7
3	88133.4	88434.5	88934.0	89226.8
4	88106.8	88407.6	88906.1	*89210.4*
5	88074.5	88374.0	88872.6	89191.6
6	88033.3	88336.1		
7	87984.8	88288.4		
8		88228.6		
9		88158.0		

4.4 Paper 4

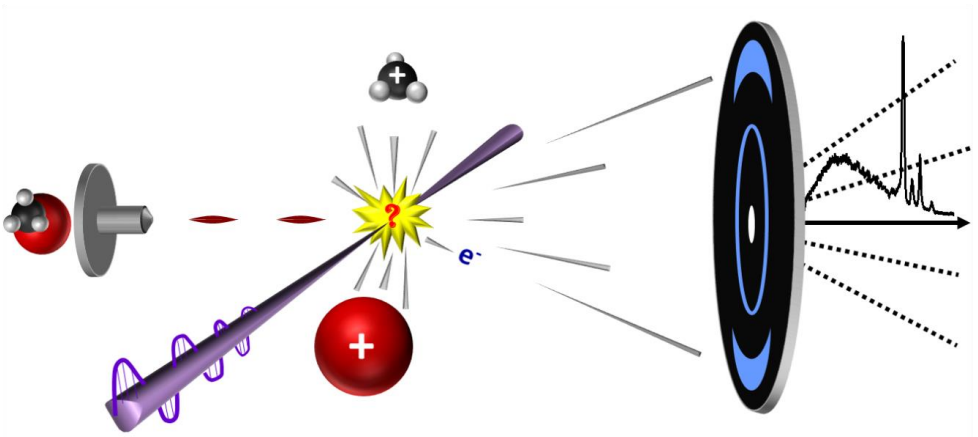

Arnar Hafliðason, Pavle Glodic, Greta Koumarianou, Peter C. Samartzis, Ágúst Kvaran. *Multiphoton Rydberg and valence dynamics of CH_3Br probed by mass spectroscopy and slice imaging*. Physical Chemistry Chemical Physics, 2018, **20**, 17423-17433.

DOI: 10.1039/c8cp02350f

PCCP

PAPER

Cite this: *Phys. Chem. Chem. Phys.*, 2018, **20**, 17423

Multiphoton Rydberg and valence dynamics of CH_3Br probed by mass spectrometry and slice imaging†

Arnar Hafliðason,[a] Pavle Glodic,[b] Greta Koumarianou,[b] Peter C. Samartzis*[b] and Ágúst Kvaran*[a]

Received 12th April 2018,
Accepted 6th June 2018

DOI: 10.1039/c8cp02350f

rsc.li/pccp

The multiphoton dynamics of CH_3Br were probed by Mass Resolved MultiPhoton Ionization (MR-MPI), Slice Imaging and Photoelectron Imaging in the two-photon excitation region of 66 000 to 80 000 cm^{-1}. Slice images of the CH_3^+ and Br^+ photoproducts of ten two-photon resonant transitions to np and nd Rydberg states of the parent molecule were recorded. CH_3^+ ions dominate the mass spectra. Kinetic energy release spectra (KERs) were derived from slice and photoelectron images and anisotropy parameters were extracted from the angular distributions of the ions to identify the processes and the dynamics involved. At all wavelengths we observe three-photon excitations, *via* the two-photon resonant transitions to molecular Rydberg states, forming metastable, superexcited ($CH_3Br^{\#}$) states which dissociate to form CH_3 Rydberg states (CH_3**) along with Br/Br*. A correlation between the parent Rydberg states excited and CH_3** formed is evident. For the three highest excitation energies used, the $CH_3Br^{\#}$ metastable states also generate high kinetic energy fragments of CH_3(X) and Br/Br*. In addition for two out of these three wavelengths we also measure one-photon photolysis of CH_3Br in the A band forming CH_3(X) in various vibrational modes and bromine atoms in the ground (Br) and spin–orbit excited (Br*) states.

I. Introduction

The methyl halides play an important role in the chemistry of the atmosphere.[1–4] Although far less abundant than methyl chloride in the stratosphere, methyl bromide is found to be much more efficient in ozone depletion.[4] Furthermore, bromocarbons are known to have a high global warming potential.[5] This has triggered a considerable interest in the spectroscopy[3,6–11] and photofragmentation dynamics[11–19] of methyl bromide over the last few decades. Additionally, the molecule is a simple prototype of a halogen-containing organic molecule for fundamental studies of photodissociation and photoionization involving formation of the cornerstone fragment CH_3.[15,18,20]

Photofragmentation studies of methyl bromide can be classified into two groups. One group focuses on the characterization of photofragments CH_3 + $Br(^2P_{3/2})$/$Br^*(^2P_{1/2})$ resulting from photodissociation in the A band[13–15,18,21–23] whereas the other group concerns the involvement of higher energy Rydberg and ion-pair states ("the Rydberg state region").[11,16,17,19,20] In the first group, single-wavelength excitation studies (193 and 222 nm,[12,23] 205 nm,[13] 213 and 230 nm,[15,24] and 216 nm[15]) as well as wavelength range excitations (215–251 nm[14] and 240–280 nm[22]) have been performed by the use of time-of-flight[12,22] and imaging[13–15,23,24] techniques. In the second group the emphasis has been on the involvement of Rydberg and ion-pair states in photodissociation processes to form ion pairs.[11,16,17,20] Photoionization studies are focused on the lowest energies of the ion and its breakdown.[11,25,26] Multiphoton dissociation studies focus on excitations to the lowest Rydberg states (5s) of the molecule.[19] The energetics of methyl bromide (CH_3Br) in the Rydberg state region have been studied quite thoroughly to map the Rydberg state structure of the molecule both by absorption spectroscopy[7] and by Resonance Enhanced MultiPhoton Ionization (REMPI),[11,20] as well as theoretically.[27]

Recently we have been exploring the effect of state interactions within the Rydberg state region on photofragmentation processes for the hydrogen halides.[28–33] These studies have revealed effect of Rydberg to valence as well as Rydberg to Rydberg state interactions on both the photodissociation and photoionization mechanisms within the molecules on a rotational and vibrational

[a] *Science Institute, University of Iceland, Dunhagi 3, 107 Reykjavík, Iceland. E-mail: agust@hi.is, arnahaf@hi.is; Fax: +354-552-8911; Tel: +354-525-4800*
[b] *Institute of Electronic Structure and Laser, Foundation for Research and Technology-Hellas, Vassilika Vouton, 71110 Heraklion, Greece. E-mail: sama@iesl.forth.gr, glodic_pavle@yahoo.com, gr.koumarianou@gmail.com; Fax: +30-2810-391305; Tel: +30-2810-391467*

† Electronic supplementary information (ESI) available. See DOI: 10.1039/c8cp02350f

energy level basis. We now expand this approach to polyatomic molecules, starting with methyl bromide (CH_3Br). In this paper we present (1) Mass-Resolved MultiPhoton Ionization (MR-MPI) for both Resonance Enhanced MPI (REMPI) and Non-Resonant MPI, (2) slice imaging and (3) photoelectron imaging data for excitation of CH_3Br involving two-photon resonant excitation to np and nd Rydberg states of the molecule for the two-photon wavenumber region of 66 000–80 000 cm^{-1} by a one-color excitation scheme. Despite the use of two-photon resonances, three-photon excitations followed by dissociations to form Rydberg states of CH_3 are found to dominate the dynamics. For the three highest energy excitations an additional three-photon channel opens, generating translationally hot CH_3(X) and Br/Br* and for two of these three excitations one-photon processes are also observed. These results are discussed in view of previous work on the low and high energy excited state dynamics of CH_3Br.

II. Experimental

The Velocity Map Imaging (VMI)/Slicing setup used in this work has been described in detail before.[34,35] Hence, only a brief description will be given here. A supersonic molecular beam, typically a mixture of 20% CH_3Br in He, was formed by expansion through a home-made piezoelectrically-actuated nozzle valve (∅ 1 mm orifice) and skimmed (∅ 1.5 mm, Beam Dynamics) prior to entering the interaction region of a slice imaging setup. A stagnation pressure of $P_0 \sim 1$ bar was used. A photolysis/photofragment ionization laser beam was focused (f = 30 cm) on the geometric focal point of a single-electrode repeller-extractor plate arrangement where it intersected the collimated molecular beam at right angles. The laser beam (typically 1.5 mJ per pulse) was generated by a pulsed Nd^{3+}:YAG laser (Spectra Physics Quanta Ray Pro 250) pumping a master oscillator–power oscillator system (Spectra Physics MOPO 730-10) set at the appropriate wavelength.

For the slicing experiments, reported here, the repeller is pulsed ON at the appropriate time delay (~300 ns) following the photolysis/ionization. The charged photofragments traverse a field-free time-of-flight region (45 cm) and a gated, position-sensitive detector (dual, imaging-quality Micro-Channel Plates (MCP) array coupled to a phosphor screen) images the center slice of the photofragment sphere. The image frame is recorded asynchronously every second (~10 laser shots) by a Charge-Coupled Device (CCD) camera and several thousand frames are averaged to form images. Each final image is integrated from its center over angle to extract the speed and over radius to extract the angular distributions of the corresponding fragments. For photoelectrons, the repeller is negatively charged and both the repeller electrode and the detector are not gated (*i.e.* they are always ON).

III. Results and analysis

A. Mass resolved MPI

(2 + m) as well as (3 + m) REMPI spectra (where 2 and 3 refer to the number of photons for resonant excitation to CH_3Br Rydberg states and m refers to the number of additional photons needed to generate the observed ions) and spectral assignments for CH_3Br have been reported in ref. 20 and 11. The (2 + m) REMPI spectrum for CH_3^+ ion detection from ref. 11 for the two-photon resonant excitation region of 66 000–80 000 cm^{-1} is reproduced in Fig. 1 along with mass spectra for selected molecular Rydberg state resonances normalized to the CH_3^+ signal intensity. All the mass spectra show the CH_3^+ ion mass signal (I(CH_3^+)) to be the strongest and the signal intensities to vary as, $CH_3^+ > CH_2^+ > CH^+ > (Br^+, CBr^+)$. The relative ion intensities, $I(M^+)/I(CH_3^+)$, for $M^+ = CH_2^+$, CH^+ and Br^+ are found to vary with wavenumber and to reach maxima as the wavenumber values get closer to the ion-pair threshold ($CH_3^+ + Br^-$; Fig. 1b). Closer inspection of the REMPI spectra shows that these have two major contributions, an underlying continuum, gradually increasing with excitation wavenumber and superimposed REMPI peaks. The latter are due to transitions to discrete quantum levels and, therefore, by definition, involve resonant transitions (*i.e.* REMPI). They correspond to two-photon resonant transitions to the parent

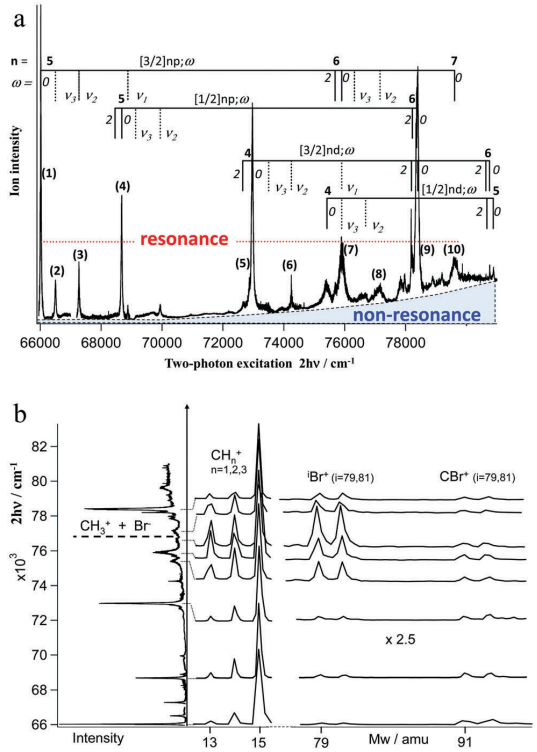

Fig. 1 Mass Resolved (MR) MPI for CH_3Br: (a) CH_3^+ signal (MPI spectrum) for the two-photon wavenumber range of 66 000–80 000 cm^{-1} and CH_3Br Rydberg state (CH_3Br^{**}) assignments. Separation of the spectrum into resonant and non-resonant contributions is indicated. The numbers of slice images recorded are indicated (see Table 1). (b) Mass spectra of selected CH_3Br Rydberg state resonances. Signals for masses larger than 78 amu have been expanded by a factor of 2.5.

molecular Rydberg states as an initial excitation[11,20] prior to further excitation/dissociation/ionization processes (*i.e.* (2 + *m*) REMPI). The continuum, on the other hand, involves transitions to non-quantized energy levels, *i.e.* non-resonant transitions (Fig. 1a), of which initial one-photon transitions to repulsive molecular valence states are the most likely.[14,15,22] Such transitions are followed by dissociation (*i.e.* one-photon photodissociation) to form CH_3 in the ground electronic state (X) and bromine atoms in their ground ($Br(^2P_{3/2})$, henceforth denoted Br) or spin–orbit excited ($Br(^2P_{1/2})$, henceforth denoted Br*) states, which are subsequently ionized by (non-resonant) multiphoton ionization (MPI). From now on these two contributions will be referred to as resonant and non-resonant contributions to the MPI spectrum, respectively.

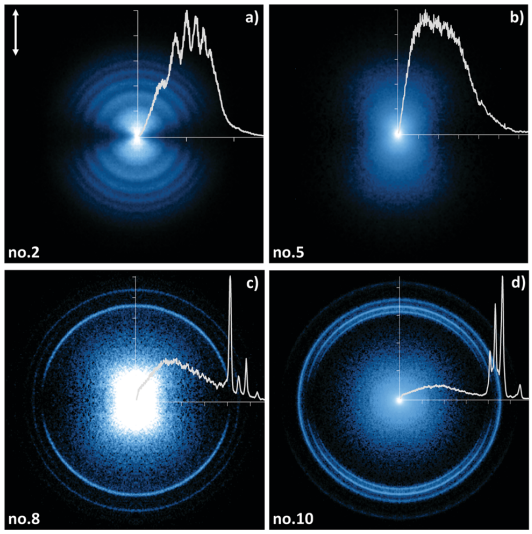

Fig. 2 CH_3^+ slice images and the corresponding kinetic energy release spectra (KERs) for excitation numbers 2 (a), 5 (b), 8 (c) and 10 (d) (see Table 1). The image intensity scale has been adjusted to show all major features. The KERs are normalized to the strongest peak in each spectrum. The laser polarization is indicated by the double arrow in panel (a).

B. Slice images and kinetic energy release spectra (KERs)

CH_3^+. CH_3^+ ion slice images (Fig. 2) were recorded for MPI of CH_3Br corresponding to (2 + *m*) REMPI for resonant excitation to a total of ten molecular Rydberg states (with np and nd Rydberg electron configurations and different vibrational states), converging to both spin–orbit components of the ground ionic states $X(^2\Pi_{3/2})$ and $X^*(^2\Pi_{1/2})$ in the two-photon excitation region of 66 000–80 000 cm^{-1} (see Table 1). Kinetic energy release spectra (KERs) were derived from the images (see Fig. 3). Two major spectral components could be identified from the images/KERs corresponding to the non-resonant and resonant contributions mentioned above. Large non-resonant contributions are observed at two of the highest energy two-photon resonant excitations only (77 165 cm^{-1} and 79 610 cm^{-1}; transitions no. 8 and 10 in Table 1). The non-resonant MPI spectral contributions (see Fig. 1a) appear as clear rings in the images/sharp peaks in the KERs (Fig. 2 and 3) as to be expected for direct non-resonant photodissociation processes (see further discussion in Section IV.B). Very small non-resonant spectral contributions were also observed for the excitations 75 905 cm^{-1} (7) and 78 370/78 401 cm^{-1} (9). The MPI spectral contributions (Fig. 1a) due to the resonant transitions are observed for all the data as broad "underlying" KER spectral structures peaking at low KER as to be expected for resonance excitations followed by delayed dissociation processes (see further discussion in Section IV.A. Vibrational structure is exhibited for the lowest four energy excitations (66 019–68 684 cm^{-1}) (Fig. 3).

The non-resonant contributions observed can be assigned to the stepwise processes,

$$CH_3Br + 1h\nu \rightarrow CH_3Br^*; \quad \text{non-resonant transition} \quad (1a)$$

$$CH_3Br^* \rightarrow CH_3(X; \nu_1\nu_2\nu_3\nu_4) + Br/Br^*; \quad \text{dissociation} \quad (1b)$$

$$CH_3(X; \nu_1\nu_2\nu_3\nu_4) + 3h\nu \rightarrow CH_3^+ + e^-; \quad \text{photoionization} \quad (1c)$$

where $CH_3(X; \nu_1\nu_2\nu_3\nu_4)$ refers to the ground electronic state of $CH_3(X)$ and vibrational levels ν_1,ν_2,ν_3,ν_4 and Br/Br* refer to the ground (Br) and spin–orbit excited (Br*) states of bromine, respectively. Since the kinetic energy release by the CH_3^+ ions

Table 1 Velocity map images for CH_3^+ and Br^+ and the corresponding photoelectron images recorded for (2 + *m*) REMPI of CH_3Br *via* resonant excitation to specified molecular Rydberg states

Image no.	CH_3Br Rydberg states; $[\Omega_c]nl$; ω,$(\nu_1\nu_2\nu_3)^a$	One-photon excitation/nm	Two-photon excitation/cm^{-1}	CH_3 Rydberg states detected
1	[3/2]5p; 0, (000)	302.943	66 019[c]	3p; $^2A_2$
2	[3/2]5p; 0, (001)	300.738	66 503[d]	3p; $^2A_2$
3	[3/2]5p; 0, (010)	297.287	67 275[d]	3p; $^2A_2$
4	[1/2]5p; 0, (000)	291.188	68 684[c]	3p; $^2A_2$
5	[3/2]4d; 0, (000)	274.059	72 977[c]	3d; $^2E/^2A_1$
6	[3/2]4d; 0, (010)	269.364	74 249[d]	3d; $^2E/^2A_1$
7	[3/2]6p; 0, (000)/[3/2]4d; 0, (100)/[1/2]4d; 0, (001)[b]	263.487	75 905[c]	4p; $^2A_2$, 3d; $^2E/^2A_1$
8	[3/2]6p; 0, (010)[b]	259.185	77 165[d]	4p; $^2A_2$, 3d; $^2E/^2A_1$
9	[1/2]6p; 0, (000)/[3/2]5d; 0, (000)	255.199, 255.099	78 370[c], 78 401[c]	4p; $^2A_2$, 3d; $^2E/^2A_1$, 4f; 2E
10	[3/2]7p; 0, (000)	251.225	79 610[c]	4p; $^2A_2$, 3d; $^2E/^2A_1$

[a] $[\Omega_c]$: total angular momentum quantum number for the core ion. *n*: principal quantum number for the Rydberg electron. *l*: Rydberg electron orbital (p,d). ω: total angular momentum quantum number for the Rydberg electron. (ν_1, ν_2, ν_3): vibrational quantum numbers referring to vibrational modes, ν_1 (symmetric stretch), ν_2 (umbrella) and ν_3 (C–Br stretch). [b] Spectral overlap. [c] Ref. 20. [d] Ref. 11.

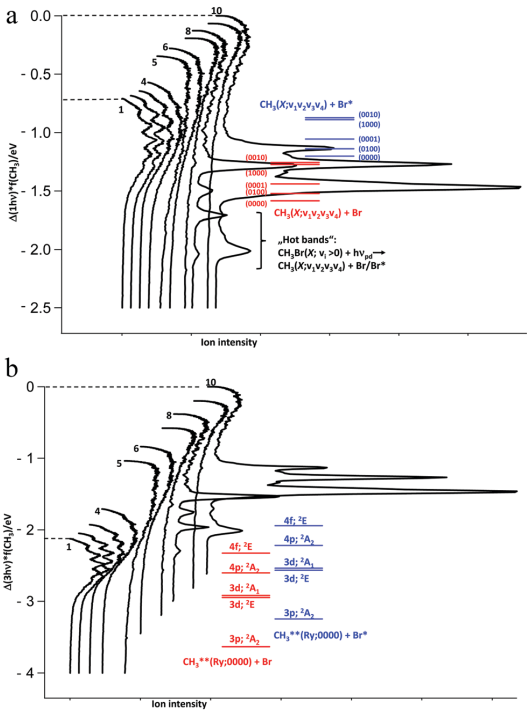

Fig. 3 CH_3^+ kinetic energy release spectra (KERs) derived from images no. 1–10 (see Table 1 and Fig. 1a). The spectra are normalized to the height of the lowest KER spectra contributions, corresponding to resonant contributions (see main text) in each spectrum. The spectra are plotted as a function of a relative scale $\Delta(1h\nu)^*f(CH_3)$ (a) and $\Delta(3h\nu)^*f(CH_3)$ (for $CH_3{}^{79}Br$) (b) (see explanation in main text) and tilted to the right (*i.e.* plotted vertically). Common energy thresholds (energy maxima) for the formation of $CH_3(X, v_1v_2v_3v_4)$ + Br/Br* after non-resonant one-photon photodissociation of CH_3Br are indicated in (a). Common energy thresholds (energy maxima) for the formation of CH_3**(Ry, $v_1v_2v_3v_4$) + Br/Br* after three-photon photodissociation of CH_3Br *via* resonant excitation to CH_3Br Rydberg states are indicated in (b).

formed is determined by the initial step (1a) it is convenient to compare the corresponding KERs contributions on a relative one-photon energy scale ($\Delta(1h\nu) = 1h\nu_i - 1h\nu_0$, where ν_0 and ν_i are one-photon excitation frequencies of a reference spectrum (ν_0) and a spectrum i (ν_i) for $\nu_0 > \nu_i$) weighted by the mass ratio factor for CH_3, $f(CH_3) = m(^jBr)/m(CH_3{}^jBr)$ (j = 79, 81), to take account of the conservation of momentum. Thus, spectral peaks due to the formation of the same species/thresholds, $CH_3(X; v_1v_2v_3v_4)$ + Br/Br*, will match. This has been carried out in Fig. 3a, which shows the KERs shifted by the weighted one-photon energy difference ($\Delta(1h\nu)^*f(CH_3)$) where the "zero kinetic energy released" for the two-photon excitation to the [3/2]7p; 0, (000) CH_3Br Rydberg state (image/KER no. 10/79 610 cm^{-1}; see Table 1) has been set to zero (reference spectrum). Thresholds corresponding to the "maximum possible kinetic energy released" for formation of the various $CH_3(X; v_1v_2v_3v_4)$ species (along with Br/Br*) are also marked in Fig. 3a. All sharp peaks observed in spectrum no. 8/77 165 cm^{-1} are found to match peaks in no. 10/79 610 cm^{-1}. Some overlap of the peaks is observed in spectrum no. 10/79 610 cm^{-1}. The peaks observed in the region of $\Delta(1h\nu)^*f(CH_3) = -1.6$ to 0.0 eV are due to excitations of $CH_3Br(X)$ in its ground vibrational state, whereas those of $\Delta(1h\nu)^*f(CH_3) < -1.6$ eV are due to excitations of vibrationally excited $CH_3Br(X)$ molecules ("hot bands"). We assign the peaks at about $\Delta(1h\nu)^*f(CH_3) = -1.49$ eV (Fig. 3a), both in spectra no. 8 and 10 and at about $\Delta(1h\nu)^*f(CH_3) = -1.13$ eV in no. 10 to the formation of a vibrationally excited $CH_3(X)$ in the out-of-plane bending (umbrella) mode ($\nu_2 = 1$), *i.e.* $CH_3(X; 0100)$ along with Br and Br*, respectively. The peaks at about $\Delta(1h\nu)^*f(CH_3) = -1.27$ eV (Fig. 3a), both in spectra no. 8 and 10 are due to the formation of a vibrationally excited $CH_3(X)$ in stretching modes ($\nu_1 = 1$ and/or $\nu_3 = 1$), *i.e.* $CH_3(X; 1000)$ and/or $CH_3(X; 0010)$, along with Br.

Comparison of the KERs of the resonant contributions as well as analysis of the corresponding photoelectron spectra (PES, see below) reveals that the kinetic energy released by the CH_3^+ ions is determined by a dissociation after an initial three-photon excitation step. Therefore, in Fig. 3b, the corresponding KER spectra are compared on a weighted relative three-photon energy scale ($\Delta(3h\nu)^*f(CH_3)$; $\Delta(3h\nu) = 3h\nu_i - 3h\nu_0$). Furthermore, analysis of the PES (see below) suggests that electrons are released by one-photon ionization of Rydberg states of CH_3 (CH_3**). We, therefore, propose that the overall excitation process involves formation of CH_3** along with Br/Br* by three-photon photodissociation (two photons to an intermediate Rydberg state (see Table 1) plus one additional photon to reach one or more "superexcited" repulsive state denoted here as $CH_3Br^{\#}$) followed by one-photon ionization of CH_3** to form CH_3^+ as follows,

$$CH_3Br + 2h\nu \rightarrow CH_3Br^{**}(Ry; \nu_1\nu_2\nu_3); \quad \text{resonant transition} \quad (2a)$$

$$CH_3Br^{**}(Ry; \nu_1\nu_2\nu_3) + 1h\nu \rightarrow CH_3Br^{\#}; \quad \text{photoexcitation} \quad (2b)$$

$$CH_3Br^{\#} \rightarrow CH_3{}^{**} + Br/Br^*; \quad \text{dissociation} \quad (2c)$$

$$CH_3{}^{**} + 1h\nu \rightarrow CH_3{}^+ + e^-; \quad \text{photoionization} \quad (2d)$$

where $CH_3Br^{**}(Ry; \nu_1\nu_2\nu_3)$ represents vibrational levels ν_1, ν_2, ν_3 of a parent molecular Rydberg state and $CH_3Br^{\#}$ represents one or more superexcited state.

The vibrational structure with a progression frequency corresponding to about 1300 cm^{-1} observed for the lowest excitation KERs (no. 1–4; Fig. 3) resembles that to be expected for transitions to vibrational levels of a CH_3** Rydberg state of an out of plane/umbrella mode.[36,37] The position of the thresholds for CH_3**($3p^2A_2$) + Br/Br* formation following the three-photon excitation process (Fig. 3b; see also text above) in the tail of the KER spectra on the high energy side of the vibrational structure, as well as analysis of the corresponding photoelectron spectra (see below) suggests that the vibrational structure corresponds to the formation of CH_3**($3p^2A_2$; $\nu_1\nu_2\nu_3\nu_4$) for varying quantum levels of the out-of-plane bending mode (ν_2). Structure analysis of the four lowest excitation energy KER

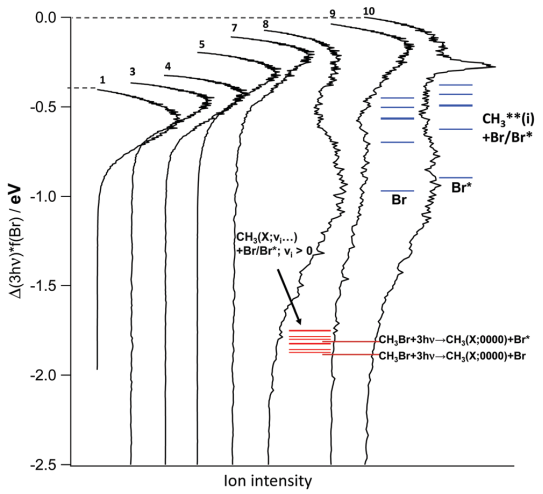

Fig. 4 Br^+ kinetic energy release spectra (KERs) derived from images no. 1, 3–5, and 7–10 (see Table 1 and Fig. 1a). The spectra are normalized to the height of the lowest KER spectra contributions, corresponding to resonant contributions (see main text) in each spectrum. The spectra are plotted as a function of a relative scale $\Delta(3h\nu)*f(\mathrm{Br})$ (for $CH_3{}^{79}Br$) (see explanation in main text of Section IV) and tilted to the right (*i.e.* plotted vertically). Common energy thresholds for the formation of CH_3**(Ry, $\nu_1\nu_2\nu_3\nu_4$) + Br/Br* as well as CH_3(X, $\nu_1\nu_2\nu_3\nu_4$) + Br/Br* after three-photon photodissociation of CH_3Br *via* resonant excitation to CH_3Br Rydberg states are indicated.

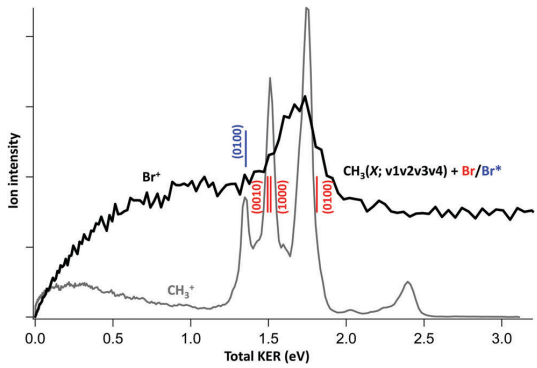

Fig. 5 Br^+ (black, above) and $CH_3{}^+$ (grey, below) kinetic energy release spectra (KERs) as a function of total kinetic energy released. Common energy thresholds for the formation of CH_3(X, $\nu_1\nu_2\nu_3\nu_4$) + Br/Br* after non-resonant one-photon photodissociation of CH_3Br are indicated.

spectra in the two-photon region of 66 019–68 684 cm^{-1} revealed the vibrational constants $\omega_e = 1311 \pm 5$ cm^{-1} and $\omega_e x_e = 11 \pm 1$ cm^{-1} for the out-of-plane (ν_2) vibrational mode of CH_3**($3p^2A_2$). This is to be compared with the vibrational wavenumber value of 1323 cm^{-1} reported for CH_3**($3p^2A_2$) in NIST.[36,37]

Br^+. Br^+ ion slice images were recorded following CH_3Br resonance excitations to Rydberg states in the two-photon excitation region of 66 000–80 000 cm^{-1} listed in Table 1 (except for no. 2/66 503 and no. 6/74 249 cm^{-1}). KERs were derived from the images (see Fig. 4). All the KERs exhibit a broad spectral structure peaking at low kinetic energies in the region of about 0.2 eV KER. The peak shifts to lower KER as the excitation energy increases. An additional broad peak is present at around 1 eV KER for the excitations no. 8/77 165 cm^{-1}, no. 9/78 370 cm^{-1} and no. 10/79 610 cm^{-1} spectra (Fig. 4). For the no. 10/79 610 cm^{-1} spectrum there is also a sharp peak at about 0.27 eV KER.

We attribute the sharp peak in the no. 10/79 610 cm^{-1} KER spectrum to the non-resonant contribution producing Br ground state along with CH_3(X; $\nu_1\nu_2\nu_3\nu_4$) by one-photon dissociation, *i.e.*

$$CH_3Br + 1h\nu \rightarrow CH_3Br^*; \quad \text{non-resonant transition} \quad (3a)$$

$$CH_3Br^* \rightarrow CH_3(X;\ \nu_1\nu_2\nu_3\nu_4) + Br; \quad \text{dissociation} \quad (3b)$$

$$Br + 3h\nu \rightarrow Br^+ + e^-; \quad \text{photoionization} \quad (3c)$$

Comparison of the total KERs (see Fig. 5) derived from the no. 10 images of Br^+ and $CH_3{}^+$ shows a sharp peak for Br to match the strongest sharp peak for CH_3, which corresponds to the formation of CH_3 with one quantum in the umbrella mode (CH_3(X; 0100)).

The broad low kinetic energy peak present in all KERs (Fig. 4) fits energetically the production of Br/Br* along with CH_3** Rydberg states (channels (2a)–(2c)). As discussed for CH_3 this is a three-photon process in two steps: First CH_3Br is excited resonantly with two photons (channel 2a) to a Rydberg state (Table 1), which subsequently absorbs an additional photon towards a superexcited $CH_3Br^{\#}$ state (or states; 2b) dissociating to CH_3** + Br/Br*. The broad, high kinetic energy contribution, only seen in the no. 8/77 165 cm^{-1}, no. 9/78 370 cm^{-1} and no. 10/79 610 cm^{-1} spectra (Fig. 4), on the other hand, is due to Br/Br* formed along with CH_3(X, $\nu_1\nu_2\nu_3\nu_4$) after a three-photon photodissociation process *via* the molecular Rydberg states ((2a) and (2b)). In both cases, Br^+ is subsequently generated by three-photon-MPI of Br/Br*. Relevant energy thresholds for these two processes are shown in Fig. 4 along with the KERs plotted on a $\Delta(3h\nu)*f(\mathrm{Br})$ scale.

C. Angular distributions

$CH_3{}^+$. Significant variations in angular distributions are observed for the $CH_3{}^+$ ions depending on the rings/channels involved (see Fig. 2). Signals associated with the resonant excitations mostly display shapes corresponding to parallel or isotropic distributions, whereas those due to the non-resonant excitations are found to display shapes corresponding to both parallel and perpendicular transitions. In an attempt to quantify the anisotropy of the rings, angular distributions, in the form of signal intensities as a function of the angle from 0 to 180°, derived from the images, were fitted by the simplified expression corresponding to a one-step photodissociation,[28]

$$P(\theta) = A[1 + \beta_2 P_2(\cos(\theta)) + \beta_4 P_4(\cos(\theta))] \quad (4)$$

where P_2 and P_4 are the second and fourth order Legendre polynomials and β_2 and β_4 are the corresponding anisotropy

parameters. A is a scaling factor. The β_2 parameter, which can be in the range between +2 (purely parallel transition) and −1 (purely perpendicular transition), can then be related to the overall transition symmetry and the corresponding dynamics. The β_4 parameter is usually associated with vector correlation effects, however considering the complexity of the processes involved (see eqn (1)–(3) above) it is unrealistic to interpret them in this way here, where it is better viewed simply as a fitting parameter. β_2 parameters derived for the various KERs features can be found in the ESI.† [38]

Fig. 6a shows β_2 values plotted for the various rings detected in images no. 8 and 10 (see Table 1) for the non-resonant process. These are shown along with the corresponding KERs plotted on a relative one-photon energy scale. A reasonably good agreement is found between the parameter values derived from the rings/KERs peaks of both images (no. 8 and 10) which have been assigned to common channels (see above), which further supports the validity of the assignments. The β_2's range from a value near +2, corresponding to a purely parallel transition for the CH_3(X; 0100) + Br* intermediates, to a negative value of about −0.2 corresponding to a significant contribution of a perpendicular transition for CH_3(X; 0100) + Br. Positive values of β_2 in the range of +0.8 to +1.6 obtained for CH_3(X; 1000/0010) + Br and high KER hot bands which form CH_3(X; $\nu_1\nu_2\nu_3\nu_4$) + Br suggest dominating parallel transitions mixed with some character of perpendicular transitions. Since the ion formation mechanism involves a simple one-photon photodissociation step, the anisotropy will be largely determined by the symmetry change of the initial photoexcitation step from the ground state of CH_3Br(X; $\nu_1\nu_2\nu_3$) to the repulsive valence states $^3Q_1$, $^3Q_0$ and $^1Q_1$ which correlate with CH_3(X; $\nu_1\nu_2\nu_3\nu_4$) + Br/Br*.[22] Considering symmetry alterations in possible transitions and the known shape of the potential energy surfaces involved[22] the following initial photoexcitation processes are proposed:

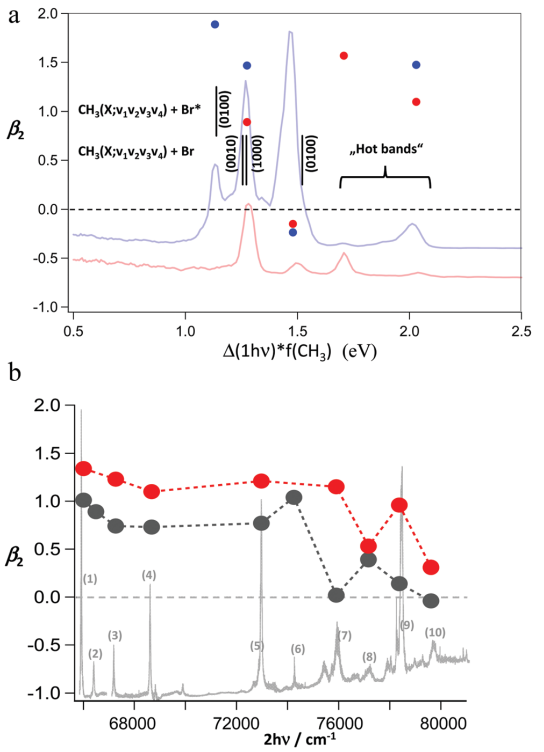

Fig. 6 (a) Effective anisotropy parameters β_2 extracted from CH_3^+ images no. 8 (red dots) and 10 (blue dots) (see Table 1) as a function of the kinetic energy released (eV) along with the corresponding KER spectra plotted on a relative energy scale ($\Delta(1h\nu)*f(CH_3)$) (see main text). Common energy thresholds for one-photon photodissociation processes to form CH_3(X; $\nu_1\nu_2\nu_3\nu_4$) + Br/Br* labelled by ($\nu_1\nu_2\nu_3\nu_4$) are indicated. "Hot bands": see Fig. 3a. (b) Effective anisotropy parameters β_2 extracted from CH_3^+ (grey dots) and Br^+ (red dots) images as a function of two-photon resonant excitations to CH_3Br Rydberg states along with the corresponding CH_3^+ REMPI spectrum. Image numbers are indicated (see Table 1).

(i) Formation of CH_3(X; 0100) + Br*, where CH_3 is vibrationally excited by one quantum in the out-of-plane bending mode (ν_2), mainly occurs by a parallel transition to the $^3Q_0$ state followed by a dissociation on the same (*i.e.* the diabatic) potential curve.

(ii) Formation of CH_3(X; 1000/0010) + Br, where CH_3 is vibrationally excited by one quantum in a stretching mode (ν_1 and/or ν_3), occurs largely by a parallel transition to the $^3Q_0$ state followed by a curve crossing, *i.e.* a dissociation on the adiabatic potential curve.

(iii) Formation of CH_3(X; 0100) + Br, where CH_3 is vibrationally excited by one quantum in the out-of-plane bending mode (ν_2), occurs to a significant extent by perpendicular transitions to the $^3Q_1$ and/or $^1Q_1$ states followed by a dissociation on the same/diabatic potential curve.

(iv) Formation of CH_3(X; $\nu_1\nu_2\nu_3\nu_4$) + Br from vibrationally excited CH_3Br(X; $\nu_1\nu_2\nu_3$) largely occurs by a parallel transition to the $^3Q_0$ state followed by a dissociation on the adiabatic potential curve.

Since the resonant contributions to the CH_3^+ images and KERs mostly involve three-photon excitations *via* molecular Rydberg states prior to dissociation to form CH_3** Rydberg states (channel (2)) the anisotropy of the images will depend on the two-photon resonant step as well as the one-photon dissociation step and possible mixing of states involved. Therefore, it cannot be easily interpreted. We observe a trend (Fig. 6b, grey dots) of decreasing β_2 parameter (more perpendicular contribution) with increasing excitation energy. A correlation with the symmetry of the parent Rydberg state seems to exist: transitions through 5p and 4d Rydberg states of CH_3Br generate CH_3^+ with rather parallel distributions (β_2 ranging between 1.3 and 0.7) whereas 6p and 7p Rydberg states of CH_3Br generate CH_3^+ with almost isotropic distributions.

Br^+. Br^+ images associated with the resonant excitations, both low and high KER components (see above), mostly display shapes corresponding to parallel transitions with positive values of β_2. Fig. 6b (red dots) shows the β_2 values derived for the broad low KER peaks of the resonant transitions along with

the corresponding values for the CH_3^+ signals. Comparison of the β_2 parameters of the signals for Br^+ and CH_3^+ reveals some correlation (common trend and analogous values of β_2) between the signals. This is to be expected for fragments formed by the same channel, prior to ionization, as proposed for CH_3^{**} and Br/Br* (see eqn (2a)–(2c) above). Although close in value they are not identical; this can be attributed to the existence of some additional smaller contributions affecting the CH_3^+ and Br^+ distributions, such as dissociation of CH_3^+ (we do observe CH_2^+, CH^+ and C^+ ions as minor channels; discussion of these results will be dealt with in a separate publication).

The no. 10 excitation Br^+ signal due to the non-resonant transition cannot be separated from the underlying resonant contribution of the same KER (~0.27 eV) which makes up about 2/3 of the signal (Fig. 4 and 5). The total signal however, is found to display a close to isotropic shape (Fig. 2d) with β_2 of about +0.24, suggesting that the non-resonant part of it (1/3 of the total) is significantly perpendicular in nature. This matches the observed angular distribution (and $\beta_2 = -0.2$) of the signal for CH_3^+ due to the formation of the corresponding CH_3(X, 0100) fragment which we believe to be the major fragment produced along with Br prior to ionization (see above and Fig. 5).

C. Photoelectron spectra (PES)

Images of photoelectrons were recorded for the excitations listed in Table 1. No negative ions were found to be present in the time-of-flight KER distributions (Fig. 7) derived from the images. It is convenient to compare the photoelectron spectra with respect to the non-resonant contributions on a relative three-photon energy scale ($\Delta(3h\nu)^*f(e)$; $\Delta(3h\nu) = 3h\nu_0 - 3h\nu_i$; $f(e) = m(CH_3^+)/m(CH_3) \sim 1$; see text above for comparison and definitions) and those with respect to the resonant contributions on a relative one-photon energy scale ($\Delta(1h\nu) = 1h\nu_0 - 1h\nu_i$).

Fig. 7a shows the photoelectron spectra plotted on the relative one-photon energy scale, where the zero kinetic energy release of no. 10/79 610 cm^{-1} has been set to zero (reference spectrum). Thresholds corresponding to ionization of specific CH_3^{**} states (formed along with Br/Br*) line up in the plot. One photoelectron peak dominates the four lowest energy excitations (*i.e.* images/KERs no. 1–4; Table 1) which match in Fig. 7a. The peaks correspond to the formation of the CH_3^{**} ($3p^2A_2$) Rydberg state. These PES correspond to the images/KERs which show vibrational structures (see above). Small satellite peaks close by are indicative of vibrational excitations and hot bands as shown in Fig. 7b for excitation no. 4. The next two excitations (no. 5 and 6) generate photoelectron peaks that shift to higher energy but also match each other, corresponding to one-photon ionization of the CH_3^{**} ($3d^2E$) and/or CH_3^{**} ($3d^2A_1$) states, that lie close in energy. Finally, excitations no. 7–10 exhibit several photoelectron peaks corresponding to ionization of different CH_3 Rydberg states ($3p^2A_2$, $3d^2E$, $3d^2A_1$, $4p^2A_2$) as listed in Table 1. The PES structures of no. 8/77 165 and no. 10/79 610 cm^{-1}, which correspond to significant non-resonant contributions, are less clear. However, there are some indications of ionization/formation of CH_3(X; $\nu_1\nu_2\nu_3\nu_4$) species based on weak high kinetic energy electron peaks as shown by the inserted figure expansion for no. 8 in Fig. 7a.

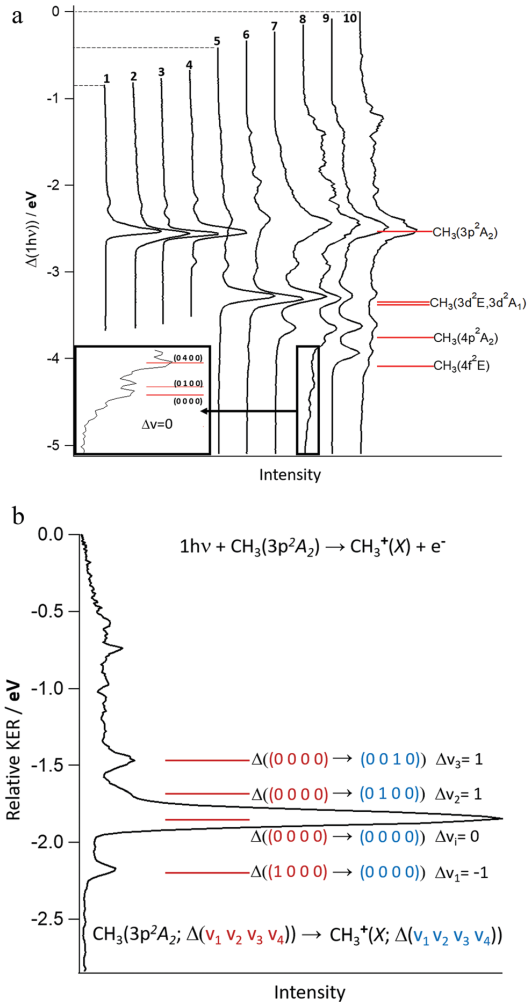

Fig. 7 Photoelectron spectra (PES), (a) derived from images no. 1–10 (see Table 1), plotted as a function of a relative energy scale $\Delta(1h\nu)$ (see explanation in the main text) and tilted to the right (*i.e.* plotted vertically). Common energy thresholds (energy maxima) for ionization of Rydberg states of CH_3 (CH_3^{**}(Ry)) after its formation along with Br/Br* by three-photon photodissociation of CH_3Br are indicated. The inset shows detail of the PES no. (8) at high energy with thresholds for ionization of CH_3(X; $v_1v_2v_3v_4$) and its formation along with Br/Br*. (b) For image no. 4 plotted as a function of the relative kinetic energy released (eV) tilted to the right (*i.e.* plotted vertically). Energy thresholds (energy maxima) for specific one-photon ionization processes of $CH_3^{**}(3p^2A_2; v_1v_2v_3v_4)$ states to form CH_3^+(X; $v_1v_2v_3v_4$), after its formation along with Br/Br* by three-photon photodissociation of CH_3Br, are indicated by ($v_1v_2v_3v_4$) numbers. Assignments of ionization processes with respect to changes in vibrational quantum numbers (Δv_i) are shown, furthest to the right.

IV. Discussion

As noted in the previous section, REMPI, slice and photoelectron imaging data converge on the existence of two major pathways when CH_3Br is excited at wavenumbers corresponding to two-photon transitions to reach rovibrational levels of molecular Rydberg states in the 66 000 to 80 000 cm^{-1} region: (a) two-photon-resonant transitions, followed by one-photon photolysis to give $CH_3(X)/CH_3^{**}$ + Br/Br* and (b) non-resonant, one-photon photolysis towards $CH_3(X)$ + Br/Br*. These two pathways will now be discussed.

A. Resonant processes

The results relevant to the resonant spectra contributions, as presented above, can be interpreted as being due to dissociations on excited state potential energy surfaces to form (a) Rydberg states of CH_3 (CH_3^{**}) along with Br/Br* or (b) ground state $CH_3(X)$ along with Br/Br* prior to ionization of either CH_3 or Br. This occurs after a total of three-photon excitation to metastable superexcited molecular states ($CH_3Br^{\#}$) *via* two-photon accessible Rydberg states (Fig. 8). Formation of $CH_3(X)$ directly following the two-photon resonant excitation (*i.e.* by predissociation of the resonance-excited molecular Rydberg states) was not detected. Whereas a minor contribution of such a channel cannot be ruled out, the results suggest that its probability is low.

In the case of the metastable molecular state(s) ($CH_3Br^{\#}$), prior to a dissociation the excess energy can be redistributed among the molecule's internal degrees of freedom to form fragments of relatively low translational energy but high internal (ro-vibrational) energy, typically appearing as broad KER spectral peaks for the CH_3 and Br fragments. The relatively low KER, broad spectral structures of the KERs observed for the resonant contributions suggests that step (2b) involves such a mechanism. The $CH_3Br^{\#}$ state(s), being higher in energy than the ionization limit, is (are) most likely one or more superexcited state(s) belonging to a Rydberg series converging to an excited ionic state (*i.e.* $CH_3Br^{\#} = [CH_3Br^{+\star}]nl;\omega)$. This involves a one-photon excitation within the ion core of the resonant Rydberg state ($CH_3Br^{**} = [CH_3Br^{+}]nl;\omega)$ to make an overall two-electron transfer to form $CH_3Br^{\#}$.

Looking at a summary of the CH_3^{**} Rydberg states detected (Table 1) there seems to be a correlation between the formation of CH_3^{**}(Ry) and excitations to CH_3Br^{**}(Ry) with respect to the Rydberg electron orbital symmetries (l quantum numbers). Thus, the 3p Rydberg state of CH_3 ($CH_3^{**}(3p^2A_2)$) is primarily

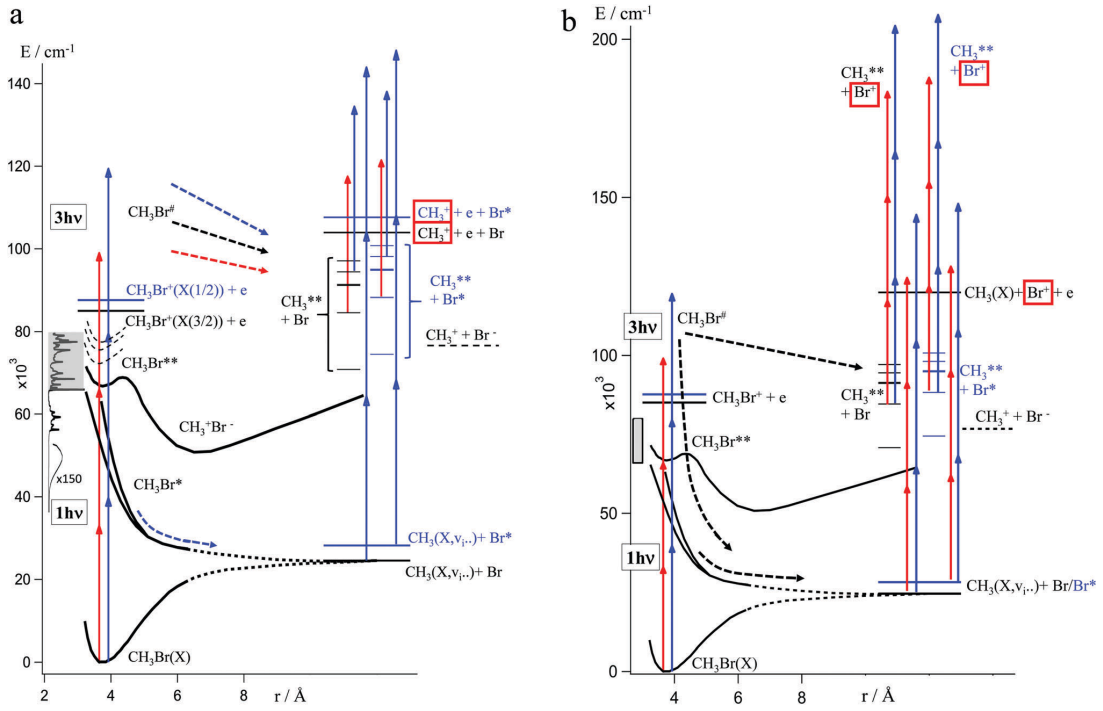

Fig. 8 Schematic energy diagrams for excitation processes of CH_3Br leading to CH_3^+ (a) and Br^+ (b) formation showing calculated potential energies as a function of the CH_3–Br bond distance[18,27] as well as relevant energy thresholds and transitions. Red vertical arrows correspond to the two-photon resonant transition of 66 019 cm^{-1} (excitation no. 1) and blue vertical arrows correspond to the two-photon resonant transition 79 610 cm^{-1} (excitation no. 10) (see Table 1). Broken arrows indicate paths of photodissociation processes as marked in boxes (see main text). The two-photon resonance scanning region is indicated by grey shaded boxes. The one-photon absorption spectrum[3,9] is tilted to the right (*i.e.* plotted vertically) in figure (a).

formed *via* excitation to the 5p Rydberg state of CH_3Br and the 3d Rydberg state(s) of CH_3 ($CH_3^{**}(3d^2E; 3d^2A_1)$) is (are) largely formed *via* excitation to the 4d Rydberg state of CH_3Br. This must be associated with a conservation of momentum during the combined process of one-photon excitation of CH_3Br^{**} to $CH_3Br^{\#}$ and its dissociation on an excited state potential surface to form CH_3^{**} and Br/Br*. Furthermore, an increasing number and changing proportion of CH_3^{**} states are formed as the excitation energy increases (Table 1 and Fig. 7a). This must be associated with an opening of an increasing number of channels to form CH_3^{**} + Br/Br* and/or changes in transition probabilities along different surfaces as the energy increases. The disappearance of the vibrational structure assigned to the $CH_3^{**}(3p^2A_2)$ state (see Section III.B) for excitation energies beyond that for no. 4 (Fig. 3) is a further indication of an increasing contribution of CH_3^{**} states and overlapping vibrational structures.

Whereas, no multiphoton dissociation studies for resonant excitations *via* p and d Rydberg states of CH_3Br exist in the literature, Wang *et al.* have reported studies of excitations *via* lower energy 5s Rydberg states.[19] Images and corresponding KERs for CH_3^+ are found to show comparable structures to those reported here, appearing as broad peaks with vibrational structures at low KERs and sharp peaks at medium high kinetic energies. These observations, however, are interpreted differently as being due to photodissociation of the parent molecular ions $CH_3Br^+(X)$ to form $CH_3^+(X)$ along with Br* and Br, respectively. Furthermore, rings/sharp KER peaks observed at still higher KERs are proposed to be due to two-photon resonant photodissociations to form $CH_3(X)$ along with Br and Br*.

B. Non-resonant processes

The results relevant to the non-resonant contributions, as presented above, can be interpreted as being due to one-photon excitations to repulsive electronic valence states (CH_3Br^*) followed by dissociation. This agrees with the observed increase in the corresponding spectral continuum with photon energy (Fig. 1a) in accordance with an increasing absorption (*i.e.* one-photon) cross section in the excitation region (see Fig. 8).[3,9] Relatively large signals appearing as rings in the images/sharp KERs peaks, due to the non-resonant contributions were seen for the excitations which show relatively large underlying non-resonant contributions in the REMPI spectra (see Fig. 1a), *i.e.* in images/KERs no. 8 and 10 for CH_3^+ (Fig. 3) and in no. 10 for Br^+ (Fig. 4).

Photodissociation studies in the first continuum absorption band (A band) of CH_3Br have been performed by a number of groups.[13–15,21–24] The reported value for β_2 of 1.9 ± 0.1 for $CH_3(X; 0100)$ formation along with Br* for 251.00 nm excitation[22] agrees with our value (1.9) for the corresponding fragment formation for 251.28 nm one-photon excitation (no. 10/79 610 cm^{-1}) and the value for β_2 of 0.2 ± 0.2 for $CH_3(X; 0100)$ along with Br for 251.00 nm excitation[22] is of an intermediate size analogous to our values of −0.15 and −0.24 for the corresponding fragment formation derived for the 259.23 (no. 8/77 165 cm^{-1}) and 251.28 nm (no. 10/79 610 cm^{-1}) excitations, respectively. Furthermore, our upper limit value of β_2 = +0.24, largely due to the formation of Br along with $CH_3(X; 0100)$ (see Section III.C) for 251.28 nm one-photon excitation can be compared with the values of about zero for excitations in the region of 251–278 nm.[22] Thus, the formation of $CH_3(X)$ in the out-of-plane bending mode along with Br is found to display isotropic to perpendicular fragment angular distributions, whereas its formation along with Br* displays a parallel angular distribution. This is in agreement with previous observations and has been shown to be consistent with a strong non-adiabatic coupling between spin–orbit states of the parent molecule.[22]

V. Summary and conclusions

CH_3^+ and Br^+ ion slice images as well as photoelectron velocity map images were recorded for multiphoton excitation of CH_3Br at ten wavelengths involving two-photon – resonant transitions to np and nd vibrational levels of molecular Rydberg states ($CH_3Br^{**}(Ry; \nu_1\nu_2\nu_3)$) between 66 000 and 80 000 cm^{-1} (Table 1). At all wavelengths CH_3^+ is the majority of the ion signal (Fig. 1). Kinetic energy release spectra (KERs) as well as angular distributions and relevant fit parameters (β_2 and β_4) were derived from the ion slice images. Photoelectron spectra were derived from the photoelectron images.

The majority of the photoelectrons formed are due to one-photon ionization of different Rydberg states of methyl photofragments (CH_3^{**}). These states are formed by two-photon-resonant excitation to an np or nd vibrational levels of parent Rydberg states followed by one-photon excitation to metastable, superexcited molecular states ($CH_3Br^{\#}$) which then dissociate towards $CH_3^{**}(Ry; \nu_1\nu_2\nu_3\nu_4)$ + Br/Br*. This contribution dominates all but two excitation wavelengths used in this work. A correlation is found between the angular momentum quantum numbers (l) of the resonantly excited molecular Rydberg states, CH_3Br^{**} and the CH_3 Rydberg states formed.

For the highest excitation energies, two additional channels are found to be present. The first channel is a dissociation of the metastable, superexcited $CH_3Br^{\#}$ states towards $CH_3(X; \nu_1\nu_2\nu_3\nu_4)$ + Br/Br* which generates fast CH_3^+ and Br^+ ions. The second channel is the formation of $CH_3(X; \nu_1\nu_2\nu_3\nu_4)$ + Br/Br* assigned as a one-photon photolysis *via* the A band with angular distributions of CH_3 and Br/Br* fragments agreeing well with the literature.

The results of this paper add to information relevant to the energetics and fragmentation processes of the methyl halides. It will hopefully render further theoretical interpretation of the characteristic processes involved in the very interesting dynamics observed here. Furthermore, the content of this paper is of relevance to various intriguing fields. The observed involvement of high energy superexcited molecular states in the formation of halogen atom radicals and fragment ions and electrons is of relevance to further understanding of atmospheric photochemistry as well as plasma chemistry/physics. Selective photoexcitation to form the reactive electronically

excited state of the CH_3, as identified, could be of interest for organic photosynthesis purposes.

Conflicts of interest

There are no conflicts to declare.

Acknowledgements

The financial support of the University Research Fund, University of Iceland is gratefully acknowledged. The imaging part of the reported results was carried out at the Ultraviolet Laser Facility at IESL-FORTH, supported in part by the European Union's Horizon 2020 research and innovation programme LASERLAB-EUROPE (Grant Agreement No. 654148).

References

1 D. E. Robbins, Photodissociation of Methyl-Chloride and Methyl-Bromide in Atmosphere, *Geophys. Res. Lett.*, 1976, **3**(4), 213–216.
2 D. E. Robbins, Correction, *Geophys. Res. Lett.*, 1976, **3**(12), 757.
3 L. T. Molina, M. J. Molina and F. S. Rowland, Ultraviolet-Absorption Cross-Sections of Several Brominated Methanes and Ethanes of Atmospheric Interest, *J. Phys. Chem.*, 1982, **86**(14), 2672–2676.
4 N. J. Warwick, J. A. Pyle and D. E. Shallcross, Global modelling of the atmospheric methyl bromide budget, *J. Atmos. Chem.*, 2006, **54**(2), 133–159.
5 Ozone-Depleting Substances. https://www.epa.gov/ozone-layer-protection/ozone-depleting-substances.
6 W. C. Price, The Far Ultraviolet Absorption Spectra and Ionization Potentials of the Alkyl Halides. Part I, *J. Chem. Phys.*, 1936, **4**(9), 539–547.
7 G. C. Causley and B. R. Russell, Vacuum Ultraviolet-Absorption Spectra of Bromomethanes, *J. Chem. Phys.*, 1975, **62**(3), 848–857.
8 S. Felps, P. Hochmann, P. Brint and S. P. McGlynn, Molecular Rydberg Transitions; The lowest-Energy Rydberg Transitions of s-Type in CH_3X and CD_3X, X = Cl, Br, and I, *J. Mol. Spectrosc.*, 1976, **59**, 355–379.
9 R. Locht, B. Leyh, H. W. Jochims and H. Baumgartel, The vacuum UV photoabsorption spectrum of methyl bromide (CH_3Br) and its perdeuterated isotopomer CD_3Br: a Rydberg series analysis, *Chem. Phys.*, 2005, **317**(1), 73–86.
10 R. Locht, B. Leyh, D. Dehareng, H. W. Jochims and H. Baumgartel, The vacuum UV photoabsorption spectrum of methyl bromide (CH_3Br) and its perdeuterated isotopomer CD_3Br: a vibrational analysis, *Chem. Phys.*, 2005, **317**(1), 87–102.
11 A. Kvaran, H. Wang, K. Matthiasson and A. Bodi, Two-Dimensional (2 + *n*) REMPI of CH_3Br: Photodissociation Channels via Rydberg States, *J. Phys. Chem. A*, 2010, **114**, 9991–9998.
12 G. N. A. Van Veen, T. Baller and A. E. De Vries, Photofragmentation of CH_3Br in the A-Band, *Chem. Phys.*, 1985, **92**(1), 59–65.
13 W. P. Hess, D. W. Chandler and J. W. Thoman, Photofragment imaging: the 205 nm photodissociation of CH_3Br and CD_3Br, *Chem. Phys.*, 1992, **163**(2), 277–286.
14 T. Gougousi, P. C. Samartzis and T. N. Kitsopoulos, Photodissociation study of CH_3Br in the first continuum, *J. Chem. Phys.*, 1998, **108**(14), 5742–5746.
15 V. Blanchet, P. C. Samartzis and A. M. Wodtke, UV photodissociation of methyl bromide and methyl bromide cation studied by velocity map imaging, *J. Chem. Phys.*, 2009, **130**, 3.
16 D. A. Shaw, D. M. P. Holland and I. C. Walker, Ion-pair formation mechanisms in chloromethane, bromomethane and dichlorodifluoromethane, *J. Phys. B: At., Mol. Opt. Phys.*, 2006, **39**(17), 3549–3560.
17 D. D. Xu, J. H. Huang, R. J. Price and W. M. Jackson, Velocity Imaging Studies on Ion-Pair Dissociation of $CH_3Br + h\nu_{VUV} \rightarrow CH_3^+ + Br^-$ as a Function of Wavelength, *J. Phys. Chem. A*, 2004, **108**(45), 9916–9923.
18 C. Escure, T. Leininger and B. Lepetit, Ab initio study of methyl-bromide photodissociation in the A band, *J. Chem. Phys.*, 2009, **130**(24), 244305.
19 F. Y. Wang, M. L. Lipciuc, X. M. Yang and T. N. Kitsopoulos, Multiphoton dissociation dynamics of CH_3Br, *Phys. Chem. Chem. Phys.*, 2009, **11**(13), 2234–2240.
20 T. Ridley, J. T. Hennessy, R. J. Donovan, K. P. Lawley, S. Wang, P. Brint and E. Lane, Evidence for Rydberg doorway states in photoion pair formation in bromomethane, *J. Phys. Chem. A*, 2008, **112**(31), 7170–7176.
21 G. N. A. Vanveen, T. Baller and A. E. Devries, Photofragmentation of Ch_3Br in the A-Band, *Chem. Phys.*, 1985, **92**(1), 59–65.
22 J. G. Underwood and I. Powis, Photofragmentation of CH_3Br in red wing of the first continuum absorption band, *Phys. Chem. Chem. Phys.*, 2000, **1**, 747–756.
23 F. Y. Wang, M. L. Lipciuc, A. Kartakoullis, P. Glodic, P. C. Samartzis, X. M. Yang and T. N. Kitsopoulos, Slice imaging of methyl bromide photofragmentation at 193 nm, *Phys. Chem. Chem. Phys.*, 2014, **16**(2), 599–606.
24 M. L. Lipciuc and M. H. M. Janssen, High-resolution slice imaging of quantum state-to-state photodissociation of methyl bromide, *J. Chem. Phys.*, 2007, **127**, 224310.
25 Y. Song, X. M. Qian, K. C. Lau, C. Y. Ng, J. B. Liu and W. W. Chen, High-resolution energy-selected study of the reaction $CH_3X^+ \rightarrow CH_3^+ + X$: Accurate thermochemistry for the CH_3X/CH_3X^+ (X = Br, I) system, *J. Chem. Phys.*, 2001, **115**(9), 4095–4104.
26 X. Tang, X. Zhou, Z. Sun, S. Liu, F. Liu, L. Sheng and B. Yan, Dissociation of internal energy-selected methyl bromide ion revealed from threshold photoelectron-photoion coincidence velocity imaging, *J. Chem. Phys.*, 2014, **140**, 044312.
27 C. Escure, T. Leininger and B. Lepetit, Ab initio study of valence and Rydberg states of CH_3Br, *J. Chem. Phys.*, 2009, **130**(24), 244306.

28 H. R. Hrodmarsson, A. Kartakoullis, D. Zaouris, P. Glodic, H. Wang, P. C. Samartzis and A. Kvaran, Excitation Dynamics Involving Homogeneous Multistate Interactions: One and Two Color VMI and REMPI of HBr, *Phys. Chem. Chem. Phys.*, 2017, **19**(18), 11354–11365.
29 H. R. Hrodmarsson and Á. Kvaran, Revealing photofragmentation dynamics through interactions between Rydberg states: REMPI of HI as a case study, *Phys. Chem. Chem. Phys.*, 2015, **17**, 32517.
30 H. R. Hrodmarsson, H. Wang and A. Kvaran, State interactions and illumination of hidden states through perturbations and observations of new states: High energy resonance enhanced multiphoton ionization of HI, *J. Chem. Phys.*, 2015, **142**(24), 244312.
31 J. Long, H. Wang and A. Kvaran, Phtofragmentation, state interactions, and energetics of Rydberg and ion-pairstates: Resonance enhanced multiphoton ionization via E and V(B) states of HCl and HBr, *J. Chem. Phys.*, 2013, **138**(4), 044308.
32 P. Glodic, D. Zaouris, P. C. Samartzis, A. Hafliðason and Á. Kvaran, Effect of a triplet to singlet interaction on photofragmentation dynamics: Highly excited states of HBr probed by VMI and REMPI as a case study, *Phys. Chem. Chem. Phys.*, 2016, **18**(37), 26291–26299.
33 D. Zaouris, A. Kartakoullis, P. Glodic, P. C. Samartzis, H. R. Hrodmarsson and A. Kvaran, Rydberg and valence state excitation dynamics: a velocity map imaging study involving the E-V state interaction in HBr, *Phys. Chem. Chem. Phys.*, 2015, **17**(16), 10468–10477.
34 C. R. Gebhardt, T. P. Rakitzis, P. C. Samartzis, V. Ladopoulos and T. N. Kitsopoulos, Slice Imaging: A New Approach to Ion Imaging and Velocity Mapping, *Rev. Sci. Instrum.*, 2001, **72**(10), 3848.
35 V. Papadakis and T. N. Kitsopoulos, Slice Imaging and Velocity Mapping Using a Single Field, *Rev. Sci. Instrum.*, 2006, **77**(8), 5.
36 B. Zhang, J. Zhang and K. Liu, Imaging the "missing" bands in the resonance-enhanced multiphoton ionization detection of methyl radical, *J. Chem. Phys.*, 2005, **122**, 104310.
37 NIST Chemistry WebBook - (National Institute of Standards and Technology) https://webbook.nist.gov/chemistry/name-ser/, accessed Jan 2018.
38 See ESI†.

4.4.1 Supporting information

Multiphoton Rydberg & valence dynamics of CH_3Br probed by Mass Spectrometry and Slice Imaging

Arnar Hafliðason[2], Pavle Glodic[1], Greta Koumrianou[1],
Peter C. Samartzis[1]* and Ágúst Kvaran[2]*

1. *Institute of Electronic Structure and Laser, Foundation for Research and Technology-Hellas, Vassilika Vouton, 71110 Heraklion, Greece.*
2. *Science Institute, University of Iceland, Dunhagi 3, 107 Reykjavík, Iceland.*

Supplementary information

Content: **pages:**

Fig. S1:

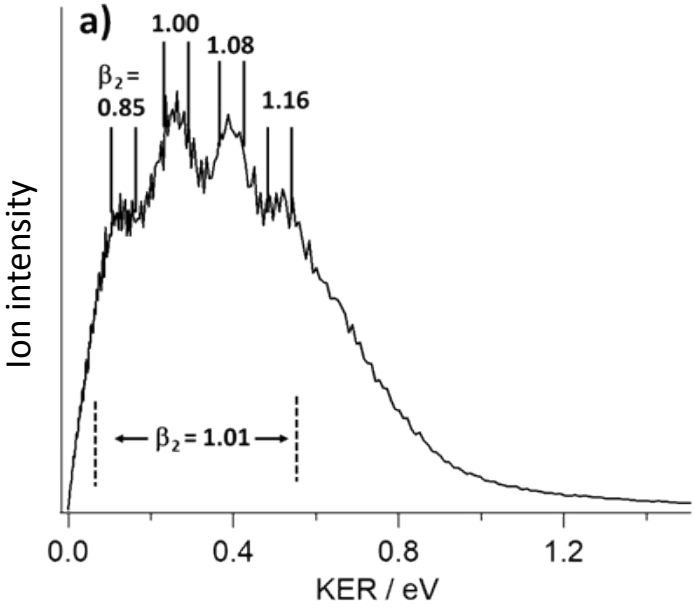

Figure S1-a: *CH_3 KER spectrum for peak 1, found in 2hv REMPI spectra at 66019 cm^{-1}.*

Fig. S1:

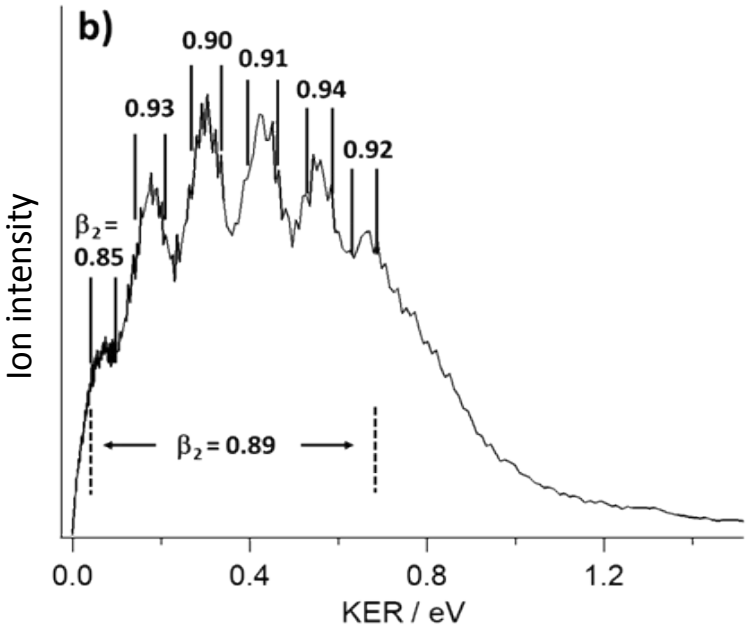

Figure S1-b: *CH_3 KER spectrum for peak 2, found in 2hv REMPI spectra at 66503 cm^{-1}.*

Fig. S1:

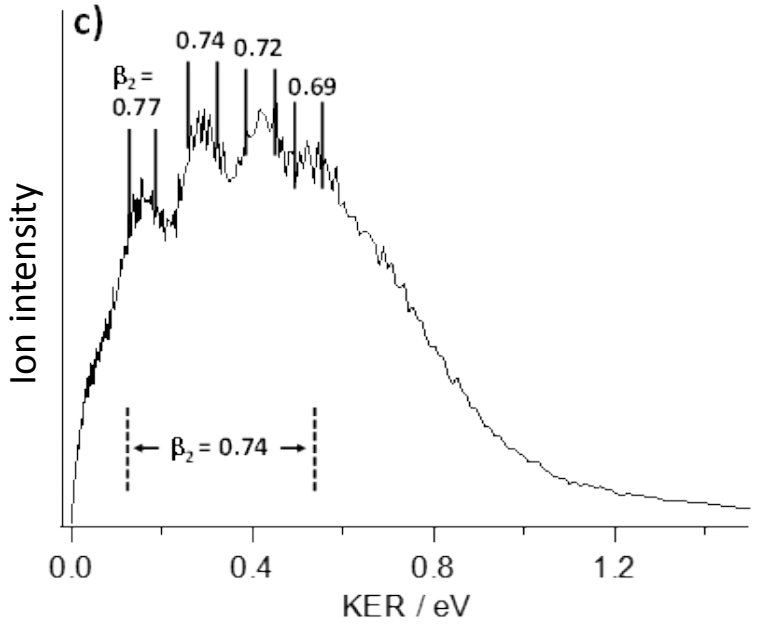

Figure S1-c: *CH_3 KER spectrum for peak 3, found in 2hv REMPI spectra at 67275 cm^{-1}.*

Fig. S1:

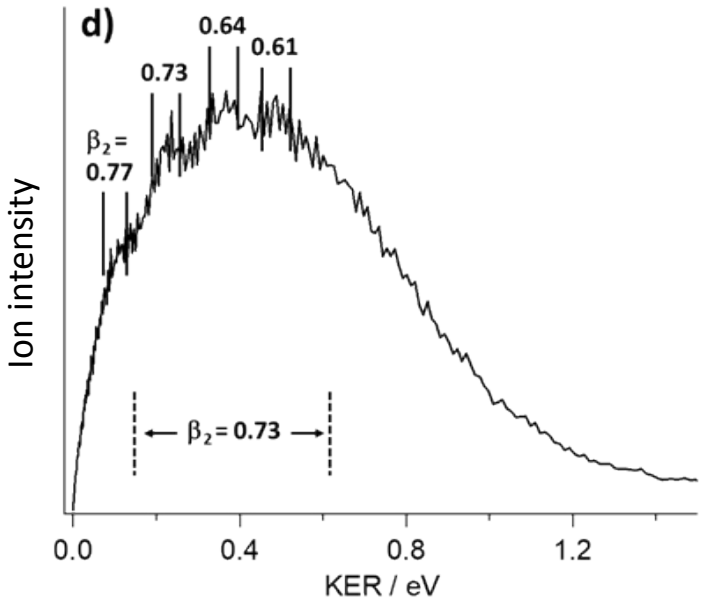

Figure S1-d: *CH_3 KER spectrum for peak 4, found in 2hv REMPI spectra at 68684 cm^{-1}.*

Fig. S1:

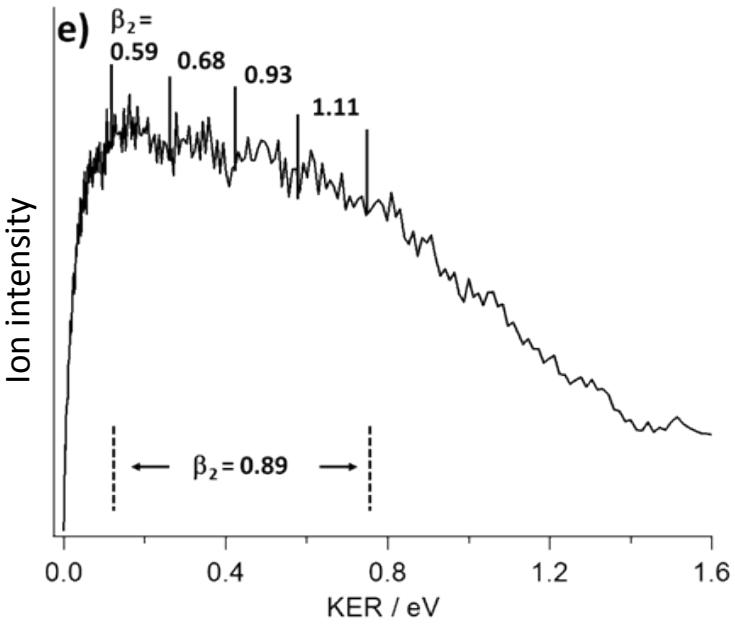

Figure S1-e: *CH_3 KER spectrum for peak 5, found in 2hv REMPI spectra at 72977 cm^{-1}.*

Fig. S1:

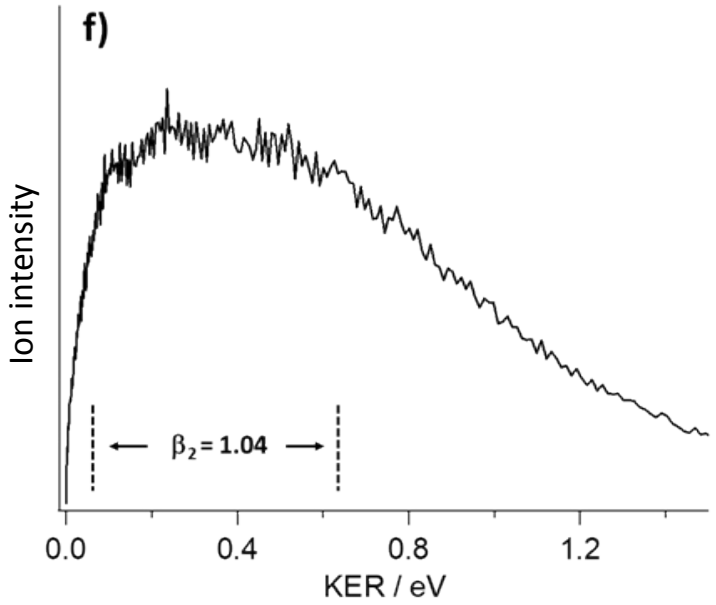

Figure S1-f: *CH_3 KER spectrum for peak 6, found in 2hv REMPI spectra at 74249 cm^{-1}.*

Fig. S1:

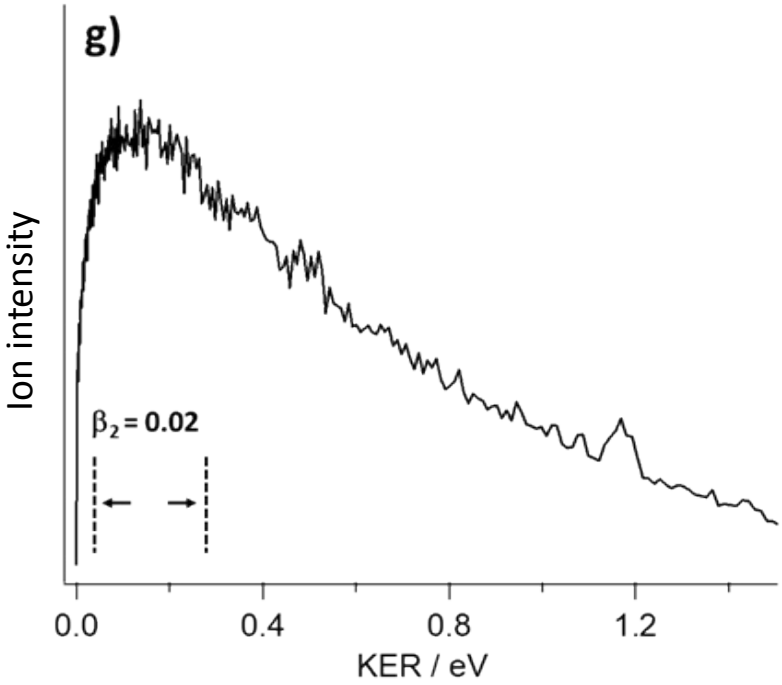

Figure S1-g: *CH_3 KER spectrum for peak 7, found in 2hv REMPI spectra at 75905 cm^{-1}.*

Fig. S1:

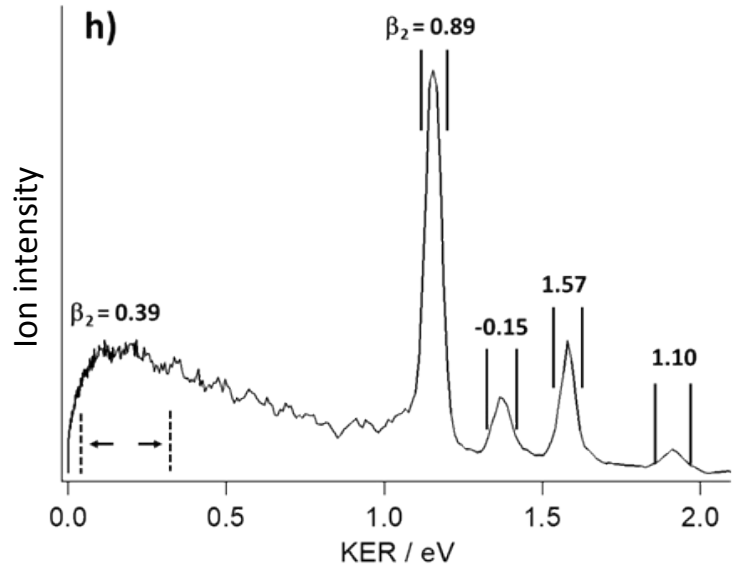

Figure S1-h: *CH_3 KER spectrum for peak 8, found in 2hv REMPI spectra at 77165 cm^{-1}.*

Fig. S1:

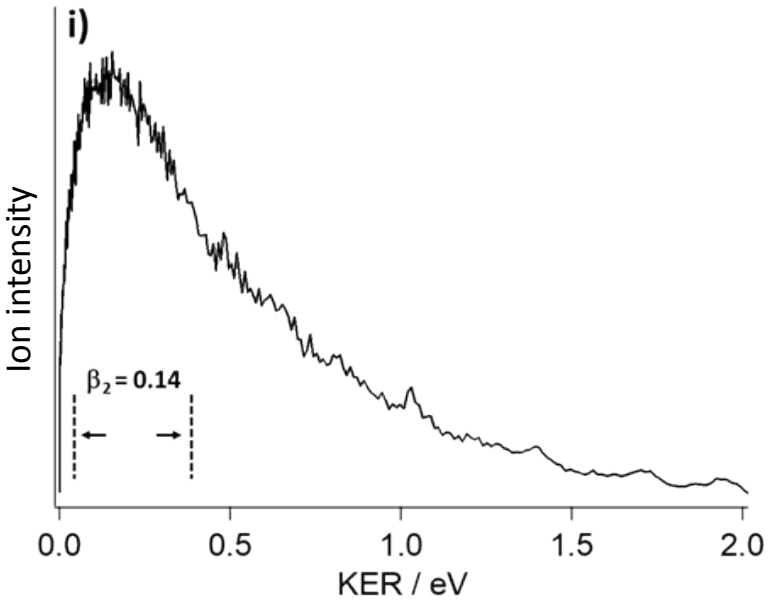

Figure S1-i: *CH_3 KER spectrum for peak 9, found in 2hv REMPI spectra at 78370 cm^{-1}.*

Fig. S1:

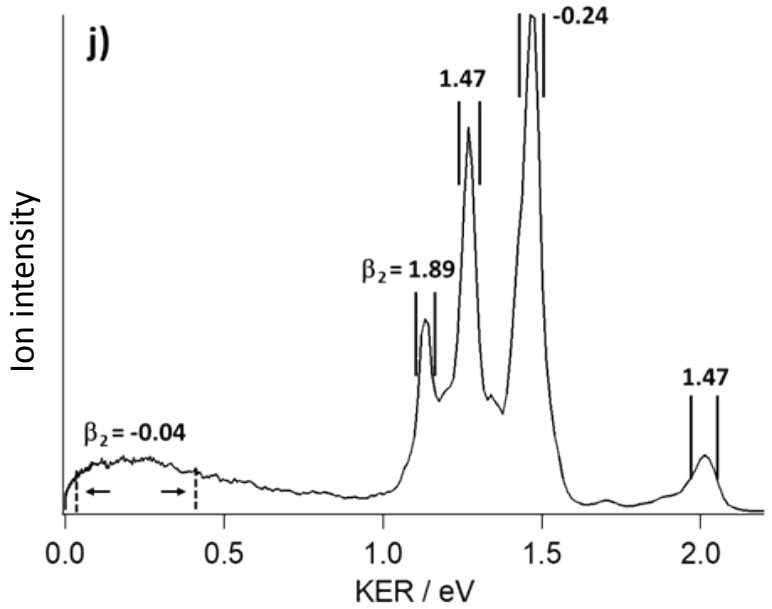

Figure S1-j: *CH_3 KER spectrum for peak 10, found in 2hv REMPI spectra at 79610 cm^{-1}.*

Fig. S2:

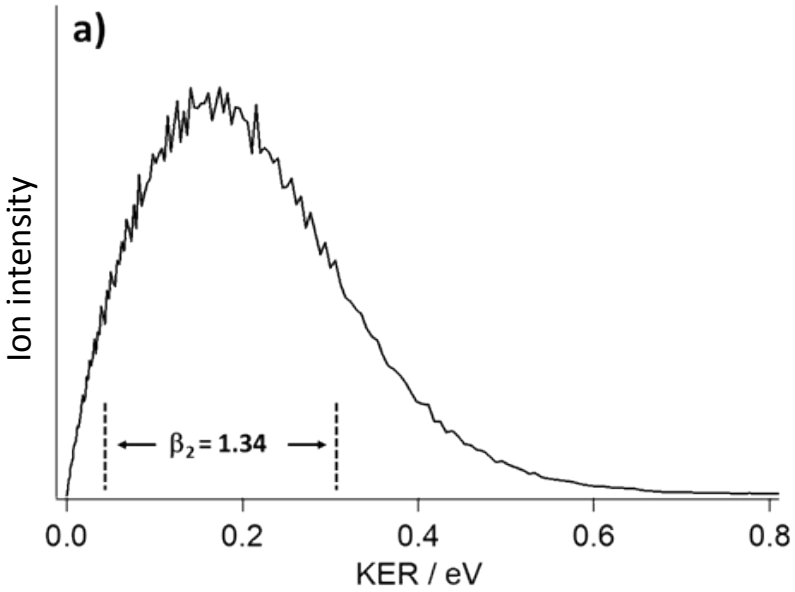

Figure S2-a: *Br KER spectrum for peak 1, found in 2hv REMPI spectra at 66019 cm^{-1}.*

Fig. S2:

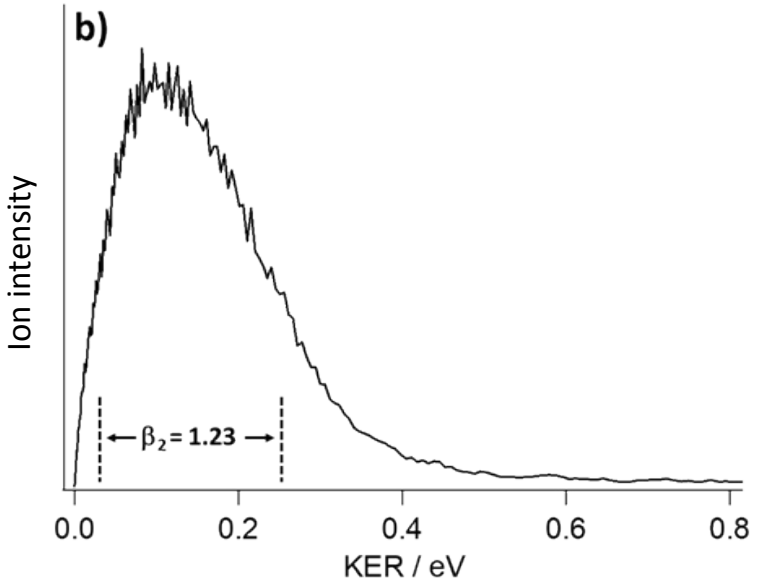

Figure S2-b: *Br KER spectrum for peak 3, found in 2hv REMPI spectra at 67275 cm^{-1}.*

Fig. S2:

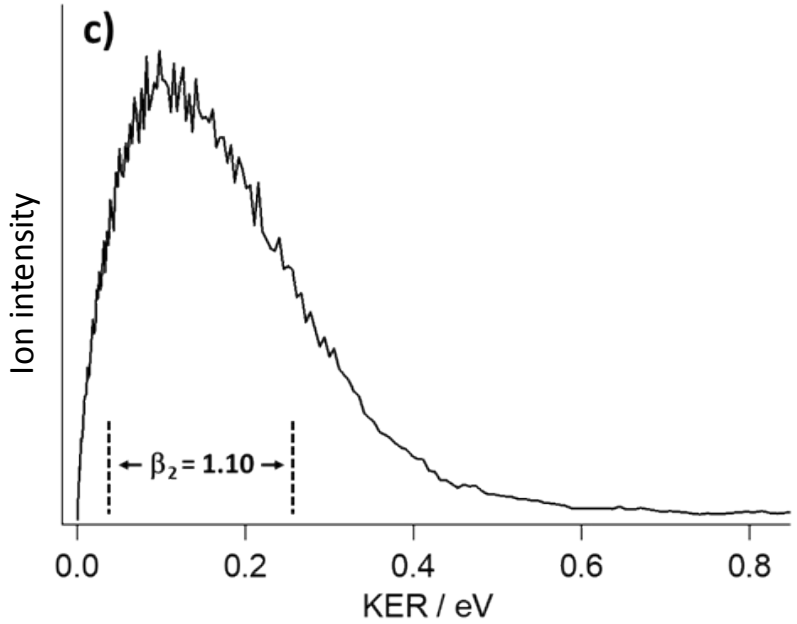

Figure S2-c: *Br KER spectrum for peak 4, found in 2hv REMPI spectra at 68684 cm^{-1}.*

Fig. S2:

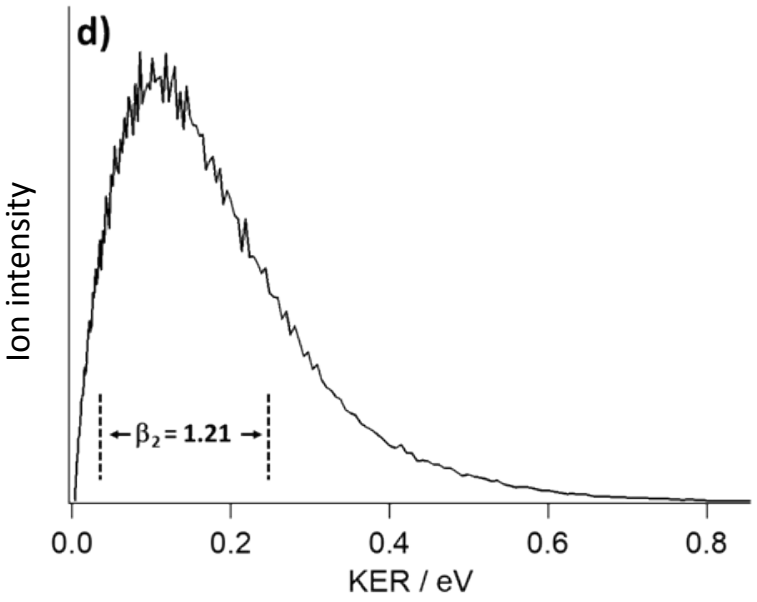

Figure S2-d: *Br KER spectrum for peak 5, found in 2hv REMPI spectra at 72977 cm^{-1}.*

Fig. S2:

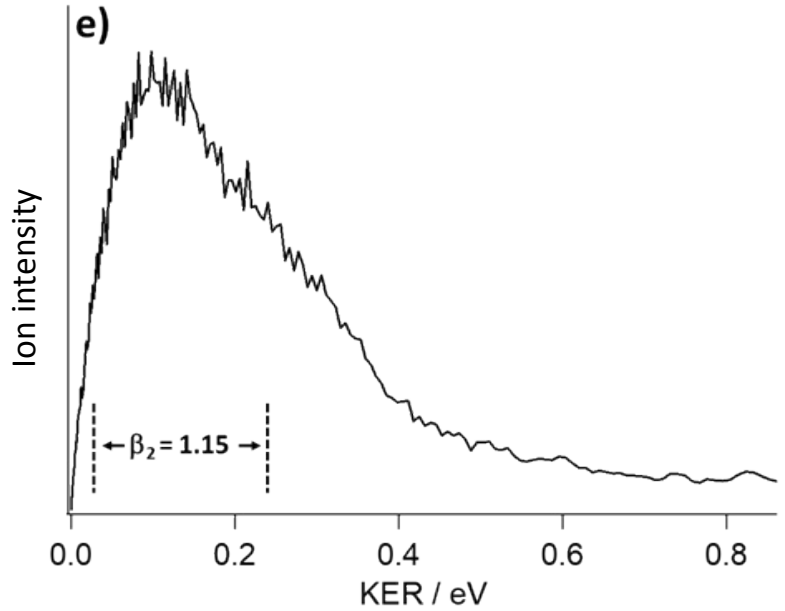

Figure S2-e: *Br KER spectrum for peak 7, found in 2hv REMPI spectra at 75905 cm^{-1}.*

Fig. S2:

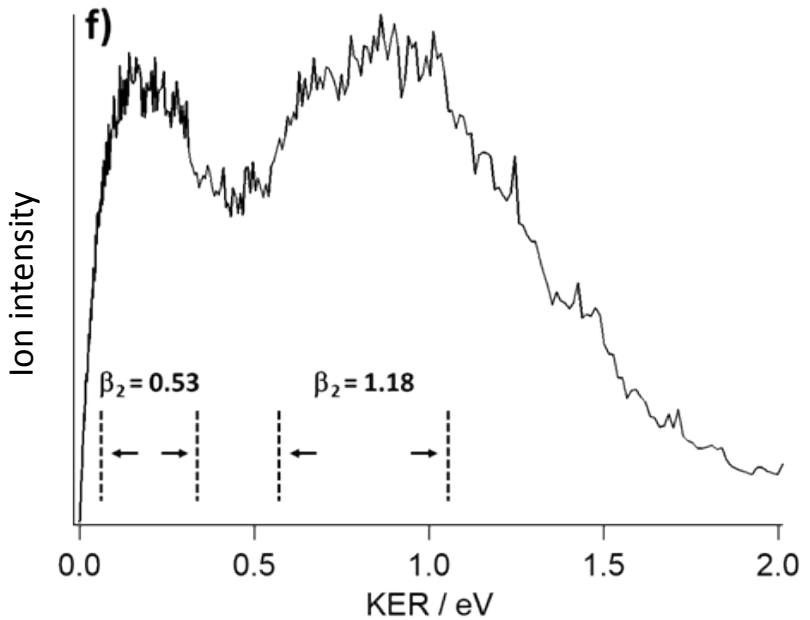

Figure S2-f: *Br KER spectrum for peak 8, found in 2hv REMPI spectra at 77165 cm^{-1}.*

Fig. S2:

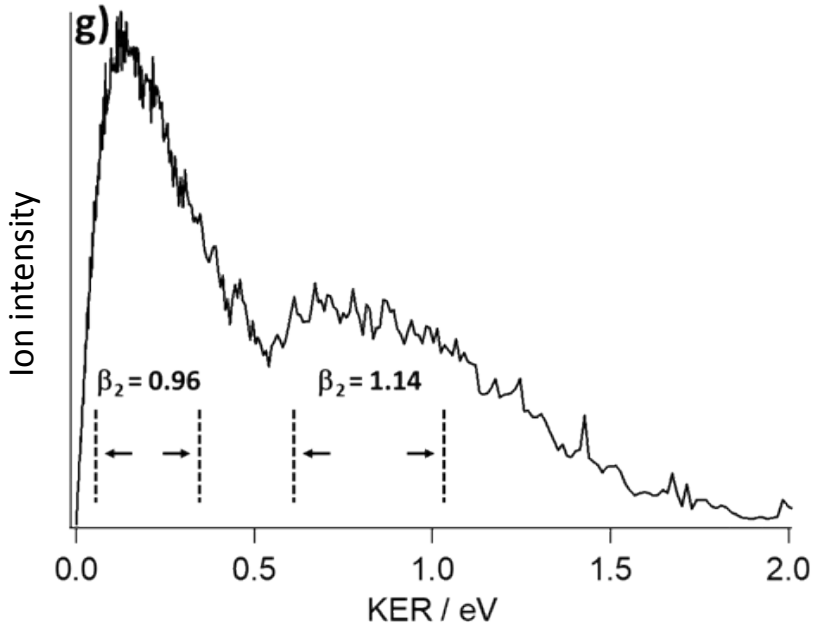

Figure S2-g: *Br KER spectrum for peak 9, found in 2hv REMPI spectra at 78370 cm^{-1}.*

Fig. S2:

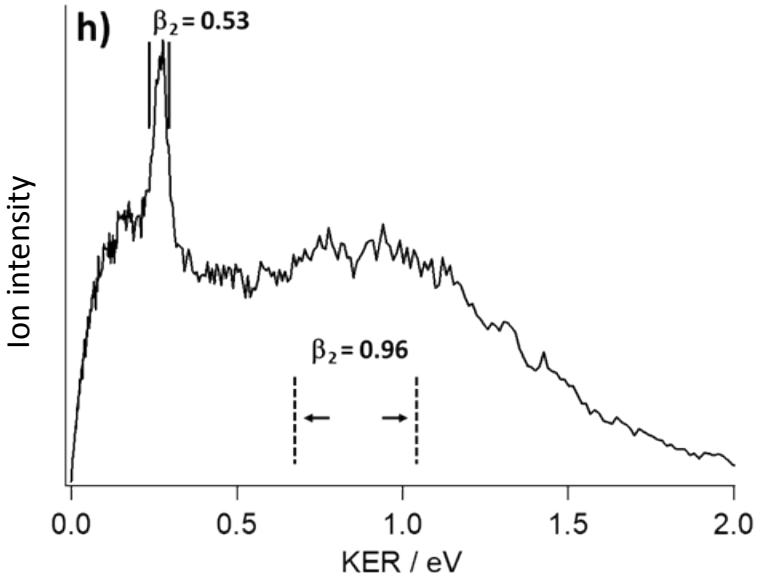

Figure S2-h: *Br KER spectrum for peak 10, found in 2hv REMPI spectra at 79610 cm^{-1}.*

Tables S1 a):

CH_3

	1			2			3			4		
	beta	Δ	**KER[eV]**	***beta***	Δ	**KER[eV]**	***beta***	Δ	**KER[eV]**	***beta***	Δ	**KER[eV]**
β_2	1.01	±0.01	0.098-0.533	0.89	±0.02	0.055-0.653	0.74	±0.02	0.133-0.533	0.73	±0.03	0.153-0.612
β_4	-0.38			-0.40			-0.45			-0.44		

	5			6			7			8		
	beta	Δ	**KER[eV]**	***beta***	Δ	**KER[eV]**	***beta***	Δ	**KER[eV]**	***beta***	Δ	**KER[eV]**
β_2	0.77	±0.01	0.126-0.788	1.04	±0.01	0.058-0.628	0.02	±0.01	0.024-0.272	0.39	±0.01	0.044-0.392
β_4	-0.07			-0.09			-0.03			-0.12		

	9			10		
	beta	Δ	**KER[eV]**	***beta***	Δ	**KER[eV]**
β_2	0.14	±0.01	0.021-0.392	-0.04	±0.01	0.018-0.453
β_4	-0.02			-0.02		

Tables S1 b):

Br

	1			2			3			4		
	beta	Δ	**KER[eV]**	***beta***	Δ	**KER[eV]**	***beta***	Δ	**KER[eV]**	***beta***	Δ	**KER[eV]**
β_2	1.34	±0.18	0.05-0.311		N/A		1.23	±0.01	0.033-0.235	1.10	±0.01	0.030-0.245
β_4	0.71				N/A		-0.10			-0.08		

	5			6			7		
	beta	Δ	**KER[eV]**	***beta***	Δ	**KER[eV]**	***beta***	Δ	**KER[eV]**
β_2	1.21	±0.01	0.055-0.220		N/A		1.15	±0.02	0.044-0.220
β_4	0.04				N/A		-0.05		

	8			9			10		
	beta	Δ	**KER[eV]**	***beta***	Δ	**KER[eV]**	***beta***	Δ	**KER[eV]**
β_2	0.53	±0.01	0.068-0.329	0.96	±0.02	0.050-0.329	0.31	±0.04	0.240-0.294
β_4	0.02			0.03			0.06		
β_2	1.18	±0.06	0.533-1.088	1.14	±0.06	0.612-1.088	1.20	±0.09	0.696-1.088
β_4	0.04			-0.15			0.15		

4.5 Paper 5

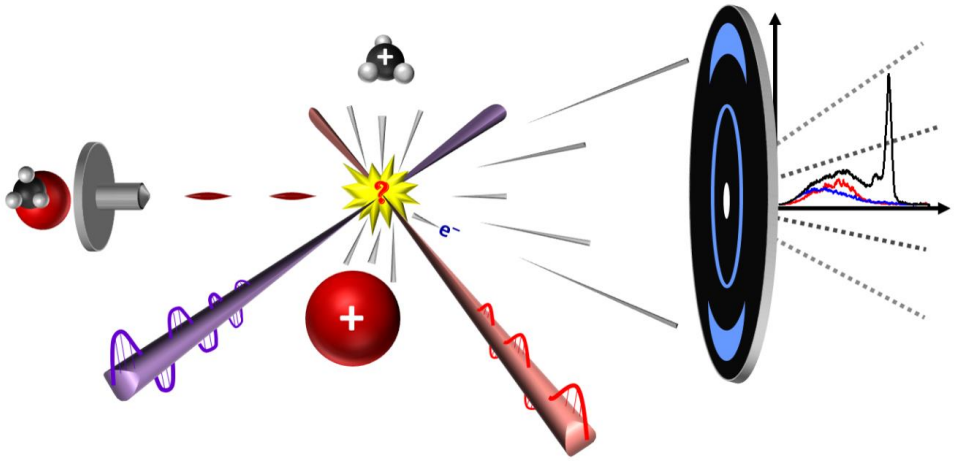

Arnar Hafliðason, Pavle Glodic, Greta Koumarianou, Peter C. Samartzis, Ágúst Kvaran. *Two-color REMPI study of CH_3Br, probing CH_3 and Br formation with MPI and Slice Imaging*. Physical Chemistry Chemical Physics, 2018, (*submitted*).

DOI: N/A

Two-color excitation dynamics of CH_3Br, probing CH_3 and Br formation with MPI and Slice Imaging

Arnar Hafliðason[1], Pavle Glodic[2], Greta Koumarianou[2],
Peter C. Samartzis[2]* and Ágúst Kvaran[1]*

1. *Science Institute, University of Iceland, Dunhagi 3, 107 Reykjavík, Iceland.*
2. *Institute of Electronic Structure and Laser, Foundation for Research and Technology-Hellas, Vassilika Vouton, 71110 Heraklion, Greece.*

Total number of pages in manuscript: 34
Tables: 1
Figures: 6
Supplementary information / ESI enclosed.
Manuscript file: "CH3Br_two_color"

*Correspondence should be addressed to:

Petros Samartzis
Permanent address:
Institute of Electronic Structure and Laser,
Foundation for Research and Technology-Hellas,
Vassilika Vouton, 71110 Heraklion, Greece
Phone: +30-2810-391467 (office)
Fax: +30-2810-391305
E-mail: sama@iesl.forth.gr

Ágúst Kvaran
Permanent address:
Science Institute, University of Iceland,
Dunhagi 3, 107 Reykjavík, Iceland
e-mail: agust@hi.is
www: https://notendur.hi.is/~agust/
Phone: +354-525-4800 (office)
Fax: +354-552-8911 (main office)

Graphical abstract:

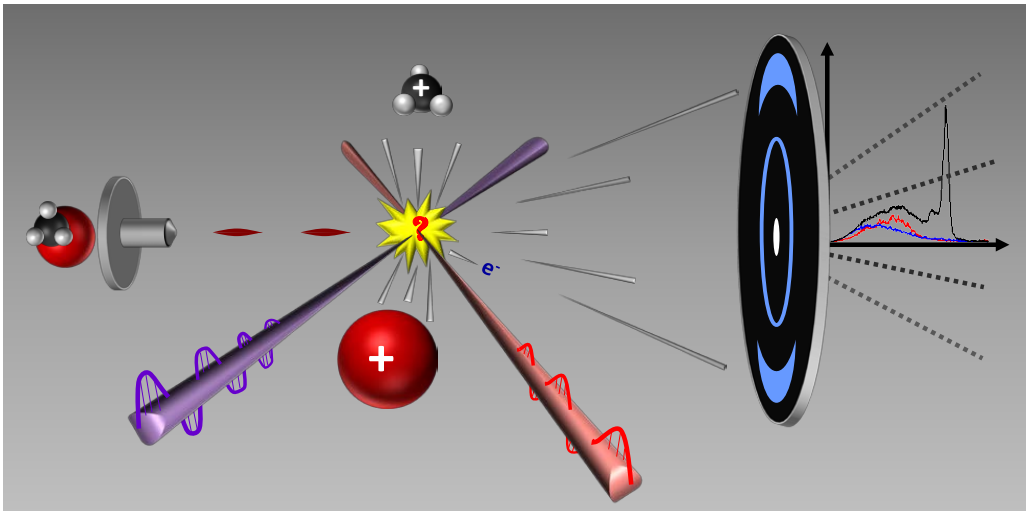

Abstract

Two-color, pump and probe experiments, were performed to explore the multiphoton dynamics of CH_3Br at high excitation energies. They involved initial two-photon resonant excitations to a number of np and nd Rydberg states (pump) followed by REMPI detection (probe) of the Br, Br* and $CH_3(X)$ photoproducts. Slice images of Br^+ and CH_3^+ ions were recorded in pump-only, probe-only and pump + probe experiments. Kinetic energy release spectra (KERs) as well as spatial anisotropy parameters were extracted from the images to identify the processes and the dynamics involved. In addition to dissociations following three-photon excitations via the p/d molecular Rydberg states, observed previously,[1] predissociation channels following the two-photon resonant excitations and non-resonant photodissociation forming $CH_3(X)$ and Br/Br* were identified and characterized. Furthermore, probe excitations for $CH_3(X)$ involved near-resonant excitations to lower energy 5s Rydberg states of CH_3Br. In three-photon excitation processes, a striking contrast is seen between excitations via the p/d and the s Rydberg states. Involvement of Rydberg to ion-pair state interactions in high energy photofragmentation processes are found to be evident.

I. Introduction

Significant emphasis has been placed on the photodissociation dynamics of the halocarbons for decades; in particular so for the methyl monohalides.[1-13] Whereas most attention has been on the photochemistry of methyl iodide (CH_3I) [14-28], less but substantial work has also been done on methyl bromide (CH_3Br) [1-4, 6, 9-12, 19, 20, 29-32]. Most of those studies have explored the dynamics of repulsive valence states in the A-band spectral region,[2-8] whereas less is known about the effect of excitations to higher energies where Rydberg states dominate the spectrum (hereby named "the Rydberg states region").[1, 9-13] Laser excitations by the method of resonance enhanced multi-photon ionization (REMPI) are suitable to access Rydberg states conveniently by use of visible or near-UV radiation.[1, 9, 11-13, 21, 22, 24, 25, 30, 33-36] Furthermore, more states may be accessed by the use of multiphoton excitation than by single-photon absorption due to selection rules.[37-40] State interactions gradually increase with excitation energy due to the larger density of states. This can cause spectral perturbations which may appear as line shifts and/or line broadenings.[41-46] Interactions between Rydberg states and the ion-pair / valence state, $CH_3^+Br^-$, could be involved in photoion pair formations, analogous to observations for some halogen-containing diatomic molecules.[47-51] By further analogy with observations for the hydrogen halides there is a reason to believe that Rydberg to ion-pair interactions are important in predissociation processes.[44, 45, 52-56]

REMPI data of CH_3Br for one-, two- and three-photon resonance excitations to series of Rydberg states have been reported.[9, 12, 13] In (2 + m) REMPI formation of CH_3^+ ions is found to dominate whereas parent ion signals are found to be negligible. Ion signals are typically found to vary as $CH_3^+ > CH_2^+ > CH^+ > (Br^+, CBr^+)$.[1, 9] Slice imaging experiments revealed neutral fragments of CH_3 in ground ($CH_3(X)$) and excited Rydberg states (CH_3^{**}) and bromine atoms in

ground ($Br(^2P_{3/2})$ henceforth denoted as "Br") and spin-orbit excited ($Br(^2P_{1/2})$ henceforth denoted as Br*) states to be formed prior to ionization to give CH_3^+ and Br^+.[1] The fragment species were found to be formed mainly: 1) by three-photon photodissociation via two-photon resonance excitations to Rydberg states, to give CH_3^{**} and Br or Br* and, 2) by one-photon photodissociation via non-resonant excitation to repulsive valence states (the A-band) to give $CH_3(X)$ and Br/Br*. Surprisingly no clear evidence was observed for two-photon photodissociation channels via predissociation of the resonance Rydberg states. Ion signals due to process 1 (resonance contributions) appear as sharp peaks in REMPI spectra (**Fig. 1a**) but as broad features peaking at low kinetic energies in images and KER distributions (KERs). The sharp REMPI peaks are two-photon resonance excitations to CH_3Br Rydberg states (CH_3Br^{**}) and the broad KERs are due to energy redistribution among the molecule's internal degrees of freedom prior to dissociation in metastable states. Ion signals due to process 2 (non-resonance contributions) appear as a broad underlying continuum in the REMPI spectra (**Fig. 1a**) and as sharp peaks in KER distributions. The broad continuum in REMPI spectra and the sharp KERs are the signals expected for direct non-resonant, prompt one-photon photodissociation of CH_3Br.

In this paper we present data and analysis of two-color (pump and probe) multiphoton excitations for CH_3Br. A pump laser pulse was typically set at a wavelength corresponding to two-photon resonance excitation to a chosen vibrational level of a Rydberg state in the wavenumber region of 66 000 – 80 000 cm^{-1}. A probe laser pulse was tuned to specific REMPI lines of the fragment species Br, Br* and CH_3 in the ground electronic state and various vibrational modes (v_1,v_2,v_3,v_4) (i.e. $CH_3(X,v_1v_2v_3v_4)$) for detection. This allowed quantum-state-selective detection of neutral photofragments and revealed additional processes (predissociation following two-photon excitation) and more details concerning fragmentation channels than by use of the one-color excitation scheme.

II. Experimental

The VMI/Slicing apparatus used in this work has been described in detail before,[57, 58] so only a brief description is given here. A molecular beam of 20% CH_3Br in He (around 1 bar total backing pressure) is formed by supersonic expansion through a home-made piezoelectrically-actuated nozzle valve (ø1mm diameter) and skimmed (ø1.5 mm, Beam Dynamics) before it enters the detection chamber where the ion optics are positioned. The collimated molecular beam is intersected at right angles by the pump and photoionization lasers at the geometric focal point of a single-electrode repeller-extractor plate arrangement. The CH_3, Br and Br* photofragment images were recorded in two-color experiments where the pump laser was used for excitation of the parent molecule and the photoionization laser was used for (2 + 1) REMPI detection of the photofragments. The pump and the photodissociation laser beams (typically 2-3 mJ/pulse) were generated by (1) a pulsed Nd^{3+}:YAG laser (Spectra Physics Quanta Ray Pro 250) pumping a master oscillator - power oscillator system (Spectra Physics MOPO 730-D10), and (2) by frequency doubling of the output of an excimer-pumped (Lambda-Physik LPX300, operating with XeCl) dye laser (LPD3000) using the appropriate dyes. The CH_3 photofragments were probed via the 0_0^0 (333.5 nm), 1_1^1 (333.9 nm), 2_1^1 (329.5 nm) and 2_2^2 (325.8 nm) transitions from the ground electronic state $CH_3(X)$ to the Rydberg state CH_3**(3p, $^2A_2$).[59] The probe laser transitions used for the detection of Br and Br* photofragments were $Br(^2P_{3/2}) \rightarrow\rightarrow 5p\ (^4P^0_{3/2})$ at 266.634 nm (two-photon wavenumber: 75 009.13 cm^{-1}) and $Br^*(^2P_{1/2}) \rightarrow\rightarrow 5p(^2D^0_{3/2})$ at 266.697 nm (two-photon wavenumber: 74 991.41 cm^{-1}).[60] The probe laser pulses were delayed with respect to the photolysis pulse, in order to allow a sufficient density of photofragments to build up prior to REMPI detection. Moreover, the time delay had to be carefully adjusted in order

to avoid ‘‘fly-out’’ of the photofragments. Typically, the delay was set in the range of about 0 – 5 ns. For the slicing experiments reported here, the repeller is pulsed ON at the appropriate time delay (~300 ns) following the photolysis/ionization. The photofragments traverse a field-free time-of-flight region (45 cm) and a gated, position-sensitive detector (dual, imaging-quality MCP array coupled to a phosphor screen) images the center slice of the photofragment sphere. The image frame is recorded asynchronously every second (~10 laser shots) by a CCD camera and several thousand frames are averaged to form images such as those shown in **Fig.2a**. Each final image is integrated from its center over angle to extract the speed and over radius to extract the angular distributions of the corresponding fragments**.**

III. Results and analysis

A. Mass resolved MPI

The (2 + *m*) REMPI spectrum for CH_3^+ from reference [9] for the two-photon resonant excitation region of 66 000 – 80 000 cm^{-1} is reproduced in **Fig. 1a**. The relative ion intensities, $I(M^+)/I(CH_3^+)$, for $M^+ = CH_2^+$, CH^+ and Br^+ are found to vary with wavenumber and to reach maxima as the wavenumber values get closer to the ion-pair threshold ($CH_3^+ + Br^-$) whereas those for $M^+ = CBr^+$ remain unchanged (see **Fig. 1b** and reference [60]). This suggests some interaction between the Rydberg and ion-pair states and will be further discussed in Section IV.

B. Slice images and kinetic energy release spectra (KERs)

i. Br/Br*

Br^+ ion slice images (**Fig. 2a**) were recorded for MPI of CH_3Br and kinetic energy release distributions (KERs) were derived from the images. First (1; pump excitation), images for excitations corresponding to (2 + *m*) REMPI for resonant excitation to total of five molecular Rydberg states, in the two-photon excitation region of 66 000 – 80 000 cm^{-1} were recorded (see **Table 1** and **Figs. 1a** and **2a.i**). Second (2; probe excitation), images for resonance excitations of Br and/or Br* fragments (see Section II above) were recorded (see **Figs. 2a.ii**). Third, (3; pump and probe) images for pump excitations followed by probe excitations were recorded (see **Figs. 2a.iii**).

The KERs for the pump excitations (1) either exhibit a broad spectral structure or a vibrational structure peaking at low kinetic energies in the region of about 0.1 eV (**Figs. 2b - 2c**). This signal has been attributed to a three-photon excitation process to superexcited molecular Rydberg states,[1] via the resonant excited Rydberg states, followed by photodissociation to form Br/Br* along with Rydberg states of CH_3 (CH_3**) prior to three-photon non-resonant ionization of Br/Br*, i.e.

$$CH_3Br + 2h\nu \rightarrow CH_3Br^{**}(p/d\ Ry;\ v_1v_2v_3)\ ; \qquad \text{resonant transition} \qquad (1a)$$

$$CH_3Br^{**}(p/d\ Ry;\ v_1v_2v_3) + 1h\nu \rightarrow CH_3Br^{\#}\ ; \qquad \text{photoexcitation} \qquad (1b)$$

$$CH_3Br^{\#} \rightarrow CH_3^{**}(Ry;\ v_1v_2v_3v_4) + Br/Br^*\ ; \qquad \text{dissociation} \qquad (1c)$$

$$Br/Br^* + 3h\nu \rightarrow Br^+ + e^- \qquad \text{photoionization} \qquad (1d)$$

where CH_3Br^{**}(Ry; $v_1v_2v_3$) represents vibrational levels v_1, v_2, v_3 of a parent molecular Rydberg state and $CH_3Br^{\#}$ represents one or more superexcited state. The vibrational structure observed corresponds to formation of vibrationally excited $CH_3^{**}(3p\ ^2A_2)$ fragments in the umbrella / bending mode, v_2 (i.e. CH_3^{**} ($3p\ ^2A_2$; $0v_200$).[1, 61] The vibrational structure observed in the Br^+ KERs is found to be "out of phase" with respect to that observed for CH_3^+ in the sense that peaks in the CH_3^+ KERs match troughs in the Br^+ KERs and vice versa.[61]

The images and KERs for the probe excitations (2) show clear rings and peaks, respectively (**Figs. 2a - 2c**). The KER peaks typically appear slightly below and slightly above 0.2 eV KER for the Br* and Br detections, respectively. As seen in **Fig. 1a**, the probe excitations of Br and Br* correspond to non-resonant excitations within the CH_3Br molecule. Therefore, the KERs can be attributed to one-photon non-resonant transitions to repulsive valence states (A band) followed by dissociation (i.e. direct photodissociation) to form Br and Br* along with CH_3 prior to (2 + 1) REMPI of Br/Br*, i.e.

$$CH_3Br + 1h\nu \rightarrow CH_3Br^* ; \qquad \text{non-resonant transition} \qquad (2a)$$

$$CH_3Br^* \rightarrow CH_3(X,v_1v_2v_3v_4) + Br/Br^* ; \qquad \text{dissociation} \qquad (2b)$$

$$Br/Br^* + 2h\nu \rightarrow Br^{**} ; \qquad \text{resonant transition} \qquad (2c)$$

$$Br^{**} + 1h\nu \rightarrow Br^+ + e^- \qquad \text{photoionization} \qquad (2d)$$

where CH_3Br^* represents a repulsive valence state, $CH_3(X,v_1v_2v_3v_4)$ refers to the ground electronic state of CH_3 and vibrational levels v_1,v_2,v_3,v_4 and Br** refers to bromine atomic Rydberg states.

Images and KERs for the pump and probe excitations (3) show the same features as in (1; pump) and (2; probe) as well as additional signal which extends to higher KER (see **Figs. 2a - 2c** and **3a - 3b**). Due to the Br/Br* resonance detection/probing, signals detected in one-color (pump) excitations will be enhanced and otherwise weak or undetected Br/Br* may appear. Thus the signals due to the three-photon excitation processes (eqs. (1)) clearly appear in the pump-probe signal as shoulders at low KER. Signals formed by one-photon non-resonant photodissociation processes analogous to eqs. (2) also appear in the pump-probe signal (near 0.2 eV). The relative contribution of the high KER component to that of the (1; pump) component is found to be comparable for all the KERs recorded for the Br detection on one hand and for the Br* detection on the other hand, whereas the relative contribution of the probe components varies with excitation wavelength. This suggests that the initial resonance excitation process (eq. 1a) is common for both processes involved. Furthermore, thresholds for formation of $CH_3(X,0000)$ + Br/Br* after two-photon resonance excitations are found to be close to the high energy edges of the KERs for the Br and Br* detections, respectively (see **Figs. 3a - 3b**). The high KER contributions, therefore can be assigned to the stepwise processes,

$$CH_3Br + 2h\nu \rightarrow CH_3Br^{**}(Ry; v_1v_2v_3)\ ; \qquad \text{resonant transition} \qquad (3a)$$

$$CH_3Br^{**}(Ry; v_1v_2v_3) \rightarrow CH_3(X,v_1v_2v_3v_4) + Br/Br^*; \quad \text{predissociation} \qquad (3b)$$

$$Br/Br^* + 2h\nu \rightarrow Br^{**}\ ; \qquad \text{resonant transition} \qquad (3c)$$

$$Br^{**} + 1h\nu \rightarrow Br^+/Br^{*+} + e^- \qquad \text{photoionization} \qquad (3d)$$

Since the kinetic energy release of the Br^+ ions formed is determined by the initial step (3a) it is convenient to compare the corresponding KERs contributions on a relative two-photon energy scale $\Delta(2h\nu) = 2h\nu_i - 2h\nu_0$, where ν_0 and ν_i are two-photon excitation frequencies of a reference

spectrum (ν_0) and a spectrum i (ν_i) for $\nu_0 > \nu_i$) weighted by the mass ratio factor for Br, f(Br) = m(CH_3)/m(CH_3Br), to take account of the conservation of momentum. Thus, spectral peaks due to the formation of the same species/thresholds, $CH_3(X,\nu_1\nu_2\nu_3\nu_4)$ + Br/Br*, will match. This has been carried out in **Figs. 3a - 3b**, which shows the KERs shifted by the weighted two-photon energy difference ($\Delta(2h\nu)$*f (Br)) where the ‘‘zero kinetic energy released’’ for image / KER no. (5) (see **Table 1**) has been set to zero (reference spectrum). The corresponding thresholds for the formation of $CH_3(X,0000)$ + Br and Br* are shown in **Figs. 3a** and **3b**, respectively.

Closer investigation of the high KER components reveals the following observations and interpretations:

i) The high KER / two-photon excitation contributions appear as high energy peaks for the Br* detections but as broader overlapping structures for the Br detections (**Figs. 3a – 3b**). Furthermore, comparable shape of sharp peaks is observed in the KERs of Br* derived for resonance transitions to 5p molecular Rydberg states (images / KERs no. (1) – (3)), whereas broader structures are observed for transitions to higher energy 4d Rydberg state (no. (4) and (5)) (see **Figs. 1a** and **3b** and **Table 1**). Broad KERs are indications of an energy redistributed among the molecule’s internal degrees of freedom prior to dissociation, whereas sharper KERs indicate less such effect associated with a different delay prior do dissociation.[1] We, therefore, first, conclude that the lifetime of the 5p molecular Rydberg states, with respect to predissociation (eq. 3b) to form Br* is shorter than those of the 4d states, and second, that the lifetime of the 5p state, with respect to formation of Br* is shorter than that with respect to formation of Br.

ii) The relative signal intensity of the high KER / two-photon excitation components to the (1; pump) / three-photon excitation component is significantly larger for Br* than for Br (see **Figs. 2a – 2c** and **3**). Since both processes involve two-photon resonance excitations prior to predissociation on the one hand (3; high KER component) and prior to additional one-photon excitation on the other hand (1) this observation indicates a competition between these two secondary processes. This suggests that the formation of Br* by predissociation is more favourable than by three-photon excitation via $CH_3Br^{\#}$, whereas the formation of Br by predissociation is less favourable than by three-photon excitation via $CH_3Br^{\#}$. This further indicates that the bending mode vibrational structures observed following three-photon excitation both in the Br^+ and CH_3^+ KERs (see above) are more favourable for formation of the CH_3**(3p $^2A_2$, $0v_200$) fragments along with Br rather than Br*.

ii. CH_3

CH_3^+ ion slice images (**Fig. 4a**) were recorded for MPI of CH_3Br and kinetic energy release spectra (KERs) were derived from the images. Recordings were made for excitations corresponding to (2 + *m*) REMPI for resonant excitation to a total of three molecular Rydberg states, in the two-photon excitation region of 66 000 – 80 000 cm^{-1} (see **Table 1** and **Figs. 1a** and **4a**). Analogous to the recording or the Br^+ images as described in previous section (III, B, Br/Br*) images were recorded (1) -for pump excitations (see **Fig. 4a.i**), (2) -for probe excitations of $CH_3(X; v_1v_2v_3v_4)$ fragments (see Section II above) (see **Figs. 4a.ii**) and (3) -for pump and probe excitations (see **Figs. 4a.iii**).

The KERs for the pump excitations (1) exhibit a broad spectral structure peaking at low kinetic energies in the region of about 0.2 eV (**Figs. 4b**). This structure has been attributed to the three-photon excitation process and dissociations according to eqs. (1a) – (1c) above prior to one-photon ionization of CH_3**(Ry; $v_1v_2v_3v_4$).[1]

The images and KERs for the probe excitations (2) show vibrational structures (**Figs. 4a.ii**, **4b** and **5**) of a frequency corresponding to an out of plane / umbrella vibrational mode (v_2) for CH_3^+ and CH_3 fragments.[62] KERs recorded for different CH_3(X, $v_1v_2v_3v_4$) probe wavelengths (see section II) show vibrational peaks to line up reasonably well / within experimental error on a weighted relative one-photon energy scale ($\Delta(1h\nu)$*f (CH_3); $\Delta(1h\nu) = 1h\nu_i - 1h\nu_0$; see definitions in section III, B, Br/Br* for comparison) (see **Fig. 5**). The probe excitations used, correspond to near-resonant two-photon transitions to 5s CH_3Br molecular Rydberg states.[61] Furthermore, images of CH_3^+ showing vibrational structure obtained by one-color excitations in this region have been attributed to three-photon excitation process followed by autoionization and one-photon photodissociation of CH_3Br^+(*X3/2*) to form CH_3^+(X,0$v_2$00) for different v_2 levels.[12] **Fig. 5** shows some relevant thresholds. We conclude that the KERs can be assigned to the stepwise processes,

$CH_3Br + 2h\nu \rightarrow CH_3Br^{**}(5s\ Ry;\ v_1v_2v_3)$;	near-resonant transition	(4a)
$CH_3Br^{**}(5s\ Ry;\ v_1v_2v_3) + 1h\nu \rightarrow CH_3Br^{\#}$;	photoexcitation	(4b)
$CH_3Br^{\#} \rightarrow CH_3Br^+(X3/2) + e^-$;	autoionization	(4c)
$CH_3Br^+(X3/2) + 1h\nu \rightarrow CH_3Br^{+*}$;	photoexcitation	(4d)
$CH_3Br^{+*} \rightarrow CH_3^+ (X,0v_200) + Br/Br^*$	dissociation	(4e)

Analysis of the vibrational structure reveal a vibrational progression of frequency corresponding to $\omega_e = 1382 \pm 25$ cm^{-1} for the bending mode of $CH_3^+(X,0\nu_2 00)$. This is to be compared with the vibrational value of 1359 ± 7 cm^{-1} reported for $CH_3^+(X)$ in NIST.[62] Observation of a single vibrational progression suggests that either one of the two formation channels (4e) is dominant. By analogy with our observations concerning the Br images mentioned above and by considering the different energetics we believe that formation of CH_3^+ $(X,0\nu_2 00)$ along with Br dominates that of its formation along with Br*.

Images and KERs for the pump and probe excitations (3) show structures corresponding to overlap of those observed the (1; pump) and (2; probe) data as well as two sharp peaks at high KER (see **Figs. 4a.iii** and **4b**), lower intensity inner rings and higher intensity outer rings. KERs plotted on a weighted relative one-photon energy scale ($\Delta(1h\nu)$*f (CH_3); $\Delta(1h\nu) = 1h\nu_i - 1h\nu_0$; see definitions in section III, B, Br/Br* for comparison) show the positions of these peaks to match common thresholds for the various $CH_3(X, \nu_1\nu_2\nu_3\nu_4)$ + Br/Br* formations by one-photon photodissociation. We, therefore, conclude that these high KER peaks are due to direct one-photon photodissociation followed by detection of $CH_3(X, \nu_1\nu_2\nu_3\nu_4)$ by (2 + 1) REMPI, i.e.,

$$CH_3Br + 1h\nu \rightarrow CH_3Br^*; \qquad \text{non-resonant transition} \qquad (5a)$$

$$CH_3Br^* \rightarrow CH_3(X,\nu_1\nu_2\nu_3\nu_4) + Br/Br^*; \qquad \text{dissociation} \qquad (5b)$$

$$CH_3(X,\nu_1\nu_2\nu_3\nu_4) + 2h\nu \rightarrow CH_3^{**}(3p\ ^2A_2;\ \nu_1\nu_2\nu_3\nu_4); \qquad \text{resonant transition} \qquad (5c)$$

$$CH_3^{**}(3p\ ^2A_2;\ \nu_1\nu_2\nu_3\nu_4) + 1h\nu \rightarrow CH_3^+ + e^- \qquad \text{photoionization} \qquad (5d)$$

In all cases the signals for the $CH_3(X,\nu_1\nu_2\nu_3\nu_4)$ + Br* formations are found to be noticeably less than those for $CH_3(X,\nu_1\nu_2\nu_3\nu_4)$ + Br formations.

C. Angular distributions:

Significant variations in angular distributions are observed for the Br^+ and CH_3^+ ions depending on the rings / channels involved (see **Figs. 2a** and **4a**). In an attempt to quantify the anisotropy of the rings, angular distributions, in the form of signal intensities as a function of the angle from 0 to 180°, derived from the images, were fitted by the simplified expression corresponding to a one-step photodissociation[12, 56-58]

$$P(\theta) = A\left[1 + \beta_2 P_2(\cos(\theta)) + \beta_4 P_4(\cos(\theta))\right] \quad (6)$$

to derive the anisotropy parameters β_2 and β_4.[61] P_2 and P_4 are the second and fourth order Legendre polynomials and A is a scaling factor. The β_2 parameter, which can be in the range between +2 (purely parallel transition) to -1 (purely perpendicular transition), can be related to the overall transition symmetry and the corresponding dynamics.

i. Br/Br*

The Br^+ images (no. 1 – 5) for the pump excitations (1) display shapes corresponding to dominant parallel transitions with positive values of β_2 in the range between about 1.1 – 1.4 for the broad low KER peaks as shown before.[1] These signals are due to a total of three-photon excitation prior to dissociation (1a – c) as well as possible state mixing. Therefore, these results cannot be easily interpreted. However the involvement of two-photon resonant parallel transitions corresponding of dominant halogen p orbital to p/d Rydberg orbital transitions (see **Fig. 1a**) could be a controlling factor in determining the effective anisotropy.

The images for the probe excitations (2) display shapes corresponding to purely parallel transitions with β_2 values of about +2 for Br* detection (**Fig.2a** and *ref.* [30]) but shapes corresponding to virtually isotropic transitions with β_2 values of about 0 for Br detection.[61] The former observation ($\beta_2 \approx +2$) is in agreement with formation of Br* along with $CH_3(X)$ by one-photon photodissociation by a parallel transition from the ground state to the $^3Q_0$ state followed by a dissociation on the same (*i.e.* the diabatic) potential curve.[7] The latter observation ($\beta_2 \approx 0$) could be due to a combination of one-photon photodissociation by parallel and perpendicular transitions to $^3Q_0$ and $^3Q_1/^1Q_1$, respectively, followed by dissociations, involving curve crossing, to form Br and $CH_3(X)$.[7]

The images for the pump and probe excitations (3) (see **Fig. 2a**) display shapes at low KER analogous to those observed for the pump excitations (1) (see above) and rings in the intermediate KER region analogous to those observed for the probe excitations (2) (see above). In addition they display broad shapes (and KERs) at high KER corresponding to dominant perpendicular transitions with negative values of β_2 in the range between about -0.5 to -1 for the two-photon resonance transitions to the p-orbital Rydberg states (images no. 1,2 and 3) both for Br* and Br detections. On the other hand they display broad shapes (and KERs) at high KER corresponding to dominant parallel transitions with positive β_2 values of about +0.5 for the two-photon resonance transitions to the d-orbital Rydberg states (images no. 4 and 5) both for Br* and Br detections.[61] This must be associated with the difference in the two-photon transitions to the p and d molecular Rydberg states, prior to predissociation.

ii. CH_3

The CH_3^+ image no. 4 for the pump excitations (1) displays shape corresponding to dominant parallel transitions with a positive β_2 value of about 0.75 for the broad low KER peak as shown before,[1] similar to that observed for the corresponding Br^+ image (see above) as might be expected for fragments formed by the same channels (1a – c), prior to ionization. The CH_3^+ corresponding images no. 6 – 7, on the other hand display shapes of virtually isotropic transitions with β_2 values of about 0.

All the images for the probe excitations (2), which show vibrational structures, display ring shapes corresponding to dominant parallel transitions (**Fig. 4a.ii**) with positive β_2 -values in the range of about +1 to +1.5. This is in close agreement with the observations made by Wang *et al.*,[12] who attributed it to parallel transitions from $CH_3Br^+(X)$ to the first excited electronic state of the ion ($CH_3Br^+*(A)$) followed by dissociation (see eqs. 4d – e) by assuming C_s symmetry for the dissociative molecular ion.[63]

The images for the pump and probe excitations (3) (see **Fig. 4aiii**) display shapes at low and intermediate KER analogous to those observed for the pump (1) and probe (2) excitations (see above). In addition they display shapes of the sharp rings (sharp peaks) at high KER corresponding to dominant parallel transitions (lower intensity inner rings) with positive values of β_2 of about +1.15 (lower intensity inner rings) and shapes corresponding to virtually isotropic transitions or slightly perpendicular transitions with β_2 values of about -0.6 (higher intensity outer rings). This is in close compliance with our observations made from the Br images for the probe excitations (2) due to one-photon photodissociation processes. Thus the former observation ($\beta_2 \approx$ +1.15) suggests that $CH_3(X)$ is formed along with Br* by a dominant parallel transition from the

ground state to the $^3Q_0$ state followed by a dissociation on the same (*i.e.* the diabatic) potential curve,[7] whereas the latter observation ($\beta_2 \approx -0.6$) could involve a combination of parallel and perpendicular transitions to $^3Q_0$ and $^3Q_1/^1Q_1$, respectively, followed by dissociations, to form $CH_3(X)$ and Br.[7]

IV. Discussion

The detection of the Br/Br* and $CH_3(X)$ fragments by resonant excitations of the second laser beam in the two-color scheme allows detection of otherwise, undetected, channels in addition to those observed by a one-color scheme reported before.[1] Thus, predissociation of Rydberg states following two-photon resonant excitations (channels (3)) as well as one-photon photodissociation (channel (2)), not previously seen, are now evident in multiphoton excitations of CH_3Br of chosen Rydberg states (**Table 1;** no. 1- 6) in addition to a three-photon (1) photodissociation channel, reported before (**see Fig.6**).[1]

Although we did not detect any Br^- in our experiments, which would be direct evidence for the involvement of ion-pair states in the dynamics in the region studied, several correlation observations indicate that interactions between the molecular Rydberg states and the ion-pair state are playing important part in the multiphoton excitation dynamics of CH_3Br as reported in the literature.[13] Among those observations are,

i) -the characteristic alteration in relative ion signals (see Section III. A., **Fig. 1b** and references [1] and [60]) such as an increase in the $I(Br^+)/I(CH_3^+)$ ratios with excitation wavenumber below the ion-pair threshold ($CH_3^+ + Br^-$) followed by a sudden drop.

ii) –opening up of a photodissociation channel to form CH_3(X) and Br/Br* following two-photon resonance excitations to Rydberg states higher in energy than the ion-pair threshold, not seen for lower energy excitations. This is seen in one-color excitations.[1]

These observations indicate, first, that the photodissociation of the resonantly excited Rydberg states of energies lower in energy than the ion-pair threshold differ from those of energies higher in energy than the threshold and, second, that this difference varies with energy lower than the threshold. These observations could be associated with the following effects of state interactions. In the former case (lower energy) an interaction between a Rydberg state and an ion-pair state corresponds to the bound energy region of the ion-pair state (**Fig. 6**) to cause an effective enhancement in the bond distance of the mixed state. Furthermore, that bond distance will increase largely as the energy approaches the ion-pair threshold. In the latter case (higher energy), on the other hand, an interaction will lead to a dissociation in which case the ion-pair formation will compete with the photodissociation channel. This kind of Rydberg-to-ion-pair interactions are well known for diatomic molecules,[39, 44, 45, 47-56] whereas indirect observations, as mentioned above, strongly support the existence of this state interaction effects, direct observations for ion-pair formations from the images were not evident.

There is a striking contrast between the excitation dynamics following three-photon excitation via the higher energy p and d molecular Rydberg states,[1] on the one hand and via the lower energy s Rydberg states, on the other hand [12] (see **Figs. 6a – 6b**). Thus, in the former case superexcited states formed ($CH_3Br^{\#}$) (pre)dissociate to form CH_3** Rydberg states (eqs.1), whereas in the latter case $CH_3Br^{\#}$ autoionizes to form $CH_3Br^{+}(X)$ (eqs. 4). This could be due to reasons, such as:

i) Formation of $CH_3Br^+(X, \text{low } v_i)$ by autoionization of $CH_3Br^{\#}$ is more favourable / probable for lower than higher energy difference between $CH_3Br^+(X, \text{low } v_i)$ and $CH_3Br^{\#}$.

ii) Three-photon excitations to $CH_3Br^{\#}$ via the 5s/5s´ Rydberg states are too low in energy to overcome energy barriers prior to dissociation to form CH_3** + Br/Br* whereas excitations via the p/d state are of high enough energies.

Whereas formation of $CH_3(X)$ + Br/Br* is not detected by one-photon photodissociation for excitations corresponding to two-photon excitations to the 5s/5s´states (**Fig. 6b** and reference [12]) it is clearly observed for those corresponding to resonance excitations to the p and d Rydberg states. This must be for energetic reasons. The transition probabilities, hence absorption cross section, corresponding to one-photon excitations to the repulsive valence states (*A* band), although low, are high enough in the latter case for $CH_3(X)$ formed along with Br/Br* to be detected as opposed to that in the former case (**Figs. 6a – 6b**).

Finally, predissociation following two-photon resonance excitation to the 5s/5s´ Rydberg states to form $CH_3(X)$ and Br/Br*, analogous to our observation for corresponding excitations to the p and d Rydberg states has been observed by Wang *et al*.[12] This channel is evident in the Br/Br* images and KERs, whereas the CH_3 co-fragment is too fast to be measured with our current extraction voltage/detector combination.

V. Summary and conclusions

Br^+ and CH_3^+ ion slice images were recorded for multiphoton excitation of CH_3Br followed by REMPI probing of the Br, Br* and $CH_3(X, v_1v_2v_3v_4)$ photofragments (two-color

experiments). Measurements were performed at seven wavelengths involving two-photon resonant transitions to np and nd vibrational levels of molecular Rydberg states ($CH_3Br^{**}(Ry;v_1v_2v_3)$) (**Table 1**). The probing of Br, Br* and $CH_3(X, v_1v_2v_3v_4)$ was done by (2 + 1) REMPI for resonance excitations to Rydberg states of bromine (Br**) and CH_3 (CH_3**(3p $^2A_2$)). Slice images of Br^+ and CH_3^+ photoproducts were recorded for 1) -the pump and 2) -the probe wavelengths, independently, as well as for the combination of 3) -pump followed by probe excitations. Kinetic energy release spectra (KERs) as well as angular distributions and relevant fit parameters (β_2 and β_4) were derived from the ion images.

For all the pump wavelengths the major excitation channel has been found to involve three-photon excitation of the molecule to (a) superexcited state(s) ($CH_3Br^{\#}$) followed by dissociation to form Rydberg states of CH_3** along with Br/Br*.[1] For two of these (no. 6-7 in **Table 1**) the three-photon excitation was also found to form $CH_3(X)$ along with Br/Br* and for one of these (no. 7 in **Table 1**) one-photon photodissociation towards $CH_3(X)$ + Br/Br* was additionally detected. The resonance detection of the fragment species (Br, Br* and $CH_3(X, v_1v_2v_3v_4)$) revealed channels in addition to those observed before: predissociation of the np and nd molecular Rydberg states following the two- photon resonance excitations as well as one-photon photodissociation.

Comparison of results relevant to the excitations involving REMPI via the p/d Rydberg states and those of the second color / probe excitation, which involves REMPI via the s Rydberg states [12] reveals a striking difference in the excitation dynamics following three-photon excitations. In the former case superexcited states formed ($CH_3Br^{\#}$) (pre)dissociate to form CH_3** Rydberg states (eqs.1), whereas in the latter case $CH_3Br^{\#}$ autoionize to form $CH_3Br^+(X)$ (eqs. 4). Abrupt variations in relative ion signal intensities and dissociation channels associated

with the ion-pair energy threshold strongly suggest that the dynamics of multiphoton dissociation and ionization via the molecular Rydberg states is affected by Rydberg to ion-pair state interactions.

In addition to adding to information relevant to fragmentation processes of the methyl halides we feel that the content of this paper is of importance to shed light on the effect of various competing channels on photoexcitation dynamics of molecules involving high energy Rydberg states in general. We sincerely hope that it will render further theoretical interpretation of the characteristic processes involved.

Acknowledgements

The financial support of the University Research Fund, University of Iceland and the Icelandic Research Fund (Grant No. 184693-051) is gratefully acknowledged. The imaging part of the reported results was carried out at the Ultraviolet Laser Facility at IESL-FORTH, supported in part by the European Union's Horizon 2020 research and innovation programme LASERLAB-EUROPE (Grant Agreement No. 654148).

Figure captions:

Fig.1

Mass Resolved MultiPhoton Ionization(MR-MPI) for CH_3Br:

(a) CH_3^+ signal (MPI spectrum) and CH_3Br Rydberg state (CH_3Br^{**}) assignments. Separation of the spectrum into resonant and non-resonant contributions in indicated. The numbers refer to transitions used in this work (**see Table 1**). Two-photon excitation wavenumbers for Br and Br* detections are marked in green (dashed line (Br*) and solid line (Br)).

(b) Ion signal intensity ratios $I(Br^+)/I(CH_3^+)$ (open squares) and $I(CBr^+)/I(CH_3^+)$ (open circles for molecular resonant signals and filled circles for non-resonant signals) as a function of two-photon excitation wavenumber) along with the MPI spectrum in (a). The threshold for ion-pair formation ($CH_3^+ + Br^-$) is indicated.

Fig.2

Slice images and KERs for Br^+:

a) Br^+ slice images and corresponding kinetic energy release spectra (KERs) of measurement no. 3 (see **Table 1**) for i) pumping (two-photon excitation (2hν): 68 684 cm^{-1}), ii) probing of Br* (2hν : 74 991 cm^{-1}) and iii) pump + probe. The images intensity scales have been adjusted to show all major features. The KERs are normalized to the strongest peak in each spectrum. The laser polarization is indicated by the double arrow. Br^+ kinetic energy release spectra (KERs) of measurement no. 3 (b) and no. 2 (c) (see **Table 1**) for, pumping (blue), probing of Br*(b) / Br(c) (red) and iii) pump + probe (black). The KERs have been approximately adjusted to show comparable intensities 1) – of the probe signals/peaks in the probe-only (red) and pump + probe

(black) spectra and 2) – of the pump signals in the pump-only (blue) and pump + probe (black) spectra.

Fig.3

Br^+ kinetic energy release spectra (KERs) derived from images no. 1 – 5 (See **Table 1** and **Fig. 1a**) for pump + probe excitations and Br* (a) and Br (b) detections. The spectra are normalized to the height of the highest KER spectra contributions, corresponding to the two-photon resonant contributions (see main text) in each spectra. The spectra are plotted as a function of a relative scales $\Delta(2h\nu)*f(Br)$ (for $CH_3{}^{79}Br$) (see explanation in main text) and tilted to the right (i.e. plotted vertically). The common energy thresholds (energy maxima) for the formation of CH_3(X, 0000) + Br/Br* after the resonant two-photon excitations of CH_3Br are indicated.

Fig.4

Slice images and KERs for CH_3^+:

a) CH_3^+ slice images and corresponding kinetic energy release spectra (KERs) of measurement no. 6 (see **Table 1**) for i) pumping (two-photon excitation (2hν): 78 334 cm^{-1}), ii) probing of $CH_3(X, 0100)$ (2hν for transition $2_1{}^1$ (see text): 60 698 cm^{-1}) and iii) pump + probe. The images intensity scales have been adjusted to show all major features. The KERs are normalized to the strongest peak in each spectrum. The laser polarization is indicated by the double arrow.
b) CH_3^+ kinetic energy release spectra (KERs) of measurement no. 6 (see **Table 1**) for, pumping (blue), probing of $CH_3(X, 0000)$ (2hν for transition 0_0^0 (see text): 59 972 cm^{-1}) (red) and iii)

pump + probe (black) for comparable ion intensities of individual channel signals (see main text). Energy thresholds (energy maxima) for the formation of $CH_3(X, 0000)$ + Br/Br* after non-resonant one-photon excitations of CH_3Br are indicated.

Fig.5

CH_3^+ kinetic energy release spectra (KERs) derived from measurements no. 6 (See **Table 1** and **Fig. 1a**) for excitations corresponding to the 1_1^1 (furthest to the left), 0_0^0, 2_1^1 and 2_2^2 (furthest to the right) $CH_3(X)$ resonances (see main text). The KERs are normalized to the strongest peak in each spectrum. The spectra are plotted as a function of a relative scale $\Delta(1h\nu)*f(CH_3)$ (see explanation in main text) and tilted to the right (i.e. plotted vertically). Common energy thresholds (energy maxima) for the formation of $CH_3^+(X, 0000)$ + Br/Br* after one-photon photodissociation of CH_3Br^+ are indicated.

Fig. 6

Semi-schematic energy diagrams and excitation processes of CH_3Br leading to CH_3^+ and Br^+ formation based on this work and references [1] and [12] showing relevant energy thresholds (horizontal lines), photoexcitations (vertical arrows) and fragmentation channels (black bended arrows). The number of photons (n = 1 – 3) in photoexcitations prior to dissociations are indicated in boxes as nhν. Vertical arrows in (a) are for excitations no. 1 (red) and 4 (purple) (see **Table 1**). Vertical arrows in (b) are excitations corresponding to the 1_1^1 (red) and 2_2^2 (purple) $CH_3(X)$ resonances. The one-photon absorption spectrum[30, 64] is tilted to the right in the figures.

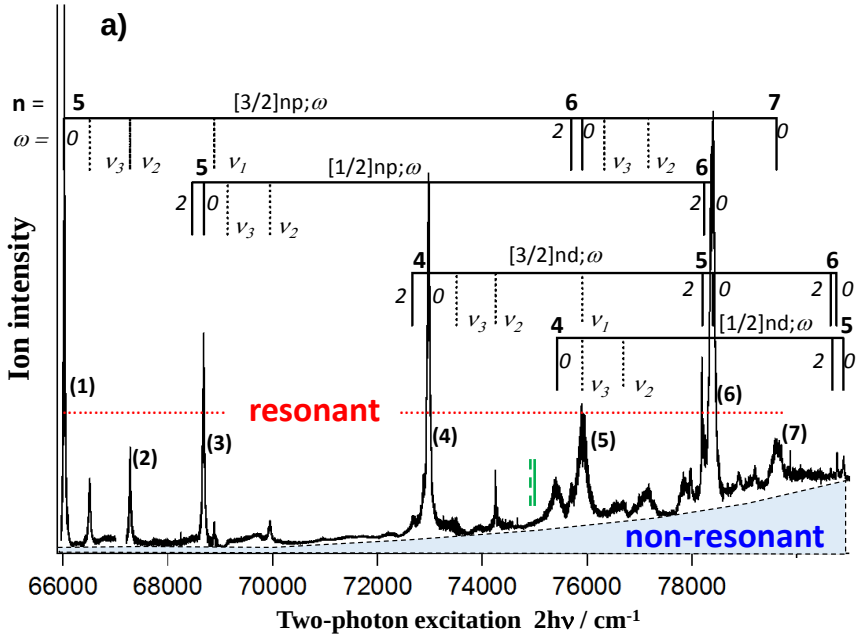
a)
n =
ω =
[3/2]np;ω
[1/2]np;ω
[3/2]nd;ω
[1/2]nd;ω
Ion intensity
resonant
non-resonant
(1)
(2)
(3)
(4)
(5)
(6)
(7)
66000
68000
70000
72000
74000
76000
78000
Two-photon excitation 2hν / cm-1

Fig. 1a

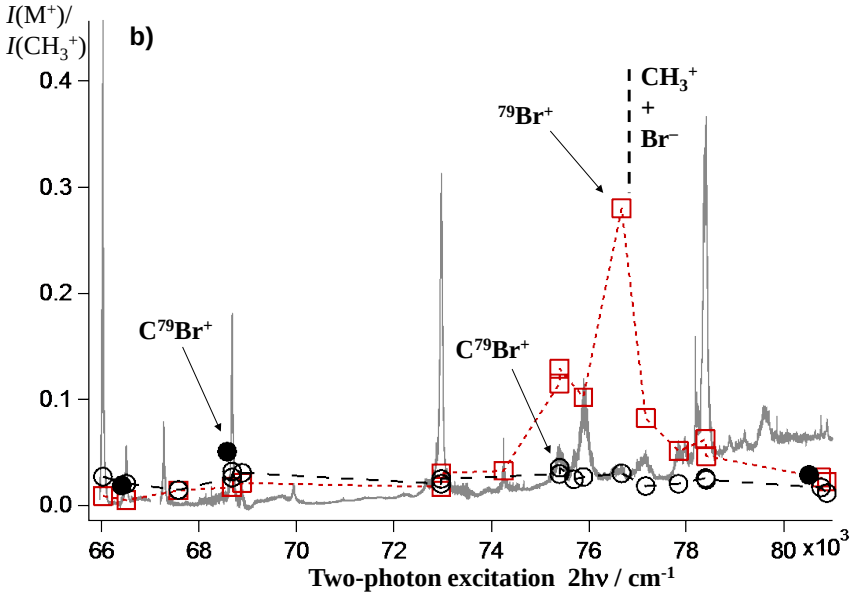
I(M+)/
I(CH3+)
b)
0.4
0.3
0.2
0.1
0.0
CH3+
+
Br−
79Br+
C79Br+
C79Br+
66
68
70
72
74
76
78
80 x10-3
Two-photon excitation 2hν / cm-1

Fig.1b

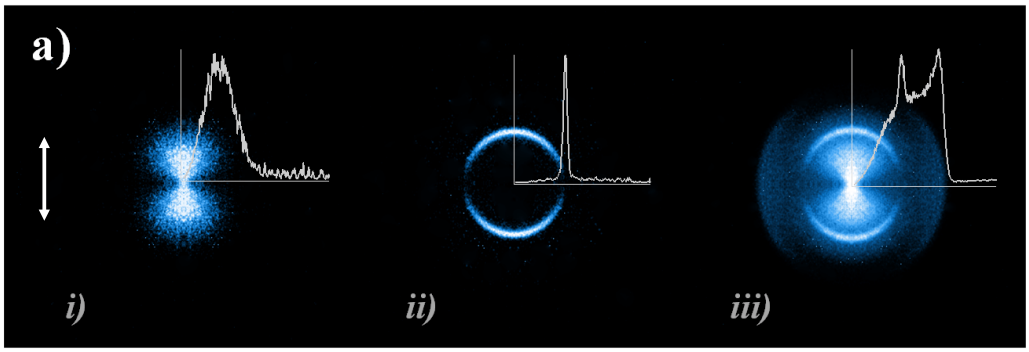

Fig.2a

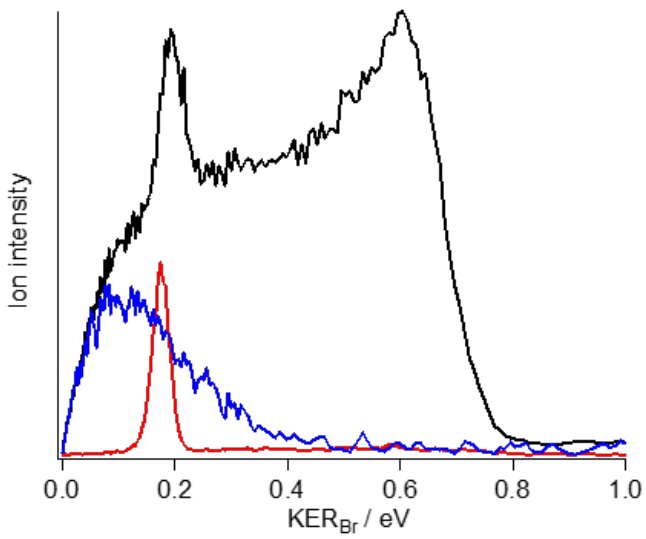

Fig.2b

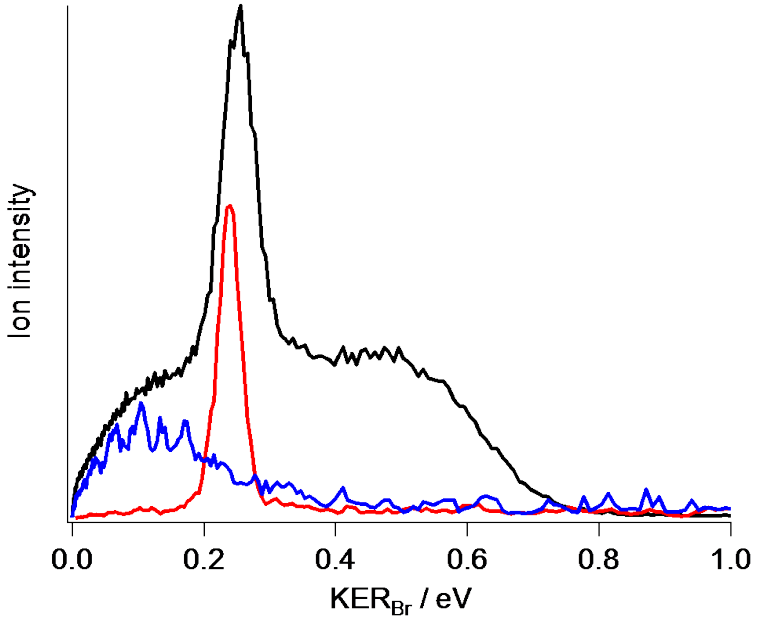
Ion intensity
0.0
0.2
0.4
0.6
0.8
1.0
KER$_{Br}$ / eV

Fig.2c

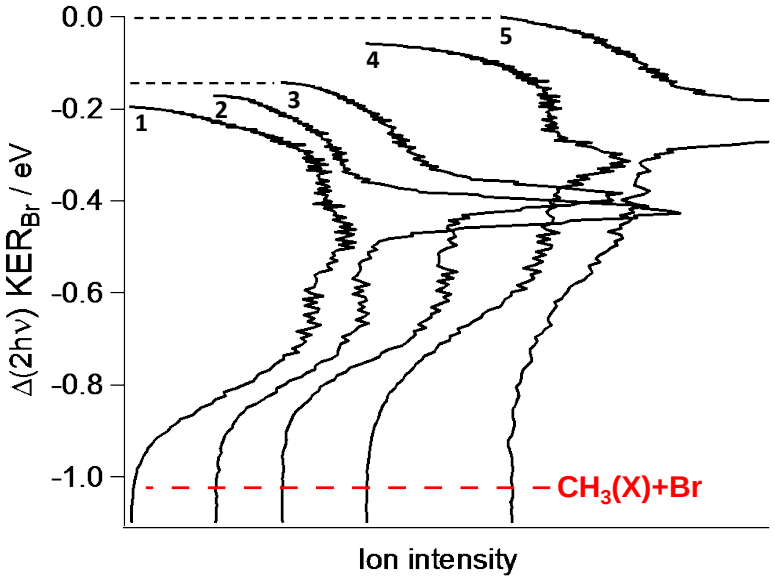
0.0
-0.2
-0.4
-0.6
-0.8
-1.0
Δ(2hν) KER$_{Br}$ / eV
1
2
3
4
5
CH$_3$(X)+Br
Ion intensity

Fig.3a

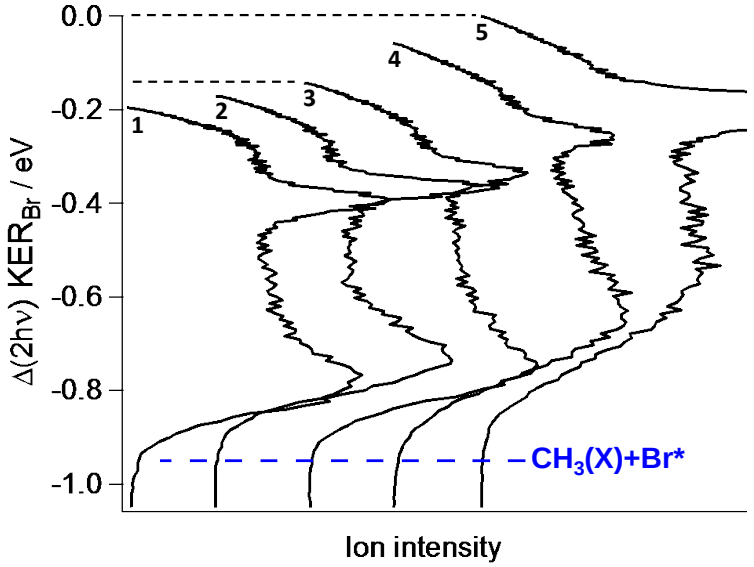
0.0
-0.2
-0.4
-0.6
-0.8
-1.0
Δ(2hν) KER$_{Br}$ / eV
1
2
3
4
5
CH$_3$(X)+Br*
Ion intensity

Fig.3b

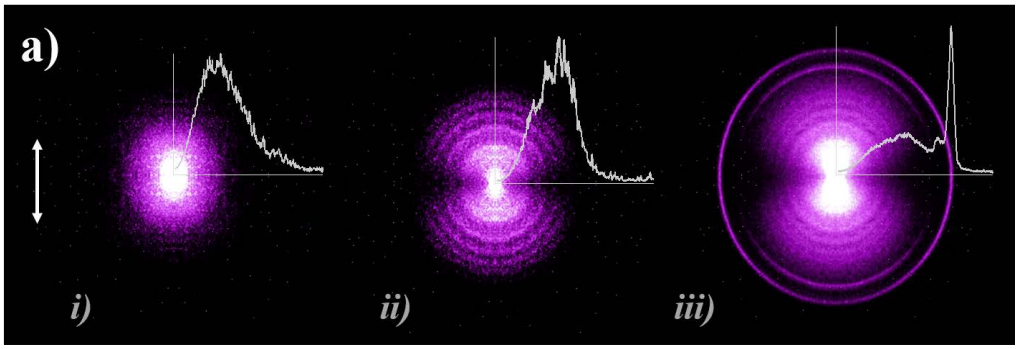
a)
i)
ii)
iii)

Fig.4a

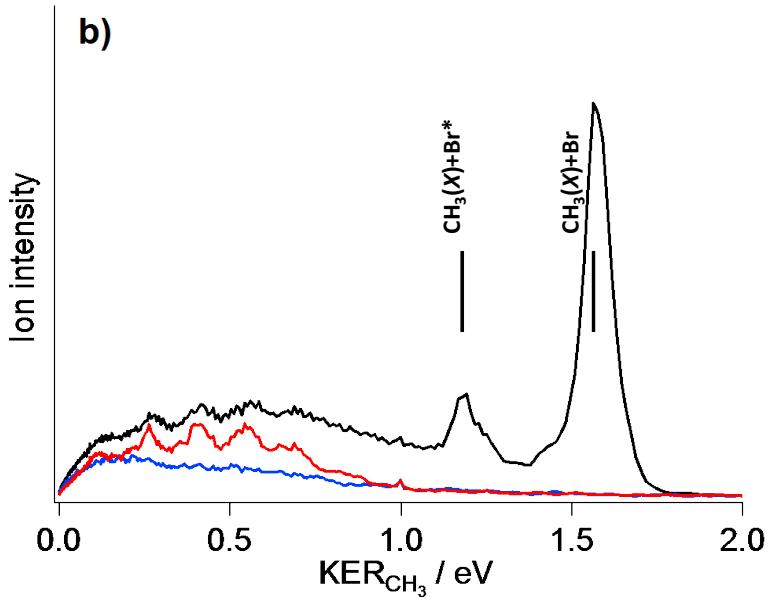
b)
Ion intensity
CH3(X)+Br*
CH3(X)+Br
0.0
0.5
1.0
1.5
2.0
KERCH3 / eV

Fig.4b

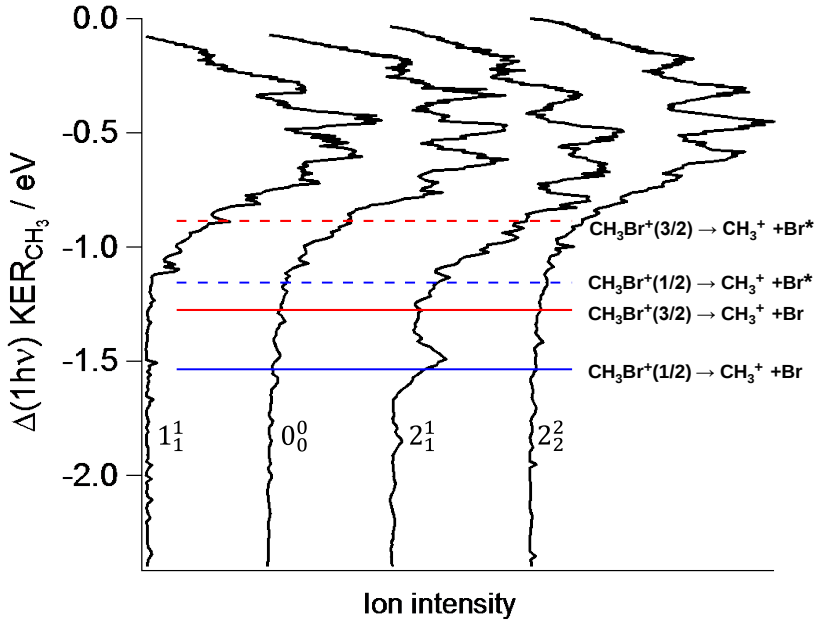
0.0
-0.5
-1.0
-1.5
-2.0
Δ(1hν) KERCH3 / eV
CH3Br+(3/2) → CH3+ +Br*
CH3Br+(1/2) → CH3+ +Br*
CH3Br+(3/2) → CH3+ +Br
CH3Br+(1/2) → CH3+ +Br
1_1^1
0_0^0
2_1^1
2_2^2
Ion intensity

Fig.5

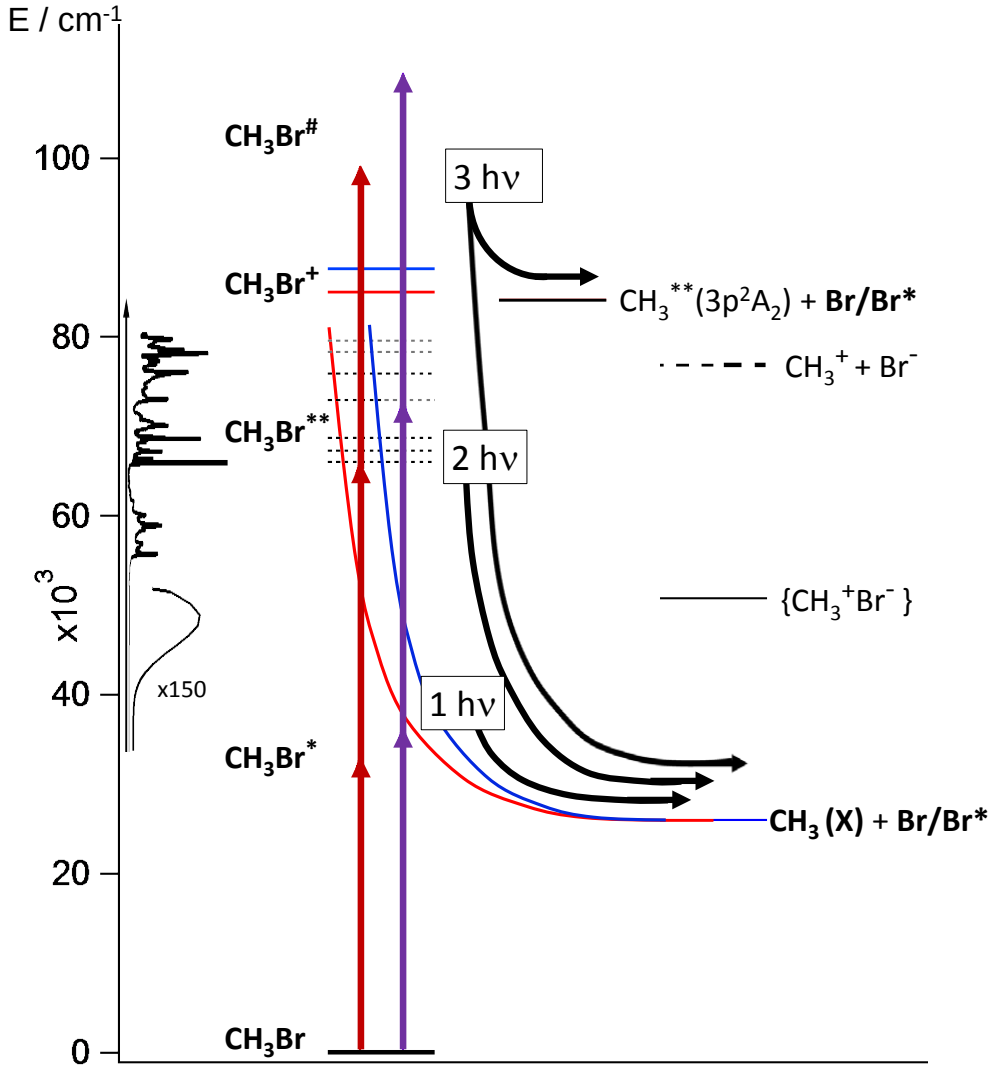
E / cm-1
100
80
60
40
20
0
x10 3
x150
CH3Br#
CH3Br+
CH3Br**
CH3Br*
CH3Br
3 hν
2 hν
1 hν
CH3 **(3p2A2) + Br/Br*
CH3 + + Br -
{CH3 +Br - }
CH3 (X) + Br/Br*

Fig. 6a

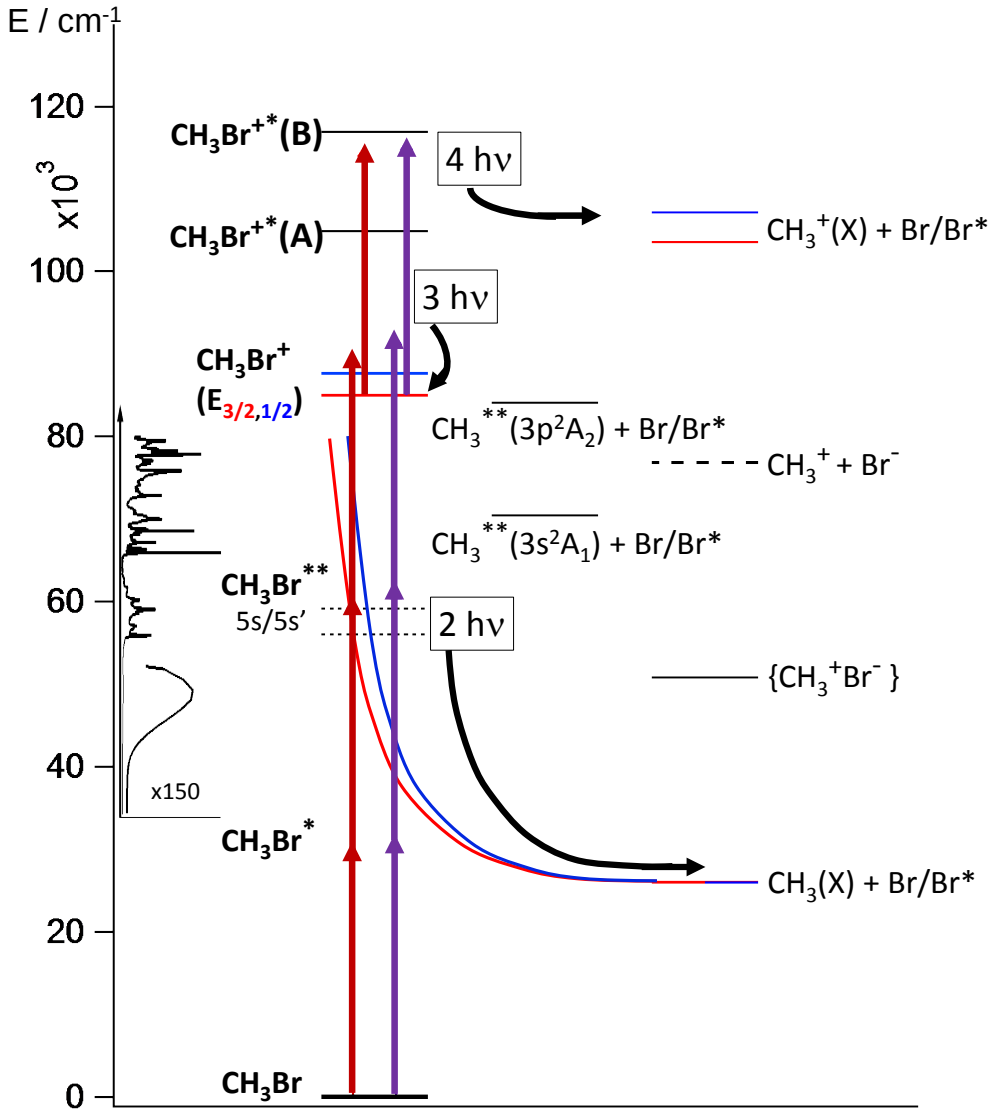
E / cm-1
x10^3
120
100
80
60
40
20
0
CH3Br+*(B)
CH3Br+*(A)
CH3Br+
(E3/2,1/2)
CH3Br**
5s/5s'
CH3Br*
CH3Br
x150
4 hν
3 hν
2 hν
CH3+(X) + Br/Br*
CH3**(3p2A2) + Br/Br*
CH3+ + Br-
CH3**(3s2A1) + Br/Br*
{CH3+Br- }
CH3(X) + Br/Br*

Fig. 6b

Table.1 *Slice images for CH_3^+ and Br^+ recorded for MPI of CH_3Br including resonant excitation to specified molecular Rydberg states.*

Image no.	CH_3Br Rydberg State; $[\Omega_c]nl$; $\omega,(v_1v_2v_3)$ [a]	One-photon / nm	Two-photon / cm^{-1}	Fragment probed
1	[3/2]5p; 0, (000)	302.94	66019[c]	Br
2	[3/2]5p; 0, (010)	297.29	67275[d]	Br
3	[1/2]5p; 0, (000)	291.19	68684[c]	Br
4	[3/2]4d; 0, (000)	274.06	72977[c]	Br / CH_3
5	[3/2]6p; 0, (000)/[3/2]4d; 0, (100)/[1/2]4d; 0, (001)[b]	263.49	75905[c]	Br
6	[1/2]6p; 0, (000)/[3/2]5d; 0, (000)	255.32	78334[c]	CH_3
7	[3/2]7p; 0, (000)	251.24	79610[c]	CH_3
	Resonant state [e]; vibrational transition [f]			
Probe CH_3	$3p\ ^2A_2$; 1_1^1	333.90	59898	CH_3
Probe CH_3	$3p\ ^2A_2$; 0_0^0	333.49	59972	CH_3
Probe CH_3	$3p\ ^2A_2$; 2_1^1	329.50	60698	CH_3
Probe CH_3	$3p\ ^2A_2$; 2_2^2	325.80	61387	CH_3
Probe Br*	$^2D[3/2]$	266.70	74991	Br
Probe Br	$^4P[3/2]$	266.63	75009	Br

[a] $[\Omega_c]$: total angular momentum quantum number for the core ion. *n*: principal quantum number for the Rydberg electron. *l*: Rydberg electron orbital (p,d). ω: total angular momentum quantum number for the Rydberg electron. (v_1, v_2, v_3): vibrational quantum numbers referring to vibrational modes, v_1 (symmetric stretch), v_2 (umbrella) and v_3 (C–Br stretch). [b] Spectral overlap. [c] Ref. 13. [d] Ref. 9. [e] Selected resonant Rydberg states for probed fragments. [f] Selected vibrational transition $v_n^{v',v''}$ for, v_n (vibrational mode), v''(ground state vibrational level) and v'(excited state vibrational level).

References.

1. A. Hafliðason, P. Glodic, G. Koumarianou, P. C. Samartzis and A. Kvaran, *Phy. Chem. Chem. Phys.*, 2018, **20**, 17423.
2. W. P. Hess, D. W. Chandler and J. W. Thoman, *Chem. Phys.*, 1992, **163**, 277-286.
3. T. Gougousi, P. C. Samartzis and T. N. Kitsopoulos, *J. Chem. Phys.*, 1998, **108**, 5742-5746.
4. V. Blanchet, P. C. Samartzis and A. M. Wodtke, *J. Chem. Phys.*, 2009, **130**, 034304.
5. C. Escure, T. Leininger and B. Lepetit, *J. Phys. Chem.*, 2009, **130**, 244305.
6. G. N. A. Van Veen, T. Baller and A. E. De Vries, *Chem. Phys.*, 1985, **92**, 59-65.
7. J. G. Underwood and I. Powis, *Phys. Chem. Chem. Phys.*, 2000, **1**, 747-756.
8. F. Y. Wang, M. L. Lipciuc, A. Kartakoullis, P. Glodic, P. C. Samartzis, X. M. Yang and T. N. Kitsopoulos, *Phys. Chem. Chem. Phys.*, 2014, **16**, 599-606.
9. A. Kvaran, H. Wang, K. Matthiasson and A. Bodi, *J. Phys. Chem. A*, 2010, **114**, 9991-9998.
10. D. A. Shaw, D. M. P. Holland and I. C. Walker, *J. Phys. B: At., Mol. Opt. Phys.*, 2006, **39**, 3549-3560.
11. D. Xu, J. Huang, R. J. Price and W. M. Jackson, *J. Chem. Phys. A*, 2004, **108**, 9916-9923.
12. F. Y. Wang, M. L. Lipciuc, X. M. Yang and T. N. Kitsopoulos, *Phys. Chem. Chem. Phys.*, 2009, **11**, 2234-2240.
13. T. Ridley, J. T. Hennessy, R. J. Donovan, K. P. Lawley, S. Wang, P. Brint and E. Lane, *J. Chem. Phys. A*, 2008, **112**, 7170-7176.
14. M. Kawasaki, H. Sato, T. Kikuchi, S. Kobayashi and T. Arikawa, *J. Chem. Phys.*, 1987, **87**, 5739-5745.
15. C. Rist and M. H. Alexander, *J. Chem. Phys.*, 1993, **98**, 6196.
16. M. R. Bassford, G. Nickless, P. G. Simmonds, A. C. Lewis, M. J. Pilling and M. J. Evans, *Atmospheric Enviroment*, 1999, **33**, 2373.
17. A. Bodi, N. S. Shuman and T. Baer, *Phys. Chem. Chem. Phys.*, 2009, **11**, 11013.
18. L. Rubio-Lago, A. Garcia-Vela, A. Arregui, G. A. Amaral and L. Banares, *J. of Chem. Phys.*, 2009, **131**, 174309.
19. W. C. Price, *J. Chem. Phys*, 1936, **4**, 539-547.
20. S. Felps, P. Hochmann, P. Brint and S. P. McGlynn, *J. Mol. Spectrosc.*, 1976, **59**, 355-379.
21. N. Thire, R. Cireasa, D. Staedter, V. Blanchet and S. T. Pratt, *Phys. Chem. Chem. Phys.*, 2011, **13**, 18485-18496.
22. L. Li, X. Kong and S. Zhang, *Chine. Opt. Lett.* , 2007, **5**, 315.
23. M. E. Corrales, G. J. Vázquez, G. Balerdi, I. R. Solá, R. de Nalda and L. Banares, *nature chem.*, 2014, **6**, 785-790.
24. R. Locht, B. Leyh, H. W. Jochims and H. Baumgartel, *Chem. Phys.*, 2009, **365**, 109-128.
25. S. P. Sapers and D. J. Donaldson, *Chem.Phys.Letters*, 1990, **173**, 257-264.
26. A. T. J. B. Eppink and D. H. Parker, *J. Chem. Phys.*, 1999, **110**, 832.
27. C. Hu, S. Pei, Y.-L. Chen and K. Liu, *J. Phys. Chem.*, 2007, **111**, 6813.
28. A. Kartakoullis, P. C. Samartzis and T. N. Kitsopoulos, *J. Phys. Chem.*, 2013, **117**, 22383.
29. G. C. Causley and B. R. Russell, *J. Chem. Phys.*, 1975, **62**, 848-857.
30. R. Locht, B. Leyh, H. W. Jochims and H. Baumgartel, *Chem. Phys.*, 2005, **317**, 73-86.
31. R. Locht, B. Leyh, D. Dehareng, H. W. Jochims and H. Baumgartel, *Chem. Phys.*, 2005, **317**, 87-102.
32. C. Escure, T. Leininger and B. Lepetit, *J. Chem. Phys.*, 2009, **130**, 244306.
33. M. G. Szarka, D. S. Green, D. T. Cramb and S. C. Wallace, *J. Phys. Chem.*, 1997, **101**, 1818.
34. R. J. Donovan, J. T. Hennessy, K. P. Lawley and T. Ridley, *J. Chem. Phys.*, 2013, **138**, 134308.

35. H. Shen, L. Q. Hua, C. J. Hu and B. Zhang, *J. Mol. Spectrosc.*, 2009, **257**, 200-204.
36. B. Urban and V. E. Bondybey, *J. Chem. Phys.*, 2002, **116**, 4938.
37. R. G. Bray and R. M. Hochstrasser, *Mol. Phys.*, 1976, **31**, 1199-1211.
38. J. B. Halpern, H. Zacharias and R. Wallenstein, *J. Mol. Spectrosc.*, 1980, **79**, 1-30.
39. A. Kvaran, H. Wang and B. G. Waage, *Can. J. Physics*, 2001, **79**, 197-210.
40. B. G. Waage, A. Kvaran and H. Wang, *J. Chem. Phys.*, 2000, **113**, 1755-1761.
41. K. Matthiasson, A. Kvaran, H. Wang, A. Bodi and E. Jónsson, *J. Chem. Phys.*, 2008, **129**, 164313.
42. K. Matthiasson, A. Kvaran and H. Wang, *J. Chem. Phys.*, 2009, **131**, 044324.
43. K. Matthiasson, J. Long, H. Wang and A. Kvaran, *J. Chem. Phys.*, 2011, **134**, 164302.
44. J. Long, H. R. Hrodmarsson, H.Wang and A. Kvaran, *J. Chem. Phys*, 2012, **136**, 214315.
45. J. Long, H. Wang and A. Kvaran, *J. Chem. Phys.*, 2013, **138**, 044308.
46. H. R. Hrodmarsson, H. Wang and A. Kvaran, *J. Chem. Phys.*, 2014, **140**, 244304.
47. A. J. Yencha, D. K. Kela, R. J. Donovan, A. Hopkirk and A. Kvaran, *Chem. Phys. Letters*, 1990, **165**, 283-288.
48. A. Kvaran, A. J. Yencha, D. K.Kela, R. J. Donovan and A. Hopkirk, *Chem. Phys. Letters*, 1991, **179**, 263-267.
49. D. Kaur, A. J. Yencha, R. J. Donovan, A. Kvaran and A. Hopkirk, *Org. Mass Spectrom.*, 1993, **28**, 327-334.
50. A. J. Yencha, D. Kaur, R. J. Donovan, A. Kvaran, A. Hopkirk, H.Lefebvre-Brion and F. Keller, *J.Chem. Phys.*, 1993, **99**, 4986-4992.
51. K. P. Lawley, A. C. Flexen, R. R. J. Maier, A. Manck, T. Ridley and R. J. Donovan, *Phys. Chem. Chem. Phys.*, 2002, **4**, 1412-1418.
52. A. Logadóttir, A. Kvaran and H. Wang, *J. Chem. Phys.*, 2000, **112**, 10811-10820.
53. J. Long, H. Wang and A. Kvaran, *J. Mol. Spectrosc.*, 2012, **282**, 20-26.
54. D. Zaouris, A. Kartakoullis, P. Glodic, P. C. Samartzis, H. R. Hrodmarsson and A. Kvaran, *Phy. Chem. Chem. Phys.*, 2015, **17**, 10468.
55. P. Glodic, D. Zaouris, P. C. Samartzis, A. Hafliðason and A. Kvaran, *Phy. Chem. Chem. Phys.*, 2016, **18**, 26291-26299.
56. H. R. Hrodmarsson, A. Kartakoullis, D. Zaouris, P. Glodic, H. Wang, P. C. Samartzis and A. Kvaran, *Phys. Chem. Chem. Phys.*, 2017, **19**, 11354-11365.
57. C. R. Gebhardt, T. P. Rakitzis, P. C. Samartzis, V. Ladopoulos and T. N. Kitsopoulos, *Rev. Sci. Instrum.*, 2001, **72**, 3848.
58. V. Papadakis and T. N. Kitsopoulos, *Rev.Sci.Instrum.*, 2006, **77**, 5.
59. J. W. Hudgens, T. G. DiGiuseppe and M. C. Lin, *J. Chem. Phys*, 1983, **79**, 571.
60. NIST Atomic Spectra Database (ver. 5.3), [Online], http://physics.nist.gov/asd, (accessed March 2016, National Institute of Standards and Technology, Gaithersburg, MD).
61. *See ESI*.
62. NIST Chemistry WebBook - (National Institute of Standards and Technology) https://webbook.nist.gov/chemistry/name-ser/, (accessed Jan 2018).
63. H.-W. Xi and M.-B. Huang, *J. Chem. Phys.*, 2006, **110**, 8167-8173.
64. L. T. Molina, M. J. Molina and F. S. Rowland, *Journal of Physical Chemistry*, 1982, **86**, 2672-2676.

4.5.1 Supporting information

Two-color REMPI study of CH_3Br, probing CH_3 and Br formation with MPI and Slice Imaging

Arnar Hafliðason[1], Pavle Glodic[2], Greta Koumarianou[2],
Peter C. Samartzis[2]* and Ágúst Kvaran[1]*

1. *Science Institute, University of Iceland, Dunhagi 3, 107 Reykjavík, Iceland.*
2. *Institute of Electronic Structure and Laser, Foundation for Research and Technology-Hellas, Vassilika Vouton, 71110 Heraklion, Greece.*

Supplementary material

Content: **pages:**

Fig. S1

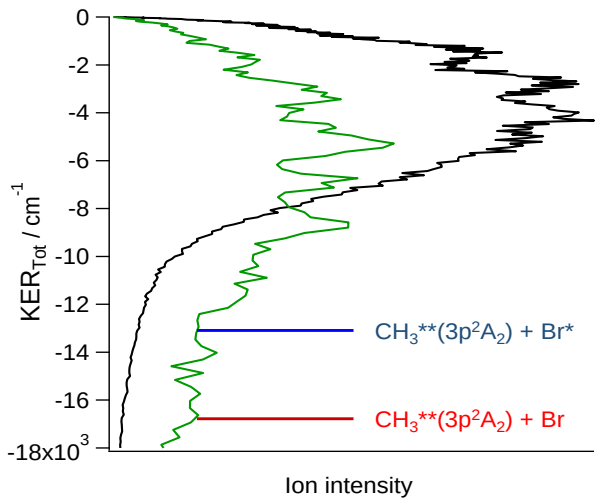

Fig. S1: *Vibrational structure, for OPLA mode in $3p^2A_2$ state of CH_3, observed on CH_3 KER (black) and Br KER (green) from REMPI peak 2 / 67275 cm^{-1}. Thresholds for formation of CH3**($3p^2A_2$) + Br/Br* are shown.*

Fig. S2

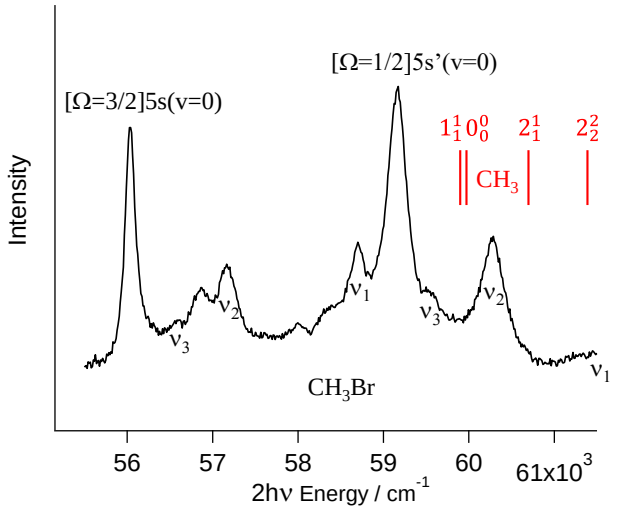

Fig. S2: *CH_3Br absorption spectrum (black) in the region of 5s/5s' Rydberg states, along with vibrational modes ν_i. Resonant probing transitions $\nu_{\nu''}^{\nu'}$ for CH_3 are shown (red).*

Fig. S3

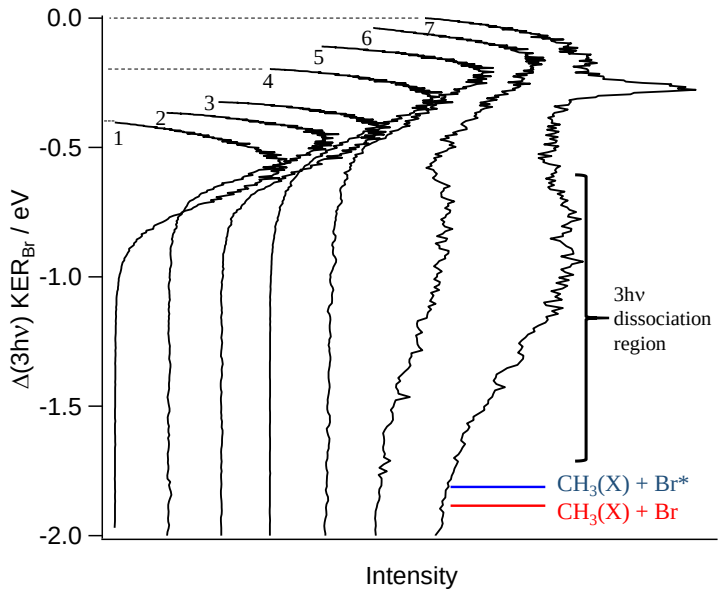

Fig. S3: *Peak 1-7 compared for Br KER spectra (KER data from One color article[ref]). Each KER spectrum has been shifted by Δ(3hν) relative to the top spectrum (no.7)(see explanation in main article). Peaks 6 and 7 / 78334 and 79610 cm^{-1}, show evidence of dissociation of parent molecule forming ground state fragments: $CH_3Br^{\#} \rightarrow CH_3(X) + Br/Br^*$, following a 2hν resonant transition to Rydberg states followed by 1hν transition to a superexcited state ($CH_3Br^{\#}$). A rough estimate of KER region for these channels is showed. Thresholds for formation of $CH_3(X)$ + Br/Br* are indicated.*

Fig. S4

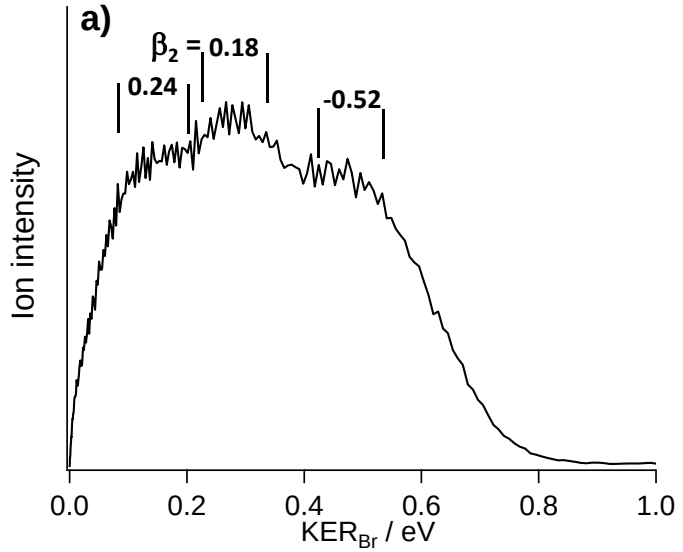

Fig. S4-a: *Two-color Br KER spectrum for peak 1, found in 2hν REMPI spectra at 66019 cm^{-1}.*

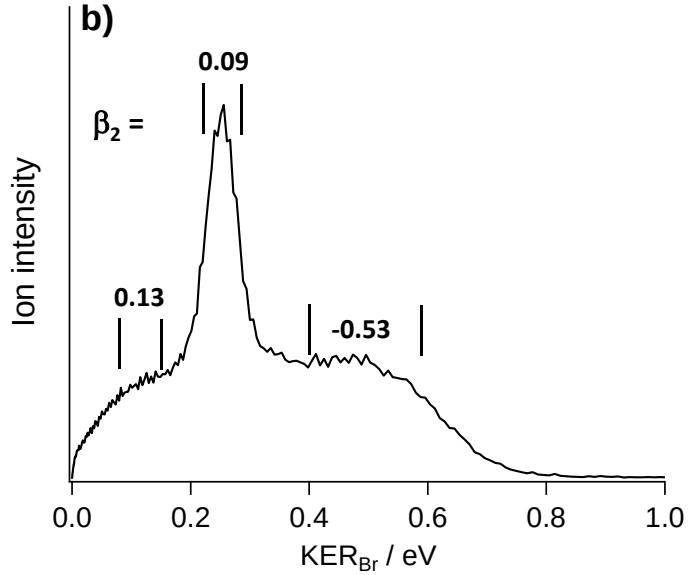

Fig. S4-b: *Two-color Br KER spectrum for peak 2, found in 2hν REMPI spectra at 67275 cm^{-1}.*

Fig. S4

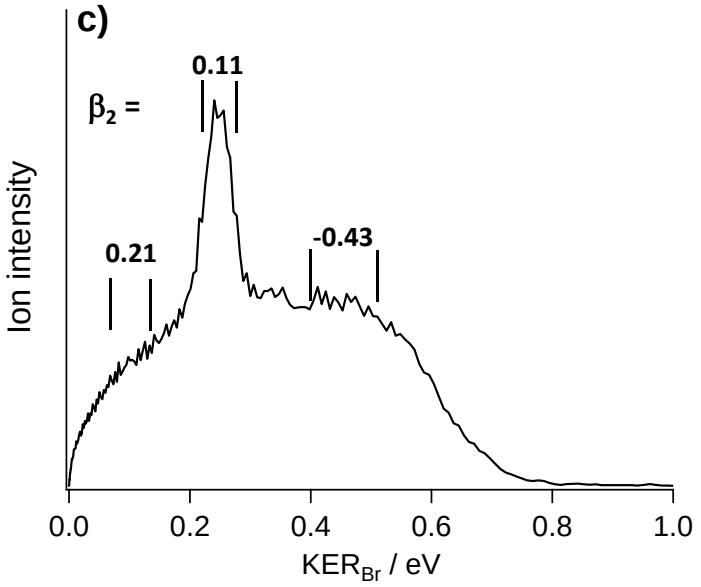

Fig. S4-c: *Two-color Br KER spectrum for peak 3, found in 2hv REMPI spectra at 68684 cm^{-1}.*

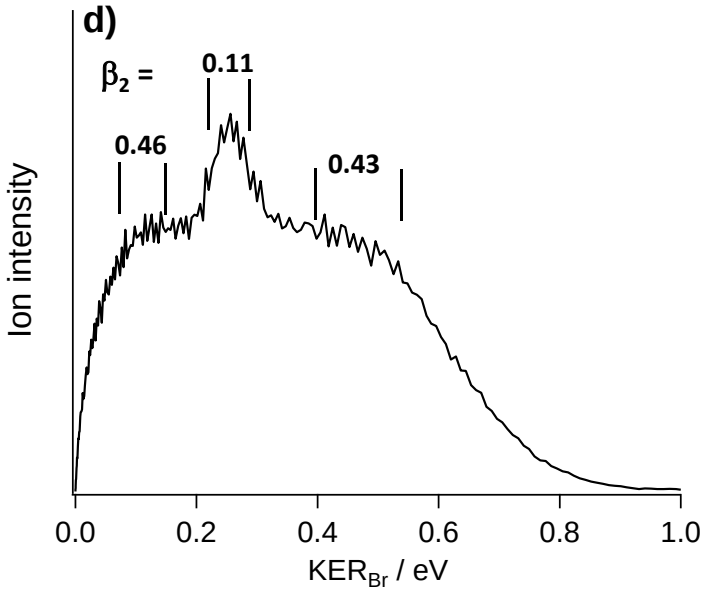

Fig. S4-d: *Two-color Br KER spectrum for peak 4, found in 2hv REMPI spectra at 72977 cm^{-1}.*

Fig. S4

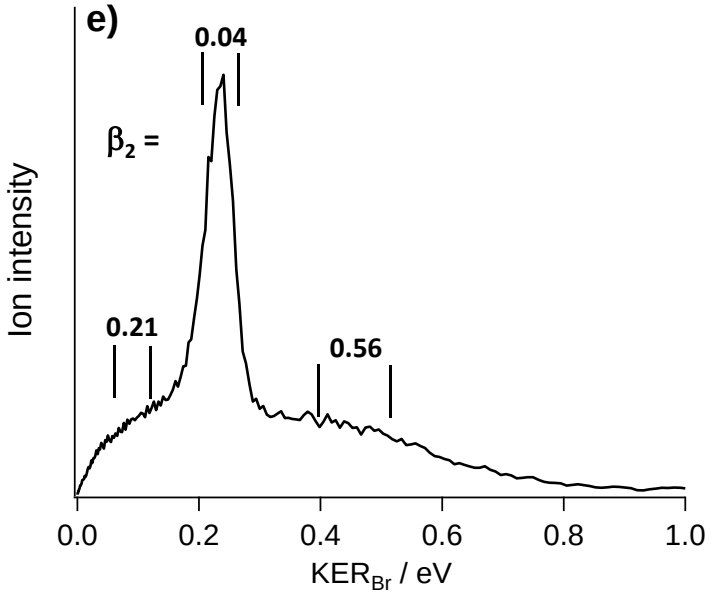

Fig. S4-e: *Two-color Br KER spectrum for peak 5, found in 2hv REMPI spectra at 75905 cm^{-1}.*

Fig. S5

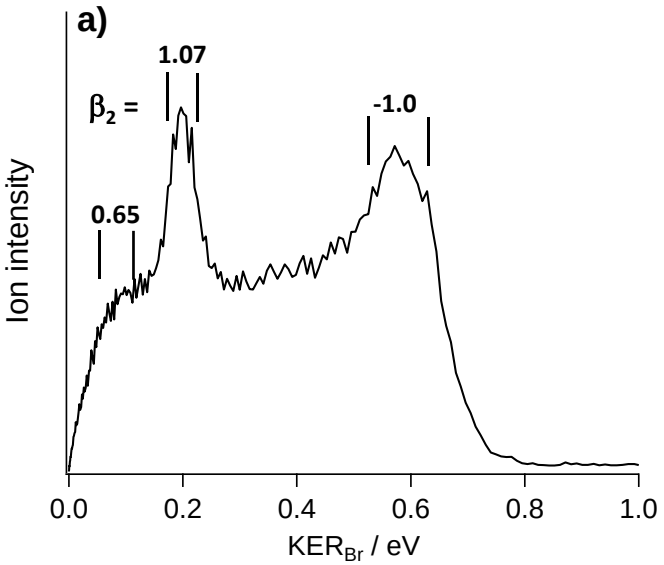

Fig. S5-a: *Two-color Br* KER spectrum for peak 1, found in 2hv REMPI spectra at 66019 cm^{-1}.*

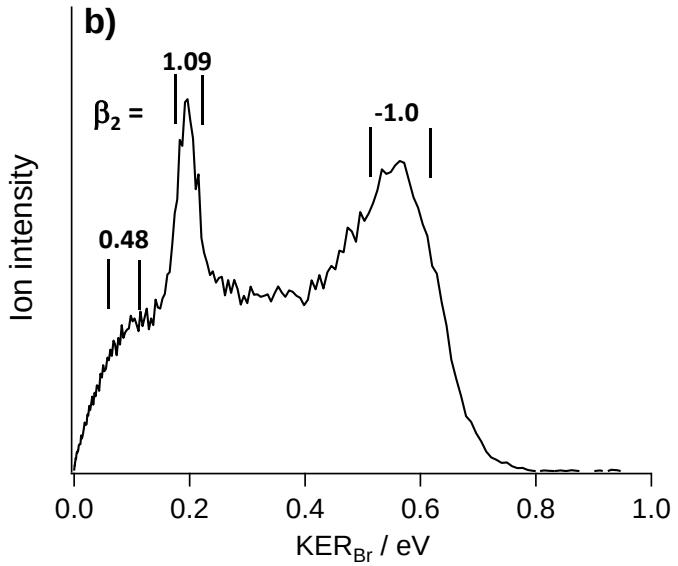

Fig. S5-b: *Two-color Br* KER spectrum for peak 2, found in 2hv REMPI spectra at 67275 cm^{-1}.*

Fig. S5

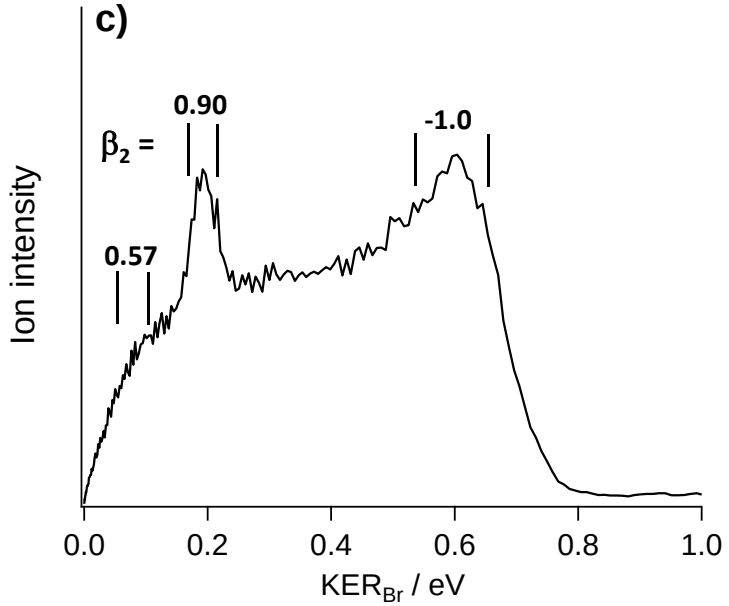

Fig. S5-c: *Two-color Br* KER spectrum for peak 3, found in 2hv REMPI spectra at 68684 cm^{-1}.*

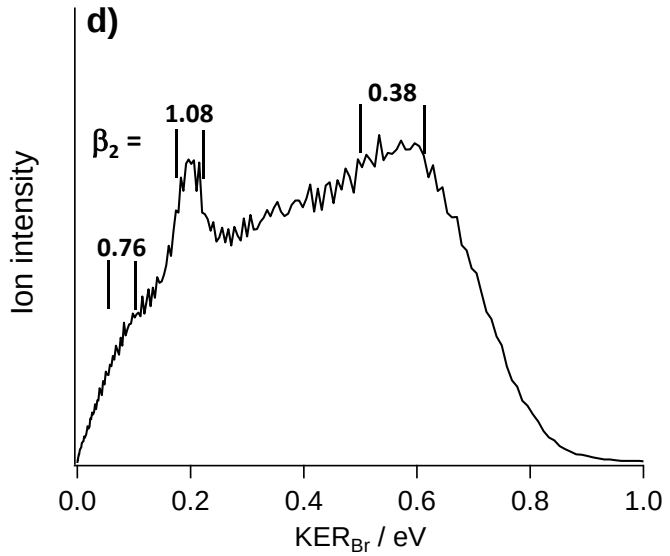

Fig. S5-d: *Two-color Br* KER spectrum for peak 4, found in 2hv REMPI spectra at 72977 cm^{-1}.*

Fig. S5

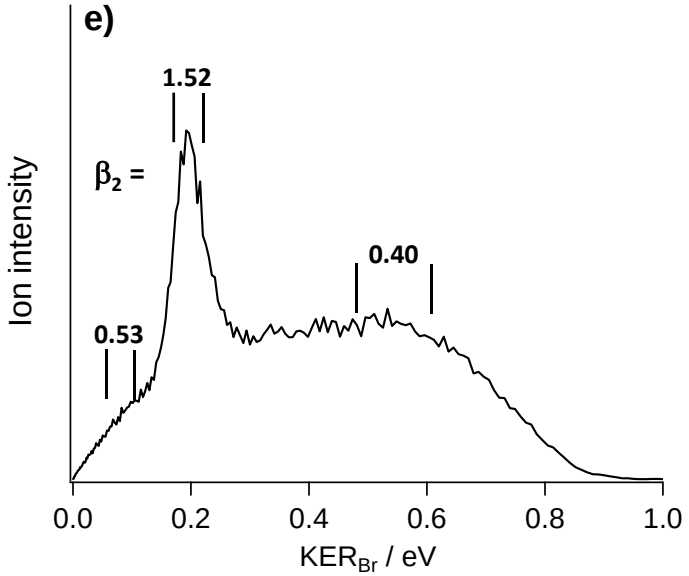

Fig. S5-e: *Two-color Br* KER spectrum for peak 5, found in 2hv REMPI spectra at 75905 cm^{-1}.*

Fig. S6

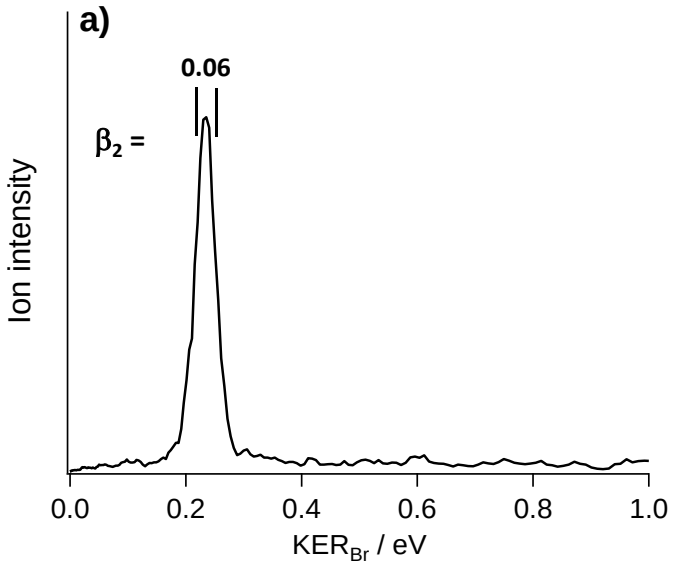

Fig. S6-a: *Probe laser Br KER spectrum, found in 2hν REMPI spectra at 75009 cm^{-1}.*

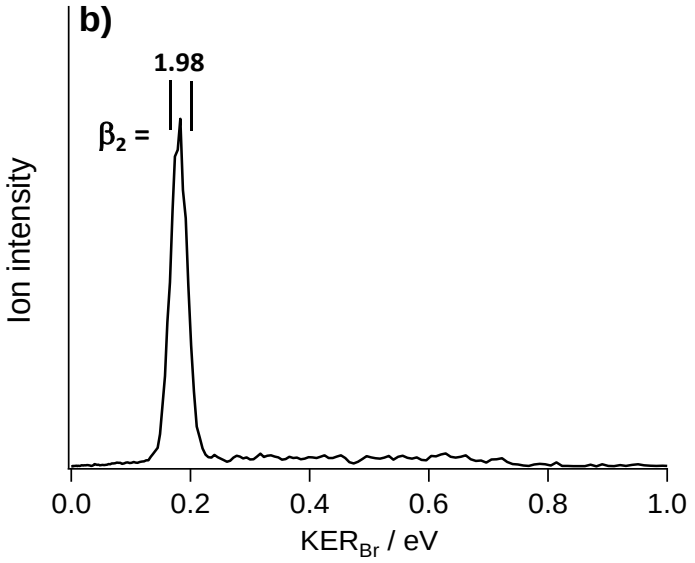

Fig. S6-b: *Probe laser Br* KER spectrum, found in 2hν REMPI spectra at 74991 cm^{-1}.*

Fig. S7

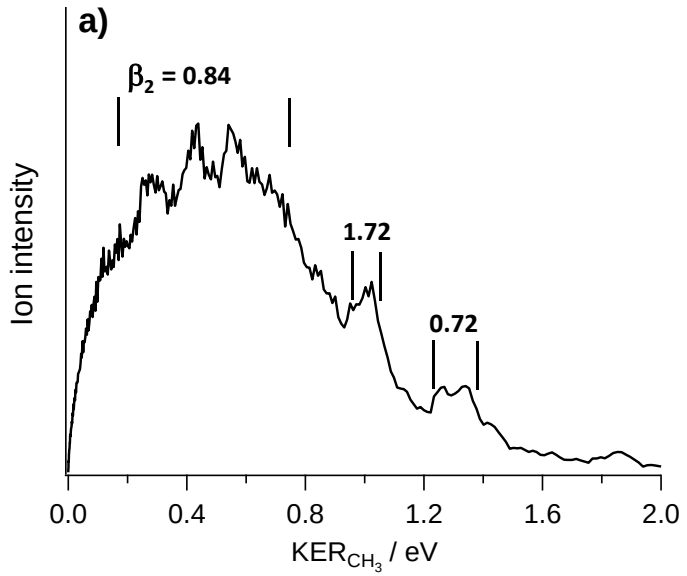

Fig. S7-a: *Two-color CH_3 KER spectrum for peak 4, found in 2hv REMPI spectra at 72977 cm^{-1}.*

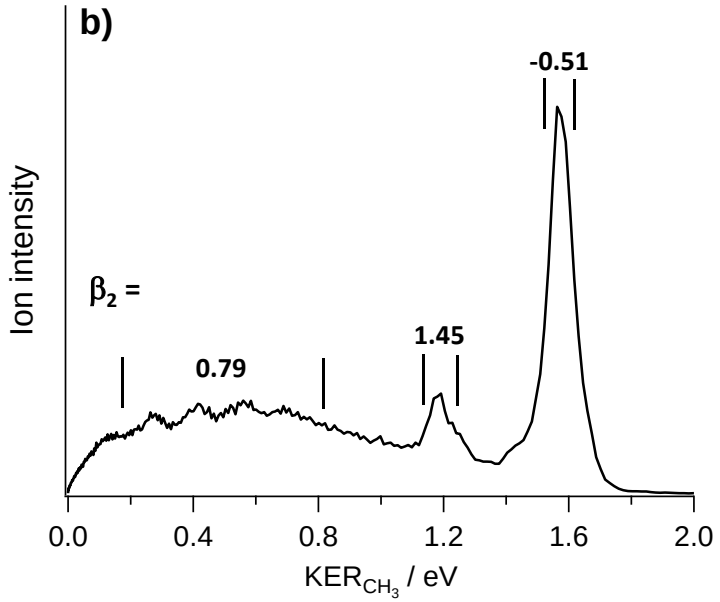

Fig. S7-b: *Two-color CH_3 KER spectrum for peak 6, found in 2hv REMPI spectra at 78334 cm^{-1}.*

Fig. S7

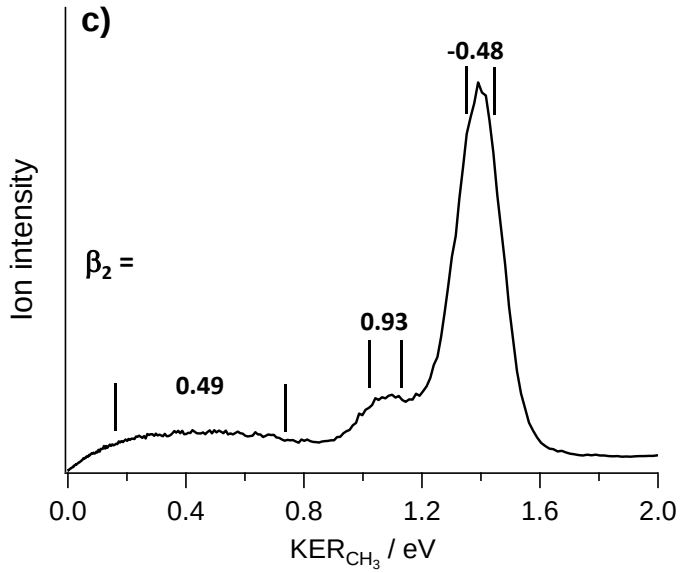

Fig. S7-c: *Two-color CH_3 KER spectrum for off resonance, found in 2hv REMPI spectra at 79051 cm^{-1}.*

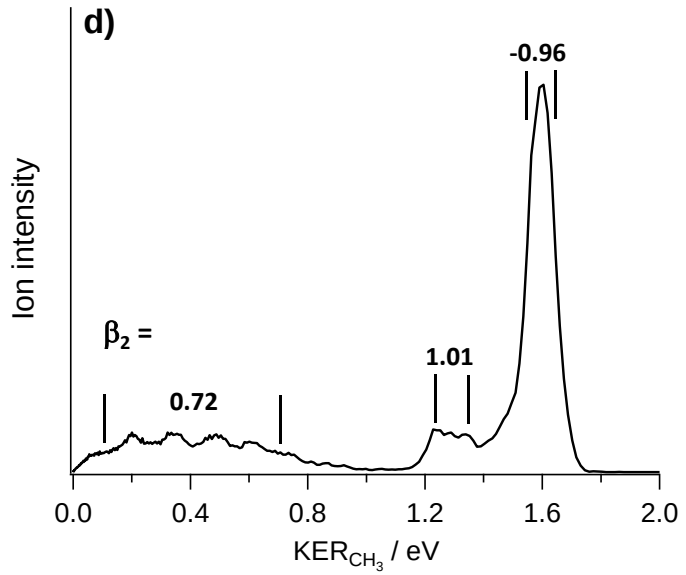

Fig. S7-d: *Two-color CH_3 KER spectrum for peak 7, found in 2hv REMPI spectra at 79610 cm^{-1}.*

Fig. S8

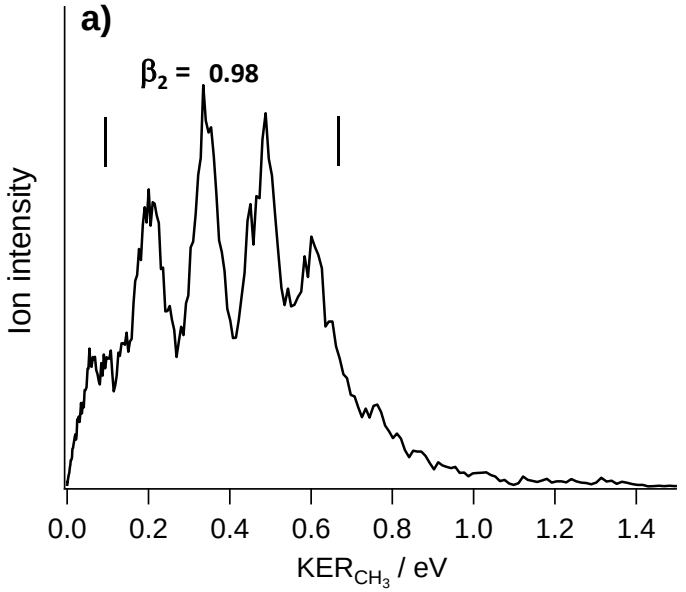

Fig. S8-a: *Probe laser CH_3 KER spectrum for 0_0^0, found in 2hv REMPI at 59972 cm^{-1}.*

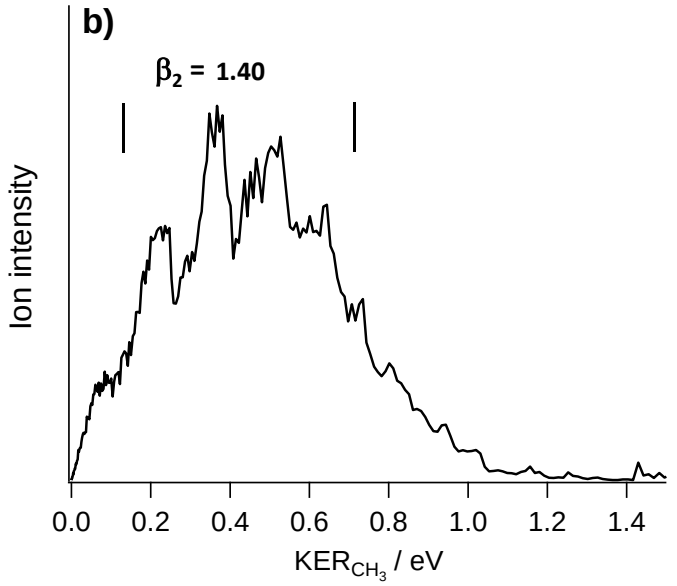

Fig. S8-b: *Probe laser CH_3 KER spectrum for 1_1^1, found in 2hv REMPI at 59898 cm^{-1}.*

Fig. S8

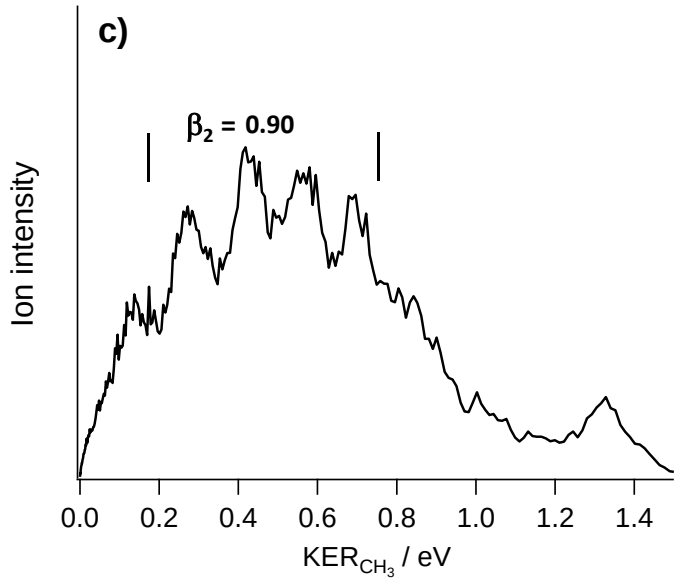

Fig. S8-c: *Probe laser CH_3 KER spectrum for 2_1^1, found in 2hv REMPI at 60698 cm^{-1}.*

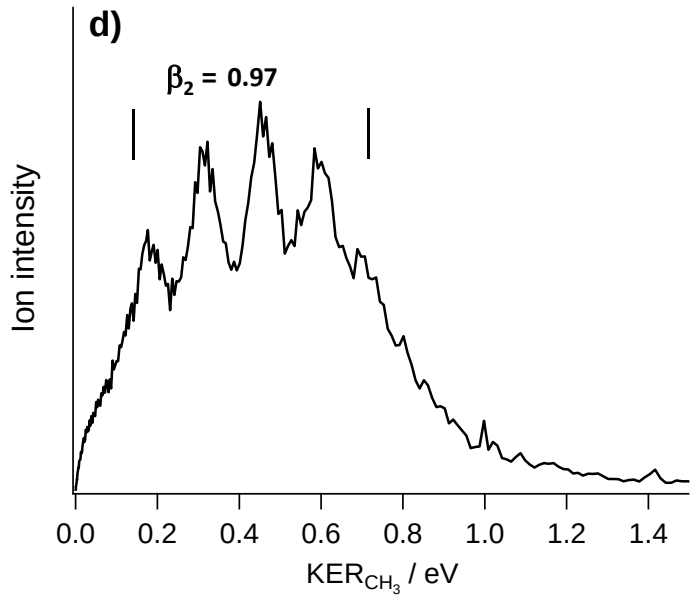

Fig. S8-d: *Probe laser CH_3 KER spectrum for 2_2^2, found in 2hv REMPI at 61387 cm^{-1}.*

Fig. S9

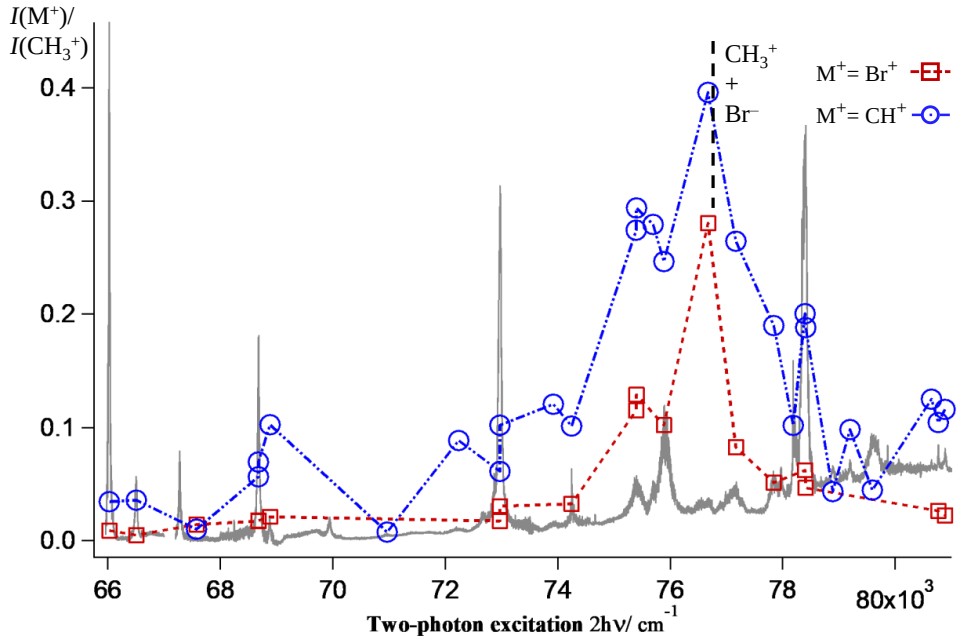

Fig. S9: *Ion signal intensity ratios for masses $I(Br^+)/I(CH_3^+)$ (red open squares) and $I(CH^+)/I(CH_3^+)$ (blue open circles) as a function of two-photon excitation wavenumber, along with the MPI spectrum from CH_3^+ ions. The threshold for ion-pair formation ($CH_3^+ + Br^-$) is indicated as a black vertical broken line.*

5 Summary and conclusion

5.1 HBr

The MR-REMPI spectra in the two-photon excitation region of 84 740 – 85 120 cm^{-1} due to transitions from the ground state ($X^1\Sigma^+(\Omega = 0^+; v'= 0)$) of $H^{79}Br$ and $H^{81}Br$, revealed rotational lines due to two-photon resonant transitions to the $6p\pi^3\Sigma^-(\Omega = 0^+; v'= 0)$ Rydberg state and the $V^1\Sigma^+(\Omega=0^+; v'= m+17)$ ion-pair state (henceforth denoted $6p\pi(0)$ and $V(m + 17)$). On either side of the Q-branch observed for $6p\pi(0)$ there are the rotational lines for $J'= 7$ and $J'= 8$ of the $V(m+17)$ state. The singlet-triplet interaction ($^3\Sigma^- \leftrightarrow {}^1\Sigma^+$), having $\Delta\Omega = 0$, involves a relatively weak homogeneous coupling. Spectral perturbations were observed as LS- and LI-effect alterations, in particular for the $J'= 7$ and $J'= 8$ rotational lines of the $6p\pi(0)$ Rydberg state. The localized LS-effects, observed, are found to be due to near-degenerate interactions between the states, for couplings of rotational levels, close in energy, with same J' quantum numbers. Exploration of ion intensity ratios $I(^{79}Br^+)/I(H^{79}Br^+)$ and $I(H^+)/I(H^{79}Br^+)$ for Q rotational line intensities, $J' = 2 - 9$, of the $6p\pi(0)$ spectrum, showed relative rise in signal intensities for fragment ions, peaking at $J'= 8$, with respect to the parent ion formation around $J' = 6 - 9$. This further indicated interaction between $6p\pi(0)$ and $V(m + 17)$. It is believed to involve an excitation at long internuclear distance (i.e. a long-range interaction) due to the ion-pair character in the state mixing.

H^+ ion slice images were recorded for two-photon resonant excitations to the $6p\pi(0)$ state. The excitation energy region included the Q-branch, $J' = 0 - 8$. Four major photo-fragmentation channels were identified, i.e. formations of H*(n = 2) + Br*, H*(n = 2) + Br, HBr^+ and HBr^+*. Additionally, a minor formation of H**(n = 3) + Br was observed. The channel contributions, based on the relative ion signal intensities, were found to differ significantly for J'. Thus, for low values of J' ($J' < 7$) the HBr^+/HBr^+* formation channels are found to dominate. For high values of J' ($J' > 6$) the H*(n = 2) + Br* formation increased significantly whereas the H*(n = 2) + Br and H**(n = 3) + Br channels grew marginally larger and the HBr^+/HBr^+* channel decreased. Furthermore, low v^+ states of HBr^+/HBr^+* were favoured in cases of excitations to a pure (unmixed) Rydberg state (i.e. for short range excitations), whereas high v^+ states of HBr^+/HBr^+* were formed in cases of transitions to a mixed state (i.e. for short range excitations). The angular distributions of H^+ for $J'= 0$-8, displayed shapes corresponding to strong parallel distributions with anisotropic parameters in the range of $\beta_2 = 1.5$-2. For the H*(n= 2) + Br/Br* channels the H^+ signals displayed shapes of angular distributions corresponding to isotropic distributions, with $\beta_2 \approx 0$, for $J'= 0$-2, whereas for higher J' these displayed some parallel character, ($\beta_2 = 1$ for H*(n = 2) + Br* ; $\beta_2=0.5$ for H*(n = 2) + Br)) for $J'= 8$. The signals for the H**(n = 3) + Br channel, on the other hand, exhibited perpendicular character with $\beta_2 \approx -0.5$ for $J'= 7 - 8$.

5.2 DCl

A mixture of HCl and DCl gas, was analyzed by MR-REMPI for two-photon resonant excitations to Rydberg and ion-pair states, in the energy region of 80 500 – 89 500 cm^{-1}. Mass spectra were recorded for H^iCl^+, D^iCl^+, $^iCl^+$, H^+ and D^+, with i = 35,37. Signals due to known REMPI spectra of $H^{35}Cl$ were used for wavelength calibration. Nine spectral bands for transitions to Rydberg states, for v'= 0 were assigned. Furthermore, spectral bands for the vibrational states v'= 0 - 3 of the $E^1\Sigma^+$ and $F^1\Delta_2$ Rydberg states were assigned. Five new bands were identified for transitions to Rydberg states, i.e. for $E^1\Sigma^+(v'=1, v'=3)$, $F^1\Delta_2(v'=3)$, $I^1\Delta_2(v'=0)$ and $i^3\Delta_2(v'=0)$. The excitations to the ion-pair state $V^1\Sigma^+(\Omega=0^+)$, revealed eighteen bands due to transitions to vibrational states v'= 11-28, thereof eight new bands for v'=11, 22-28.

Strongest intensity of spectral lines were observed for the $^{1,3}\Delta_2(v'=0)$ states (i.e. for $\Delta\Omega = 2$ and $\Delta\Lambda = 2$). On the other hand spectra due to transitions to the $^{1,3}\Delta_1$(v'= 0) and $^{1,3}\Pi_1$(v'= 0) states were much less intense and displayed fewer rotational lines. Spectra of Π and Δ states exhibited O, P, Q, R and S lines. The $F^1\Delta_2$ state vibrational spectra, decreased in intensity from v'= 0 to v' = 3, with a particularly weak Q, R and S lines for the $F^1\Delta_2(v'=3)$ state. The spectrum for the $g^3\Sigma^-$ state displayed O, Q and S lines, whereas only Q lines were observed for other $^{1,3}\Sigma$ Rydberg states as well as for the vibrational states of $V^1\Sigma^+$. Mainly DCl^+ ions were detected for pure (unmixed) Rydberg states (e.g. $^1\Delta$, $^3\Delta$ states), whereas Cl^+, D^+ as well as DCl^+ ions were observed for those mixed (e.g. $^1\Sigma$ states) with the ion-pair state. In the latter case long-range excitations, induced by the ion-pair character of the mixed states could explain this observation difference. A comparison was made between our results for DCl and those by Green *et al*. for HCl,[11-13] with respect to effects of the $V^1\Sigma^+$ and $^1\Sigma^+$ states homogeneous interactions (see paper 3, chapter 4.3). Non-degenerate interactions were observed from shifts of near lying vibrational bands in both spectra. Evaluated rotational constants, *B'*, as a function of vibrational levels, for the $V^1\Sigma^+$ state showed shifts to higher values for those in the vicinity of vibrational levels of the $E^1\Sigma^+$ and $H^1\Sigma^+$ Rydberg states, indicating level-to-level interactions between the ion-pair state and the Rydberg states. Chlorine isotope shifts of $D^{35}Cl$ and $D^{37}Cl$ were derived from the spectral bands of the $V^1\Sigma^+$ state. Observed alterations in isotope shifts, depending on energy differences of vibrational levels for the $V^1\Sigma^+$ and $E^1\Sigma^+$ states, were further indications of state interactions.

5.3 CH and CD

Photofragmentation processes for formation of the CH radical were studied. Two-photon resonant excitations to Rydberg states of $CHBr_3$ in the energy region of 76 000 – 84 000 cm^{-1} (one-photon excitation region of 38 000 – 42 000 cm^{-1}) were performed. The excitations formed the CH*($A^2\Delta$; v'= 0) Rydberg state, along with ground state Br_2 and Br/Br*, by photodissociation. CH*($A^2\Delta$; v'= 0) was detected by (1 + 1)REMPI. A weak spectral structure for CH^+ was observed in the one-photon excitation region of 40 380 – 41 150 cm^{-1} which was assigned to the CH**($D^2\Pi$; v'= 2). Peaks were assigned to P, Q, and R rotational lines based on simulation calculations and spectroscopic constants derived. Peaks exhibited large spectral linewidth (4 - 6 cm^{-1}) attributed to short lifetime of excited states. Therefore, splitting of peaks due to the two transitions, F_1[CH**($D^2\Pi$; Ω = 3/2) ← CH*($A^2\Delta$;

$\Omega = 5/2)$] and F_2[CH**($D^2\Pi$; $\Omega = 1/2$) ← CH*($A^2\Delta$; $\Omega = 3/2$)] could not be resolved except for high rotational quantum numbers. Position of bandheads formed the basis for further simulation analysis of the

More spectral features observed were attributed to one-photon transitions from CH*($A^2\Delta$) to other near lying Rydberg states, i.e. the *(3)*$^2\Pi$(v'=0), *(4)*$^2\Pi$(v'=0) and *(3)*$^2\Sigma^+$(v'=0) states. These have already been reported, both experimentally and theoretically, in the energy region of concern. Also reported in this energy region is a repulsive state, $^2\Pi$, which is predicted to interact strongly with the $^2\Pi$ Rydberg states. The total spectral structure for CH could not be assigned easily. Further clarification was sought by exploring and comparing the corresponding CD spectrum by CD^+ detection for REMPI of $CDBr_3$. The spectra were found to differ significantly. Thus, linewidths of the spectra were found to be smaller for CD than for CH which allowed peaks splittings (see above) to be resolved. This brought significant clarity to the spectral analysis. New line series were assigned and band origins for the *(4)*$^2\Pi$(v'=0) and *(3)*$^2\Sigma^+$(v'=0) states identified. Unassigned spectral features were assigned to the *(3)*$^2\Pi$(v'=0) state.

5.4 REMPI and VMI of CH_3Br; One vs. Two colour excitation schemes

5.4.1 MR-REMPI of CH_3Br

MR-REMPI spectra of CH_3Br were recorded for the two-photon resonant excitation energy region of 66 000 – 80 000 cm^{-1}. Ion signals due to resonant transitions from the ground state of CH_3Br to a number of Rydberg states [Ω_c]*nl*;ω (Ω_c= 3/2, 1/2; ω = 0, 2; *l* = 1(*p*), 2(*d*); n*p* = 5-7, n*d* = 4-6) and various vibrational states (ν_1, ν_2, ν_3) were identified. Ion intensities vary as, $CH_3^+ > CH_2^+ > CH^+ > C^+ > (CBr^+, Br^+)$.

Relative ion intensities, $I(M^+)/I(CH_3^+)$, for $M^+ = CH_2^+$, CH^+ and Br^+, were found vary with wavenumber and to reach maxima as the values got closer to the ion-pair threshold followed by sudden drop beyond the limits. The ion intensity ratio $I(CBr^+)/I(CH_3^+)$, however, remained unchanged.

5.4.2 One colour excitation scheme

Ion slice- and photoelectron images, as well as MR-MPI (see above), were used to explore the multiphoton dynamics of CH_3Br in a one-colour excitation scheme. Slice images of the CH_3^+ and Br^+ photoproducts for ten two-photon resonant transitions to np and nd Rydberg states of the parent molecule were recorded. KERs were derived from the images and anisotropy parameters were extracted from the angular distributions of the ions to identify and characterize the dynamic processes involved. The CH_3^+ ion forms the strongest signals in REMPI of CH_3Br. The majority of the photoelectrons formed were due to one-photon ionization of different Rydberg states of methyl photofragment (CH_3**). The CH_3** states were formed by two-photon resonant excitation to parent molecular Rydberg states followed by one-photon excitation to metastable, superexcited molecular states ($CH_3Br^{\#}$) which then dissociated to form CH_3**(*Ry*; $\nu_1\nu_2\nu_3\nu_4$) along with Br/Br*. This mechanism was observed for all the excitation wavelengths and it dominated for all except two of these wavelenghts. A

correlation between the parent Rydberg states excited and CH_3** formed was found to be evident. For the highest excitation energies, two additional channels were found to be present, both forming $CH_3(X;\ v_1v_2v_3v_4)$ + Br/Br*. The former channel is a one-photon photolysis via the A band of CH_3Br to form CH_3 and Br/Br*. The latter of these involves a dissociation of the metastable, superexcited $CH_3Br^{\#}$ state to produce CH_3 and Br/Br* prior to ionization. All the three-photon excitations, forming the metastable superexcited ($CH_3Br^{\#}$) states prior to dissociating to form the CH_3 Rydberg states (CH_3**) along with Br/Br*, appeared as broad peaks at low energies in the KERs. For the three highest excitation energies applied, high kinetic energy fragments of $CH_3(X)$ and Br/Br* were also formed from $CH_3Br^{\#}$. The one-photon photolysis of CH_3Br forming $CH_3(X;\ v_1v_2v_3v_4)$ + Br/Br*, was observed as strong sharp peaks in the KER spectra.

5.4.3 Two colour excitation scheme

Ion slice images were recorded for CH_3Br in a two-colour / pump-and-probe excitation scheme. A selection of resonant excitations (pumping) to np/nd molecular Rydberg states in the energy region of 66 000 – 80 000 cm^{-1} for CH_3Br were performed. Slice images for Br^+ and CH_3^+ were recorded for multiphoton excitations of CH_3Br followed by probing of the Br, Br* and $CH_3(X,\ v_1v_2v_3v_4)$ photofragments by REMPI (two-colour experiments). Measurements were performed for seven pump. The probing of Br, Br* and $CH_3(X,\ v_1v_2v_3v_4)$ was done by (2 + 1) REMPI for resonance excitations to Rydberg states of bromine (Br**) and CH_3 (CH_3**($3p^2A_2$)). Slice images of the Br^+ and CH_3^+ photoproducts were recorded for 1) -the pump excitations, 2) -the probe excitations, independently, as well as for 3) -the combination of pump and probe excitations. Kinetic energy release spectra (KERs) as well as angular distributions were derived from the images. Relevant fit parameters (β_2 and β_4) were derived from the angular distributions.

For all the pump excitations the major photofragmentation channel was found to involve three-photon excitation of the molecule to $CH_3Br^{\#}$ state(s) followed by dissociation to form Rydberg states of CH_3** along with Br/Br* as mentioned before (see 5.4.2). The REMPI detection of the fragment species (Br, Br* and $CH_3(X,\ v_1v_2v_3v_4)$) further revealed predissociation channels for the n*p* and n*d* molecular Rydberg states following the two-photon resonance excitations as well as one-photon photodissociation. Comparison of results for resonant excitations to *p*/*d* molecular Rydberg states and 5*s* Rydberg states reveals a dramatic difference in the overall excitation dynamics following three-photon excitations. In the former case $CH_3Br^{\#}$ is primarily found to dissociated to form CH_3** Rydberg states, whereas in the latter case $CH_3Br^{\#}$ largely autoionizes to form CH_3Br^+ in the ground state. Abrupt variations in relative ion signal intensities and dissociation channels associated with the ion-pair energy threshold strongly suggest that the dynamics of multiphoton dissociation and ionization via the molecular Rydberg states is affected by Rydberg to ion-pair state interactions.

5.5 Conclusion

The multiphoto-fragmentation processes which have been presented here for various halogen containing reagents involve photodissociation and photoionization processes, resonant and non-resonant excitations as well as autoionization. The major processes, common to number of molecular systems, apparently can be generalized, to some extent. In what follows the major common processes are summarized, categorized by initial excitations of parent molecule (AB) (where initial step(s) is(are) in *italics*):

One-photon:

$AB + h\nu \rightarrow AB^*$ *Non-resonant excitation* (36)

$AB^* \rightarrow A + B$ Dissociation (36a)

$A + nh\nu \rightarrow A^+ + e^-$ Multiphoton ionization (36a)

Two-photon:

$AB + 2h\nu \rightarrow AB^{**}$ *Two-photon resonant excitation* (37)

$AB^{**} + h\nu \rightarrow AB^+ + e^-$ Photoionization (37a)

or

$AB^{**} \rightarrow A^{**} + B$ Dissociation (37b)

$A^{**} + h\nu \rightarrow A^+ + e^-$ Photoionization (37b)

or

$AB^{**} \rightarrow A + B$ Dissociation (37c)

$A + nh\nu \rightarrow A^+ + e^-$ Multiphoton ionization (37c)

Three-photon:

$AB + 2h\nu \rightarrow AB^{**}$ *Two-photon resonant excitation* (38)

$AB^{**} + h\nu \rightarrow AB^{\#}$ *Photoexcitation* (38)

$AB^{\#} \rightarrow A^+ + e^-$ Autoionization (38a)

or

$AB^{\#} \rightarrow A^{**} + B$ Dissociation (38b)

$A^{**} + h\nu \rightarrow A^+ + e^-$ Photoionization (38b)

or

$AB^{\#} \rightarrow A + B$ Dissociation (38c)

$A + nh\nu \rightarrow A^+ + e^-$ Multiphoton ionization (38c)

or

$AB^{\#} \rightarrow AB^+ + e^-$ Autoionization (38d)

$AB^+ + h\nu \rightarrow AB^{+\#} \rightarrow A^+ + B$ Photodissociation (38d)

AB, AB*, AB** and $AB^{\#}$ are the molecule (AB) in ground-, valence-, Rydberg- and superexcited- states, respectively. AB^{+}, A^{+}(or B^{+}) are the molecular and fragment ions, respectively. $h\nu$ and e^{-} are the photon energy and the electron, respectively.

One-, two- and three-photon excitation processes have been observed, forming ground state fragments via dissociation prior to ionization. Parent molecular ion formation was observed for diatomic hydrogen halide molecules, whereas fragment ions were observed in interaction with the ion-pair states. Polyatomic molecules displayed either photodissociation processes or parent molecular ion formations, depending on the initial excitation step. Many excitation channels observed involved superexcited states ($AB^{\#}$), prior to fragmentation. Those type of processes are planned to be further investigated in the future by using a pump-and-probe experimental setup to explore further multiphoton dynamics of molecules.

6 Additional observations and future work

6.1.1 HCl and DCl

Spectral perturbations in the REMPI spectra of DCl and HCl revealed strong homogenous ($\Delta\Omega = 0$) interaction between the $E^1\Sigma^+$ Rydberg state and the $V^1\Sigma^+$ ion-pair state. These interactions cause a repulsion of rovibrational energy levels with the same J' quantum numbers, inversely proportional to the energy difference. This appears as shifts of rotational lines and vibrational bands in the spectra of the interacting states. For DCl, the $E^1\Sigma^+(v'=0)$ level is claimed to be located between $V^1\Sigma^+(v'=14)$ and $V^1\Sigma^+(v'=15)$, energy wise[8, 85] whereas for HCl it is told to be between $V^1\Sigma^+(v'=10)$ and $V^1\Sigma^+(v'=11)$.[11, 12, 85] $E^1\Sigma^+(v'=1)$ is told to be located between $V^1\Sigma^+(v'=17)$ and $V^1\Sigma^+(v'=18)$ for DCl but between $V^1\Sigma^+(v'=14)$ and $V^1\Sigma^+(v'=15)$ for HCl (see Fig.19).

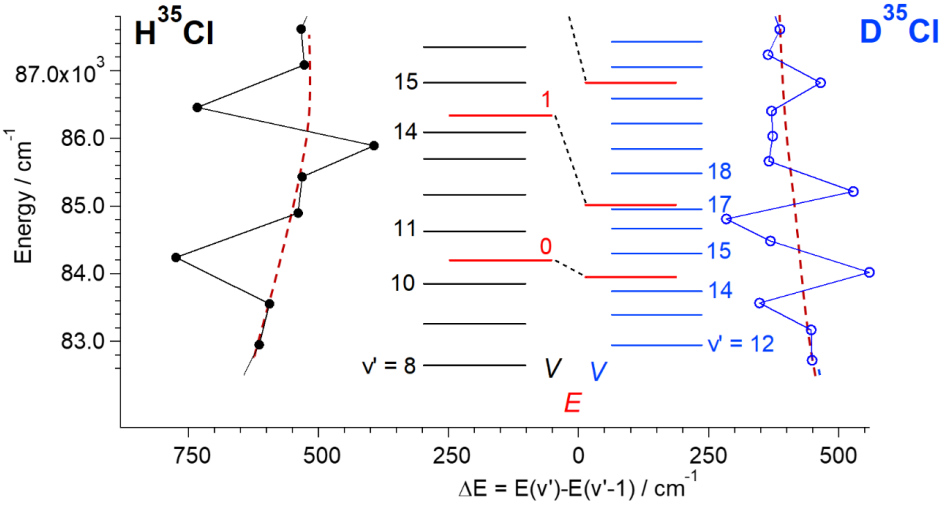

Figure 19 *$D^{35}Cl$ and $H^{35}Cl$: Vibrational energy levels for the $E^1\Sigma^+$(red) and $V^1\Sigma^+$ (blue ($D^{35}Cl$); black ($H^{35}Cl$)) states as well as vibrational energy level spacing ($\Delta v^0(v' + 1, v') = v^0(v' + 1) - v^0(v')$; cm^{-1}). Red vertical broken lines show expected unperturbed spectral behaviour.*

Fig. 19 shows observed energy spacings between vibrational levels for the $V^1\Sigma^+$state of HCl and DCl along with estimated spacings for unperturbed energy states. Clearly large deviations in the spacings (hence energy levels), from that to be expected for an unperturbed system, is observed. Due to the level-to-level repulsion effect of the interactions this appears as enhanced energy gaps of the v' levels for the V state nearest (above and below) in energy to those for the E state. Consequently, drops in the energy gaps for the V state, above and below

in energy, are to be expected. This latter effect is clearly observed for DCl, whereas, for HCl, $E^1\Sigma^+(v'=0)$ it is not. This could be due to incorrect assignments of the vibrational levels involved. Our first conclusion has led to the reassignment of band origin of states $E^1\Sigma^+(v'=0)$ and $V^1\Sigma^+(v'=11)$. Further investigation, including deperturbation calculations, is needed in order to verify this.

6.1.2 CH_3Br

KER spectra for CH_3Br derived from slice images of the CH_3^+ ion for the two-photon resonant excitations 77 165 and 79 610 cm^{-1} in one-colour experiments showed sharp peaks assigned to the formation of $CH_3(X; v_1v_2v_3v_4)$ + Br/Br* by one-photon photodissociation (see paper 4, chapter 4.4). The largest signal observed for 79 610 cm^{-1} was attributed to the formation of $CH_3(X; 0100)$. Further investigations by pump-and-probe experiments (see paper 5, chapter 4.5), however, led to reassignment of peaks. Thus, the largest signal, for the 79 610 cm^{-1} resonant excitation, is now assigned to the $CH_3Br(X; 000) + h\nu \rightarrow CH_3(X; 0000)$ + Br, dissociation channel, and corresponding peak for $CH_3(X; 0000)$ + Br* channel.

6.1.3 CH/CD

A weak and perturbed CH (CD) REMPI spectral structure recorded in one-colour REMPI of $CHBr_3$ ($CDBr_3$) (see paper 1, chapter 4.1) needs further clarification. Two-colour, pump and probe experiments might be useful for that purpose. Thus, by scanning (probing) the spectral region corresponding to transitions of $CH(A^2\Delta(v'=0))$ to higher lying Rydberg states after initial photodissociation (pumping) of $CHBr_3$ might help with further clarifications the CH spectral structure as well as dissociation channels involved.

Reference

1. R. P. Feynman, R. B. Leighton and M. Sands, *The Feynman Lectrures on Physics*, Addison-Wesley Publishing Company, Inc., Reading, MA, London, 2nd edn., 1964.
2. K. J. Laidler, J. H. Meiser and B. C. Sanctuary, *Physical Chemistry*, Houghton Mifflin Company, Boston, NY, 4th edn., 2003.
3. A. K. Ramdas and S. Rodriguez, *Rep. Prog. Phys.*, 1981, **44**, 1297.
4. I. Noda, Y. Liu and Y. Ozaki, *J. Phys. Chem.*, 1996, **100**, 8674-8680.
5. A. Hafliðason, H. Wang and Á. Kvaran, *Physical Chemistry Chemical Physics*, 2016, **18**, 1797-1806.
6. P. Glodic, D. Zaouris, P. C. Samartzis, A. Hafliðason and A. Kvaran, *Phy. Chem. Chem. Phys.*, 2016, **18**, 26291-26299.
7. A. Hafliðason, P. Glodic, G. Koumarianou, P. C. Samartzis and A. Kvaran, *Phy. Chem. Chem. Phys.*, 2018, **20**, 17423.
8. A. Hafliðason, H. Wang and A. Kvaran, *J. Mol. Spectrosc.*, 2017, **341**, 1-9.
9. C. Cohen-Tannoudji, B. Diu and F. Laloe, *Quantum Mechanics*, Hermann and John Wiley & Sons. Inc., Canada, 2005.
10. A. E. Douglas and F. R. Greening, *Can. J. Phys.*, 1979, **57**, 1650-1661.
11. D. S. Green, G. A. Bickel and S. C. Wallace, *J. Mol. Spectrosc.*, 1991, **150**, 303-353.
12. D. S. Green, G. A. Bickel and S. C. Wallace, *J. Mol. Spectrosc.*, 1991, **150**, 354-387.
13. D. S. Green, G. A. Bickel and S. C. Wallace, *J. Mol. Spectrosc.*, 1991, **150**, 388-469.
14. D. S. Green and S. C. Wallace, *J.Chem.Phys.*, 1992, **96**, 5857-5877.
15. D. Ascenzi, S. Langford, M. Ashfold and A. Orr-Ewing, *PCCP*, 2001, **3**, 29-43.
16. S. G. Tilford and M. L. Ginter, *J. Mol. Spectrosc.*, 1971, **40**, 568-579.
17. M. L. Ginter, S. G. Tilford and A. M. Bass, *J. Mol. Spectrosc.*, 1975, **57**, 271.
18. D. S. Ginter, M. L. Ginter and S. G. Tilford, *J. Mol. Spectrosc.*, 1981, **90**, 152.
19. D. S. Ginter, M. L. Ginter and S. G. Tilford, *J. Mol. Spectrosc.*, 1982, **92**, 40.
20. D. S. Ginter, M. L. Ginter, S. G. Tilford and A. M. Bass, *J. Mol. Spectrosc.*, 1982, **92**, 55.
21. R. F. Barrow and J. G. Stamper, *Proc. Roy.Soc.Ser.A.*, 1961, **263**, 259-276.
22. R. F. Barrow and J. G. Stamper, *Proc. Roy.Soc.Ser.A.*, 1961, **263**, 277-288.
23. J. A. Myer and J. S. R. Samson, *J.Chem.Phys.*, 1970, **52**, 716-718.
24. J. Nee, M. Suto and L. Lee, *J. Phys.B: At. Mol.Phys.*, 1985, **18**, L293-L294.
25. Á. Kvaran and H. Wang, *J. Mol. Spectrosc.*, 2004, **228**, 143-151.
26. K. Matthiasson, A. Kvaran, H. Wang, A. Bodi and E. Jónsson, *J. Chem. Phys.*, 2008, **129**, 164313.
27. K. Matthiasson, H. Wang and Á. Kvaran, *J. Mol. Spectrosc.*, 2009, **255**, 1-5.
28. K. Matthiasson, Á. Kvaran and H. Wang, *Journal of Chemical Physics*, 2009, **131**, 044324.
29. K. Matthiasson, J. Long, H. Wang and A. Kvaran, *J. Chem. Phys.*, 2011, **134**, 164302.
30. J. Long, H. Wang and A. Kvaran, *J. Mol. Spectrosc.*, 2012, **282**, 20-26.
31. J. Long, H. R. Hrodmarsson, H.Wang and A. Kvaran, *J. Chem. Phys*, 2012, **136**, 214315.
32. J. Long, H. Wang and A. Kvaran, *J. Chem. Phys.*, 2013, **138**, 044308.
33. H. R. Hróðmarsson, H. Wang and Á. Kvaran, *J. Mol. Spectrosc.*, 2013, **290**, 5-12.
34. B. G. Waage, A. Kvaran and H. Wang, *J. Chem. Phys.*, 2000, **113**, 1755-1761.

35. W. C. Price, *J. Chem. Phys*, 1936, **4**, 539-547.
36. T. Gougousi, P. C. Samartzis and T. N. Kitsopoulos, *J. Chem. Phys.*, 1998, **108**, 5742-5746.
37. J. G. Underwood and I. Powis, *Phys. Chem. Chem. Phys.*, 2000, **1**, 747-756.
38. R. Locht, B. Leyh, H. W. Jochims and H. Baumgartel, *Chemical Physics*, 2005, **317**, 73-86.
39. R. Locht, B. Leyh, D. Dehareng, H. W. Jochims and H. Baumgartel, *Chem. Phys.*, 2005, **317**, 87-102.
40. R. Locht, B. Leyh, D. Dehareng, K. Hottmann, H. W. Jochims and H. Baumgartel, *Chemical Physics*, 2006, **323**, 458-472.
41. R. Locht, B. Leyh, H. W. Jochims and H. Baumgartel, *Chem. Phys.*, 2009, **365**, 109-128.
42. D. A. Shaw, D. M. P. Holland and I. C. Walker, *J. Phys. B: At., Mol. Opt. Phys.*, 2006, **39**, 3549-3560.
43. T. Ridley, J. T. Hennessy, R. J. Donovan, K. P. Lawley, S. Wang, P. Brint and E. Lane, *J. Chem. Phys. A*, 2008, **112**, 7170-7176.
44. R. J. Donovan, J. T. Hennessy, K. P. Lawley and T. Ridley, *J. Chem. Phys.*, 2013, **138**, 134308.
45. V. Blanchet, P. C. Samartzis and A. M. Wodtke, *J. Chem. Phys.*, 2009, **130**, 034304.
46. A. Kvaran, H. Wang, K. Matthiasson and A. Bodi, *J. Phys. Chem. A*, 2010, **114**, 9991-9998.
47. D. W. Chandler, J. W. T. Jr., M. H. M. Janssen and D. H. Parker, *Chem.Phys.Letters*, 1989, **156**, 151-158.
48. W. P. Hess, D. W. Chandler and J. W. Thoman, *Chem. Phys.*, 1992, **163**, 277-286.
49. S. Eden, P. Limao-Vieira, S. V. Hoffmann and N. J. Mason, *Chemical Physics*, 2007, **331**, 232-244.
50. D. E. Robbins, *Geophys Res Lett*, 1976, **3**, 213-216.
51. B. Urban and V. E. Bondybey, *Journal of Chemical Physics*, 2002, **116**, 4938-4947.
52. K. A. Peterson and J. S. Francisco, *Journal of Chemical Physics*, 2002, **117**, 6103-6107.
53. G. N. A. Van Veen, T. Baller and A. E. De Vries, *Chem. Phys.*, 1985, **92**, 59-65.
54. A. M. Woodward, S. D. Colson, W. A. Chupka and M. G. White, *J. Phys. Chem.*, 1986, **90**, 274-278.
55. M. O. Hale, G. E. Galica, S. G. Glogover and J. L. Kinsey, *J. Phys. Chem.*, 1986, **90**, 4997-5000.
56. C. Escure, T. Leininger and B. Lepetit, *J. Phys. Chem.*, 2009, **130**, 244305.
57. F. Y. Wang, M. L. Lipciuc, A. Kartakoullis, P. Glodic, P. C. Samartzis, X. M. Yang and T. N. Kitsopoulos, *Phys. Chem. Chem. Phys.*, 2014, **16**, 599-606.
58. D. D. Xu, J. H. Huang, R. J. Price and W. M. Jackson, *Journal of Physical Chemistry A*, 2004, **108**, 9916-9923.
59. F. Y. Wang, M. L. Lipciuc, X. M. Yang and T. N. Kitsopoulos, *Phys. Chem. Chem. Phys.*, 2009, **11**, 2234-2240.
60. G. Herzberg, *Molecular Spectra and Molecular Structure; I. Spectra of Diatomic Molecules*, Van Nostrand Reinhold Company, New York, 2nd edn., 1950.
61. G. Herzberg and J. W. T. Spinks, *Atomic Spectra and Atomic Structure*, Dover Publications, NY, 1944.
62. S. Solomon, *Reviews of Geophysics*, 1999, **37**, 275-316.
63. J. H. Seinfeld and S. N. Pandis, *Atmospheric chemistry and physics: from air pollution to climate change* John Wiley and Sons, 2006.

64. M. J. Simpson, R. P. Tuckett, K. F. Dunn, C. A. Hunniford and C. J. Latimer, *Journal of Chemical Physics*, 2009, **130**.
65. E. Herbst, *Chem. Soc. Rev.*, 2001, **30**, 168.
66. J. I. Lunine, *Astrobiology*, Pearson - Addison-Wesley 2005.
67. A. M. Shaw, *Astrochemistry; From Astronomy to Astrobiology*, Wiley 2006.
68. N. Hoffmann, *Chem. Rev.*, 2008, **108**, 1052.
69. F. B. Mallory and C. W. Mallory, *Photocyclization of stilbenes and related molecules*, Robert E. Krieger Publishing company, 1988.
70. Q. Liu, L. Wu, R. Jackstell and M. Beller, *Nat. Commun.*, 2015, **6**, 5933.
71. A. Fridman, *Plasma Chemistry*, Cambridge University Press, NY, 1st edn., 2008.
72. D. W. Bauerle, *Laser Processing and Chemistry*, Springer, 2011.
73. W. Burmeister, *Berliner Diss. Verh. d. Deutsch. Phys. Ges.*, 1913, **15**, 589.
74. W. C. Price, *Proc. Roy. Soc. Ser. A*, 1938, **167**, 216.
75. S. G. Tilford, M. L. Ginter and J. T. Vanderslice, *J. Mol. Spectrosc.*, 1970, **33**, 505-519.
76. S. G. Tilford, M. L. Ginter and A. M. Bass, *J. Mol. Spectrosc.*, 1970, **34**, 327.
77. J. A. Coxon, P. G. Hajigeorgiou and K. P. Huber, *J. Mol. Spectrosc.*, 1988, **131**, 288-300.
78. J. A. Coxon and U. K. Roychowdhury, *Can. J. Phys.*, 1985, **63**, 1485-1497.
79. J. B. Nee, M. Suto and L. C. Lee, *J. Chem. Phys.*, 1986, **85**, 719-724.
80. J. B. Nee, M. Suto and L. C. Lee, *J. Chem. Phys.*, 1986, **85**, 4919.
81. Á. Logadóttir, Á. Kvaran and H. Wang, *J. Chem. Phys.*, 1998, **109**, 5856-5867.
82. A. Logadóttir, A. Kvaran and H. Wang, *J. Chem. Phys.*, 2000, **112**, 10811-10820.
83. H. R. Hrodmarsson, H. Wang and A. Kvaran, *J. Chem. Phys.*, 2014, **140**, 244304.
84. D. Zaouris, A. Kartakoullis, P. Glodic, P. C. Samartzis, H. R. Hrodmarsson and A. Kvaran, *Phy. Chem. Chem. Phys.*, 2015, **17**, 10468.
85. R. Callaghan, S. Arepalli and R. J. Gordon, *J. Chem. Phys*, 1987, **86**, 5273-5280.
86. H. R. Hrodmarsson, H. Wang and A. Kvaran, *J. Chem. Phys.*, 2015, **142**, 244312.
87. Y. Xie, P. T. A. Reilly, S. Chilukuri and R. J. Gordon, *J. Chem. Phys.*, 1991, **95**, 854 - 864.
88. T. A. Spiglanin, D. W. Chandler and D. H. Parker, *Chem.Phys.Lett.*, 1987, **137**, 414-420.
89. E. d. Beer, W. J. Buma and C. A. d. Lange, *J.Chem.Phys.*, 1993, **99**, 3252-3261.
90. D. S. Ginter and M. L. Ginter, *J. Mol. Spectrosc.*, 1981, **90**, 177-196.
91. S. T. Pratt and M. L. Ginter, *J. Chem. Phys.*, 1995, **102**, 1882-1888.
92. M. L. Ginter and S. G. Tilford, *J. Mol. Spectrosc.*, 1970, **34**, 206-221.
93. M. L. Ginter and S. G. Tilford, *J. Mol. Spectrosc.*, 1971, **37**, 159-178.
94. S. Arepalli, N. Presser, D. Robie and R. J. Gordon, *Chem. Phys. Lett.*, 1985, **117**, 64-66.
95. R. Callaghan and R. J. Gordon, *J. Chem. Phys.*, 1990, **93**, 4624-4636.
96. S. Manzhos, C. Romanescu, H. P. Loock and J. G. Underwood, *J. Chem. Phys*, 2004, **121**, 11802-11809.
97. T. P. Rakitzis, P. C. Samartzis, R. L. Toomes and T. N. Kitsopoulos, *Journal of Chemical Physics*, 2004, **121**, 7222-7227.
98. C. Romanescu and H.-P. Loock, *PCCP*, 2006, **8**, 2940-2949.
99. C. Romanescu and H. P. Loock, *J. Chem. Phys.*, 2007, **127**, 124304.
100. L. Pauling, 1932, **54**.
101. R. S. Mulliken, *Phys. Rev.*, 1936, **50**, 1017.
102. J. K. Jacques and R. F. Barrows, *Letters to the Editor*, 1959, 538-539.

103. J. G. Stamper, *Can. J. Phys.*, 1962, **40**, 1274.
104. P. Natalis, P. Pennetreau, L. Longton and J. E. Collin, *Chem. Phys.*, 1982, **73**, 191-201.
105. A. Kvaran, H. Wang and B. G. Waage, *Can. J. Physics*, 2001, **79**, 197-210.
106. H. Wang and Á. Kvaran, *J. of Molec. Structure*, 2001, **563-564**, 235-239.
107. W. C. Price, *J. Chem. Phys.*, 1936, **4**, 539-547.
108. G. C. Causley and B. R. Russell, *J. Chem. Phys.*, 1975, **62**, 848-857.
109. I. C. Lane and I. Powis, *J. Phys. Chem.*, 1993, **97**, 5803-5808.
110. D. Xu, J. S. Francisco, J. Huang and W. M. Jackson, *J. Chem. Phys*, 2002, **117**, 2578.
111. P. Sharma, R. K. Vasta, D. K. Maity and S. K. Kulshreshtha, *Chem. Phys. Lett.*, 2003, **382**, 637-643.
112. S. Chiang, Y. Fang, K. Sankaran and Y. Lee, *J. Chem. Phys*, 2004, **120**, 3270-3276.
113. M. L. Lipciuc and M. H. M. Janssen, *J Chem. Phys*, 2007, **127**, 224310.
114. J. Long, H. Wang and Á. Kvaran, *J. Phys. Chem. A*, 2014, **118**, 1826-1831.
115. N. J. Warwick, J. A. Pyle and D. E. Shallcross, *Journal of Atmospheric Chemistry*, 2006, **54**, 133-159.
116. P. Zou, J. Shu, T. J. Sears, G. E. Hall and S. W. North, *Journal of Physical Chemistry*, 2004, **108**, 1482-1488.
117. A. J. Drummond, J. R. Hickey, W. J. Scholes and E. G. Laue, *Nature*, 1968, **218**, 259-261.
118. R. S. Mulliken, *J Chem. Phys*, 1940, **8**, 382.
119. R. S. Mulliken, *Phys. Rev.*, 1942, **61**, 277.
120. R. S. Mulliken and E. Teller, *Phys. Rev.*, 1942, **61**, 283.
121. S. J. Paddison and E. T.-Roux, *J. Phys. Chem.*, 1998, **102**, 6191-6199.
122. C. H. Greene, *Nature*, 2009, **458**, 975-976.
123. L. Ji, Y. Tang, R. Zhu, Z. Wei and B. Zhang, *Spectrochim.Acta*, 2007, **67**, 273-280.
124. G. Herzberg and J. W. C. Johns, *The Astrophysical Journal*, 1969, **158**, 399-418.
125. J. E. Hesser and B. L. Lutz, *Astrophys. J.*, 1970, **159**, 703-718.
126. R. Anderson, D. Wilcox and R. Sutherland, *Nucl. Instr. and meth.*, 1973, **110**, 167-171.
127. P. F. Bernath, C. R. Brazier, T. Olsen, R. Hailey, W. T. M. L. Fernando, C. Woods and J. L. Hardwick, *Journal of Molecular Spectroscopy*, 1991, **147**, 16-26.
128. E. F. van Dishoeck, *Journal of Chemical Physics*, 1986, **86**, 196-214.
129. A. Metropoulos and A. Mavridis, *Chem. Phys. Lett.*, 2000, **331**, 89-94.
130. Y. Chen, J. Jin, L. Pei, X. Ma and C. Chen, *Journal of Electron Spectroscopy and Related Phenomena*, 2000, **108**, 221-224.
131. G. J. Vázquez, J. M. Amero, H. P. Liebermann, R. J. Buenker and H. Lefebvre-Brion, *Journal of Chemical Physics*, 2007, **126**, 164302-164313.
132. "Constants of diatomic molecules", NIST Chemistry WebBook, http://webbook.nist.gov/cgi/cbook.cgi?ID=C7698057&Units=SI&Mask=1000, (accessed May 2017).
133. J. M. Hollas, *Modern Spectroscopy*, John Wiley and Sons, 2004.
134. P. Rives, J. L. Teyssier, J. Galy, A. Birot, H. Brunet and H. Asselman, *J. Chem. Phys*, 1995, **102**, 1217.
135. J. Long, PhD PhD, University of Iceland, 2013.
136. WaveMetrics, *IgorPro, Technical graphing and data analysis software for scientists and engineers: https://www.wavemetrics.com/*, WaveMetrics, Inc. USA, 1988-2014.

137. C. M. Western, *PGOPHER, a Program for Simulating Rotational Structure, C. M. Western, University of Bristol, http://pgopher.chm.bris.ac.uk* University of Bristol 9.0.116 edn., 2003-2015.
138. D. W. Chandler and P. L. Houston, *J. Chem. Phys.*, 1987, **87**, 1445.
139. T. J. B. Eppink and D. H. Parker, *Rev.Sci.Instrum.*, 1997, **68**, 3477.
140. M. N. R. Ashfold and D. H. Parker, *Phy. Chem. Chem. Phys.*, 2014, **16**, 381.
141. R. N. Zare, *Mol. Photochem.*, 1972, **4**, 1.
142. C. R. Gebhardt, T. P. Rakitzis, P. C. Samartzis, V. Ladopoulos and T. N. Kitsopoulos, *Rev. Sci. Instrum.*, 2001, **72**, 3848.
143. V. Papadakis and T. N. Kitsopoulos, *Rev.Sci.Instrum.*, 2006, **77**, 5.

Appendix: Conference presentations

Posters

(2+n)REMPI Spectroscopy: State interactions and photofragmentations of CH_3Br. EFNÍS conference, Reykjavík, Iceland, November 2013

The $CH(A^2\Delta)$ spectra following REMPI of CH_mBr_{4-m}; m = 1,2,3: LONG-TERM PUZZLE REVISITED. The 23rd International Conference on High Resolution Molecular Spectroscopy, Bologna, Italy, September 2014

The $CH(A^2\Delta)$ spectra following REMPI of CH_mBr_{4-m}; m = 1,2,3: LONG-TERM PUZZLE REVISITED, (Upgraded version). SDGM2015: Annual meeting of the Spectroscopy and Dynamics Interest Group of the Royal Society of Chemistry, Nottingham, England, January 2015

Use of VMI and mass resolved REMPI to study the effect of state interaction on photofragmentation dynamics: HBr. SDGM2016: Annual meeting of the Spectroscopy and Dynamics Interest Group of the Royal Society of Chemistry, Coventry, England, January 2016

Talks

REMPI of Bromomethanes: Rydberg States—Photodissociation and Fragmentation. SDGM2015: Annual meeting of the Spectroscopy and Dynamics Interest Group of the Royal Society of Chemistry, Nottingham, England, January 2015

Víxlverkun ljóseinda við efni (e. Interaction between photons and matter). Science Day, The School of Engineering and Natural Sciences hosted the Science Day in Askja, Reykjavik, Iceland, October 2015

Norðurljósin (Aurora Borealis). Science Day, The School of Engineering and Natural Sciences hosted the Science Day in Askja, Reykjavik, Iceland, October 2016

Multiphoto-fragmentation of molecules: REMPI and VMI of HBr. 4th International Conference on Physical and Theoretical Chemistry, Dublin, Ireland, September 2017

Multiphoto-dissociation and ionization of molecules: Analysis via MR-REMPI, VMI and PES. Current topics in Chemistry and Biochemistry, Reykjavik, Iceland, December 2017